Applications of the Fokker-Planck Equation in Computational and Cognitive Neuroscience

D I S S E R T A T I O N

zur Erlangung des akademischen Grades

Doctor rerum naturalium
(Dr. Rer. Nat.)
im Fach Physik
Spezialisierung: Theoretische Physik
eingereicht an der
Mathematisch-Naturwissenschaftlichen Fakultät
Humboldt-Universität zu Berlin

von

M. Sc. Sebastian Vellmer

Präsidentin der Humboldt-Universität zu Berlin:
Prof. Dr.-Ing. Dr. Sabine Kunst

Dekan der Mathematisch-Naturwissenschaftlichen Fakultät:
Prof. Dr. Elmar Kulke

Gutachter:
1. Prof. Dr. Benjamin Lindner (HU Berlin)
2. Prof. Dr. Igor M. Sokolov (HU Berlin)
3. Prof. Dr. Magnus J.E. Richardson (University of Warwick)
Tag der mündlichen Prüfung: 02. Juli 2020

Abstract

This thesis is concerned with the calculation of statistics, in particular the power spectra, of point processes generated by stochastic multidimensional integrate-and-fire (IF) neurons, networks of IF neurons and decision-making models from the corresponding Fokker-Planck equations.

In the brain, information is encoded by sequences of action potentials, the spike trains that are emitted by its most important elements, the neurons. In studies that focus on spike timing and not on the detailed shape of action potentials, IF neurons that drastically simplify the spike generation have become the standard model since they are easy to use and even provide analytical insights. Stochastic IF neurons are particularly advantageous when studying the influence of noise on the firing variability and information transmission. One-dimensional IF neurons do not suffice to accurately model neural dynamics in many situations. However, the extension towards multiple dimensions yields realistic subthreshold and spiking behavior at the price of growing complexity. The first part of this work develops a theory of spike-train power spectra for stochastic, multidimensional IF neurons. From the corresponding Fokker-Planck equation, a set of partial differential equations is derived that describes the stationary probability density, the firing rate and the spike-train power spectrum. The equations are solved numerically by a finite-difference method for three special cases. The effect of temporally correlated input fluctuations, so-called colored noise, is studied by means of a one-dimensional Markovian embedding that generates either high-pass-filtered (cyan or white-minus-red) or low-pass-filtered (white-plus-red) noise as input for a leaky IF (LIF) neuron. The theory is also applied to white-noise-driven exponential IF neurons with adaptation and, as a three-dimensional example, to a LIF neuron driven by narrow-band noise. Many examples of solutions are presented and compared to simulations in order to test the theory, to display the variety of spectra and to gain a better understanding of the influence of neural features on the spike-train statistics. Furthermore, a set of equations is derived and tested to calculate the Padé approximation of the spectrum at zero frequency yielding an analytical function that is accurate at low frequencies and also matches the high-frequency limit.

In the second part of this work, a mean-field theory of large and sparsely connected homogeneous networks of LIF neurons is developed that takes into account the self-consistent temporal correlations of spike trains. Neural input, as the sum of many independent spike trains, is approximated by colored Gaussian noise that is generated by a multidimensional Ornstein-Uhlenbeck process (OUP) yielding a multidimensional IF neuron. In contrast to the first part, the coefficients of the OUP are initially unknown but determined by the self-consistency condition and define the solution of the theory. Since finite-dimensional OUPs cannot exhibit arbitrary power spectra, approximations are introduced and solved up to two-dimensional OUPs for one network. An alternative approach is used to explore heterogeneous networks in which the distribution of power spectra is self consistent. An iterative scheme, initially introduced for homogeneous networks, is extended to determine the distribution of spectra for networks with only distributed numbers of presynaptic neurons and, additionally, distributed synaptic weights.

In the third part, the theoretical framework of the Fokker-Planck equation is applied to the problem of binary decisions from diffusion-decision models (DDM). The theory considers the temporal statistics of decisions in situations in which a subject performs consecutive trials of a decision-making experiment. The decision trains are introduced in which spikes at the decision times capture the experimental results and encode correct and incorrect decisions by their signs. For the analytically tractable DDM, a Wiener process within two boundaries, the statistics of the decision trains including the decision rates, the distributions of inter-decision intervals and the power spectra are calculated from the corresponding Fokker-Planck equation. Nonlinear DDMs arise as the approximation of decision-making processes implemented in competing populations of spiking neurons. For these models, the threshold-integration method, an efficient numerical procedure that was originally introduced for IF neurons, is generalized to solve the corresponding Fokker-Planck equations and determine the decision-train statistics and the linear response of the decision rates.

Zusammenfassung

In dieser Arbeit werden mithilfe der Fokker-Planck-Gleichung die Statistiken, vor allem die Leistungsspektren, von Punktprozessen berechnet, die von mehrdimensionalen Integratorneuronen [Engl. integrate-and-fire (IF) neuron], Netzwerken von IF Neuronen und Entscheidungsfindungsmodellen erzeugt werden.

Im Gehirn werden Informationen durch Pulszüge von Aktionspotentialen kodiert, die von den wichtigsten Komponenten, den Neuronen, ausgesandt werden. In Fällen, in denen das Hauptaugenmerk auf neuronale Pulszeiten gerichtet ist und die genaue Form der Aktionspotentiale eine untergeordnete Rolle spielt, haben sich IF Neurone als Standardmodelle etabliert, in denen der Mechanismus der zur Erzeugung von Aktionspotentialen dient, radikal vereinfacht wird. Die Modelle sind leicht anzuwenden und ermöglichen sogar analytische Lösungen, wodurch insbesondere ihre stochastischen Versionen geeignet sind, um den Einfluss neuralen Rauschens auf die Variabilität der Pulszeiten und auf die Transmission von Information zu untersuchen. Allerdings sind eindimensionale IF Modelle in vielen Situationen zu einfach und können beobachtetes Pulsverhalten nicht beschreiben. Abhilfe kann durch die Erweiterung hinzu mehrdimensionalen IF Neuronen geschafft werden, die realistische Modelle bezüglich der unterschwelligen Spannungsdynamik und auch des Pulsverhaltens hervorbringen kann. Im ersten Teil dieser Arbeit wird eine Theorie zur Berechnung der Pulszugleistungsspektren von stochastischen, multidimensionalen IF Neuronen entwickelt. Ausgehend von der zugehörigen Fokker-Planck-Gleichung wird hierzu ein System von partiellen Differentialgleichung abgeleitet, deren Lösung sowohl die stationäre Wahrscheinlichkeitsverteilung und Feuerrate, als auch das Pulszugleistungsspektrum beschreibt. Da keine analytische Lösung bekannt ist, werden die Lösungen für drei spezielle Neuronmodelle numerisch mit einer finite-Differenzen-Methode bestimmt. Mithilfe einer eindimensionalen Markovschen Einbettung, die entweder hochpassgefiltertes (zyanes oder weiß-minus-rotes) oder tiefpassgefiltertes (weiß-plus-rotes) Rauschen generiert, wird der Effekt von Eingangsströmen mit zeitlich korrelierten Fluktuationen, auch als farbiges Rauschen bekannt, auf das Pulsverhalten eines leaky IF (LIF) Neurons untersucht. Die Theorie wird auch auf ein exponentielles IF Neuron mit Adaptationsstrom, das von weißem Rauschen getrieben wird, und, als ein dreidimensionales Beispiel, auf ein LIF Neuron, das von Schmalbandrauschen getrieben wird, angewandt. Viele Beispiele von Lösungen werden gezeigt und mit direkten numerischen Simulationen verglichen, einerseits um die Theorie zu testen, andererseits um die Vielfältigkeit der Spektren aufzuzeigen und ein Verständnis zu entwickeln, wie sich neuronale Eigenschaften auf die Pulszugstatistiken auswirken. Zuletzt werden Gleichungen hergeleitet und getestet, mit denen eine Padé Approximation berechnet werden kann. Das Resultat der Annäherung ist eine analytische Funktion, die das Leistungsspektrum bei niedrigen Frequenzen präzise beschreibt und auch im Hochfrequenzlimit exakt ist.

Im zweiten Kapitel wird eine Molekularfeldtheorie für große, spärlich verbundene und homogene Netzwerke aus LIF Neuronen entwickelt, in der berücksichtigt wird, dass die zeitlichen Korrelationen von Pulszügen selbstkonsistent sind. Neuronale Eingangsströme, die sich aus der Summe vieler unabhängiger Pulszüge ergeben, werden durch farbiges Gaußsches Rauschen modelliert, das von einem mehrdimensionalen Ornstein-Uhlenbeck Prozess (OUP) erzeugt wird, sodass sich ein mehrdimensionales IF Neuron ergibt. Die Koeffizienten des OUP sind vorerst unbekannt und sind als Lösung der Theorie über die Selbstkonsistenz der Leistungsspektren des Eingangsstroms und des Pulszuges definiert. Allerdings kann durch endlichdimensionale OUPs kein Rauschen mit beliebigem Leistungsspektrum erzeugt werden. Daher werden Annäherungen zu der Theorie mit endlichdimensionalen OUPs eingeführt und für ein Beispielnetzwerk mit ein- und zweidimensionalen OUPs gelöst. Um heterogene Netzwerke zu untersuchen, in denen die Verteilung von Pulszugleistungsspektren selbstkonsistent ist, wird ein anderer Ansatz gewählt. Eine iterative Methode, die ursprünglich für homogene Netzwerke eingeführt wurde, wird erweitert um die selbstkonsistente Verteilung zu ermitteln. Zwei Beispielnetzwerke, die einerseits mit einer verteilten Anzahl von präsynaptischen Verbindungen und, im zweiten Fall, mit zusätzlich verteilten synaptischen Gewischten

ausgestattet sind, werden untersucht.

Im dritten Teil wird die Fokker-Planck-Gleichung auf Binärentscheidungen von Diffusionsentscheidungsmodellen [Engl. diffusion-decision models (DDM)] angewendet. Die Theorie ist für Situationen entworfen, in denen ein Subject in einem Experiment sequentielle Entscheidungen in aufeinander folgenden Durchläufen fällt. Zur Beschreibung der experimentellen Resultate werden die Entscheidungszüge eingeführt, in denen Pulse zu den Entscheidungszeiten korrekte und inkorrekte Entscheidungen mit ihrem Vorzeichen kodieren. Explizite Gleichungen für die Entscheidungszugstatistiken, genauer die Entscheidungsraten, Intervallverteilungen zwischen Entscheidungen und Leistungsspektren, werden für den einfachsten und analytisch lösbaren Fall von DDMs, einem Wiener Prozess innerhalb zweier Grenzen, von der Fokker-Planck-Gleichung hergeleitet. Aus der Implementierung von Entscheidungsprozessen in neuronalen Netzwerken gehen nichtlineare DDMs hervor. Für diese Modelle wird die Schwellwertintegrationsmethode [Engl. threshold-integration method] erweitert, die ursprünglich zur Bestimmung der Pulszugstatistiken von nichtlinearen IF Neuronen eingeführt wurde. Diese Methode wird auf Modelle mit zwei Schwellen verallgemeinert, um effizient Lösungen der Fokker-Planck-Gleichung zu bestimmen und damit die Statistiken von Entscheidungszügen und die Suszeptibilitäten der Entscheidungsraten zu berechnen.

List of symbols

Mathematical notation	**Meaning**
$\delta(x)$	Dirac delta function
$\delta_{i,j}$	Kronecker symbol
$\bar{\delta}_{i,j} = 1 - \delta_{i,j}$	'*Anti*'-Kronecker symbol
$\langle x \rangle$	ensemble average
$\xi(t)$	Gaussian white noise of unit intensity
$\partial_x f(x)$	derivative of $f(x)$ with respect to x
$f(x)\Big\vert_{x=a} = f(a)$	value of f at a
$\tilde{f}(\omega) = \int_0^\infty dt\, e^{i\omega t} f(t)$	Fourier transformed over positive half space
$(f * g)(t) = \int_0^\infty dt'\, f(t')g(t-t')$	convolution of f and g
$\exp(x)$	exponential function
$\sinh[x] = [\exp(x) - \exp(-x)]/2$	hyperbolic sine
$\Theta(x)$	Heaviside function
$\mathrm{Re}(x)$	real part of the complex argument
$\mathcal{D}_a(x)$	parabolic cylinder function
$\mathrm{erf}(x) = \frac{2}{\sqrt{\pi}} \int_0^x du\, e^{-u^2}$	error function
$\arg\min_x f(x)$	argument that minimizes $f(x)$
$x \bmod y$	modulo operation
$\mathbf{A}$	matrix
$\mathbf{A}^{-1}$	inverse matrix
$\mathbf{A}^\intercal$	transposed matrix
$\det(\mathbf{A})$	determinant of matrix $\mathbf{A}$
$\mathrm{adj}(\mathbf{A})$	adjoint matrix of $\mathbf{A}$

Contents

1 Introduction

Created by billions of years of evolution, the human brain is a sophisticated machine equipped with the desire and possibly even the capacity to comprehend its own mechanisms. Compared to other measurement difficulties overcome by modern physics, the spatial and temporal scales at which processes happen in the brain can be captured relatively easily (Kandel et al., 2000). The challenging problems arise when one attempts to reverse engineer the brain due to its complexity at different length scales, the lack of symmetry, the uncertainty around which dynamical details are vital for specific tasks and the fact that sensitive living tissue is examined. While microscopic ion channels and single synapses may be studied by the detailed dynamics of the underlying ions and molecules, single nerve cells, neural networks and macroscopic brain regions are much to complex and have to be described by abstract mathematical models that are accompanied by a certain degree of simplification (Koch, 1999; Dayan and Abbott, 2001; Gerstner et al., 2014). When linking the dynamics of the brain at different scales with macroscopic behavior, it is impossible to establish *a priori* which details are essential and which might be neglected in a simplified model in order to capture a certain function. For a comprehensive description of the brain, various models must be adapted to fit specific problems and then be assembled like puzzle pieces into a bigger picture. Hence, it is a crucial task for scientists working in the fields of computational neuroscience and neurophysics to create models that reproduce and predict experimental findings and then study them by developing and applying mathematical methods.

It is widely accepted that information in the brain is encoded by sequences of electric pulses, the spike trains, that are emitted by the neurons. Attempts to decipher these neural codes by using approaches from information theory are work in progress and remain a challenging task. Since *in vivo* neurons are subject to many sources of noise [see for instance Holden (1976); Tuckwell (1989)], the timing of single spikes is unreliable and its relevance regarding information transmission and processing can be questioned. For the description of neural systems, stochastic models are required that can be studied by methods of statistical physics in order to understand, for example, how fluctuations influence the statistics of neural spike trains. An appropriate approach to gain insights in the dynamics of stochastic systems is given by the application of the Fokker-Planck equation, i.e. a partial differential equation describing the temporal evolution of the probability density (Risken, 1984). By the determination of the solution of the Fokker-Planck equation corresponding to stochastic neuron models, analytical formulas have been derived for the spike-train statistics [see for instance Ricciardi (1977); Brunel and Sergi (1998); Schwalger et al. (2015)] and the dynamics of spiking neural networks

have been investigated by mean-field approaches [see for instance (Brunel, 2000)]. Recorded neural spike-trains are characterized by non-trivial temporal statistics that depend on the single-neuron properties, on the dynamics of the surrounding network that generates neural input, and on the connection between them. Experimentally measured correlations might be useful to gain insights in the underlying mechanisms of a neural network. Furthermore, it cannot be excluded that the temporal correlations of spike trains serve a purpose regarding the computations in the brain, hence, they are worth to be studied in detail. In this work, equations are derived that determine the temporal correlations represented by the spike-train power spectra of stochastic neuron models and networks of spiking neurons by the application of the Fokker-Planck equation.

Linking the dynamics of neural populations to the solution of cognitive tasks is a crucial goal of neuroscience. For perceptual decision making, being one example of a cognitive task, the underlying mechanisms might be implemented by the interaction of neural populations. In order to study the decision-making process, it has been described by means of abstract and simplified models, for instance, the diffusion-decision model that, in turn, has been linked to the dynamics of neural networks. To account for noisy perception and fluctuations in the neural networks, the models of the decision making process are stochastic. Also in the case of the diffusion-decision model, the Fokker-Planck equation can be applied to determine its statistics.

This thesis is organized as follows: in the remainder of this chapter, I briefly introduce fundamentals of probability theory and stochastic processes used in this work to treat the stochastic neuron and decision models in order to calculate the statistics of the resulting pulse trains. Furthermore, I give a short presentation of the fundamental findings of neurobiology that are relevant for this work and briefly discuss common mathematical modeling approaches regarding nerve cells with the main focus on so-called integrate-and-fire (IF) neurons. I discuss how fluctuations can be incorporated in the IF models and how the resulting stochastic models can be treated by the Fokker-Planck equation.

In the second chapter, the Fokker-Planck equation is applied to derive an analytical set of equations that determine the spike-train statistics, in particular the spike-train power spectra, of general multidimensional IF neurons.

In the first part of the third chapter, I develop a mean-field theory for large and sparsely connected networks of one-dimensional leaky IF neurons that considers the self-consistency of the temporal correlations of spike-trains based on the equations derived in the second chapter. The second part of the chapter is devoted to the determination of self-consistent power spectra in heterogeneous networks by the extension of an iterative scheme.

In the fourth chapter, sequences of binary decisions as the result of a (hypothetical) experiment are regarded as pulse trains for which analytical formulas for their statistics are derived that are valid under the assumption of independent time intervals between decisions. By the solution of the corresponding Fokker-Planck equation, the statistics of decision trains generated by the simplest case of the diffusion-decision model, a Wiener process within two boundaries, are calculated analytically. To determine the solution of the Fokker-Planck equation corresponding to general nonlinear diffusion-decision models, I generalize an efficient numerical procedure and calculate the decision-train statistics and the susceptibilities of the

decision rates.

Most of the results presented in this thesis have been published in two papers. The results in Chapter 2 and the first part of Chapter 3 have been published in Vellmer and Lindner (2019). The extension of the iterative scheme for heterogeneous networks has been published in Pena et al. (2018). The results presented in the fourth chapter have been submitted to a scientific journal and the corresponding manuscript is currently under review.

1.1 Fundamentals of probability theory and stochastic processes

In this work, equations that determine the statistics of pulse trains that originate from stochastic systems are derived from the corresponding Fokker-Planck equation describing the temporal evolution of the systems' probability densities. In general, stochastic systems are characterized by continuous random variables, such that predictions can only be made for the probability density to find the system at a certain time in a certain state. Here I introduce and briefly discuss some basics of probability theory and stochastic processes that are used in this thesis. As the main reference I use the books from Risken (1984) and Gardiner (1985). First I introduce characteristic measures of stochastic processes.

Autocorrelation function and power spectrum

A stochastic process a can be characterized by its temporal correlation statistics represented by the *autocorrelation function*:

$$C_a(t,\tau) = \langle a(t+\tau)a(t)\rangle - \langle a(t)\rangle^2. \tag{1.1}$$

Here the angular brackets denote the ensemble average. In case of a stationary process, ensemble averages and thereby the autocorrelation function do not depend on the absolute time t but only on the time lag τ. Alternatively, the temporal correlations of a can be represented by the *power spectrum* $S_{aa}(\omega)$ that is given by:

$$S_{aa}(\omega) = \lim_{T\to\infty} \frac{\langle \tilde{a}(\omega)\tilde{a}^*(\omega)\rangle}{T}, \qquad \tilde{a}(\omega) = \int_0^T e^{i\omega t}[a(t) - \langle a(t)\rangle]\, dt. \tag{1.2}$$

To deal with well defined functions, I only consider the power spectrum of random variables minus their mean value. For a stationary process, the spike-train power spectrum is given by the Fourier-transformed autocorrelation function:

$$S_{aa}(\omega) = \int_{-\infty}^{\infty} d\tau\, e^{i\omega\tau} C(\tau) \tag{1.3}$$

[cf. Gardiner (1985) Eq. 1.5.38]. This relation is also known as the Wiener-Khinchin theorem.

Markov processes and Markovian embedding

Stochastic processes belong to the important class of Markov processes, if the evolution of the probability density at a certain time t only depends on the probability density at that time and not on states of earlier times. In this case, the transition probability density $\rho(\vec{a}, t|\vec{a}'', t'')$ to $\vec{a}$ at time t under the condition of $\vec{a}''$ at time t'' can be calculated from other transition probabilities by the *Chapman-Kolmogorov equation*:

$$\rho(\vec{a}, t|\vec{a}'', t'') = \int\limits_{M_{\vec{a}'}} d\vec{a}' \, \rho(\vec{a}, t|\vec{a}', t')\rho(\vec{a}', t'|\vec{a}'', t'') \tag{1.4}$$

with $t'' \leq t' \leq t$. Here the integral denotes the integration over the entire manifold $M_{\vec{a}'}$. One simple example of a Markov process is the one-dimensional *Ornstein-Uhlenbeck process* (Uhlenbeck and Ornstein, 1930), in which the dynamics of a random variable a are given by:

$$\tau_a \dot{a} = -a + B\xi(t), \tag{1.5}$$

with the time constant τ_a and the noise strength B. Here the stochasticity arises from the Gaussian white noise $\xi(t)$ that has zero mean $\langle \xi(t) \rangle = 0$ and obeys the autocorrelation function $\langle \xi(t)\xi(t') \rangle = \delta(t - t')$ indicating no temporal correlations. The property that gives *white* noise its name in analogy to the spectrum of visible white light[1] is its flat power spectrum that can be calculated easily either by the definition in Eq. (1.2):

$$\lim_{T\to\infty} \frac{\langle \tilde{\xi}\tilde{\xi}^* \rangle}{T} = \lim_{T\to\infty} \frac{\int_0^T \int_0^T dt\, dt' e^{i\omega(t-t')} \overbrace{\langle \xi(t)\xi(t') \rangle}^{\delta(t-t')=}}{T} = \lim_{T\to\infty} \frac{T}{T} = 1, \tag{1.6}$$

or alternatively by the Wiener-Khinchin theorem in Eq. (1.3).

In this thesis, fluctuations in differential equations are incorporated by white noise. However, noise in physical systems is often characterized by temporal correlations and then also referred to as colored noise. Temporally correlated fluctuations may be generated by a Markovian embedding in which a random variable with white-noise driven dynamics is considered [see for instance Mori (1965); Langer (1969); Guardia et al. (1984); Dygas et al. (1986); Schimansky-Geier and Zülicke (1990); Hänggi et al. (1993); Hänggi and Jung (1995); Kupferman (2004); Siegle et al. (2010)]. The Ornstein-Uhlenbeck process in Eq. (1.5) is one simple example of a Markovian embedding and its power spectrum can be calculated by the Fourier

[1] Note that the common analogy is imprecise since the wavelength spectrum and not the frequency spectrum of visible white light is approximately flat [see De Mayo (2014) chapter 6].

transform of Eq. (1.5) considering only positive times for which the left-hand side reads:

$$\begin{aligned}\int_0^\infty e^{i\omega t}\partial_t a(t)\,dt &= \int_0^\infty dt\, e^{i\omega t}\partial_t \int_0^\infty d\omega'\, e^{-i\omega' t}\tilde{a}(\omega') = \int_0^\infty d\omega'(-i\omega') \int_0^\infty dt\, e^{i(\omega-\omega')t}\tilde{a}(\omega') \\ &= -\int_0^\infty d\omega'\, i\omega'\delta(\omega-\omega')\tilde{a}(\omega') = -i\omega\tilde{a}(\omega).\end{aligned} \tag{1.7}$$

The Fourier transform of a is then given by:

$$-i\omega\tau_a\tilde{a}(\omega) = -\tilde{a}(\omega) + B\tilde{\xi} \Leftrightarrow \tilde{a}(\omega) = \frac{B\tilde{\xi}}{1-i\omega\tau_a}. \tag{1.8}$$

Inserting this result in Eq. (1.2) and using Eq. (1.6), the power spectrum is obtained by:

$$S_{aa}(\omega) = \frac{B^2}{1+\tau_a^2\omega^2}. \tag{1.9}$$

Since this spectrum has a maximum at zero frequency and monotonously decreases, a is also referred to as low-pass filtered noise or to red noise in analogy to the spectrum of red visible light. Remarkably, in the limit of $\tau_a \to 0$, the Ornstein-Uhlenbeck process cannot be distinguished from white noise. Later in this thesis, noise with more complex power spectra is considered as neural input, that can be generated by multidimensional Markovian embeddings.

Fokker-Planck equation

In this work, d-dimensional stochastic differential equations with additive noise that are homogeneous in time are considered that read:

$$\dot{\vec{a}} = \vec{f}(\vec{a}) + \mathbf{B}\vec{\xi}(t). \tag{1.10}$$

The dynamics of the d-dimensional process $\vec{a}$ are determined by the drift function $\vec{f}(\vec{a})$ and the diffusion term that consists of the $d \times d$ matrix $\mathbf{B}$ with the components B_{kl} and the vector $\vec{\xi}(t)$ whose d components are independent sources of Gaussian white noise obeying $\langle \xi_i(t)\xi_j(t')\rangle = \delta_{ij}\delta(t-t')$. The temporal evolution of an ensemble of these processes with the probability density $P(\vec{a},t)$ is described by the Fokker-Planck equation that corresponds to Eq. (1.10) and reads:

$$\partial_t P(\vec{a},t) = -\sum_k \partial_{a_k}[f_k(\vec{a})P(\vec{a},t)] + \frac{1}{2}\sum_{k,l,m=1}^{d} B_{kl}B_{ml}\partial_{a_k}\partial_{a_m}P(\vec{a},t). \tag{1.11}$$

In this parabolic partial differential equation of second order, the first sum incorporates the drift terms and the second sum the diffusion terms. As shown in Fig. 1.1, a homogeneous

drift (f independent of a) causes translational motion of the probability, the diffusion term a flattening and elongating of the probability density.

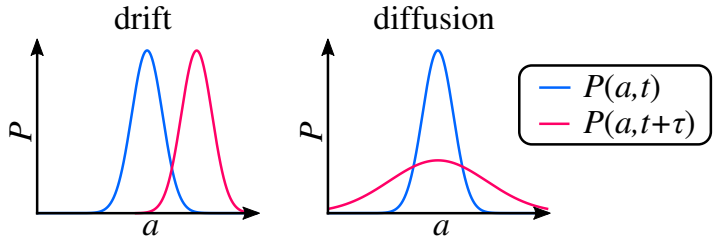

Figure 1.1.: Effects of drift and diffusion terms on the probability density

Eq. (1.11) shows only a special case of the Fokker-Planck equation. In general, the coefficients in drift and diffusion may depend on $\vec{a}$ and t. One way to derive the Fokker-Planck equation, that is also known as the forward Kolmogorov equation, is the Kramers-Moyal forward expansion of the Chapmann-Kolmogorov equation in Eq. (1.4), in which the transition probability is expressed by the series of its moments, the Kramers-Moyal coefficients. For many stochastic processes such as Eq. (1.10) it can be shown that all higher Kramers-Moyal coefficients than two are zero and the expansion results in the Fokker-Planck equation. In some cases it is beneficial to regard the Fokker-Planck equation as a continuity equation by defining the probability current $\vec{J}$:

$$\partial_t P(\vec{a},t) + \sum_{k=1}^{d} \partial_{a_k} J_k(\vec{a},t) = 0, \qquad J_i = f_i(\vec{a})P(\vec{a},t) - \frac{1}{2}\sum_{l,m=1}^{d} B_{il}B_{ml}\partial_{a_m} P(\vec{a},t). \quad (1.12)$$

Note that the amount of probability in the solution of Eq. (1.11), given by the integration over $\vec{a}$, is constant in time, if no efflux of probability is applied, for instance due to absorbing boundary conditions.

1.2 Physiological basics of neural networks

In this section, I provide a brief overview of the most relevant biological findings regarding to the generation and transmission of action potentials by neurons and synapses, using the book of Kandel et al. (2000) as the main reference.

Neurons and signal transmission by chemical synapses

Neurons are highly specialized cells for the transmission and processing of information that is encoded by electric pulses, the action potentials, and constitute the essential elements of the nervous system. A component that is crucial for the functionality of neurons is the cell membrane, a lipid bilayer that is almost impermeable for most ions. However, protein structures in the cell membrane, serving as active ion pumps and selective channels, enable certain ions to enter or to exit the cell and generate an imbalance of ion concentrations that

causes a voltage between the intracellular and the extracellular domains. The resting state, at which the net flux of ions through the membrane is zero, has a corresponding membrane potential of around -70 mV in most neurons. Voltage dependent probabilities for opening and closing of ion channels yield excitability and enable neurons to fire action potentials. When the membrane voltage is sufficiently increased, the interplay of fast opening and closing sodium channels and slower potassium channels yields a steep rise and a subsequent drop of the membrane potential that is referred to as action potential or spike. Within a neuron, action potentials are spatially transmitted to the axon terminals, at which chemical synapses are located that are one-way connections between the nerve cells. Note that some neurons are also electrically connected via gap junctions. When a chemical synapse is activated by an incoming action potential of the presynaptic neuron, vesicles are transported towards the synaptic cleft where they release neurotransmitters as illustrated in Fig. 1.2b. In turn, these neurotransmitters may bind to receptors on the postsynaptic side and open ion channels, yielding a change of the postsynaptic neuron's potential. Neurons are characterized as excitatory or inhibitory depending on whether their synapses increase or decrease the membrane voltage of the postsynaptic cells, respectively.

Depending on their location and their specific task, neurons may drastically differ in their morphology, however, most of them have some common features that are illustrated in Fig. 1.2a. They consist of three different compartments, the dendrites, the cell body also known as the soma and the axon at the end of which are the nerve terminals. The dendrites are branched extensions from the nerve cell with the primary objective of receiving electrical signals from other neurons' synapses and transmitting these to the cell body. There is also evidence that dendrites play a crucial role in certain computations [see for instance London and Häusser (2005); Sjöström et al. (2008); Schmidt-Hieber et al. (2017)]. The cell body contains the nucleus with the deoxyribonucleic acid (DNA) and all organelles that are required for the neuron to survive, however, it represents less than ten percent of the cell's volume. Originating from the soma, the axon is a long fiber used to transmit action potentials over relatively long distances. To speed up the propagation of action potentials over long distances and to save energy, parts of some axons are wrapped with myelin that serves as an isolation between intra- and extracellular domains. The axon branches into a large number of smaller fibers at the end of which synapses may be located to connect to other neurons.

Sources of noise that affect membrane voltages and signal transmission

Even if only a constant input current is applied, spikes of *in vivo* and *in vitro* neurons occur at irregular times, suggesting that the membrane voltage is subject to different sources of noise (Holden, 1976; Gerstner et al., 2014). There are mainly two intrinsic sources of noise: first of all, the membrane voltage is always subject to thermal noise, also known as Johnson-Nyquist noise (Johnson, 1928; Nyquist, 1928), however, its effect is negligibly small compared to the other fluctuations (Manwani and Koch, 1999). The more important source of intrinsic noise arises due to the finite number of ion channels in the cell membrane [see White et al. (2000) for review]. In the simplest case, channels assume either of two states, they are either open for ions to cross or closed and may switch stochastically. Note that

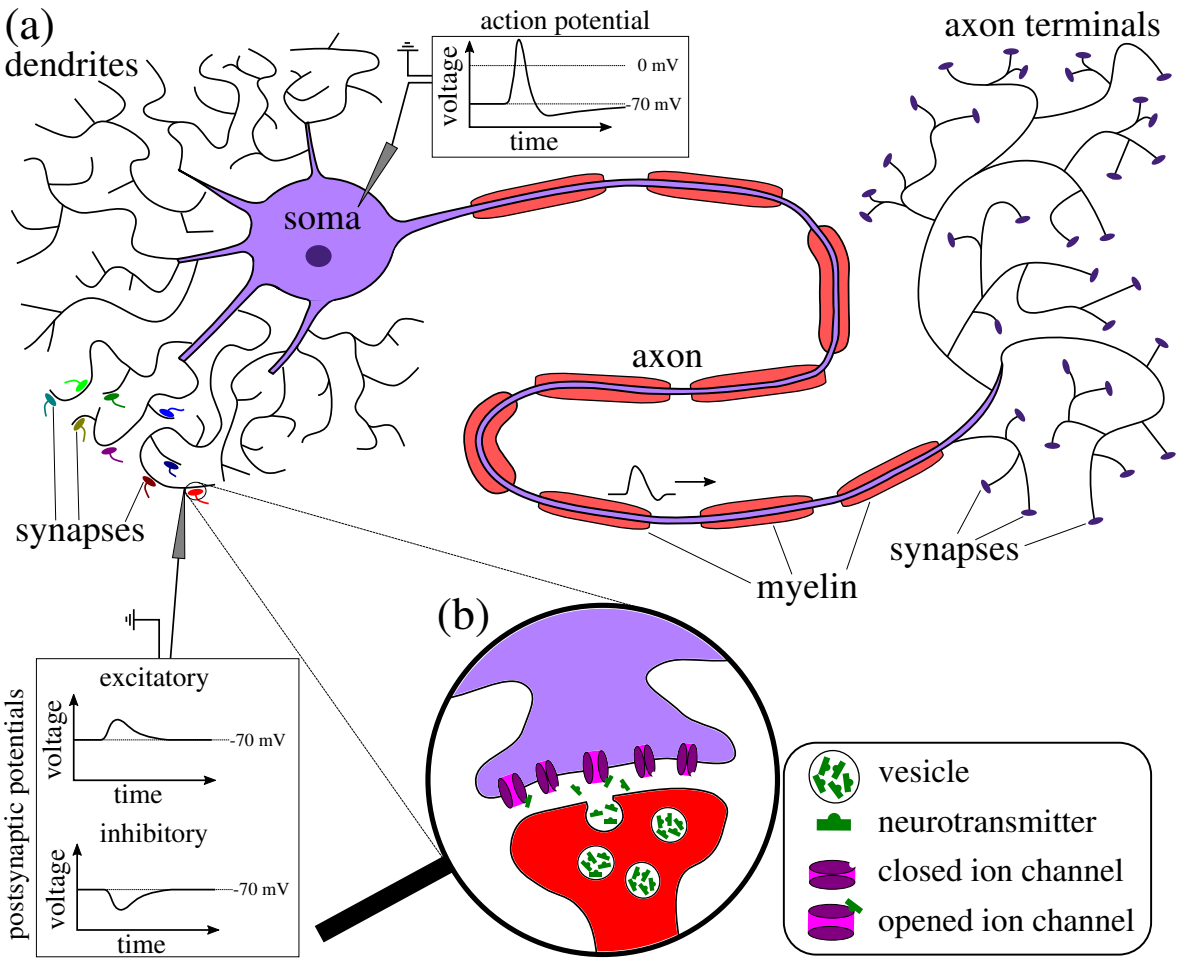

Figure 1.2.: Sketch of a nerve cell (a) and a chemical synapse (b). Neuron (a): the dendrites receive electrical signals by synapses from other neurons and transmit them to the soma. Sufficient increase of the membrane voltage in the soma yields an action potential being a rapid increase and subsequent decrease of the membrane voltage that can be transmitted over long distances by the axon. For a faster propagation of action potentials, parts of the axon may be surrounded by myelin. The axon branches into many smaller fibers at which synapses are located. Chemical synapse (b): an activated synapse releases neurotransmitter in the synaptic cleft that may bind to receptors and open postsynaptic ion channels yielding an increase or decrease of the postsynaptic potential, depending on whether the presynaptic neuron is excitatory or inhibitory, respectively.

some ion channels are much more complex and may assume several states. Although the number of ion channels per neuron is large, the fraction of open ion channels fluctuates and with it the membrane conductance and voltage. Concerning the membrane voltage of *in vivo* neurons in the cerebral cortex that are embedded in networks, spontaneous activity of the surrounding neural population is by far the dominating source of fluctuations (Destexhe and Rudolph-Lilith, 2012). These neurons are permanently exposed to the spikes of many presynaptic neurons, even if no sensory input is applied. Although these spikes may contain information, their effect on the membrane voltage is, comparable to noise, unpredictable on a small time scale and, thus, it is common to regard them as synaptic noise and model them as a stochastic process (Destexhe et al., 2003). Remarkably, synaptic noise may also occur in fully deterministic network simulations with randomly connected neurons due to the chaotic spiking behavior in such a complex system [see for instance van Vreeswijk and Sompolinsky (1996); Amit and Brunel (1997); van Vreeswijk and Sompolinsky (1998); Brunel (2000)]. Apart from that, the release of neurotransmitters by synapses with incoming action potentials is unreliable and measurements suggest that only a lower fraction of presynaptic spikes affect the postsynaptic potential (Hessler et al., 1993; Markram and Tsodyks, 1996). Note that noise does not need to be harmful to the transmission of signals, but, counterintuitively, noise may also be beneficial in nonlinear systems, a phenomenon well known in statistical physics as stochastic resonance [described for IF neurons by Longtin (1993), see also Gammaitoni et al. (1998) and Lindner et al. (2004) for reviews].

1.3 Models of stochastic spiking neurons

To reach the goal of understanding how the brain works, studying of neural dynamics by means of appropriate mathematical models is inevitable. One of the most important insights that shaped the modern conception of neuronal functionality has been gained by the quantitative description of the membrane voltage in the squid's giant axon by Hodgkin and Huxley (1952). In this famous model, the consideration of currents that arise due to the opening and closing dynamics of microscopic sodium and potassium ion channels resulted in a four-dimensional neuron model that was capable to adequately describe the generation and the shape of action potentials measured in voltage-clamp experiments. To account for further neural characteristics, the model has been extended by incorporating additional ion channels, the spatial extension, different compartments, other effects that arise due to the complex morphology and detailed synaptic dynamics [see summaries in Koch (1999); Dayan and Abbott (2001); Gerstner et al. (2014)] and detailed computer reconstructions of *in vivo* neurons have been made [see for instance Markram et al. (2015)]. If sufficient information on an experimental neuron is available, such detailed models can be fitted and may accurately reproduce neural activity. However, due to their complexity and their dependence on many parameters, these models are difficult to treat analytically and it is difficult to gain further insights in them. Furthermore, the power of detailed models which aim to mimic biological reality is limited for various reasons [see Almog and Korngreen (2016)]. To study the influence of general features on neural dynamics and computational properties of neurons, minimal models may be advantageous.

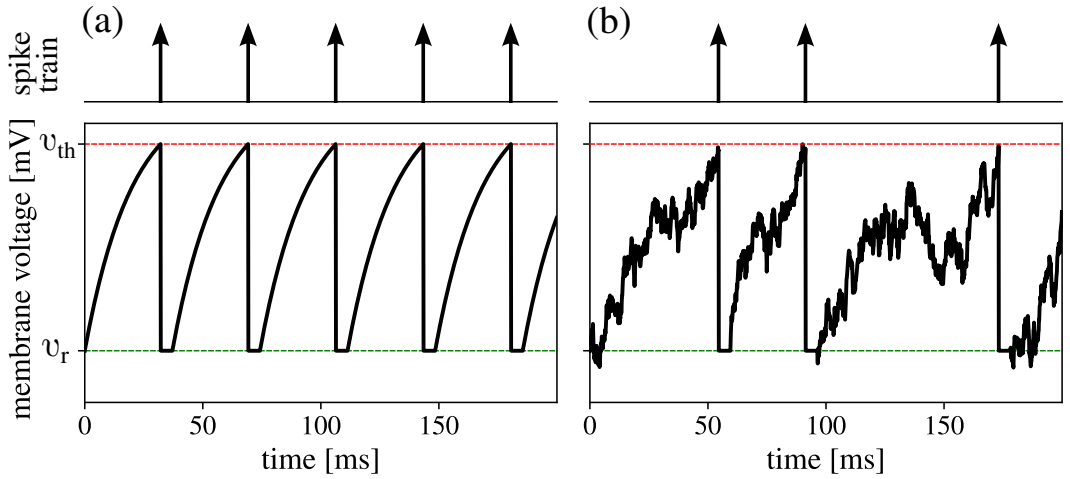

Figure 1.3.: Trajectories of the leaky IF neuron with corresponding spike trains: deterministic dynamics with μ=30 mV and $\beta = 0$ (a) and neuron in the noise-driven regime with $\mu = 15\,\mathrm{mV} < v_{\mathrm{th}}$ and β=1 mV$\sqrt{\mathrm{s}}$ (b). Threshold and reset are indicated as dashed red and green lines. Other parameters: $v_{\mathrm{r}} = 0\,mV$, v_{th}=20 mV, τ_{ref}=5 ms, τ_m=20 ms.

In cases in which only the timing of the action potential is important and its detailed shape is not relevant, *integrate-and-fire* (IF) neurons are a powerful alternative since they are easy to implement and even provide analytical insights. Dating back to Lapicque (1907), they provide a phenomenological description of spiking neurons by a drastic simplification of the action potential generation. In general, IF neurons are given by the dynamics of the membrane voltage and a fire-and-reset rule:

$$\tau_m \dot{v} = f(v,t), \qquad \text{if } v(t_k) > v_{\mathrm{th}} : v(t_k + \tau_{\mathrm{ref}}) \to v_{\mathrm{r}}. \tag{1.13}$$

Here τ_m is the membrane time constant, $f(v,t)$ incorporates both intrinsic dynamics and currents due to ion channels or applied by the experimentalist. When the voltage exceeds the threshold, the neuron is in a refractory state during the absolute refractory period τ_{ref}.

The influence of fluctuations on the neural spike trains has been studied for the stochastic leaky IF neuron that arises by the choice of $f(v) = -v + \beta\xi(t)$. In this model, the leak current incorporated by $-v$ ensures that the membrane voltage saturates at a certain value, if no other currents are applied. Neural input is given by the constant mean μ and white noise $\beta\xi(t)$ [see for instance Gerstein and Mandelbrot (1964); Ricciardi (1977); Kistler et al. (1997); Fourcaud and Brunel (2002) and Burkitt (2006a,b) for a review]. Two trajectories of this neuron model are presented in Fig. 1.3 for deterministic dynamics ($\beta = 0$) in Fig. 1.3a and for stochastic dynamics in the fluctuation-dominated regime ($\mu < v_{\mathrm{th}}$) in Fig. 1.3b. Analytical insights in this model have been gained in the above mentioned references by the application of the Fokker-Planck equation that reads in this special case:

$$\partial_t P(v,t) = -\partial_v \left[\frac{-v+\mu}{\tau_m} P(v,t) \right] + \frac{\beta^2}{2\tau_m^2} \partial_v^2 P(v,t) + J(v_{\mathrm{th}}, t - \tau_{\mathrm{ref}}) \delta(v - v_{\mathrm{r}}) \tag{1.14}$$

[cf. Eq. (1.11)]. Here the probability current term incorporates the reset of probability that crossed the threshold at $t - \tau_{\mathrm{ref}}$. The probability density obeys natural boundary conditions for $v \to \infty$ and absorbing boundary conditions at the threshold:

$$\lim_{v \to -\infty} P(v,t) = P(v_{\mathrm{th}},t) = 0. \tag{1.15}$$

The latter is a consequence of the white noise input as shown in detail in Sec. (5.7) of the book of Cox and Miller (1965). By the solution of Eq. (1.14) to a given initial distribution $P(v,0)$, the probability density for a neuron to cross the threshold at time t is given by the efflux of probability caused by the absorbing boundary condition $J(v_{\mathrm{th}},t)$. The approach has first been used by Gerstein and Mandelbrot (1964) to analytically determine the interspike-interval distribution, that in turn could be used by Lindner et al. (2002) to calculate the spike-train power spectrum. Note that neuron models with multiplicative noise yields a different Fokker-Planck equation [see Richardson (2004)].

One-dimensional IF neurons are simple models that may provide a description of spontaneous spiking activity, however, they cannot capture all neural features that have been observed in experiments. Such features require nonlinear and/or multidimensional IF neurons for which I develop a framework to determine the spike-train statistics, particularly the spike-train power spectrum, based on the corresponding Fokker-Planck equation in the following chapter.

2 Theory of spike-train power spectra for stochastic multidimensional integrate-and-fire neurons

Stochastic one-dimensional integrate-and-fire (IF) neurons have been extensively used to study the effect of noise on spike trains. However, often they do not suffice to capture observed features of sensory neurons. For instance, *in vitro* neurons may have oscillatory properties (Puil et al., 1986; Gutfreund et al., 1995), emit spike-trains with negative interval correlations (Ratnam and Nelson, 2000; Chacron et al., 2000; Farkhooi et al., 2009; Avila-Akerberg and Chacron, 2011) or exhibit a complex spiking behavior as response to a constant input current (McCormick et al., 1985; Kawaguchi, 1993; Markram et al., 2004) whereas spike-trains of the corresponding one-dimensional IF neurons with constant input current and white noise are by construction renewal processes without memory. Fortunately, the number of applicable cases for IF neurons as models of real nerve cells increases, if they are extended towards multidimensional models. For instance, only one additional adaptation variable enables IF neurons to generate spike-trains with the above mentioned resonance properties (Richardson et al., 2003; Brunel et al., 2003) and negatively correlated intervals (Liu and Wang, 2001; Chacron et al., 2001). If they are combined with nonlinear voltage dynamics, these two-dimensional neurons may also show the observed spike patterns (Izhikevich, 2003, 2007; Touboul and Brette, 2008), furthermore, Brette and Gerstner (2005); Jolivet et al. (2008); Teeter et al. (2018) have shown that they may accurately predict neural responses to noisy stimuli. Also effects that arise due to the morphology have been studied by IF neurons with multiple compartments, for instance by Ostojic et al. (2015); Doose et al. (2016).

While in all mentioned examples the further dimensions model intrinsic neuronal properties, they may also be exploited to generate temporally correlated fluctuations as neural input. One source of such temporal correlations arises from the consideration of synaptic dynamics in a second variable. A popular model, studied for instance by Brunel and Sergi (1998); Middleton et al. (2003); Lindner (2004); Moreno-Bote and Parga (2004, 2006); Schwalger and Schimansky-Geier (2008), considers synaptically filtered white Gaussian noise as neural input which yields IF models driven by an Ornstein-Uhlenbeck process. Such a one-dimensional embedding of white noise produces low-pass filtered Gaussian fluctuations also regarded to as red noise. But colored noise is required beyond this approach. Neural input in a network emerges as the sum of many presynaptic spike trains that my be approximated by Gaussian fluctuations. Most studies only apply white noise and suppose that spike-trains are close to Poisson processes. By that, they ignore the fact that spike trains are characterized by non-trivial temporal correlations, e.g. measured *in vivo* by Ghose and Freeman (1992); Edwards

et al. (1993); Bair et al. (1994). Since neural input maintains the correlations of the single spike trains, as shown by Lindner (2006), a Gaussian approximation with colored noise is more accurate and may yield qualitatively different results, as for example shown for the synchronization behavior in a feed-forward network by Câteau and Reyes (2006). Markovian embeddings, of which the most popular examples are Ornstein-Uhlenbeck processes, may generate not only red noise, but a variety of colored noise that increases with the embedding's dimensionality (Hänggi and Jung, 1995). For instance, a two-dimensional process have been used to generate band-pass-filtered noise, so-called harmonic noise (Schimansky-Geier and Zülicke, 1990), that served as neural input in order to study the electroreceptors of the paddlefish (Bauermeister et al., 2013).

The extension towards multidimensional models of course increases their complexity. During the last decades, many studies have been concerned about special cases of multidimensional IF neurons and calculated their statistics either numerically (Casti et al., 2002; Augustin et al., 2017), semianalytically (Câteau and Reyes, 2006; Apfaltrer et al., 2006), analytically by certain approximations (Brunel and Sergi, 1998; Brunel et al., 2001; Fourcaud and Brunel, 2002; Lindner, 2004; Moreno-Bote and Parga, 2010; Alijani and Richardson, 2011; Schwalger and Lindner, 2015; Schwalger et al., 2015), or populations of IF neurons by the reduction to mesoscopic equations (Deger et al., 2014; Schwalger et al., 2017). Most of the studies consider equations for the dynamics of the probability density with an instantaneous reset after firing and derive the firing rate or interval statistics from them. In this chapter, a general framework for multidimensional IF neurons with a finite refractory period is introduced based on the corresponding multidimensional Fokker-Planck equation to calculate not only firing rate, but, more importantly, also the spike-train power spectrum.

Experimentally measured power spectra provide insights in the underlying neuronal dynamics. Its low- and high-frequency limits are equal to the Fano factor of the spike train and the stationary firing rate, respectively. A high amplitude of peaks at the firing rate and its higher harmonics are an indicator of regular tonic firing caused by a strong constant stimulus. Other peaks may reveal frequencies of subthreshold oscillations, of a periodic driving signal or of narrow-band noise as input. Edwards et al. (1993) have shown that certain mechanisms such as absolute refractory periods decrease long-term variability and yield reduced power at low frequencies. Such as experimental neurons, multidimensional neurons may emit spike-trains with a rich correlation structure. With help of these models, the influence of single neural features, but also the combination of several ones on the shape of the spike-train power spectrum can be studied. Hence, if we understand the spike-train power spectra of multidimensional IF neurons, we gain understanding of the occurrence of temporal correlations in real neurons.

Moreover, the calculation of the spike-train power spectrum of IF neurons driven by colored noise is of particular interest to understand the dynamics of neural networks. As already mentioned, neural input in networks maintains the temporal correlations of the presynaptic spike trains. Thus, in a homogeneous network, the temporal statistics of neural input and output are self-consistent, more precisely, the input spectrum and the spike-train spectrum are connected by a condition of self-consistency that is given by the network topology and the synaptic dynamics. In order to determine the self-consistent temporal correlations, an

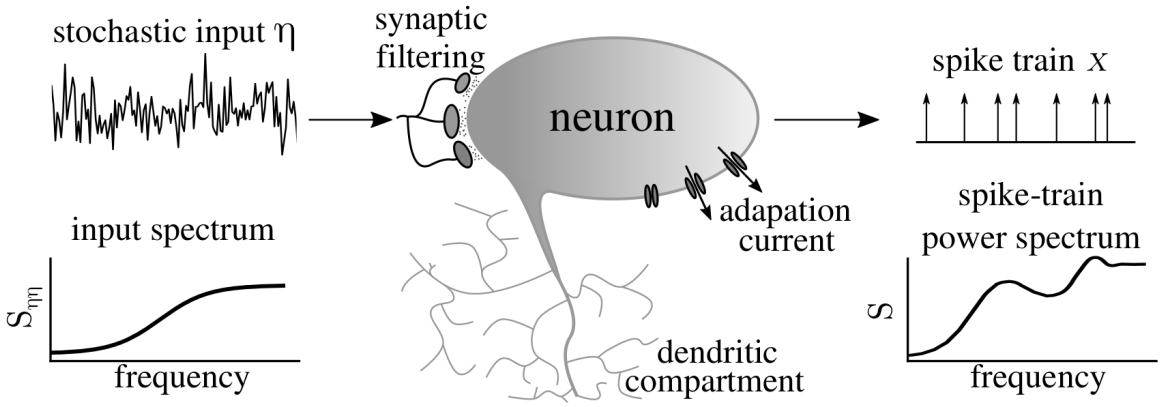

Figure 2.1.: Problem addressed in this chapter. Here a framework to calculate the spike-train power spectrum of a general stochastic multidimensional integrate-and-fire neuron is introduced. The additional dimensions can be used to include common intrinsic features such as an adaptation current and/or further neuronal compartments and/or, to generate temporally correlated input fluctuations, so-called colored noise by a Markovian embedding.

iterative scheme was proposed by Lerchner et al. (2006) and improved by Dummer et al. (2014) that was exploited by Wieland et al. (2015) to understand the amplification of slow fluctuations in neural networks. In this chapter, the preparatory work for a mean-field theory that considers the temporal correlations of spike trains is performed by the solution of the open-loop problem: the spike-train power spectrum is calculated for a given input power spectrum. In the next chapter, such a mean field theory is introduced based on the closed loop problem: the input power spectrum is searched that is self consistent with the corresponding spike-train power spectrum.

This chapter is organized as follows: at first, a comprehensible generalized two-dimensional IF model with absolute refractory period is introduced that involves many common features of IF neurons such as colored noise as neural input, an adaptation current or a second neuronal compartment. It is demonstrated how the non-local dynamics of this model, i.e. the fire-and-reset mechanism and spike-triggered adaptation, can be incorporated in the Fokker-Planck equation. From the Fokker-Planck equation, I derive a set of partial differential equations of which the solution determines the firing rate, the subthreshold probability density and, most importantly, the spike-train power spectrum. The set of equations is solved numerically by a finite-difference method for two important examples, a leaky IF neuron driven by colored noise and an exponential IF neuron with adaptation. As the second step, the model and the framework are extended to d dimensions. The resulting set of partial differential equations is the highlight of this chapter and the preparatory work for the next one. As one example of a three-dimensional neuron, the theory is applied to calculate the power spectrum of a leaky IF neuron driven by narrow-band noise. At the end of this chapter, I introduce and test a procedure to determine the Padé approximation of the power spectrum at zero frequency. In this chapter, all calculated spike-train power spectra are verified by direct simulations of the corresponding Langevin equations.

2.1 The generalized two-dimensional integrate-and-fire neuron

For the sake of better comprehensibility, at first I consider a general two-dimensional IF neuron model for which the membrane voltage v and an auxiliary process a evolve in the subthreshold regime according to the general Langevin equations:

$$\begin{aligned} \tau_m \dot{v} =& f(v,a) + \beta\xi_1(t), \\ \tau_a \dot{a} =& g(v,a) + b_1\xi_1(t) + b_2\xi_2(t). \end{aligned} \tag{2.1}$$

The time scales of the dynamics are determined by the membrane and the auxiliary time constants τ_m and τ_a, respectively. Both dynamics may influence each other via the functions $f(v,a)$ and $g(v,a)$. Here we restrict us to functions that ensure that neither v diverges towards $-\infty$ nor a diverges towards $\pm\infty$ such that a stationary ensemble distribution exists. Note that unrestricted increase of v is prevented by the fire-and-reset rule introduced below. The terms $\xi_1(t)$ and $\xi_2(t)$ are independent Gaussian white noise with zero mean $\langle\xi_i(t)\rangle = 0$ that obey the correlation $\langle\xi_i(t)\xi_j(t+\tau)\rangle = \delta_{i,j}\delta(\tau)$ with $i,j \in \{1,2\}$. Here, the symbol $\delta_{i,j}$ denotes the Kronecker delta. The coefficients β and b_1 are noise strengths of the same white noise $\xi_1(t)$; the advantage of this construction will be explained later on. For all IF neurons the action potentials are generated artificially by the fire-and-reset rule: the neuron emits a spike when the voltage variable crosses the threshold v_{th} at time t_k. Here the shape of the action potentials is roughly approximated by a rectangular pulse that is formed due to the clamping of the voltage variable to the refractory voltage $v_{\mathrm{ref}} > v_{\mathrm{th}}$ during the absolute refractory period τ_{ref}. After the refractory period has elapsed, the voltage is reset to v_{r} and continues to evolve according to Eq. (2.1). Spike-triggered adaptation can be incorporated by the instantaneous increase of the auxiliary variable $a(t_k)$ by the constant amount δ_a:

$$\begin{aligned} \text{if } v(t_k) > v_{\mathrm{th}}: \quad v(t_k+\tau) =& v_{\mathrm{ref}} \quad \text{for } 0 < \tau < \tau_{\mathrm{ref}}, \\ & v(t_k+\tau_{\mathrm{ref}}) \to v_{\mathrm{r}} \quad \text{and} \quad a(t_k) \to a(t_k) + \delta_a. \end{aligned} \tag{2.2}$$

The representation of the action potentials by rectangular pulses is uncommon in the literature. In the most studies, the combination of an absolute refractory period and a voltage dependent auxiliary variable is not considered, thus, the voltage during the refractory period is irrelevant and clamped at v_{r} [see for instance Burkitt (2006a)]. However, here the auxiliary variable may depend on the voltage via the function $g(v,a)$, and hence, the effect of an increased voltage during the action potential may be included. The sequence of the action potentials at the spike times t_k is represented as a stochastic point process, the spike train:

$$x(t) = \sum_k \delta(t - t_k). \tag{2.3}$$

The trajectories of v and a with the resulting spike train x for one example are presented in Fig. 2.2. In the following, I introduce statistics that are used to quantify the characteristics of the spike trains in this thesis.

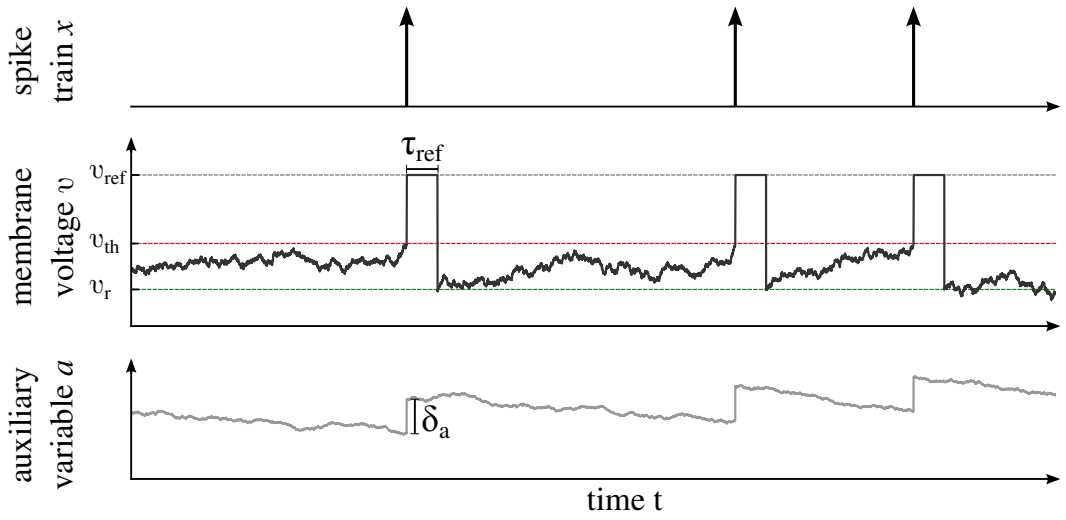

Figure 2.2.: Features of the two-dimensional integrate-and-fire neuron. From top to bottom: resulting spike train as a point process, membrane voltage and auxiliary dynamics that obey the subthreshold dynamics in Eq. (2.1) and the fire-and-reset rule in Eq. (2.2). When v exceeds v_{th}, a spike is emitted and a is incremented by δ_a. Subsequently v is clamped to v_{ref} during the absolute refractory period τ_{ref} and is reset to v_{r} afterwards. In this example, a is used as an stochastic adaptation current with spike-triggered and stochastic subthresholds adaptation as explained in detail in Sec. (2.1.4) with $f(v,a) = \mu - v - a$, $g(v,a) = Av - a$. See Tab. C.2 in Appendix for parameters.

2.1.1 Spike-train statistics of first and second order

The number of spikes of a certain spike train $x(t)$ within a time window $[T', T]$ is given by the *spike count* $N_{\mathrm{spikes}}(T', T)$:

$$N_{\mathrm{spikes}}(T', T) = \int_{T'}^{T} dt\, x(t). \tag{2.4}$$

The number of spikes per time unit is given by the firing rate. The *instantaneous firing rate* at a certain time $r(t)$ is given by the expectation value of the number of spikes within an infinitesimally small time interval Δt:

$$r(t) = \lim_{\Delta t \to 0} \left\langle \frac{N_{\mathrm{spikes}}(t - \Delta t/2, t + \Delta t/2)}{\Delta t} \right\rangle = \lim_{\Delta t \to 0} \left\langle \frac{1}{\Delta t} \int_{t-\Delta t/2}^{t+\Delta t/2} dt\, x(t) \right\rangle = \langle x(t) \rangle. \tag{2.5}$$

The expectation value is the ensemble average over realizations of the noise and the last step only holds true for an infinite ensemble size. The stationary firing rate r_0 denotes the firing rate of an ensemble with time-independent averages. The temporal correlations up to the second order are represented by the *autocorrelation function* that only depends on the time

lag τ and not on the absolute time t for a stationary ensemble[1]:

$$C(\tau) = \langle x(t+\tau)x(t)\rangle - \langle x(t)\rangle^2 = r_0(\delta(\tau) + m(\tau) - r_0) \tag{2.6}$$

[see Holden (1976) or Gabbiani and Koch (1998) Sec. 6]. The function $m(\tau)$ denotes the firing rate under the condition that a reference spike is emitted at $\tau = 0$. The reference spike itself is taken into account by the δ function such that $m(0) = 0$. Alternatively to the autocorrelation function, the temporal correlations are captured by the *spike-train power spectrum* given by:

$$S(\omega) = \lim_{T\to\infty} \frac{\langle \tilde{x}(\omega)\tilde{x}^*(\omega)\rangle}{T}, \qquad \tilde{x}(\omega) = \int_0^T e^{i\omega t}[x(t) - r_0]\, dt. \tag{2.7}$$

To be precise, we consider the power spectrum of the spike-train minus its expectation value r_0 in order to avoid the divergence of the spectrum at $\omega = 0$. The spike-train power spectrum as it is introduced here is connected to the autocorrelation function via the Wiener-Khinchin theorem by the Fourier transformation:

$$S(\omega) = \int_{-\infty}^{\infty} d\tau\, e^{i\omega\tau} C(\tau) = r_0 \left(1 + 2\mathrm{Re} \int_0^{\infty} dt\, e^{i\omega\tau}(m(\tau) - r_0)\right) \tag{2.8}$$

[cf. Gardiner (1985) Eq. 1.5.38]. Here Eq. (2.6) and symmetry of the autocorrelation function $[C(\tau) = C(-\tau)]$ are exploited in order to calculate the power spectrum by the real part of the integral over the positive half space. In the following section, an analytical set of equations is derived to calculate the stationary firing rate and the spike-train power spectrum. Note that in this work, the power spectra are plotted against the frequency $f = \omega/(2\pi)$ and *not* against the angular frequency ω, if not stated otherwise.

2.1.2 Fokker-Planck equation and spike-train power spectrum

Corresponding to the set of Langevin equations in Eq. (2.1) that describe single subthreshold trajectories of the model, the Fokker-Planck equation describes the temporal evolution for an entire ensemble of neurons. For the introduced model, the probability density $P(v, a, t)$ to find a neuron with voltage v, auxiliary value a at time t obeys the Fokker-Planck equation that is given by the operators $\hat{\mathcal{L}}$ and $\hat{\mathcal{R}}$ that incorporate the subthreshold dynamics and the fire-and-reset rule, respectively:

$$\partial_t P(v, a, t) = \hat{\mathcal{L}}\, P(v, a, t) + \{\hat{\mathcal{R}}\, P\}(v, a, t). \tag{2.9}$$

In our model, a non-vanishing white noise component in the voltage variable is considered ($\beta \neq 0$) which has infinite variance. As a consequence, neurons cannot be arbitrarily close to

[1] Non-stationary ensembles have time-dependent autocorrelation functions $C(t, \tau)$ and are not considered in this work.

the threshold without crossing it. In terms of the probability density, the infinite variance of the noise process ξ_1 yields an absorbing boundary at the voltage threshold:

$$P(v_{\mathrm{th}}, a, t) = 0. \tag{2.10}$$

A detailed mathematical explanation can be found in Cox and Miller (1965) Sec. 5.7. It is important to mention that in the case of a vanishing white noise in voltage variable ($\beta = 0$), other boundaries have to be considered [see for instance description in Brunel and Sergi (1998)], however, here at least a weak white noise component is always considered. The probability to find a neuron at very low membrane voltage, or extreme values of a goes to zero. Thus, except at the threshold, $P(v, a, t)$ obeys natural boundary conditions:

$$\lim_{v \to -\infty} P(v, a, t) = \lim_{a \to \pm\infty} P(v, a, t) = 0. \tag{2.11}$$

The deterministic and stochastic terms in Eq. (2.1) cause the drift and diffusion of probability, respectively. The probability current $\vec{J}(v, a, t)$ is given by:

$$\vec{J}(v, a, t) = \begin{pmatrix} J_v \\ J_a \end{pmatrix} = \begin{pmatrix} \frac{f(v,a)}{\tau_m} - \frac{\beta^2}{2\tau_m^2}\partial_v - \frac{\beta b_1}{2\tau_m \tau_a}\partial_a \\ \frac{g(v,a)}{\tau_a} - \frac{b_1^2 + b_2^2}{2\tau_a^2}\partial_a - \frac{\beta b_1}{2\tau_m \tau_a}\partial_v \end{pmatrix} P(v, a, t) \tag{2.12}$$

[see also Risken (1984)]. For the probability in the subthreshold regime, the continuity equation holds true and connects the evolution of the probability density with the probability current by $\partial_t P(v, a, t) = -\vec{\nabla}\vec{J}(v, a, t)$. As a consequence, the operator for the subthreshold dynamics $\hat{\mathcal{L}}$ can be identified as:

$$\hat{\mathcal{L}} = \underbrace{-\partial_v \frac{f(v,a)}{\tau_m}}_{\text{drift in } v} + \underbrace{\frac{\beta^2}{2\tau_m^2}\partial_v^2}_{\text{diffusion in } v} \underbrace{-\partial_a \frac{g(v,a)}{\tau_a}}_{\text{drift in } a} + \underbrace{\frac{b_1^2 + b_2^2}{2\tau_a^2}\partial_a^2}_{\text{diffusion in } a} + \underbrace{\frac{\beta b_1}{\tau_m \tau_a}\partial_v \partial_a}_{\text{mixed diffusion}} \tag{2.13}$$

[see Risken (1984)]. The mixed derivative in the last term arises because both variables are subject to the same white noise ξ_1. In many situations it is convenient to get rid of the mixed diffusion term by a transformation of the coordinates. Here such a transformation also affects the threshold and is omitted since it results in a more complicated fire-and-reset mechanism.

The fire-and-reset operator $\hat{\mathcal{R}}$ turns out to be cumbersome because it incorporates not only the reset, but also the spike-triggered adaptation and the evolution of probability in the refractory state. For a better understanding, it is first introduced for the special case of a vanishing refractory period and without spike-triggered adaptation ($\tau_{\mathrm{ref}} = \delta_a = 0$). The efflux of probability that crosses the threshold within a small time window $(t, t + \Delta t)$ is given by the probability current in voltage direction at the threshold times the length of the time interval $J_v(v_{\mathrm{th}}, a, t)\Delta t$ and describes the proportion of neurons that fired an action potential during the interval Δt. As illustrated in Fig. 2.3a, in the simplest case the operator

$\hat{\mathcal{R}}$ instantaneously shifts the efflux to the reset and reads:

$$\{\hat{\mathcal{R}}\,P\}(v,a,t) = \delta(v-v_\mathrm{r})J_v(v_\mathrm{th},a,t) = -\delta(v-v_\mathrm{r})\frac{\beta^2}{2\tau_m^2}\partial_v P(v,a,t)\bigg|_{v=v_\mathrm{th}} \quad (\text{for } \tau_\mathrm{ref}=\delta_a=0). \tag{2.14}$$

Note that the drift term and the diffusion term in a of J_v vanish at the threshold due to the absorbing boundary condition. Here the notation with curly brackets should clarify that the operator is acting as a functional of the probability density. Including spike-triggered adaptation ($\delta_a > 0$), the reinserted probability is also instantaneously shifted along the auxiliary dimension by the amount δ_a (see illustration in Fig. 2.3b) and $\hat{\mathcal{R}}$ reads:

$$\{\hat{\mathcal{R}}\,P\}(v,a,t) = -\delta(v-v_\mathrm{r})\frac{\beta^2}{2\tau_m^2}\partial_v P(v,a-\delta_a,t)\bigg|_{v=v_\mathrm{th}} \quad (\text{for } \tau_\mathrm{ref}=0). \tag{2.15}$$

If a finite absolute refractory period is applied ($\tau_\mathrm{ref} > 0$), it is important to take into account that the auxiliary variable a keeps evolving during the refractory period according to Eq. (2.1), while the voltage variable v is fixed at v_ref as shown in Fig. 2.3c. Considering the probability $p(a,t)$ that crossed the threshold within the time window $(t', t'+\Delta t)$, its evolution during the refractory period is given by the reduced Fokker-Planck equation that only contains the drift and diffusion term in a:

$$\partial_t p(a,t) = \hat{\mathcal{L}}_\mathrm{ref}\,p(a,t) = \left(-\partial_a\frac{g(v_\mathrm{ref},a)}{\tau_a} + \frac{b_1^2+b_2^2}{2\tau_a^2}\partial_a^2\right)p(a,t). \tag{2.16}$$

When the refractory period has passed, the evolved probability $p(a,t'+\tau_\mathrm{ref})$, as the solution of Eq. (2.16), can be calculated by the integral over the transition probability $\rho_\mathrm{ref}(a|a')$:

$$p(a,\tau+\tau_\mathrm{ref}) = \int_{-\infty}^{\infty} da'\,\rho_\mathrm{ref}(a|a')p(a',\tau). \tag{2.17}$$

In case of a linear dependency $g(v,a) = G(v) - a$, the process is an Ornstein-Uhlenbeck process with the transition probability (cf. Risken (1984) Eq. 5.28):

$$\rho_\mathrm{ref,OU}(a|a') = \sqrt{\frac{\tau_a}{\pi(b_1^2+b_2^2)(1-e^{-2\tau_\mathrm{ref}/\tau_a})}}\exp\left(-\frac{\tau_a[a-G(v_\mathrm{ref})-e^{-\tau_\mathrm{ref}/\tau_a}(a'-G(v_\mathrm{ref}))]^2}{(b_1^2+b_2^2)(1-e^{-2\tau_\mathrm{ref}/\tau_a})}\right). \tag{2.18}$$

For a nonlinear dependency on a, the transition probability can be calculated by numerical integration in time of Eq. (2.16) [see different methods in Press et al. (2007) chapter 20]. With a given transition probability, we may formulate the general fire-and-reset operator $\hat{\mathcal{R}}$

that reinserts the evolved probability density by:

$$\{\hat{\mathcal{R}}\,P\}(v,a,t) = -\delta(v-v_\mathrm{r}) \int\limits_{-\infty}^{\infty} da'\,\rho_\mathrm{ref}(a|a')\frac{\beta^2}{2\tau_m^2}\partial_v P(v,a'-\delta_a,t-\tau_\mathrm{ref})\Big|_{v=v_\mathrm{th}}. \tag{2.19}$$

The explicit representation of the effect of the operator on the probability density reveals that the resulting Fokker-Planck equation is in general neither local in time nor in the voltage nor in the auxiliary domain. As mentioned above, the proportion of neurons that cross the threshold within a small time window at a certain value of a is given by the voltage probability current at the threshold times the time interval $J_v(v_\mathrm{th},a,t)\Delta t$. Hence, the instantaneous firing rate is given by the total probability current in voltage direction at the threshold:

$$r(t) = \int\limits_{-\infty}^{\infty} da\,J_v(v_\mathrm{th},a,t) = -\int\limits_{-\infty}^{\infty} da\,\frac{\beta^2}{2\tau_m^2}\partial_v P(v,a,t)\Big|_{v=v_\mathrm{th}} \tag{2.20}$$

Neurons either evolve in the subthreshold regime or they are in the refractory state. The sum of the probabilities to be in either of both states is normalized:

$$\underbrace{\int\limits_{-\infty}^{v_\mathrm{th}} dv \int\limits_{-\infty}^{\infty} da\,P(v,a,t)}_{\text{subthreshold regime}} + \underbrace{\int\limits_{t-\tau_\mathrm{ref}}^{t} d\tau\,r(\tau)}_{\text{refractory state}} = 1. \tag{2.21}$$

At this point, the Fokker-Planck equation and the corresponding normalization condition are introduced in Eq. (2.9) with the operators in Eqs. (2.13) and (2.19) that determine the temporal evolution of a given initial probability density. In the following, I show how to calculate the spike-train statistics. At first, the stationary solution is required that determines the stationary firing rate and the initial density to calculate the conditional firing rate $m(\tau)$.

Stationary probability density and firing rate

The stationary probability density does not depend on time ($\partial_t P_0(v,a) = 0$) and is thereby given by the solution of the partial differential equation that arises from Eq. (2.9) and the normalization condition in Eq. (2.21):

$$(\hat{\mathcal{L}}+\hat{\mathcal{R}})P_0(v,a) = \partial_t P_0(v,a) = 0, \qquad \int\limits_{-\infty}^{v_\mathrm{th}} dv \int\limits_{-\infty}^{\infty} da\,P_0(v,a) + \tau_\mathrm{ref} r_0 = 1. \tag{2.22}$$

These equations uniquely determine both, the stationary density $P_0(v,a)$ and the stationary firing rate r_0, that are connected by Eq. (2.20):

$$r_0 = -\int\limits_{-\infty}^{\infty} da\,\frac{\beta^2}{2\tau_m^2}\partial_v P_0(v,a)\Big|_{v=v_\mathrm{th}}. \tag{2.23}$$

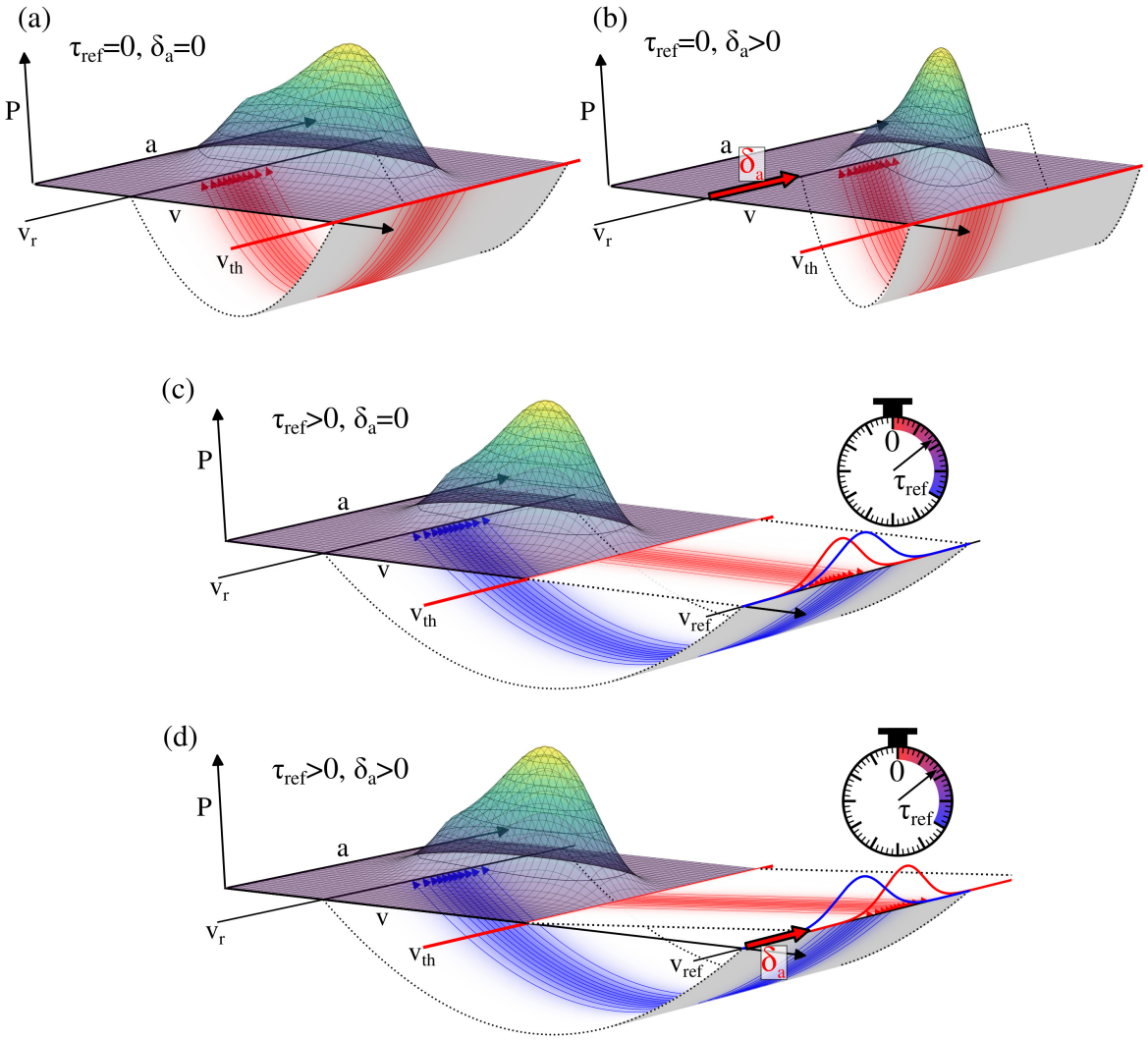

Figure 2.3.: Fire-and-reset rule in the Fokker-planck equation. Simplest case (a) ($\tau_{\mathrm{ref}} = \delta_a = 0$): efflux of probability that crosses the threshold is instantaneously reinserted at v_{r} and the auxiliary variable is unchanged. **Spike-triggered adaptation (b)** ($\tau_{\mathrm{ref}} = 0$, $\delta_a > 0$): additionally to the reset, probability also instantaneously shifted along the axis of the auxiliary variable. **Absolute refractory period (c)** ($\tau_{\mathrm{ref}} > 0$, $\delta_a = 0$): efflux of probability that crosses the threshold is transferred to the refractory state at v_{ref} where it evolves in the auxiliary variable during the refractory period. After the refractory period has elapsed, the evolved probability is reinserted. **General case (d)** ($\tau_{\mathrm{ref}} > 0$, $\delta_a > 0$): efflux of probability is shifted along the auxiliary variable and transferred to the refractory state where it evolves in a. Subsequently, the probability is reinserted after the refractory period has elapsed.

Solution in frequency domain and spike-train power spectrum

The remaining non-trivial part of the autocorrelation function in Eq. (2.6) is the conditional firing rate $m(t)$ (here t is used instead of τ). This function is the firing rate under the condition of a reference spike at $t = 0$ that is not considered in $m(t)$ [$m(0) = 0$]. Thus, we assume that the whole ensemble fired an action potential at $t = 0$ such that all probability is in the refractory state [$P(v, a, t) = 0$, for $0 < t < \tau_{\mathrm{ref}}$] and reset to v_{r} at $t = \tau_{\mathrm{ref}}$. The initial distribution of a has to reflect the distribution upon firing at $t = 0$. For instance, if the voltage is negatively influenced by the auxiliary variable ($f(v, a) = F(v) - a$), the neurons are more likely to cross the threshold at a low a than at a high a. Since we are interested in the autocorrelation function of the stationary ensemble, the initial distribution in a is determined by stationary solution:

$$P(v, a, \tau_{\mathrm{ref}}) = r_0^{-1}\{\hat{\mathcal{R}}\, P_0\}(v, a). \tag{2.24}$$

The factor r_0^{-1} ensures the normalization of the inserted probability. Note, that only in the limit of long refractory periods $\tau_{\mathrm{ref}} \gg \tau_a$, the initial distribution in a coincides with the stationary distribution of a. For $t > \tau_{\mathrm{ref}}$ the probability density evolves according to Eq. (2.9) and the conditional firing rate is given by Eq. (2.20).

The Fokker-Planck equation is difficult to solve in time domain. Instead, in the following the spike-train power spectrum is calculated from the Fourier-transformed Fokker-Planck equation. The procedure can be interpreted as an extension of the method introduced by Richardson (2008) that deals with the calculation of the spectrum for one-dimensional nonlinear integrate-and-fire neurons. The transformation has two advantages: on the one hand, we get rid of the derivative with respect to the time and, on the other hand, the fire-and-reset operation is non-local with respect to time, but it is local with respect to frequency. To ensure that the Fourier-transformed functions are well defined also at $\omega = 0$, the differences between time-dependent functions and the corresponding stationary solutions are considered for the probability density and the firing rate:

$$\begin{aligned}
\tilde{Q}(v, a, \omega) &= \int_0^\infty dt\, e^{i\omega t} \underbrace{[P(v, a, t) - P_0(v, a)]}_{:=Q(v,a,t)}, \\
\tilde{m}(\omega) &= \int_0^\infty dt\, e^{i\omega t}[m(t) - r_0] = -\frac{\beta^2}{2\tau_m^2} \int_{-\infty}^\infty da\, \partial_v \tilde{Q}(v, a, \omega)\Big|_{v=v_{\mathrm{th}}} = \int_{-\infty}^\infty da \int_{-\infty}^{v_{\mathrm{th}}} dv\, \{\hat{\mathcal{R}}\, \tilde{Q}\}(v, a, \omega).
\end{aligned} \tag{2.25}$$

The Fourier transform of the difference between Eqs. (2.9) and (2.22) yields the partial differential equations that determines $\tilde{Q}(v, a, \omega)$ and $\tilde{m}(\omega)$:

$$\int_0^\infty dt\, e^{i\omega t} \partial_t Q(v, a, t) = \int_0^\infty dt\, e^{i\omega t} (\hat{\mathcal{L}}\, Q(v, a, t) + \{\hat{\mathcal{R}}\, Q\}(v, a, t)). \tag{2.26}$$

The left hand side of the equation can be calculated using integration by parts:

$$\begin{aligned}\int_0^\infty dt\, e^{i\omega t}\partial_t Q(v,a,t) &= \int_0^\infty dt\, \partial_t(e^{i\omega t}Q(v,a,t)) - \int_0^\infty dt\, \partial_t e^{i\omega t}Q(v,a,t)\\ &= -(e^{i\omega\tau_{\rm ref}}-1)P_0(v,a) + e^{i\omega t}Q(v,a,t)\Big|_{\tau_{\rm ref}}^{\infty} - i\omega\tilde{Q}(v,a,\omega)\\ &= -i\omega\tilde{Q}(v,a,\omega) + P_0(v,a) - e^{i\omega\tau_{\rm ref}}P(v,a,\tau_{\rm ref}).\end{aligned} \tag{2.27}$$

Here it is exploited that $Q(v,a,t\to\infty)=0$ and $Q(v,a,t)=-P_0(v,a)$ for $0\le t<\tau_{\rm ref}$. The operator $\hat{\mathcal{L}}$ is local and does not contain time derivatives. Thus, the Fourier transform of the first term of the right hand side is simply given by:

$$\int_0^\infty dt\, e^{i\omega t}\,\hat{\mathcal{L}}\,Q(v,a,t) = \hat{\mathcal{L}}\int_0^\infty dt\, e^{i\omega t}Q(v,a,t) = \hat{\mathcal{L}}\,\tilde{Q}(v,a,\omega). \tag{2.28}$$

For the last term it is important to take into account the non-local structure in time of the operator $\hat{\mathcal{R}}$:

$$\begin{aligned}&\int_0^\infty dt\, e^{i\omega t}\{\hat{\mathcal{R}}\,Q\}(v,a,t) = -\delta(v-v_{\rm r})\frac{\beta^2}{2\tau_m^2}\partial_v \int_{-\infty}^{\infty} da'\,\rho_{\rm ref}(a|a')\int_0^\infty dt\, e^{i\omega t}Q(v,a',t-\tau_{\rm ref})\Big|_{v=v_{\rm th}}\\ &= -\delta(v-v_{\rm r})\frac{\beta^2}{2\tau_m^2}\partial_v \int_{-\infty}^{\infty} da'\,\rho_{\rm ref}(a|a')e^{i\omega\tau_{\rm ref}}\Bigg(\underbrace{\int_0^\infty dt\, e^{i\omega t}Q(v,a',t)}_{=\tilde{Q}(v,a',\omega)} - \underbrace{\int_{-\tau_{\rm ref}}^{0} dt\, e^{i\omega t}P_0(v,a')}_{[\exp(-i\omega\tau_{\rm ref})-1](i\omega)^{-1}P_0}\Bigg)\Bigg|_{v=v_{\rm th}}\\ &= e^{i\omega\tau_{\rm ref}}\{\hat{\mathcal{R}}\,\tilde{Q}\}(v,a,\omega) + \frac{(1-e^{i\omega\tau_{\rm ref}})}{i\omega}\{\hat{\mathcal{R}}\,P_0\}(v,a).\end{aligned} \tag{2.29}$$

All terms together yield the Fokker-Planck equation in Fourier domain that is given by [2]:

$$(i\omega+\hat{\mathcal{L}}+e_\tau\,\hat{\mathcal{R}})\tilde{Q} = \left[1+\left(\frac{e_\tau-1}{i\omega}-\frac{e_\tau}{r_0}\right)\hat{\mathcal{R}}\right]P_0 \quad (\text{for } \omega\neq 0) \tag{2.30}$$

with $e_\tau = e^{i\omega\tau_{\rm ref}}$. The partial differential equation for $\omega=0$ can be found by the calculation of the limes $\omega\to 0$ or, alternatively, by repeating the calculation in Eq. (2.29). Both procedures yield the same result. However, a technical problem arises because the left hand side reads $(\hat{\mathcal{L}}+\hat{\mathcal{R}})\tilde{Q}$ for $\omega=0$ and is invariant under the transformation of the solution $\tilde{Q}\to\tilde{Q}+\alpha P_0$ for any complex number α, by the definition of the stationary solution P_0 in Eq. (2.22) $[(\hat{\mathcal{L}}+\hat{\mathcal{R}})P_0=0]$. Consequentially, $\tilde{Q}$ is not uniquely determined by the partial differential equation only. To calculate the spectrum at zero frequency, an additional condition for $\tilde{Q}$ at $\omega=0$ is required and has to be derived from the normalization of probability in time domain

[2] For simplicity the notation is changed such that $\hat{\mathcal{R}}\,F = \{\hat{\mathcal{R}}\,F\}(v,a,\omega)$.

P. This derivation is shown in the Appendix Sec. A.1. The partial differential equation and the required normalization condition at $\omega = 0$ with the unique solution $\tilde{Q}(v, a, 0)$ are given by:

$$(\hat{\mathcal{L}} + \hat{\mathcal{R}})\tilde{Q} = [1 + (\tau_{\text{ref}} - r_0^{-1})\,\hat{\mathcal{R}}]P_0, \quad \int_{-\infty}^{v_{th}} dv \int_{-\infty}^{\infty} da \left(\frac{1}{\tau_{\text{ref}}} + \hat{\mathcal{R}}\right)\tilde{Q} = \frac{\tau_{\text{ref}} r_0}{2} - 1 \quad (\text{for } \omega = 0). \tag{2.31}$$

The firing rate and the real part of the Fourier transformed probability density determine the spike-train power spectrum via Eqs. (2.8) and (2.25). In summary, to calculate the spike-train power spectrum, the following system of equations has to be solved from top to bottom with the boundary conditions denoted in the last line:

$$\begin{aligned}
&(\hat{\mathcal{L}} + \hat{\mathcal{R}})P_0(v, a) = 0, \quad \int_{-\infty}^{v_{\text{th}}} dv \int_{-\infty}^{\infty} da\, P_0(v, a) + \tau_{\text{ref}} r_0 = 1, \quad r_0 = -\int_{-\infty}^{\infty} da\, \frac{\beta^2}{2\tau_m^2} \partial_v P_0(v, a)\Big|_{v=v_{\text{th}}}, \\
&(i\omega + \hat{\mathcal{L}} + e_\tau\,\hat{\mathcal{R}})\tilde{Q} = \left[1 + \left(\frac{e_\tau - 1}{i\omega} - \frac{e_\tau}{r_0}\right)\hat{\mathcal{R}}\right] P_0 \qquad (\text{for } \omega \neq 0), \\
&(\hat{\mathcal{L}} + \hat{\mathcal{R}})\tilde{Q} = [1 + (\tau_{\text{ref}} - r_0^{-1})\,\hat{\mathcal{R}}]P_0, \quad \int_{-\infty}^{v_{th}} dv \int_{-\infty}^{\infty} da \left(\frac{1}{\tau_{\text{ref}}} + \hat{\mathcal{R}}\right)\tilde{Q} = \frac{\tau_{\text{ref}} r_0}{2} - 1 \qquad (\text{for } \omega = 0), \\
&S(\omega) = r_0 - 2r_0 \text{Re}\left(\int_{-\infty}^{\infty} da\, \frac{\beta^2}{2\tau_m^2} \partial_v \tilde{Q}(v, a, \omega)\Big|_{v=v_{\text{th}}}\right), \\
&\lim_{|a|\to\infty} F(v, a) = \lim_{v\to-\infty} F(v, a) = F(v_{\text{th}}, a) = 0 \text{ for } F(v, a) = P_0(v, a), \tilde{Q}(v, a, \omega).
\end{aligned} \tag{2.32}$$

This set of equations represents the theory of spike-train power spectra for two-dimensional stochastic integrate-and-fire neurons. For the general case, the solution of the partial dfferential equations are unknown, hence, the solutions in the following are determined numerically. For that purpose, a numerical procedure based on finite-difference methods is used as described in detail in the Appendix Sec. (A.2). Note, that the calculation of spike-train power spectra by this numerical procedure is not necessarily more efficient than direct simulations and is rather used as a proof of principle. However, Eq. (2.32) provides a theory that might reveal novel insights by a more clever treatment in future. In the following, numerical solutions of Eq. (2.32) are presented to study the resulting power spectra and to proof the correctness of the introduced theory. In all following figures the frequency $f = \omega/(2\pi)$ is used if not stated otherwise.

2.1.3 Leaky integrate-and-fire neuron driven by cyan and white-plus-red noise

Here the theory is tested for a leaky integrate-and-fire (LIF) neuron that receives temporally correlated input fluctuations with Gaussian statistics, so-called colored noise. The auxiliary process a in Eq. (2.1) is employed as an Ornstein-Uhlenbeck process to generate colored noise by Markovian embedding. In this special case the generic model reads:

$$\begin{aligned} \tau_m \dot{v} &= -v + \mu + \overbrace{a + \beta\xi(t)}^{\eta(t):=}, \\ \tau_a \dot{a} &= -a + b\xi(t) \end{aligned} \tag{2.33}$$

with the fire-and-reset rule and no adaptation $\delta_a = 0$ [see also Câteau and Reyes (2006) for similar model but without refractory period]. The model arises from Eq. (2.1) by using an Ornstein-Uhlenbeck process $g(v, a) = -a$ that ensures that the stationary solution exists. For the voltage dynamics, the popular LIF model is chosen with $f(v, a) = -v + a + \mu$. Here the one-dimensional neuron is subject to the colored noise $\eta(t) = a + \beta\xi(t)$ that models external input fluctuations independent from both, the membrane voltage and the spike history. The mean input is given by μ. As discussed below, an additional noise term $\xi_2(t)$ in the auxiliary process does not enrich the dynamics, thus, I use $b_2 = 0$.

To calculate the power spectrum of the input fluctuations $\eta(t)$, we determine its Fourier transformed using the Fourier transformed of a in Eq. (1.7):

$$\tilde{\eta}(\omega) = \underbrace{\frac{b\tilde{\xi}}{1 - i\omega\tau_a}}_{=\tilde{a}(\omega)} + \beta\tilde{\xi}. \tag{2.34}$$

By its definition in Eq. (1.2), the power spectrum of η can be identified as:

$$S_{\eta\eta}(\omega) = \lim_{T\to\infty} \frac{\langle \tilde{\eta}(\omega)\tilde{\eta}^*(\omega)\rangle}{T} = \lim_{T\to\infty} \frac{\langle \tilde{a}\tilde{a}^*\rangle + \beta\langle \tilde{a}\tilde{\xi}^*\rangle + \beta\langle \tilde{a}^*\tilde{\xi}\rangle + \beta^2\langle \tilde{\xi}\tilde{\xi}^*\rangle}{T} = \frac{b^2 + 2b\beta}{1 + \tau_a^2\omega^2} + \beta^2. \tag{2.35}$$

The power spectrum is given by the constant high frequency limit given by β^2 plus or minus a Lorentzian with a peak at $\omega = 0$ and the full width at half maximum $2\tau_a^{-1}$. By the analogy to the spectrum of visible light it is convenient to characterize noise with a non-flat spectrum by its 'color'. As presented in Fig. 2.4, three qualitatively different cases can be distinguished depending on the fraction b/β that determines the fraction of high- and low-frequency $S_{\eta\eta}(0) = (b + \beta)^2$:

1. **White noise**: In the trivial case $b = 0$ but also if $b = -2\beta$ (indicated by the white vertical lines in Fig. 2.4) $\eta(t)$ is a white noise process with constant power spectrum.
2. **Cyan noise**: In the range of $-2 < b/\beta < 0$ (cyan region in Fig. 2.4) the sign of the Lorentzian is negative and the resulting noise is high-pass filtered. The spectrum exhibits its absolute minimum at $\omega = 0$ that is even zero in the special case $b = \beta$.

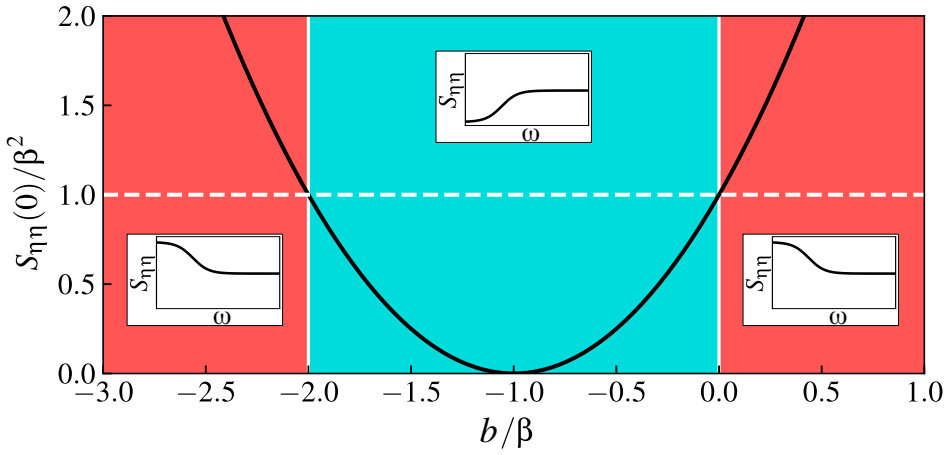

Figure 2.4.: Power spectra of one-dimensional Markovian embedding at $\omega = 0$. Low frequency limit of the power spectrum in dependence on the fraction of the noise strengths b/β. For $b < 2\beta$ or $b/\beta > 0$ the low-frequency limit is higher than the high-frequency limit β^2 yielding a low pass filtered noise plus a constant that we call *white-plus-red* noise. For $-2\beta < b < 0$ we obtain a high-pass filtered spectrum that we refer to as *cyan* (white-minus-red) noise. For the cases $b = 0$ and $b = -2\beta$ the noise is not temporally correlated and the spectrum is only a constant. Except for the special case $S_{\eta\eta}(0) = 0$ two representations of the same colored noise exists with different values for b.

Visible light in the low frequency range of visible light is perceived as red light, light that lacks power at low frequencies as the complementary color of red which is cyan [cf. (De Mayo, 2014) chapter 6]. Thus, the obtained high-pass filtered noise is referred to as *cyan* noise in this work [3].

3. **White-plus-red noise**: For the other values $b/\beta < -2$ or $b/\beta > 0$ indicated as red regions in Fig. 2.4, the sign of the Lorentzian is positive and the spectrum exhibits a maximum at $\omega = 0$ but saturates at β^2. This incompletely low-pass filtered noise is referred to as *white-plus-red* noise.

The benefit of application of the same white-Gaussian noise $\xi(t)$ in both variables v and a in Eq. (2.33) can be understood by the input spectrum in Eq. (2.35). With independent sources of noise, the mixed term $2b\beta$ vanishes in the numerator. In this case, the Lorentzian is always positive and cyan noise cannot be generated. An additional independent noise $\xi_2(t)$ in a only yields a positive bias in the numerator and, hence, cannot be used to generate noise with different power spectra.

The quadratic equation for the zero-frequency limit of the spectrum reveals an ambiguity of the spectrum's representation. Except for the case $S_{\eta\eta}(0) = 0$, the two values $b = \pm\sqrt{S_{\eta\eta}(0)} - \beta$ yield identical spectra. A similar ambiguity was found for the generalized Langevin equations by Siegle et al. (2010).

[3] The cyan noise is also referred to as green noise in the literature, based on a different color model. See for instance Guz and Sviridov (1998).

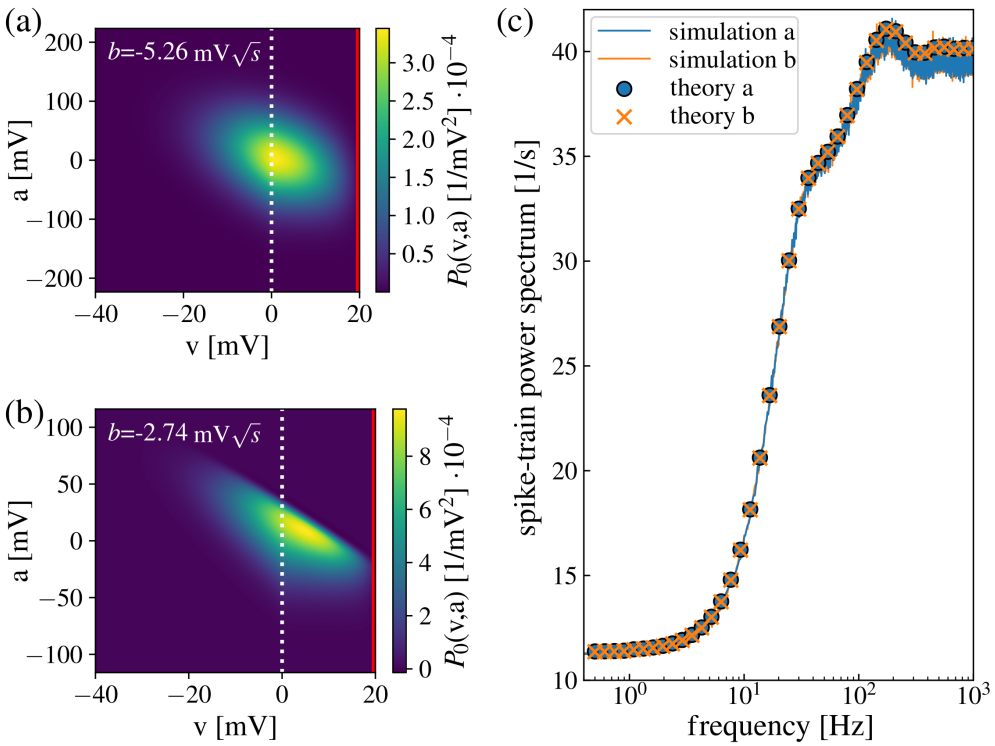

Figure 2.5.: Ambiguity in spectrum for one-dimensional Markovian embedding. Two representations of the same colored noise yield different stationary solutions as shown in panel a and b with $b = (-\sqrt{0.1} - 1)\beta$ and $b = (\sqrt{0.1} - 1)\beta$, respectively, but the same spike-train power spectrum shown in panel d. See Sec. (C.1) for parameters.

One example for a cyan input noise with $S_{\eta\eta}(0) = 0.1\beta^2$ represented by two different values of b is shown in Fig. 2.5. The resulting stationary densities are different. For the stronger noise ($b = [-\sqrt{0.1}-1]\beta$ in Fig. 2.5a), the stationary density fades out rather smoothly whereas for the weaker noise ($b = [\sqrt{0.1} - 1]\beta$ in Fig. 2.5b), it displays a sharp edge. The numerical solutions of the introduced theory and direct simulations of the Langevin equations yield the same spike-train power spectrum for both representations of the same colored noise. Only in case of an insufficient resolution, the numerical solutions for both representations of the noise differ significantly as shown in the Appendix Sec. A.2.6. It is worth mentioning that ambiguity does not only arise due to the representation of the colored noise. Also the finding of the Langevin equation to a given Fokker-Planck equation is not uniquely determined in the multidimensional case [see Risken (1984) chapter 3.4.1].

In the following, the introduced theory is tested systematically for cyan and white-plus-red noise with $S_{\eta\eta}(0) = 0.1\beta^2$ and $S_{\eta\eta}(0) = 2\beta^2$, respectively, each in both, the fluctuation-dominated and the mean-driven regime $\mu = 0.75v_{\text{th}}$ and $\mu = 1.5v_{\text{th}}$. To show the effect of the colored noise, the time constant τ_a and the noise strength β are varied. The colored noise is characterized by the frequency $f_c = (2\tau_a)^{-1}$ at which the power spectrum almost reached the high-frequency limit. The spectra are also compared to spike-train power spectra of LIF

neuron driven by white noise with strength β that are calculated by the analytical formula shown in the Appendix Sec. A.3 that has been derived by Lindner et al. (2002).

Cyan noise

Power spectra from LIF neurons driven by cyan noise are shown in Fig. 2.6. In all cases, the results of the theory in Eq. (2.32), shown by the red dots, is capable to predict the power spectra of the numerical simulations shown as blue lines. Input power spectra in units of $\mathrm{mV}^2\mathrm{s}$ are presented as orange lines. At frequencies at which the power of the input noise is reduced, the corresponding spike-train power spectrum also exhibits low power. In all cases, the absolute minimum of the spike-train spectrum is located at the position of the minimum of the corresponding input spectrum at $\omega = 0$. For high and intermediate time constants with $f_c < r_0$ (first and second row), the reduced power of the input only affects the spectra at low frequencies $f < f_c$. At higher frequencies, the spectra are similar to the spectra of an LIF neuron driven by white-noise with strength β that are presented in the first row as black dashed lines. By the application of the cyan noise input, a maximum may arise in the power spectrum located between $0 < f < r_0$ as shown in Fig. 2.6d,e,j and k if the power spectrum of the corresponding white-noise-driven LIF exhibits a maximum at $\omega = 0$. Remarkably, these peaks emerge only due to the reduction of power at low frequencies and not due to an oscillation mechanism. The increase of the time to $f_c > r_0$ yields different spectra: for low noise pronounced peaks can be found at the firing rate (cf. Fig. 2.6c and i) and, in the fluctuation dominated regime, the firing rate is significantly reduced (cf. Fig. 2.6c). Furthermore, the membrane voltage and auxiliary variable are clearly negatively correlated as shown in the stationary solutions in Fig. 2.6m,n.

White-plus-red noise

Also for the white-plus-red noise input the theory predicts the results from direct simulations. Compared to the cyan noise, the white-plus-red noise affects the spike-train power spectra in the opposite way. Here the spectra are characterized by increased power at low frequencies. Minima may emerge in the interval $0 < f < r_0$ as shown in Fig. 2.7a,b,g and h if the spectrum of the corresponding neuron driven by white noise has a minimum at $\omega = 0$. For a low time-constant and weak noise in the fluctuation dominated regime, the firing rate is increased (cf. Fig. 2.7c). Again, for $f_c < r_0$ the effect of the red-noise component only influences the spectra up to frequencies $f < f_c$. The membrane voltage and auxiliary variable are positively correlated as can be seen in the stationary solutions in Fig. 2.7m and n.

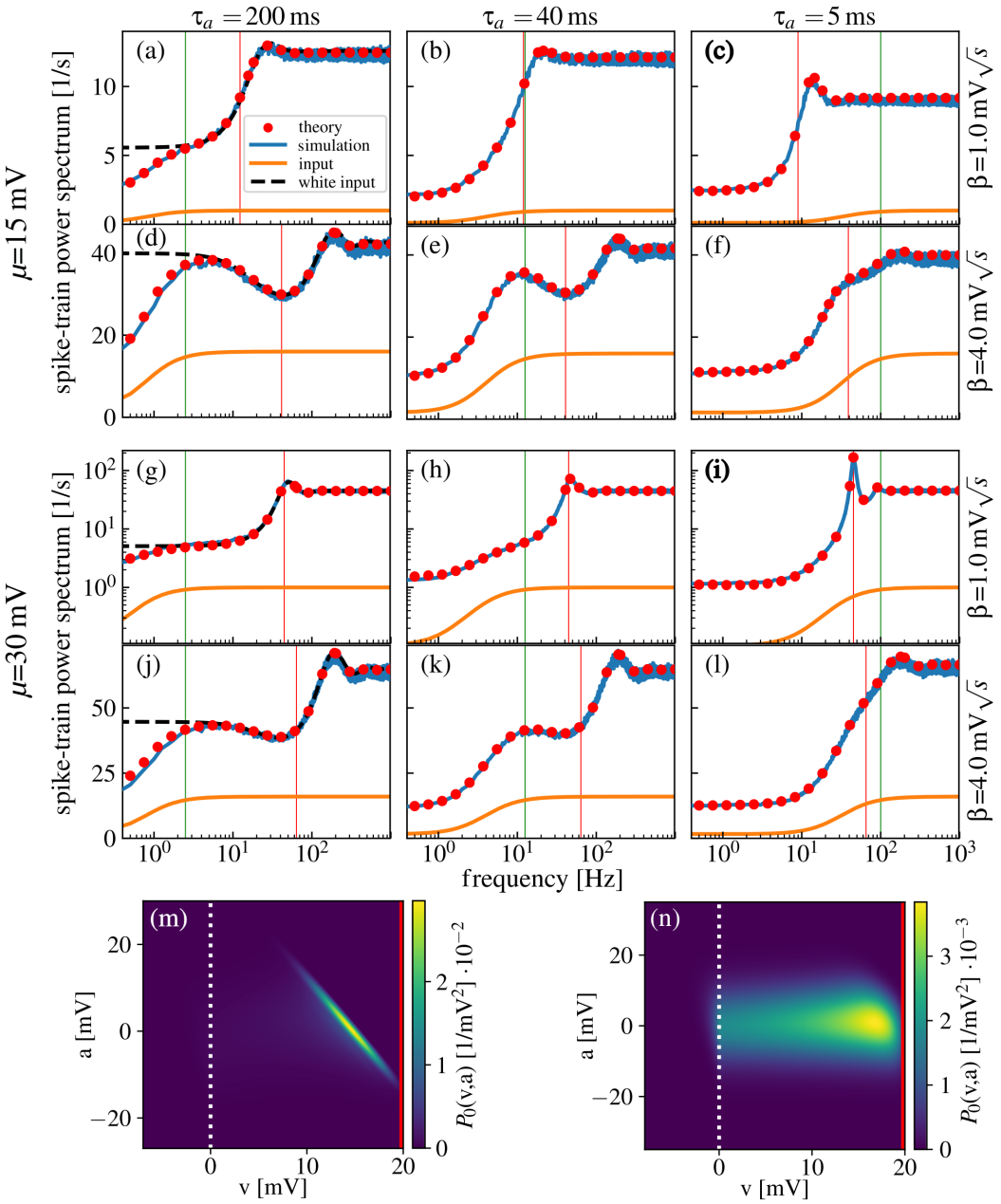

Figure 2.6.: Spike-train power spectra of LIF neuron driven by cyan noise. Cyan noise is generated with $S_{\eta\eta}(0) = 0.1\beta^2$ by $b = (\sqrt{0.1}-1)\beta$. Spectra in the fluctuation-dominated regime with $\mu = 15\,\mathrm{mV} = 0.75 v_{\mathrm{th}}$ and in the mean-driven regime with $\mu = 30\,\mathrm{mV} = 1.5 v_{\mathrm{th}}$ are presented in panels (a-f) and (g-l), respectively. The results of theory are shown as red dots, simulation results as blue lines and the input spectrum in units of $\mathrm{mV}^2\mathrm{s}$ as orange lines. The reference frequencies $f_c = 2\pi\omega_c = (2\tau_a)^{-1}$ and $f = r_0$ are indicated by green and red vertical lines, respectively. Spike-train power spectra of white-noise-driven LIF neurons with strength β are indicated by black dashed lines in panels on the left hand side. The auxiliary time constant is decreased from left to right and the noise strength β increased from top to bottom. Panels m and n show the stationary solutions corresponding to the parameter sets of c and i, respectively. See Sec. (C.1) for parameters.

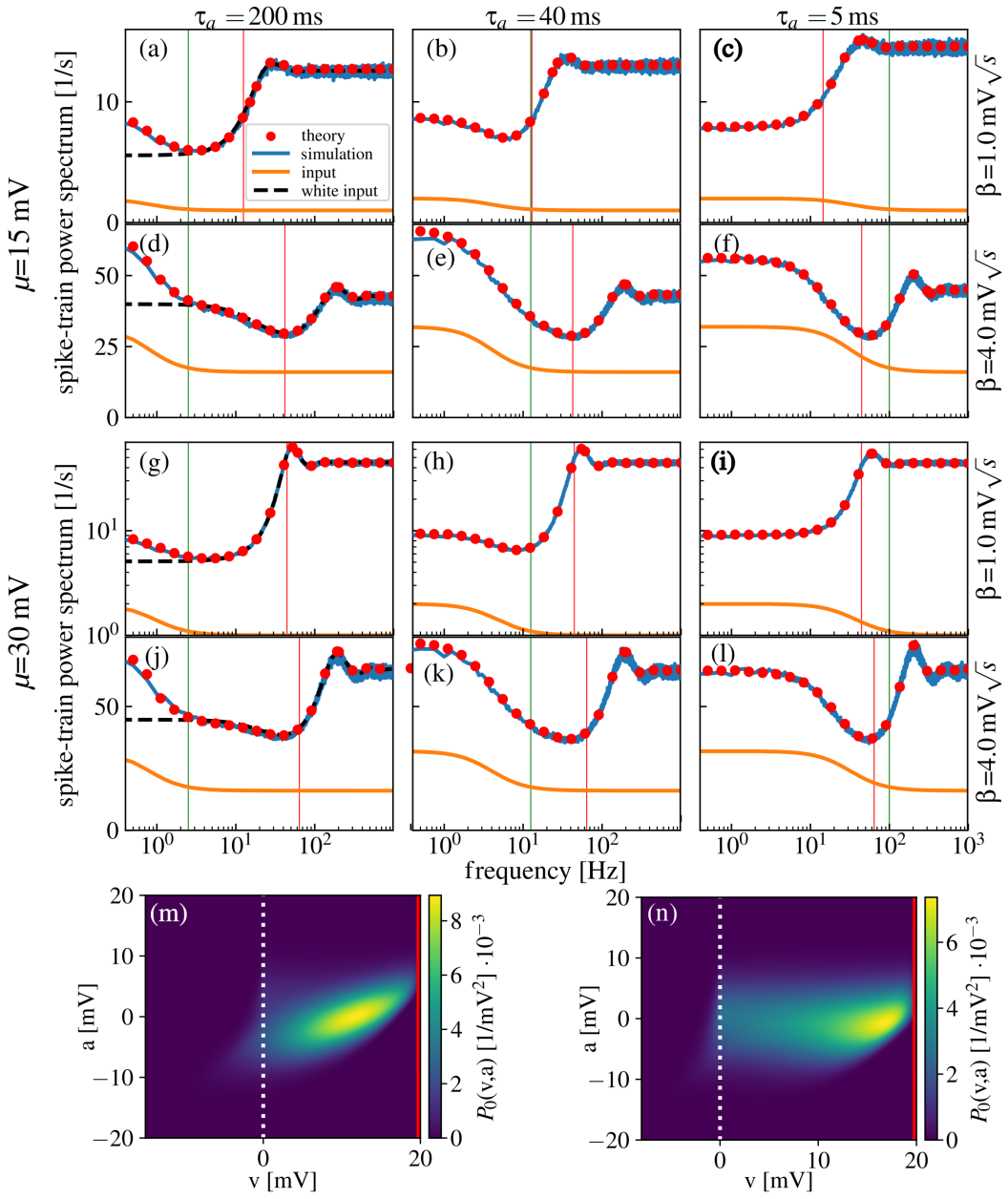

Figure 2.7.: Spike-train power spectra of LIF neuron driven by white-plus-red noise. White-plus-red noise is generated with $S_{\eta\eta}(0) = 2\beta^2$ by $b = (\sqrt{2}-1)\beta$. For detailed description see caption of Fig. 2.6.

Varying refractory period

In Fig. 2.8 the spike-train power spectra for the cyan and white-plus-red noise driven LIF neurons are presented for varying refractory periods from 0 to 100 ms. The latter value may appear rather long and uncommon, but it has been used for instance to model pyramidal neurons in the entorhinal cortex of rats by Engel et al. (2008). The neurons are in the fluctuations dominated regime with $\mu = 0.75\nu_{\mathrm{th}}$. Again, the theory adequately predicts the spectra of the direct simulations. For an increasing refractory period, the shape of the power spectra drastically change. The firing rates are reduced and the spikes are more regular with very low power at low frequencies. Sharp peaks emerge at the firing rate and its higher harmonics. Even in the case of the high refractory period the effect of the temporal correlations on the spike-train power spectrum can be seen by a higher amplitude of the first spectral peak for cyan noise compared to the peak for the white-plus-red noise input.

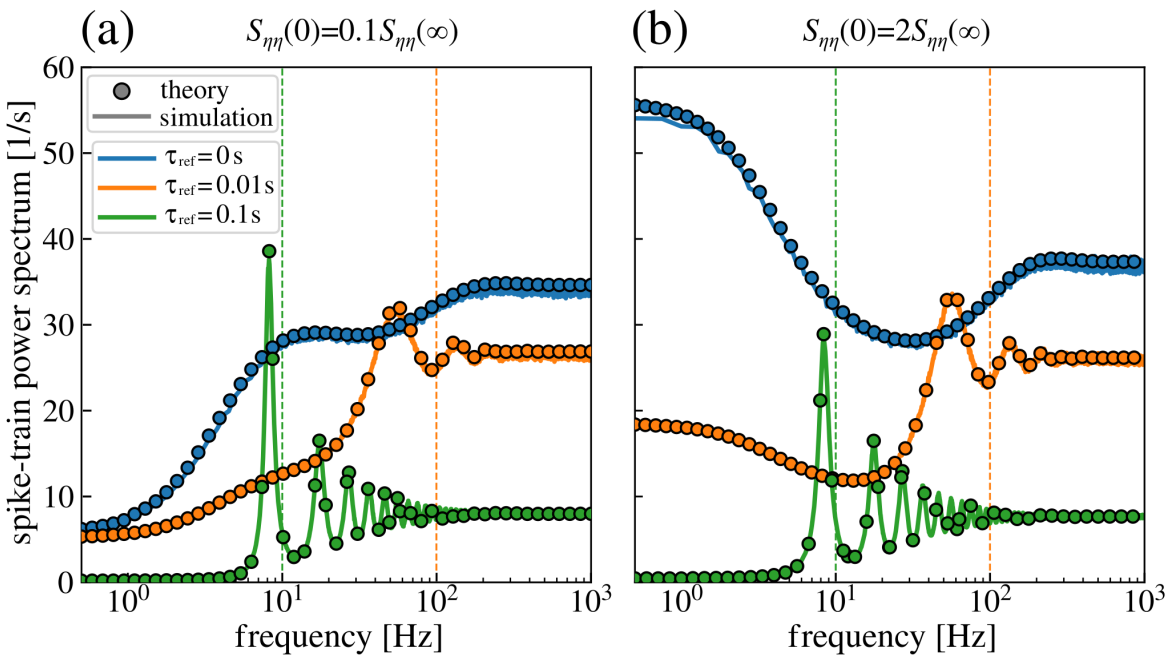

Figure 2.8.: Effects of refractory period. Spike-train power spectra of an LIF neuron driven by cyan (a) and white-plus-red noise (b). The refractory period is increased from 0 to 100 ms. Results from theory and direct simulations are presented as dots and lines, respectively. The inverse of the refractory periods $f = 1/\tau_{\mathrm{ref}}$ are indicated with the corresponding color as vertical dashed lines. See Sec. C.1 for parameters.

2.1.4 Stochastic exponential integrate-and-fire neuron with adaptation

In real neurons, action potentials are characterized by a steep rise of the membrane voltage caused by the fast opening of sodium channels in the membrane as first discovered by Hodgkin and Huxley (1952). In order to include such a steep rising membrane voltage in one-dimensional IF neurons, they have been extended by nonlinear dynamics that cause a positive feedback. As an approximation of the spike generation in more detailed biophysical models, Fourcaud-Trocmé et al. (2003) proposed an exponential term in the voltage dynamics that yields the exponential integrate-and-fire neuron (EIF) which has been verified experimentally for pyramidal cells by Badel et al. (2008); Harrison et al. (2015). A particularly interesting model arises by the combination of a positive feedback in the membrane voltage and a negative feedback caused by an adaptation current. An exponential feedback with linearized adaptation dynamics yields the adaptive EIF (AdEx) neuron introduced by Brette and Gerstner (2005). With temporally uncorrelated input fluctuations $\xi_1(t)$ with strength β and mean μ the model is given by:

$$\begin{aligned} &\tau_m \dot{v} = -v + \Delta_T \exp\left(\frac{v - v_T}{\Delta_T}\right) - a + \mu + \beta\xi_1(t), \\ &\tau_a \dot{a} = Av - a + b\xi_2(t), \\ &\text{if } v(t) > v_{\text{th}} : \\ &\quad v(t) \to v_{\text{ref}},\ v(t + \tau_{\text{ref}}) \to v_{\text{r}} \text{ and } a(t) \to a(t) + \delta_a. \end{aligned} \tag{2.36}$$

The effective threshold v_T determines at which voltage the positive feedback has an impact. For a significantly lower membrane voltage $v \ll v_T$ the exponential term is negligibly small and does not affect the voltage dynamics such that the model behaves almost like an LIF neuron in the subthreshold regime. If the membrane voltage exceeds v_T, the exponential term becomes the dominant part of the dynamics and yields a rapid increase until true threshold v_{th} is reached. In contrast to the model introduced in the previous section [Sec. (2.1.3)], the second variable models an intrinsic neuronal feature that is based on several biophysical mechanisms summarized by Benda and Herz (2003) and can be seen as extension of the GIF neuron introduced by Richardson et al. (2003); Brunel et al. (2003). In the convention used here, the adaptation current causes a negative feedback to the membrane voltage if the coefficients $\delta_a \geq 0$ and $A \geq 0$ are positive. Deterministic models with constant input that contain both, a positive feedback in the membrane voltage in combination with an adaptation current, are capable to mimic the complex spike responses to a constant input of *in vitro*. The underlying mechanism was first studied for a quadratic term in the voltage dynamics by Izhikevich (2003) and later also for an exponential term by Touboul and Brette (2008); Naud et al. (2008). Furthermore, the spiking response of an AdEx model to a stimulus may be similar to the response of detailed biophysical models and real nerve cells as shown by Clopath et al. (2007); Jolivet et al. (2008). It is worth mentioning that with a changed sign of a in the voltage dynamics, the auxiliary variable may also model a second neuronal compartment that represents the membrane voltage in the dendrites, as used for instance by Ostojic et al. (2015) and Doose et al. (2016).

Deterministic spike-triggered adaptation

First I show the influence of deterministic spike-triggered adaptation on the spike-train power spectrum by using $\delta_a > 0$ and $A = b = 0$ such that a only increases by the constant amount δ_a at the spike times and decays exponentially with the time constant τ_a in between the spikes. The spike-train power spectra resulting from the theory are in excellent agreement with the spectra from direct simulations for a neuron in the fluctuation dominated regime as presented in Fig. 2.9a and b. All used parameters are shown in Sec. C.1. The increase of the adaptation time constant τ_a by a constant adaptation strength δ_a reduces the firing rate as shown in Fig. 2.9a. The adaptation current decays more slowly for higher τ_a such that the temporally averaged value of a increases with τ_a. Put differently, the negative spike-triggered feedback is more persistent for an increased τ_a and, thus, the firing rate is decreased. Moreover, power is reduced at low frequencies up to τ_a^{-1} indicated by the solid vertical lines that follow the color encoding in Fig. 2.9a. The increase of the adaptation strength δ_a by constant τ_a also reduces the firing rate as shown in Fig. 2.9b due to the stronger negative feedback. More interesting, a higher the adaptation strength reduces the power at frequencies lower than the inverse time constant τ_a^{-1} indicated by the black vertical line in Fig. 2.9b. The range at which the power is reduced at low frequencies does not shrink or expand.

Stochastic adapatation

A biophysical motivation of spike-frequency adaptation is to incorporate the dynamics of ion channels (Benda and Herz, 2003). The finite number of these adaptation channels in the membrane causes fluctuations in the adaptation variable that can be important to describe the firing statistics of sensory neurons as shown by Fisch et al. (2012). Here these fluctuations are modeled by white Gaussian noise $b\xi_2(t)$ in the adaptation variable. As a consequence, the voltage dynamics are subject to the combination of the white noise input current $\beta\xi_1(t)$ and the noisy adaptation. Following the idea of Schwalger et al. (2010), it is convenient to study the effect of the combined noise by splitting the adaptation current into deterministic adaptation $a_1(t)$ and noisy adaptation $a_2(t)$. We obtain the two equations:

$$\begin{aligned} \tau_a \dot{a}_1 &= Av - a_1 \\ \tau_a \dot{a}_2 &= -a_2 + b\xi_2(t), \end{aligned} \tag{2.37}$$

where the incrementation due to the spike-triggered adaptation only applies to a_1 (when $v > v_{\mathrm{th}}$, $a_1 \to a_1 + \delta_a$). As the result of the separation, the influence of the stochastic adaptation can be subdivided in the deterministic spike-triggered adaptation as described in the previous subsection and the combined fluctuations that enter the v dynamics $\eta = a_2 + \beta\xi_1(t)$. These fluctuations can be identified as white-plus-red noise with the power spectrum:

$$S_{\eta\eta}(\omega) = \lim_{T\to\infty} \frac{\langle \tilde{a}_2 \tilde{a}_2^* \rangle + \beta\langle \tilde{a}_2 \tilde{\xi}_1^* \rangle + \beta\langle \tilde{a}_2^* \tilde{\xi}_1 \rangle + \beta^2 \langle \tilde{\xi}_1 \tilde{\xi}_1^* \rangle}{T} = \beta^2 + \frac{b^2}{1 + \tau_a^2 \omega^2}, \tag{2.38}$$

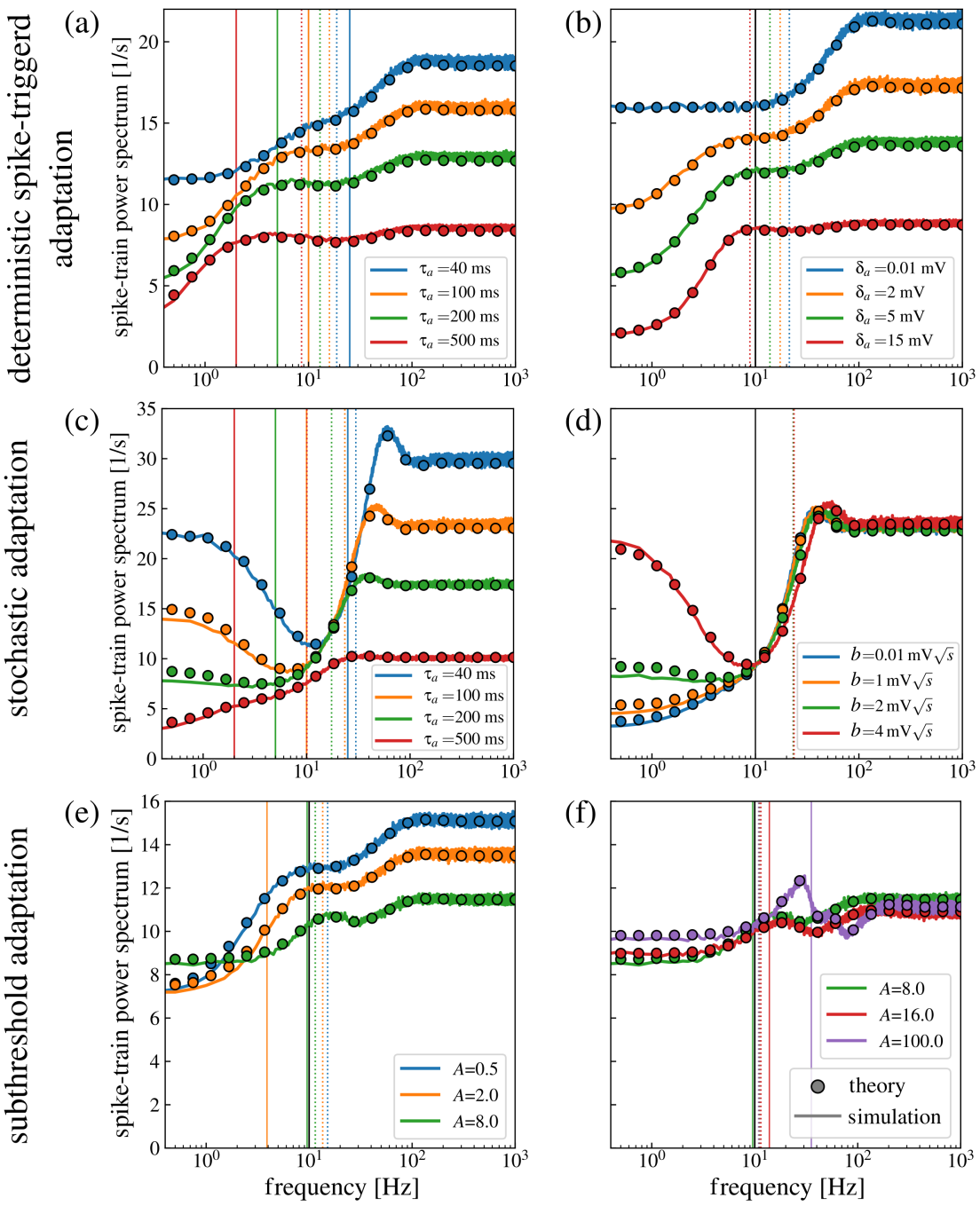

Figure 2.9.: Spike-train power spectra of exponential integrate-and-fire neurons with adaptation current. Purely deterministic spike-triggered adaptation with $\delta_a > 0$, $A = b = 0$ (a,b), additional stochastic adaptation $b > 0$ (c,d) and additional subthreshold adaptation $A > 0$ (e,f). Results from direct simulations (solid lines) are compared with the theory (colored circles). The inverse of the adaptation time constant τ_a^{-1} is represented as solid vertical line following the color encoding if it is varied, or black if constant. In (e,f), the estimated subthreshold oscillation frequencies f_{ref} are additionally indicated by colored vertical lines. Firing rates are represented as vertical dotted lines following the color encoding. See Sec. (C.1) for used parameters.

for which I used that the Fourier transformed of a_2 is given by the analogous calculation in Eq. (1.7) as:

$$\tilde{a}_2(\omega) = \frac{b\tilde{\xi}_2}{1 - i\tau_a\omega}. \tag{2.39}$$

As it is the case in the previous section in Fig. 2.6, the white-plus-red input noise increases the power of the spike train at low frequencies as presented in Fig. 2.9c. The increase of the time constant τ_a yields a reduced firing rate due to the spike-triggered adaptation and reduced power at low frequencies. The increase of the noise strength in Fig. 2.9d increases the power of the input at low frequencies such that also the spike-train power spectrum exhibits higher power at low frequencies. As in Fig. 2.7, the spectra at intermediate and high frequencies ($f > \tau_a^{-1}$) are only slightly affected by increase.

Subthreshold adaptation

If voltage-gated ion channels are responsible for the adaptation, the variable a is not only increased at spike times but also depends on v. Here linear subthreshold adaptation is considered if $A > 0$. The qualitative behavior may be changed drastically (Touboul and Brette, 2008) and a new fixed point may emerge and can be turned into a stable focus such that subthreshold oscillations occur that modulate the spike train (Richardson et al., 2003; Brunel et al., 2003) and are also observable as peaks in the spike-train power spectrum as studied by Blankenburg et al. (2015). For the introduced model, the oscillation frequency can be estimated by the eigenvalues λ of the deterministic Jacobi matrix of only the linear terms in Eq. (2.36) given by:

$$\det\begin{pmatrix} -\tau_m^{-1} - \lambda & -\tau_m^{-1} \\ A\tau_a^{-1} & -\tau_a^{-1} - \lambda \end{pmatrix} = 0 \Rightarrow \lambda = -\frac{\tau_m + \tau_a}{2\tau_a\tau_m} \pm \sqrt{\frac{\tau_m/(4\tau_a) + \tau_a/(4\tau_m) - 1/2 - A}{\tau_m\tau_a}}. \tag{2.40}$$

The frequency is given by the imaginary part of the eigenvalues $f_{\mathrm{res}} = \mathrm{Im}(\lambda)/(2\pi)$. In Fig. 2.9e and f peaks emerge roughly at the f_{res}. With high subthreshold adaptation with $A = 100$ the peak is particularly pronounced. Since the subthreshold adaptation is an additional negative feedback to the membrane voltage it also yields a reduction in the firing rate.

Bursting

As mentioned above, the AdEx model is capable to exhibit complex spike patterns observed *in vitro* and *in vivo*, for which bursting is one important example. A bursting neuron fires several rapidly consecutive action potentials and is subsequently silent for a longer period of time. In our model, bursting behavior appears if the reset voltage is higher than the effective threshold $v_{\mathrm{r}} < v_{\mathrm{T}}$ and the time constant of the adaptation τ_a is large compared to the average interspike interval. In that case, a neuron at reset voltage with low adaptation variable is directly subject to the positive feedback and spikes very fast. It continues rapid spiking until the adaptation variable is sufficiently high such that it compensates the positive feedback and pulls down the membrane voltage under the effective threshold. Than, the neuron is silent

for a longer period of time until the adaptation variable is decayed. When the adaptation is low again, the membrane voltage may cross the effective threshold and the neuron bursts again. Here we tune the parameters to obtain a bursting neuron with two or three consecutive spikes with short time intervals (intra-burst intervals) and longer pauses of around 200 ms (inter-burst intervals) as can be seen in Fig. 2.10a (see Sec. (C.1) for used parameters).

The bursting mechanism is also reflected by the stationary density presented in Fig. 2.10b. There, the reset is presented as white dotted line. If the neuron's state point in the phase plane is located somewhere right from the v-nullcline, the membrane voltage rapidly increases yielding a fast spike with an instantaneous increase of the adaptation variable by the reset. With our choice of parameters, the neuron is reset behind the v-nullcline after two spikes, however, the v-nullcline can be crossed a third time due to the noise. Otherwise, the neuron moves towards a lower membrane voltage in phase space until the adaptation variable has sufficiently decayed.

Also in this more complex case, the introduced theory (red dots) is capable to predict the spike-train power spectrum and is in excellent agreement with direct simulations (blue line) in Fig. 2.10c. The spike-train power spectrum reflects the bursting behavior by two peaks that correspond to the two types of intervals. The first one around 3.5 Hz dominates the spectrum while the second peak is less pronounced and much broader at around 200 Hz. In order to substantiate the hypothesis that the peaks belong to the two kinds of intervals, a burst is defined by sequential spikes with a maximal distance of 100 ms. The histogram in Fig. 2.10d presents the bimodal distribution of intervals that are classified as intra-bust intervals smaller than 100 ms in green, and inter-burst intervals larger than 100 ms in red. To show that the first peak belongs to the inter-burst intervals, I show the power spectrum of a manipulated spike train in which bursts are replaced by single spikes located at the averaged spike times. Their amplitudes are given by the number of replaced spikes. The power spectrum of these manipulated spike trains, shown in orange in Fig. 2.10c, agrees with the original one at low frequencies and also exhibits the first peak such that we may conclude that this peak arises from the inter-burst intervals. At intermediate and high frequencies the spectra strongly differ since in our manipulated spike train the intra-burst intervals are neglected and the spike amplitude varies such that the spectrum does not converge to the firing rate at high frequencies. To connect the second peak to the inter-burst intervals, I calculate the mean of the inter-burst intervals and replace them by intervals drawn from an exponential distribution as a Poisson process. The corresponding power spectrum presented in green is in agreement with the original one for frequencies higher than $f > 150\,\mathrm{Hz}$ but differs for lower frequencies.

Furthermore, I shuffled the inter-burst to demonstrate that intervals are correlated. The corresponding spectrum, shown in magenta, exhibits doubled power at low frequencies and the first peak is slightly shifted towards higher frequencies compared to the original spectrum.

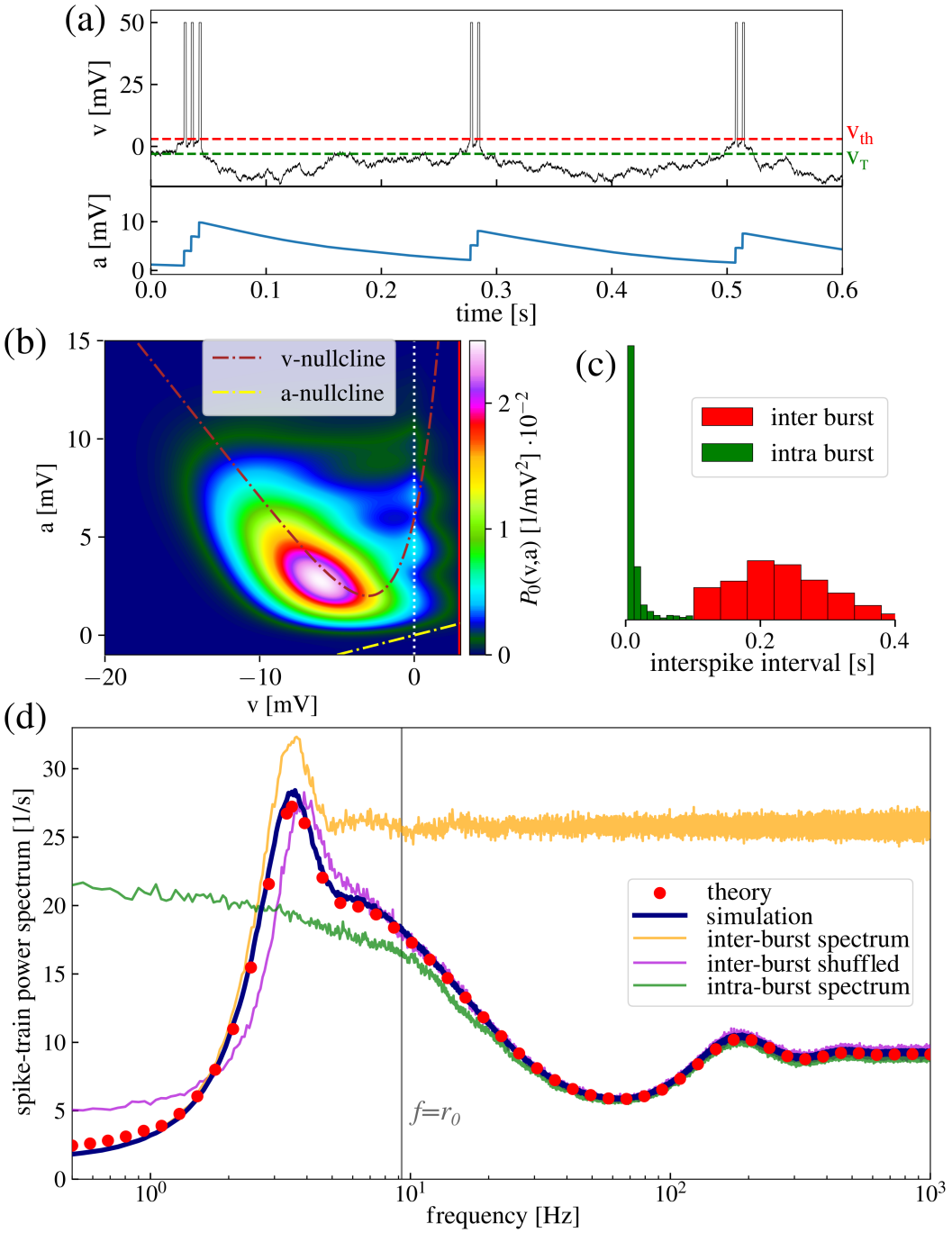

Figure 2.10.: Bursting neuron. Membrane voltage and adaptation variable with three bursts (a), stationary probability density and nullclines of v and a dynamics with threshold (red solid line) and reset voltage (white dotted line) (b), spike-train power spectra from theory and direct simulations and spectra from manipulated spike trains (c), histogram of interspike intervals that are splitted into intra- and inter burst intervals for < 100 ms and > 100 ms, respectively.

2.2 Generalization to d-dimensional models

The considered two-dimensional neuron models already possess a rich spiking behavior. However, the model cannot be used to study the influence of more complexly correlated input or multidimensional neurons driven by colored noise. Here I extend the auxiliary process a in Eq. (2.1) to d dimensions and show that the results from the two-dimensional model derived in Sec. (2.1) can be adapted to the more complex case. In its generic form, the neuron model reads:

$$\begin{aligned} \tau_m \dot{v} &= f(v,\vec{a}) + \vec{\beta}\vec{\xi}(t) \\ \dot{\vec{a}} &= \vec{g}(v,\vec{a}) + \mathbf{B}\vec{\xi}(t) \\ &\text{if } v(t) > v_{th}: \\ &\quad v(t) \to v_{\text{ref}},\ v(t+\tau_{\text{ref}}) \to v_r \text{ and } \vec{a}(t) \to \vec{a}(t) + \vec{\delta}_a. \end{aligned} \tag{2.41}$$

The dynamics of the d-dimensional auxiliary process $\vec{a}$ are now determined by the drift function $\vec{g}(v,\vec{a})$ and the diffusion term that consists of the $d\times d$ matrix $\mathbf{B}$ with the components B_{kl} and the vector $\vec{\xi}(t)$ whose d components are independent Gaussian white noise obeying $\langle \xi_i(t)\xi_j(t')\rangle = \delta_{ij}\delta(t-t')$.

The Fokker-Planck equation corresponding to Eq. (2.41) is given in time domain by:

$$\partial_t P(v,\vec{a},t) = \hat{\mathcal{L}}P(v,\vec{a},t) + \{\hat{\mathcal{R}}P\}(v,\vec{a},t) \tag{2.42}$$

where the operator $\hat{\mathcal{L}}$ describes the drift and diffusion terms in v and *all* dimensions of $\vec{a}$. In component notation it is given by:

$$\hat{\mathcal{L}} = \underbrace{-\partial_v \frac{f(v,\vec{a})}{\tau_m}}_{\text{drift in } v} + \underbrace{\frac{\vec{\beta}^2}{2\tau_m^2}\partial_v^2}_{\text{diffusion in } v} \underbrace{-\sum_{k=1}^{d}\partial_{a_k} g_k(v,\vec{a})}_{\text{drift in } \vec{a}} + \underbrace{\sum_{k,l,m=1}^{d}\frac{B_{kl}B_{ml}}{2}\partial_{a_k}\partial_{a_m}}_{\text{diffusion in } \vec{a}} + \underbrace{\sum_{k,l=1}^{d}\frac{\beta_k B_{lk}}{\tau_m}\partial_v\partial_{a_l}}_{\text{mixed diffusion}}. \tag{2.43}$$

Here ∂_{a_k} denotes the derivative in the k-th component of $\vec{a}$ and $g_k(v,\vec{a})$ the k-th component of $\vec{g}(v,\vec{a})$. Analogously to the two-dimensional case, the four steps of the fire-and-reset mechanism are incorporated by the operator $\hat{\mathcal{R}}$. Firstly, it measures the probability flux through the threshold. In contrast to the two-dimensional case, in which the threshold is only a line, here it is a d-dimensional manifold denoted by $M_{\vec{a}}$. Secondly, if spike-triggered adaptation is applied, the probability is shifted along the adaptation vector $\vec{\delta}_a \neq 0$. Thirdly, the efflux of probability within a small time bin is transferred into the refractory state in which it keeps evolving in the auxiliary dimensions according to the d-dimensional Fokker-Planck equation:

$$\partial_t p(\vec{a},t) = \left(-\sum_{k=1}^{d}\partial_{a_k} g_k(v,\vec{a}) + \sum_{k,l,m=1}^{d}\frac{B_{kl}B_{ml}}{2}\partial_{a_k}\partial_{a_m}\right) p(\vec{a},t). \tag{2.44}$$

If the transition probability during the refractory period $\rho_{\text{ref}}(\vec{a}|\vec{a}')$ is known as the solution

of Eq. (2.44), the evolution can be expressed by:

$$p(\vec{a}, \tau + \tau_{\mathrm{ref}}) = \int\limits_{M_{\vec{a}'}} d\vec{a}'\, \rho_{\mathrm{ref}}(\vec{a}|\vec{a}')p(\vec{a}', \tau). \tag{2.45}$$

Here the integral denotes integration over the whole manifold $M_{\vec{a}'}$ which is a point for $d = 0$, a line for $d = 1$, a surface for $d = 2$, a volume for $d = 3$ and so on. Finally the evolved probability is reinserted at v_{r}. All together, the whole fire-and-reset operator is given by:

$$\{\hat{\mathcal{R}}P\}(v, \vec{a}, t) = -\delta(v - v_r) \int\limits_{M_{\vec{a}'}} d\vec{a}'\, \rho_{\mathrm{ref}}(\vec{a}|\vec{a}') \frac{\vec{\beta}^2}{2\tau_m^2} \partial_v P(v, \vec{a}' - \vec{\delta}_a, t - \tau_{\mathrm{ref}})\Big|_{v=v_{\mathrm{th}}}. \tag{2.46}$$

$P(v, \vec{a}, t)$ obeys natural boundary conditions for all components $a_i \to \pm\infty$ and $v \to -\infty$ and an absorbing boundary at the threshold manifold due to the white noise in the voltage dynamics:

$$\lim_{|\vec{a}|\to\infty} P(v, \vec{a}, t) = \lim_{v\to-\infty} P(v, \vec{a}, t) = P(v_{\mathrm{th}}, \vec{a}, t) = 0 \tag{2.47}$$

Analogously to the two-dimensional case, the firing rate is the integrated efflux of probability that crosses the threshold manifold:

$$r(t) = -\int\limits_{M_{\vec{a}}} d\vec{a}\, \frac{\vec{\beta}^2}{2\tau_m^2} \partial_v P(v, \vec{a}, t)\Big|_{v=v_{\mathrm{th}}}. \tag{2.48}$$

The connection between the spike-train power spectrum an the Fourier transformed FPE can be derived analogously to the two-dimensional case just by replacing $P_0(v, a) \to P_0(v, \vec{a})$ and $\tilde{Q}(v, a, \omega) \to \tilde{Q}(v, \vec{a}, \omega)$ and considering that the total efflux over the threshold is given by the integration of the current over the manifold $M_{\vec{a}}$. Also the calculation in Sec. (2.1) is not affected by the extension of dimensionality if we simply exchange the argument $a \to \vec{a}$. As the final result, the spike-train power spectrum is given by the solution of the set of equations:

$$\hat{\mathcal{L}} = -\partial_v \frac{f(v,\vec{a})}{\tau_m} + \frac{\vec{\beta}^2}{2\tau_m^2}\partial_v^2 - \sum_{k=1}^{d} \partial_{a_k} g_k(v,\vec{a}) + \sum_{k,l,m=1}^{d} \frac{B_{kl}B_{ml}}{2}\partial_{a_k}\partial_{a_m} + \sum_{k,l=1}^{d} \frac{\beta_k B_{lk}}{\tau_m}\partial_v\partial_{a_l},$$

$$\hat{\mathcal{R}}\, F(v,\vec{a}) = -\delta(v-v_r) \int\limits_{M_{\vec{a}'}} d\vec{a}'\, \rho_{\mathrm{ref}}(\vec{a}|\vec{a}') \frac{\vec{\beta}^2}{2\tau_m^2}\partial_v F(v,\vec{a}' - \vec{\delta}_a)\Big|_{v=v_{\mathrm{th}}},$$

$$(\hat{\mathcal{L}}+\hat{\mathcal{R}})P_0(v,\vec{a}) = 0, \quad \int\limits_{-\infty}^{v_{\mathrm{th}}} dv \int\limits_{M_{\vec{a}}} d\vec{a}\, P_0(v,\vec{a}) + \tau_{\mathrm{ref}} r_0 = 1, \quad r_0 = -\int\limits_{M_{\vec{a}}} d\vec{a}\, \frac{\vec{\beta}^2}{2\tau_m^2}\partial_v P_0(v,\vec{a})\Big|_{v=v_{\mathrm{th}}},$$

$$(i\omega + \hat{\mathcal{L}} + e_\tau\, \hat{\mathcal{R}})\tilde{Q}(v,\vec{a},\omega) = \left[1 + \left(\frac{e_\tau - 1}{i\omega} - \frac{e_\tau}{r_0}\right)\hat{\mathcal{R}}\right] P_0(v,\vec{a}), \qquad (\text{for } \omega \neq 0),$$

$$(\hat{\mathcal{L}}+\hat{\mathcal{R}})\tilde{Q} = [1 + (\tau_{\mathrm{ref}} - r_0^{-1})\,\hat{\mathcal{R}}]P_0, \quad \int\limits_{-\infty}^{v_{\mathrm{th}}} dv \int\limits_{M_{\vec{a}}} d\vec{a} \left(\frac{1}{\tau_{\mathrm{ref}}} + \hat{\mathcal{R}}\right)\tilde{Q} = \frac{\tau_{\mathrm{ref}} r_0}{2} - 1 \qquad (\text{for } \omega = 0),$$

$$S(\omega) = r_0 - 2r_0 \mathrm{Re}\left(\int\limits_{M_{\vec{a}}} d\vec{a}\, \frac{\vec{\beta}^2}{2\tau_m^2}\partial_v \tilde{Q}(v,\vec{a},\omega)\Big|_{v=v_{\mathrm{th}}}\right),$$

$$\lim_{|\vec{a}|\to\infty} F(v,\vec{a}) = \lim_{v\to-\infty} F(v,\vec{a}) = F(v_{\mathrm{th}},\vec{a}) = 0 \text{ for } F(v,\vec{a}) = P_0(v,\vec{a}), \tilde{Q}(v,\vec{a},\omega). \tag{2.49}$$

To determine the solution, the numerical procedure introduced in Appendix Sec. A.2 is extended as described in the Appendix Sec. A.4. The computational requirements for such a solution drastically increase with the dimensionality which is known in literature as the *curse of dimensionality* (see for instance Pichler et al. (2013) chapter 5). Using standard techniques for partial differential equations it is only possible to adequately solve the problem with dimensionality up to $d = 2$.

2.2.1 Harmonic noise driven LIF neuron

The extension of the auxiliary process can be used to generate many qualitatively different kinds of stochastic input. As one example, here two auxiliary dimensions are linearly coupled to each other and combined with a white noise term in one variable in order to generate a stochastic harmonic oscillation. The influence of such a harmonic noise on bistable systems was studied by Schimansky-Geier and Zülicke (1990) but also on IF neuron models by Engel et al. (2009) as a model of certain electroreceptors of the paddlefish also using similar Fokker-Planck methods Bauermeister et al. (2013). Here we consider its influence on an LIF neuron for which the complete Langevin equation reads as:

$$\begin{aligned} \tau_m \dot{v} &= -v + \mu + y + \beta_1 \xi_1(t) \\ \dot{y} &= s \\ \dot{s} &= -\Gamma s - \omega_0^2 y + \beta_2 \xi_2(t), \end{aligned} \tag{2.50}$$

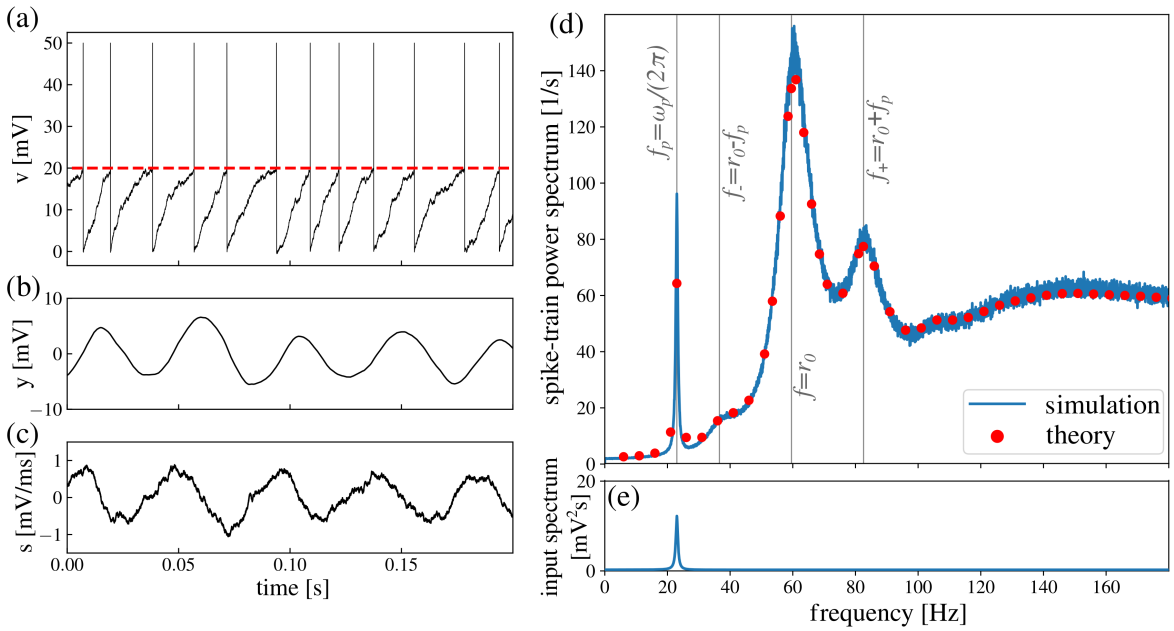

Figure 2.11.: LIF driven by harmonic noise. Trajectories of the membrane voltage (a), of the input y (b) and s (c). The resulting spike-train power spectrum determined by the introduced theory (red dots) and direct simulations of the Langevin equation (blue line) is presented in d; important freqeuncies at which peaks occur are indicated by gray vertical lines. The input power spectrum given by Eq. (2.51) is presented in panel e.

with the fire-and-reset rule in Eq. (2.41). For simplicity, neither spike-triggered adaptation nor a refractory period is applied ($\vec{\delta}_a = \tau_{\text{ref}}=0$). As an analogy to mechanics, we may see $y(t)$ as the position of a Brownian particle with velocity $s(t)$ in a parabolic potential. In this picture, the particle is driven by the thermal noise $\beta_2\xi_2(t)$ and is subject to Stokes friction with coefficient Γ. With the parameters chosen here (see Sec. C.1 for details) the trajectory of y is a noisy oscillation as shown in Fig. 2.11b. The power spectrum of the neural input $\eta(t) = y\beta_1\xi_1(t)$ is given by:

$$S_{\eta\eta}(\omega) = \frac{\beta_2^2}{\omega^2\Gamma^2 + (\omega^2 - \omega_0^2)^2} + \beta_1^2. \tag{2.51}$$

[cf. Schimansky-Geier and Zülicke (1990)]. The spectrum is characterized by a peak at $\omega_p = \sqrt{\omega_0^2 - \Gamma^2/2}$, its width is controlled by the friction coefficient Γ. In our parameter choise, we obtain a sharp peak in the input power spectrum in Fig. 2.11e. Unsurprisingly, the resulting spike-train power spectrum in Fig. 2.11d also exhibits a sharp peak at ω_p. Furthermore, as observed in experimental data in Neiman and Russell (2004); Bauermeister et al. (2013), the spectrum of a neuron in the mean-driven regime also exhibits peaks at $f_- = r_0 - \omega_p/(2\pi)$ and $f_+ = r_0 + \omega_p/(2\pi)$ if the driving frequency is around half the firing rate ($\omega_p \approx \pi r_0$) as indicated by gray vertical lines in Fig. 2.11d. The introduced theory (red

dots in Fig. 2.11d) is capable to predict the power spectrum from simulations (blue lines) also in the case of a two-dimensional Markovian embedding with rich correlation structure.

2.3 Derivatives of the power spectrum and Padé approximation

So far, single points of the spike train power spectrum have been calculated by the numerical solution of Eq. (2.49). For some applications, however, it might be beneficial to determine a continuous function as an approximation instead. For spike-train power spectra, which are symmetric with regard to the y-axis [$S(\omega) = S(-\omega)$] and saturate at the firing rate in the limit of high frequencies, a proper choice of approximation is given by the rational function:

$$S(\omega) \approx r_0 + \frac{\sum_{k=0}^{d-1} X_k \omega^{2k}}{1 + \sum_{\ell=1}^{d} Y_\ell \omega^{2\ell}}. \tag{2.52}$$

Due to the above mentioned symmetry, odd terms in ω are zero and do not need to be considered. Since the order of the fraction's denominator is higher than the order of the numerator its contribution vanishes in the limit of high frequencies and the approximation also saturates at the firing rate r_0. By the choice of $X_0 = S(0) - r_0$ Eq. (2.52) exact also at the low frequency limit $\omega = 0$. The other coefficients X_l and Y_ℓ can be determined to obtain a good approximation, for instance, they can be chosen such that the first $(4d - 2)$ derivatives at $\omega = 0$ coincide with the derivatives of the spectrum. Originally introduced by Frobenius (1881), this approximation is known as the Padé approximation in the literature (see also e.g. Press et al. (2007) chapter 5.12). The crucial part for the determination of the approximation is the calculation of the derivatives of the power spectrum at $\omega = 0$. The good news is that the corresponding set of equations that determining these derivatives arises by the n-th derivative at $\omega = 0$ of Eq. (2.49) by:

$$
\begin{aligned}
&(\hat{\mathcal{L}}+\hat{\mathcal{R}})P_0(v,\vec{a})=0, \quad \int\limits_{-\infty}^{v_{\mathrm{th}}} dv \int\limits_{M_{\vec{a}}} d\vec{a}\, P_0(v,\vec{a}) + \tau_{\mathrm{ref}} r_0 = 1, \quad r_0 = -\int\limits_{M_{\vec{a}}} d\vec{a}\, \frac{\vec{\beta}^2}{2\tau_m^2} \partial_v P_0(v,\vec{a})\Big|_{v=v_{\mathrm{th}}},\\
&(\hat{\mathcal{L}}+\hat{\mathcal{R}})\tilde{Q}_0^{\prime(n)} = \delta_{n,0} P_0 + (i\tau_{\mathrm{ref}})^n \left(\frac{\tau_{\mathrm{ref}}}{n+1} - \frac{1}{r_0}\right) \hat{\mathcal{R}}\, P_0 - ni\tilde{Q}_0^{(n-1)} - \sum_{k=0}^{n-1} \binom{n}{k} (i\tau_{\mathrm{ref}})^{n-k}\, \hat{\mathcal{R}}\, \tilde{Q}_0^{(k)},\\
&\tilde{Q}_0^{(n)} = \tilde{Q}_0^{\prime(n)} - P_0 \left[\frac{i^n \tau_{\mathrm{ref}}^{n+1}}{n+1} - \frac{i^n r_0 \tau_{\mathrm{ref}}^{n+2}}{\sum\limits_{k=1}^{n+1} 2k} + \int\limits_{-\infty}^{v_{\mathrm{th}}} dv \int\limits_{M_{\vec{a}}} d\vec{a} \left(\tilde{Q}_0^{\prime(n)} + \sum_{k=0}^{n} \binom{n}{k} \frac{i^{n-k} \tau_{\mathrm{ref}}^{n-k+1}}{n-k+1}\, \hat{\mathcal{R}}\, \tilde{Q}_0^{\prime(k)} \right) \right],\\
&S_0^{(n)} = \frac{d^n}{d\omega^n} S(\omega)\Big|_{\omega=0} = \delta_{n,0} r_0 - 2r_0 \mathrm{Re} \left(\int\limits_{M_{\vec{a}}} d\vec{a} \frac{\vec{\beta}^2}{2\tau_m^2} \partial_v \tilde{Q}_0^{(n)}\Big|_{v=v_{\mathrm{th}}} \right), \quad \tilde{Q}_0^{(n)} = \frac{d^n}{d\omega^n} \tilde{Q}(v,\vec{a},\omega)\Big|_{\omega=0},\\
&\lim_{|\vec{a}|\to\infty} F(v,\vec{a}) = \lim_{v\to-\infty} F(v,\vec{a}) = F(v_{\mathrm{th}},\vec{a}) = 0 \text{ for } F = P_0, \tilde{Q}_0^{\prime(n)}.
\end{aligned}
\tag{2.53}
$$

Here the brackets with the stacked integer numbers n and k denote the binomial coefficient n over k. The first line in Eq. (2.53) again determines the stationary solution P_0 and firing rate P_0 and r_0. The partial differential equation in the second line arises by the n-th derivative with respect to ω of the partial differential equation for $\tilde{Q}$ in the second line of Eq. (2.49) at $\omega \to 0$. Its solution $\tilde{Q}^{\prime(n)}$ is not uniquely determined since $\tilde{Q}_0^{\prime(n)} + \alpha P_0$ is a solution as well. Thus, as it is already the case in Eq. (2.49), an additional condition exploited in the line below is required to identify the unique solution $\tilde{Q}_0^{(n)}$. Such a condition can be found by the n-th derivative with respect to ω of the normalization condition as discussed in the Appendix Sec. A.1 at $\omega = 0$. The detailed derivation of the partial differential equation and the additional condition is presented in the Appendix Sec. A.5. Note that the complexity of the equations is drastically reduced if no refractory period is applied. Closer inspection of the second and third lines reveals that even and odd derivatives of $\tilde{Q}$ are purely real and purely imaginary, respectively, such that all odd derivatives of the power spectrum are zero as expected due to the symmetry $S(\omega) = S(-\omega)$ mentioned above. However, in order to calculate the even n-th derivative of the power spectrum, also the odd derivatives up to the $(n-1)$th of $\tilde{Q}$ have to be calculated because all lower-ranked ones appear occur in the partial differential equation and the additional condition. As a consequence, all derivatives have to be calculated one after the other such that, unfortunately, parallel computing of the derivatives is not possible. The fourth line relates derivatives of the probability density with the derivatives of the spike-train power spectrum and directly follows from the fourth line of Eq. (2.49). Again, probability densities obey absorbing boundary conditions at v_{th} and natural boundary elsewhere as denoted in the last line.

If the power spectrum and its first $4d-2$ derivatives at $\omega = 0$ are known, the coefficients of

the Padé approximation in Eq. (2.52) are determined by the comparison with its Maclaurin series of order $4d-2$. Inserting this series into the left hand side of Eq. (2.52) yields:

$$\sum_{m=0}^{2d-1}\sum_{\ell=0}^{d}\frac{S_0^{(2m)}}{(2m)!}Y_\ell\omega^{2(m+\ell)}=\sum_{k=0}^{d-1}X_k\omega^{2k} \tag{2.54}$$

with $S_0^{(0)}=S(0)-r_0$ and $Y_0=1$. Eq. (2.54) is correct for all order of ω such that the coefficients are given by the solution of the linear system:

$$\sum_{m}^{k}\frac{S_0^{(2m)}}{(2m)!}Y_{k-m}=\begin{cases}X_k & (\text{for } k<d)\\ 0 & (\text{for } d\le k<2d)\end{cases} \tag{2.55}$$

As a test of the Padé approximation's functionality in the context of spike-train power spectra, four examples of spectra from LIF neurons driven by cyan and white-plus-red noise are compared with their approximations of order two up to 38 that are determined by the numerical solution of Eq. (2.53) and Eq. (2.55). In the mean driven regime with low noise shown in Fig. 2.12 a,b, the spectra exhibit low power at low frequencies and a sharp peak at the firing rate as shown by the gray line from simulations and the red circles from the theory. For the cyan noise input, low-order approximations [cf. color encoding in legend of Fig. 2.12c] describe the power spectrum at low frequencies well but fail to exhibit the peak. Approximations of higher order yield divergences. For the white-plus-red noise input, divergences are obtained for low-order approximations, but for sufficiently high order, the approximations also exhibit a peak at the firing rate. In the noise driven regime with rather smooth power spectra in Fig. 2.12c,d we obtain good approximations with increasing accuracy for increasing order for cyan input noise, while approximations of lower order for white-plus-red noise exhibit divergences.

With sufficiently high order, the rational functions are good approximations on the power spectra, particularly at low frequencies. Since the approximation is local at $\omega=0$, spectral details at higher frequencies cannot be displayed adequately. However, divergences may occur for some orders of approximations such that method can only be used with some caution.

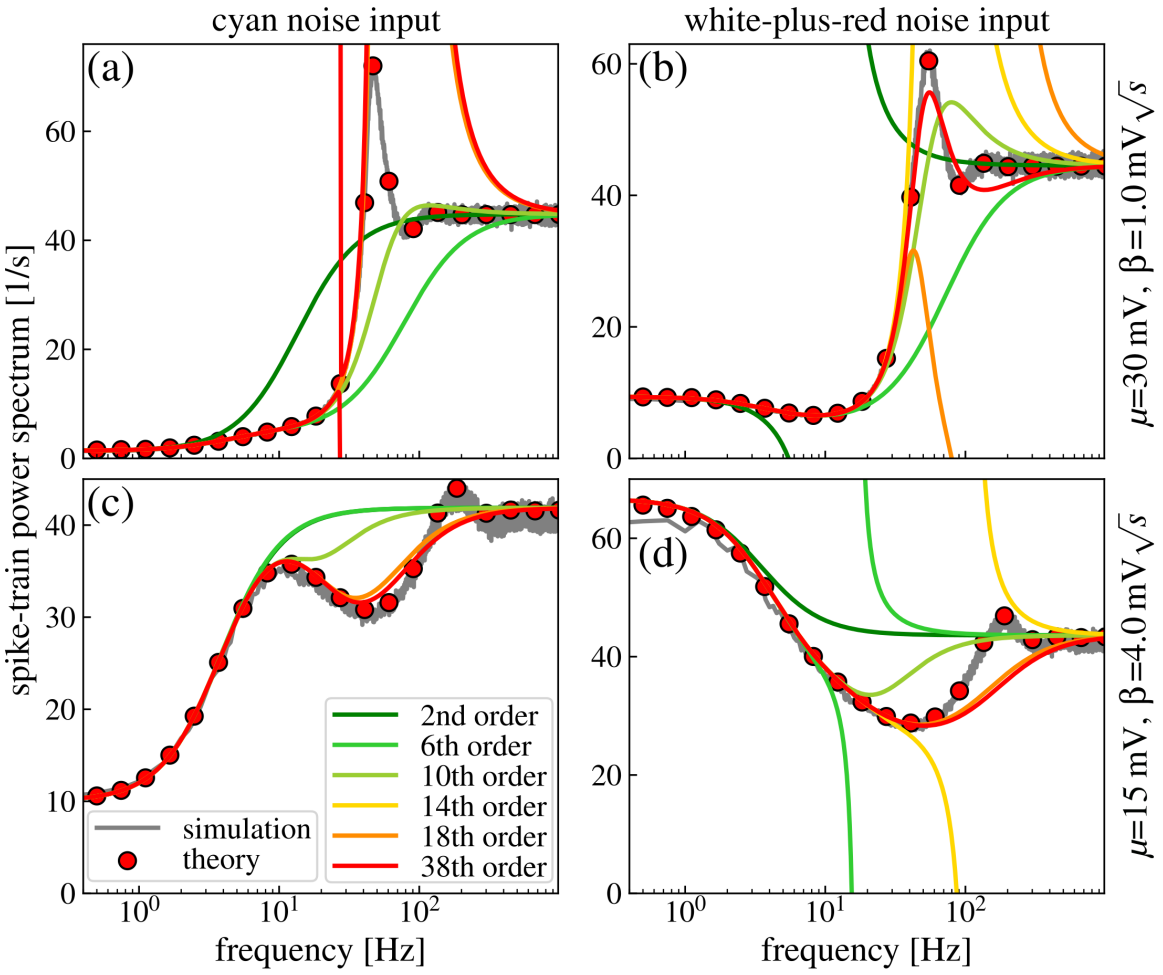

Figure 2.12.: Padé approximations of spike-train power spectra. Comparison between results from direct simulations and theory (Eq. (2.32)) as gray lines and red circles, respectively, and the corresponding Padé approximations at $\omega = 0$ (colored lines following). The order of the approximation is indicated by the color encoding and increases from green over yellow to red. Spectra are from an LIF driven by cyan (a,c) and white-plus-red noise (b,d) in the mean driven regime with high mean and weak noise input (a,b) and in the noise driven regime with low mean and strong noise input (c,d). Used parameters for (a,b,c,d) are the same as in Fig. 2.6i, Fig. 2.6l, Fig. 2.7i and Fig. 2.7l, respectively.

2.4 Summary and discussion

In this chapter, the theory of spike-train power spectra from general, stochastic, multidimensional IF neurons was developed based on the corresponding Fokker-Planck equation. The stationary solution, the firing rate and, most interestingly, the spike-train power spectrum were determined by the solution of the set of partial differential equations with the nonlocal fire-and-reset term in Eq. (2.49) that presented the main result of this chapter. By the use of approximations, the general framework here might become the origin of analytical studies for different special cases. One example of such an analytically tractable special case studied by Schwalger et al. (2015) is given by the perfect IF neuron driven by a weak purely colored noise generated by a multidimensional Ornstein-Uhlenbeck process and strong mean input. Within the framework, also nonlinear models and neurons in the excitable regime with strong input noise can be studied. However, since the analytical treatment of the general theory is difficult, a numerical procedure to determine the solutions based on a finite-difference method is described in detail in the Appendix A.2 for the two-dimensional models and A.4 for three-dimensional models. Due to the exploding demands for working memory and computation time by a further increase of the dimensionality, more efficient methods are required to deal with higher-dimensional models. A tensor decomposition method (Sun and Kumar, 2014), hybrid strategies (Chen and Maida, 2018), eigenfunction expansions (Naundorf et al., 2005; Deniz and Rotter, 2017) or the continued-fraction method [Risken (1984) Sec. 6.6.6] might be applicable and helpful to determine solutions of more complex neuron models, for instance, an adapting neuron driven by a narrow-band noise could be tractable. Moreover, the firing rate modulation for a weak time-dependent stimulus might be calculated in linear order by an extension of the theory, similar to the one-dimensional case with white noise studied by Richardson (2007, 2008).

In the theory, a non-vanishing white noise component in the voltage dynamics is assumed that yields an absorbing boundary at the threshold. Note that both synaptically filtered spike trains and channel noise yield actually purely colored noise for which the probability density obeys a different boundary condition at the threshold, as described among others by Brunel and Sergi (1998). However, at least a weak white noise term can be justified by some ion channels or synapses with fast dynamics compared to the dynamics of the membrane voltage, or by a very small but non-vanishing impact of thermal noise. Moreover, a more detailed consideration of synaptic input currents and voltage gated ion channels yields multiplicative input noise, studied for instance by Richardson (2004) that may be beneficial for signal transmission as shown by Bauermann and Lindner (2019) for simple neuron models. For the sake of simplicity, the introduced model only considers additive noise. Also the Gaussian approximation for synaptic noise is only accurate if neural input originates from the sum of many statistically independent presynpatic spike trains and low synaptic weights. In situations in which a neuron only receives few spikes with high synaptic amplitudes, the fluctuations are more appropriately represented by shot noise [see for instance Kuhn et al. (2003); Richardson and Gerstner (2005, 2006); Helias et al. (2010); Richardson and Swarbrick (2010)]. The development of a general framework that also considers multiplicative noise and/or shot noise is an important task for future research.

To test the theory and to display the variety of spike-train power spectra and thereby to gain an understanding how neuronal features shape the spectra, the theory was applied to three different IF neuron models. In all cases, the numerical solutions of the theory were in agreement with the results of direct simulations. As the first example, the theory was applied to study the spike-train power spectra of an LIF neuron driven by colored noise from a two-dimensional Markovian embedding, also used by Câteau and Reyes (2006) without a refractory period. Two qualitatively different kinds of colored noise can be generated, that I referred to as cyan [also green in the literature (Guz and Sviridov, 2001)] and white-plus-red noise. Even in this rather simple case, the Markovian embedding is not unique and two different parameter sets yield the same colored noise, as also observed by Siegle et al. (2010). If more complex and higher-dimensional Markovian embeddings are considered, even more ambiguities arise as discussed in the following chapter for the two-dimensional embedding. It is not clear, whether a certain representation is advantageous compared to the other for either analytical or numerical calculations, thus, the problem of ambiguities, particularly for higher-dimensional embeddings, is worth to be studied in more detail. The resulting spike-train power spectra adopt the key features of the input power spectra, i.e. increased or decreased power at low up to intermediate frequencies. Surprisingly, the colored noise input may cause new maxima and minima in the spectrum without any obvious oscillatory mechanism. As the second example, the theory was applied to a white-noise driven exponential IF neuron with deterministic and stochastic spike-triggered and subthreshold adaptation. The resulting power spectra reflect the adaptation time-scale and may reveal resonances caused by subthreshold adaptation. Furthermore, the two different timescales of the bursting mechanism yield two distinct peaks in the spike-train power spectrum. As a third example, an LIF neuron driven by narrow-band noise was studied. Also in that case, the numerical solution of the theory could predict the power spectrum and capture the system's rich correlation structure.

In the last part, a set of equations was derived that can be solved to obtain the Padé approximation of the spike-train power spectrum at zero frequency. The resulting rational function accurately approximates the spike-train power spectrum at low frequencies and is exact at the high-frequency limit. With increasing order, the approximation became accurate also at intermediate frequencies and could exhibit spectral peaks. However, since it may happen that the resulting function diverges, the method has to be used with caution.

In the following chapter, networks of spiking neurons are considered in which neural input is generated by the presynaptic neurons and can be approximated by colored Gaussian noise. The dynamics of the whole network are determined by one or few representative neurons for which the input and output statistics are self-consistent. Related to this problem, the theory in this chapter can be seen as the open-loop problem in which the output statistics are calculated for a given input. In that sense, the next chapter presents how the loop can be closed.

3 Mean-field theory of large and sparse recurrent networks including self-consistent temporal correlations of spike trains

In the brain, large networks of synaptically connected neurons are employed for information transmission and filtering, computations, memory consolidation and for the solution of any other task. Hence, it is a crucial goal of the field of computational neuroscience to identify the dynamical properties of neural populations and link them to the characteristics and the connectivity of the single neurons. Neural populations in the mammalian brain consist of large numbers of neurons each of which has a large number of around thousand synaptic connections (Gerstner et al., 2014). To gain insights into the dynamics of spontaneous activity of large networks, mean-field techniques have been applied, in which the complexity of a whole population is reduced to the dynamics of a single or few representative neurons that obey a self-consistency condition regarded to neural input and output. The approach was extensively used and provided even analytical results. Many studies were devoted to the synchronization in neural networks with random connections or the transition into chaotic regimes and investigated them by means of simplified rate models (Sompolinsky et al., 1988; Mirollo and Strogatz, 1990; Hansel and Sompolinsky, 1992; Buice et al., 2010; Aljadeff et al., 2015; Kadmon and Sompolinsky, 2015; Crisanti and H. Sompolinsky, 2018), Ising-like binary neuron models (Ginzburg and Sompolinsky, 1994; Renart et al., 2010; Helias et al., 2014) or oscillators (van Meegen and Lindner, 2018).

Particularly interesting are networks of spiking IF neurons, studied for instance by Abbott and van Vreeswijk (1993); Treves (1993); Amit and Brunel (1997); Brunel and Hakim (1999); Fusi and Mattia (1999); Brunel (2000); Nykamp and Tranchina (2000); Knight et al. (2000); Di Volo et al. (2019) since they resemble biological populations but also permit analytical insights. Neurons that are embedded in large and sparsely connected networks, for instance in the neocortex, are exposed to the bombardment of many action potentials from the presynaptic neurons. In a network with asynchronous irregular firing activity, incoming spikes appear to arrive at random times from the perspective of one neuron. As a consequence of the central limit theorem and in agreement with experimental observations of synaptic noise (Destexhe et al., 2003), it is reasonable to approximate neural input by Gaussian noise, if presynaptic firing rates are sufficiently high, synaptic weights low and spike trains are sufficiently asynchronous. Insights in sparsely connected networks of spiking neurons have been gained by approximating the sum of presynaptic spike trains by Gaussian white noise [see

for instance Amit and Brunel (1997); Brunel and Hakim (1999); Fusi and Mattia (1999); Brunel (2000)], whereby neural input and output can be described by a single variable, the stationary firing rate, that has to be determined self-consistently. The further analysis of the stability of the self-consistent firing rate was exploited by Brunel (2000) to classify different dynamical regimes of synchrony, asynchrony, regularity and irregularity and link them to network parameters.

However, there are strong arguments in early work by Mari (2000) and, particularly by Lerchner et al. (2006) against the application of temporally uncorrelated input noise. Neural spike-trains from real nerve cells (Bair et al., 1994) as well as from theoretical neuron models (Lindner et al., 2002) are characterized by nontrivial temporal correlations and neural input, as the sum of them, maintains these correlations as shown by Lindner (2006). In contrast, the application of white Gaussian noise as neural input assumes that neural spike-trains resemble Poisson processes without any temporal correlations which is only a reasonable approximation in the limit of vanishing firing rates (Lindner, 2006). In general, the white noise approximation ignores the temporal correlations and cannot be justified. A more comprehensive mean-field theory can only be achieved if not only the firing rates, but also the temporal correlations of spike trains, represented by either the autocorrelation function or the spike-train power spectrum, are considered to be self-consistent. For the determination of the self-consistent spike-train statistics, Lerchner et al. (2006) proposed a numerical scheme, based on techniques developed for spin systems by Eissfeller and Opper (1992), in which neurons are iteratively driven by Gaussian colored noise. The statistics of neural input are determined by the autocorrelation function of the previous iteration. A more efficient scheme for homogeneous networks was proposed by Dummer et al. (2014), in which colored Gaussian noise as neural input is generated numerically from the spike-train power spectrum of the previous iteration.

In this chapter, a mean-field theory for large and sparsely connected homogeneous networks of LIF neurons is developed in which the self-consistency of the temporal correlations of the spike-trains is considered. For the theory, an analytical representation of general colored noise as neural input is required which is incorporated here by a multidimensional Markovian embedding, to be precise, a multidimensional Ornstein-Uhlenbeck process. I present arguments that state that such a process is a suitable candidate to generate colored Gaussian noise that serves as neural input for a representative neuron. The theory arises by extending the theory of spike-train power spectra applied to the corresponding LIF neuron driven by the multidimensional Ornstein-Uhlenbeck process by the condition of self-consistent power spectra. Different approximations of the theory are introduced and numerically solved for up to two-dimensional input processes for one network. In the second part, as an alternative approach, the iterative scheme by Dummer et al. (2014) is extended to reproduce the distribution of the spike-train statistics for heterogeneous networks in which the numbers of presynaptic neurons and the synaptic weights are distributed.

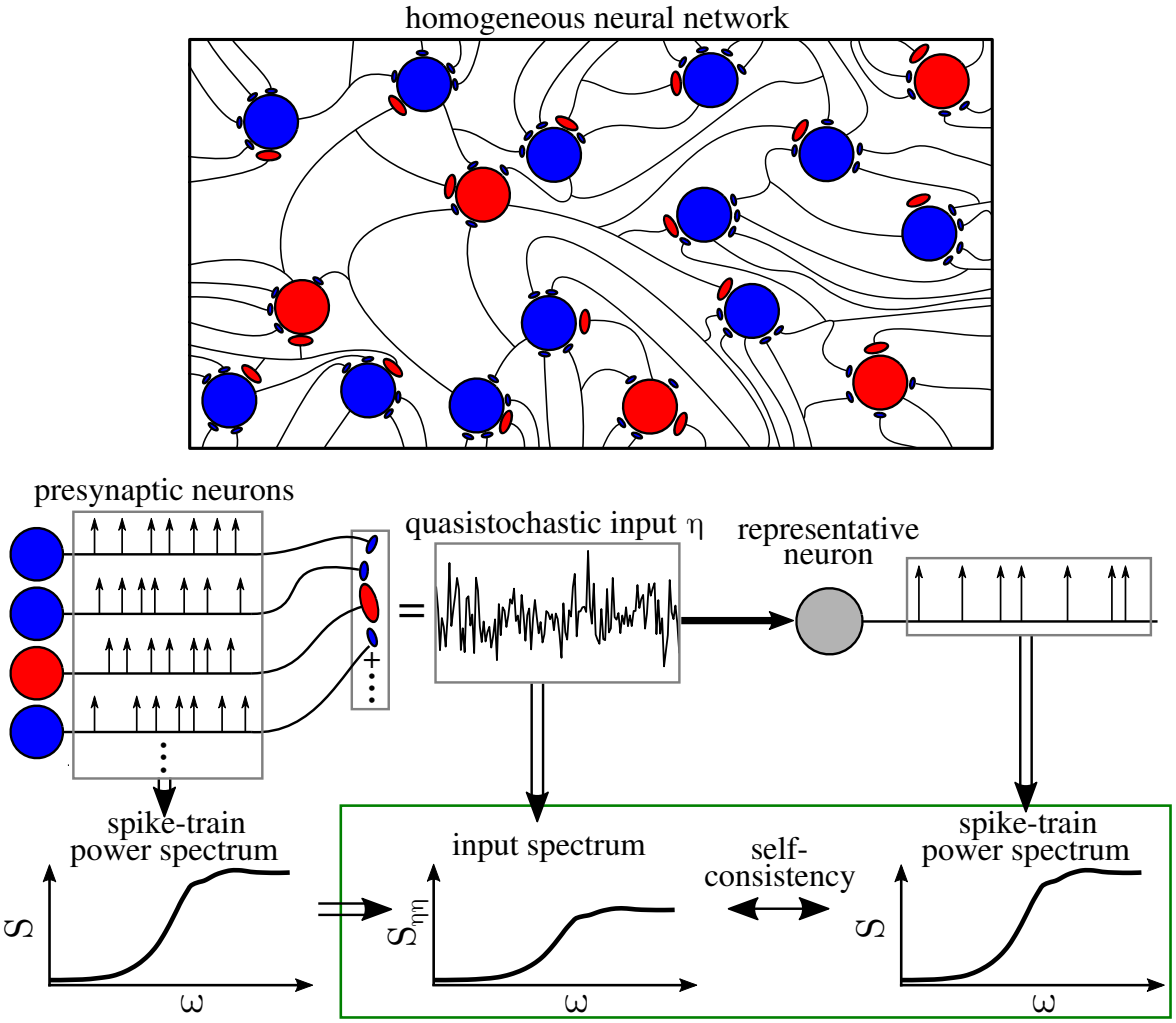

Figure 3.1.: Self-consistency of power spectra. In a large and sparsely connected network of spiking neurons, neural input is generated by the sum of many independent spike trains of presynaptic neurons. This neural input can be approximated by a stochastic process η with the input spectrum $S_{\eta\eta}(\omega)$. In a homogeneous recurrent network, every neuron generates the input for others, thus, the spike-train power spectrum of a representative neuron is related to the power spectrum of its input, yielding the condition of self-consistent power spectra $S_{\eta\eta}(\omega) = \phi S(\omega)$ in Eq. (3.4).

3.1 Homogeneous network

The mean-field theory is introduced for a simple homogeneous network of LIF models in which all neurons have equal properties including the same parameters and a fixed in-degree, i.e. identical numbers of synaptic excitatory and inhibitory input connections for every neuron. Indeed, such a network is far from biological reality, however, theoretical methods and gained insights might be transferred to more detailed and biologically relevant models. The detailed network dynamics and topology is introduced in the following.

3.1.1 Network dynamics and topology

The mean-field theory is developed for a standard network model of LIF neurons that was originally proposed by Brunel (2000) as a simplified model of a single cortical column and often studied afterwards, for instance, by Dummer et al. (2014); Ostojic (2014); Wieland et al. (2015). It consists of N_E excitatory and N_I inhibitory LIF neurons which all obey the subthreshold dynamics and the fire-and-reset rule:

$$\begin{aligned} &\tau_m \dot{v}_\ell = -v_\ell + RI_\ell(t), \\ &\text{if } v_\ell(t) > v_{\text{th}} : \; v_\ell(t) \to v_{\text{ref}},\, v_\ell(t+\tau_{\text{ref}}) \to v_{\text{r}}. \end{aligned} \tag{3.1}$$

The input current $RI_\ell(t)$ of the ℓ-th neuron is composed of a constant external current RI_{ext} and the sum of the spike trains of presynaptic excitatory and inhibitory neurons:

$$RI_\ell(t) = \underbrace{RI_{ext}}_{\text{external current}} + \tau_m J \underbrace{\sum_{i=1}^{C_E} \sum_k \delta(t - t_i^k - D)}_{\text{excitatory presynaptic spikes}} - g\tau_m J \underbrace{\sum_{j=1}^{C_I} \sum_l \delta(t - t_j^l - D)}_{\text{inhibitory presynaptic spikes}} . \tag{3.2}$$

Here the k-th and l-th spike time of the i-th excitatory and the j-th inhibitory presynaptic neuron are denoted by t_i^k and t_j^l, respectively. A time gap between presynaptic spike and increase or decrease of the membrane voltage is incorporated by the delay time D to take into account that after a presynaptic neuron fired a spike, some time is required for the action potential to reach and subsequently activate the synapse and for the emitted neurotransmitters to reach the ion channels. Synapses and ion channels are assumed to be very fast such that the change of the membrane voltage can be approximated by the δ-functions as instantaneous kicks. The increase and decrease of the membrane voltage per excitatory and inhibitory spike are given by the synaptic weights or synaptic strengths J or $-gJ$, respectively. In Brunel's notation, inhibitory synapses are g times stronger than excitatory ones. For each neuron ℓ, a fixed number of C_E excitatory and C_I inhibitory presynaptic neurons are randomly chosen. Neurons may only have one connection to another neuron and a neuron is never connected to itself. The network is assumed to be sparsely connected, i.e. C_E/N_E, $C_I/N_I \ll 1$.

Neurons that are embedded in large networks may exhibit various spike patterns depending on the network topology and neural parameters. Spike trains can be regular or irregular with almost constant or strongly varying interspike-intervals; furthermore, different degrees of

synchrony between spike trains may occur. If the spikes in the network are not synchronized, a neuron in the network receives many action potentials at quasi-random times due to the chaotic firing activity of the network [see for instance van Vreeswijk and Sompolinsky (1996); Amit and Brunel (1997); van Vreeswijk and Sompolinsky (1998)]. Although the network dynamics are fully deterministic, the membrane voltage appears to changes stochastically and neural input can be approximated by a stochastic process. For many neurons, this synaptic noise is the dominant source of noise (Destexhe and Rudolph-Lilith, 2012) and intrinsic sources of noise, such as channel noise, can often be neglected.

In the study of Brunel (2000), a mean-field approach, explained below in more detail, with subsequent stability analysis was applied to introduce a classification of different firing regimes in the parameter space. In the most important regime in terms of signal transmission, neurons fire irregularly and asynchronously, similar to experimental spikes observed in neurons of awake behaving animals (Renart et al., 2010). In the standard network model, asynchronous irregular activity can be found in sparsely connected networks with balanced or dominating inhibition. Moreover, Ostojic (2014) distinguishes between the classical homogeneous asynchronous irregular state and the heterogeneous asynchronous irregular state in which neural firing rates vary over long time scales. The homogeneous and the heterogeneous states arise in the cases of weak and strong synapses, respectively, and have different computational properties. The theory introduced in this chapter is restricted to both asynchronous irregular regimes.

3.1.2 Mean-field conditions and approximations

For the homogeneous network in which all neurons share the same properties and statistics, it is convenient to study the network dynamics on the basis of a single representative neuron. Such a neuron is the target of many presynaptic spikes, which decrease or increase the membrane voltage by J or $-gJ$ depending on the kind of presynaptic neuron. From the neuron's perspective, these received voltage kicks appear to arrive at random times due to the random connectivity although they are generated by the deterministic network dynamics. If the synaptic weights are relatively low compared to the difference $v_{\mathrm{th}} - v_{\mathrm{r}}$, the neural input can be approximated by a stochastic process with constant mean μ and fluctuations $\eta(t)$ that obey Gaussian statistics as a consequence of the *central limit theorem*. In the asynchronous irregular regime, spike-trains of presynaptic neurons are approximately independent from each other. Assuming that the network is stationary and all neurons have the same firing rate r, the mean input of one representative neuron may be identified by the ensemble average:

$$\mu = \langle RI_\ell(t) \rangle = RI_{ext} + \tau_m J(C_E - gC_I)r. \tag{3.3}$$

Here global network oscillations also described for instance by Brunel (2000) are explicitly neglected such that the mean input is constant in time. Due to the finite number of presynaptic neurons, the input current for the representative neuron is not constant in time but can be described by the Gaussian fluctuations $\eta(t)$. Using the definition in Eq. (2.7), the power spectrum of these fluctuations can be linked to the power spectrum of the presynaptic

spike trains $S(\omega)$ by:

$$\begin{aligned}
S_{\eta\eta}(\omega) &= \lim_{T\to\infty} \frac{\langle \tilde{RI}_\ell \tilde{RI}_\ell{}^* \rangle}{T} = \lim_{T\to\infty} \tau_m^2 J^2 \frac{\left\langle \sum_{i,j=1}^{C_E} \tilde{x}_i \tilde{x}_j^* - g \sum_{i=1}^{C_E}\sum_{k=1}^{C_I} (\tilde{x}_i \tilde{y}_k^* + \tilde{x}_i^* \tilde{y}_k) + g^2 \sum_{k,\ell=1}^{C_I} \tilde{y}_k \tilde{y}_\ell^* \right\rangle}{T} \\
&= \lim_{T\to\infty} \tau_m^2 J^2 \frac{\sum_{i=1}^{C_E} \langle \tilde{x}_i \tilde{x}_i^* \rangle + g^2 \sum_{k=1}^{C_I} \langle \tilde{y}_k \tilde{y}_k^* \rangle + \sum_{\substack{i,j=1 \\ i\neq j}}^{C_E} \langle \tilde{x}_i \tilde{x}_j^* \rangle - 2g \sum_{i=1}^{C_E}\sum_{k=1}^{C_I} \mathrm{Re}(\langle \tilde{x}_i \tilde{y}_k^* \rangle) + g^2 \sum_{\substack{k,\ell=1 \\ k\neq\ell}}^{C_I} \langle \tilde{y}_k \tilde{y}_\ell^* \rangle}{T} \\
&\approx \tau_m^2 J^2 (C_E + g^2 C_I) \lim_{T\to\infty} \frac{\langle \tilde{x}_i \tilde{x}_i^* \rangle}{T} = \underbrace{\tau_m^2 J^2 (C_E + g^2 C_I)}_{=:\phi} S(\omega).
\end{aligned} \tag{3.4}$$

Here the Fourier transformed spike trains of the presynaptic excitatory and inhibitory neurons i and k are denoted by $\tilde{x}_i$ and $\tilde{y}_k$, respectively. In the last line of Eq. (3.4), the spike-train power spectrum is the same for excitatory and inhibitory neurons ($\langle \tilde{x}_i \tilde{x}_i^* \rangle = \langle \tilde{y}_i \tilde{y}_i^* \rangle$) because they are indistinguishable in their dynamics. Moreover, if the network is sparsely connected and in the asynchronous state is assumed, cross-correlations are so weak that they can be neglected, even though far more terms contribute to them than to the power spectrum ($\langle \tilde{x}_i \tilde{x}_j^* \rangle \approx \langle \tilde{\chi}_i \tilde{\chi}_j^* \rangle \approx \langle \tilde{x}_k \tilde{\chi}_l^* \rangle \approx 0$ for all $i \neq j$). This approximation yields the simple proportionality with the factor ϕ between the input and the spike-train power spectrum that has already been used by Brunel (2000) as the strength of white noise and by Dummer et al. (2014) for colored noise. Note that the input statistics μ and $S_{\eta\eta}$ are equal for all neurons in the homogeneous network, hence, the index ℓ has been omitted.

In summary, both Eqs. (3.3) and (3.4) set the self-consistency conditions for the single representative neuron expressed by the following stochastic equations:

$$\begin{aligned}
\tau_m \dot{v} &= -v + \mu + \eta(t), \qquad \text{if } v(t) > v_{\mathrm{th}} : \; v(t) \to v_{\mathrm{ref}},\, v(t+\tau_{\mathrm{ref}}) \to v_{\mathrm{r}}, \\
\mu &= RI_{ext} + \tau_m J (C_E - gC_I) r, \qquad S_{\eta\eta}(\omega) = \phi S(\omega)
\end{aligned} \tag{3.5}$$

with the fire-and-reset rule in Eq. (3.1) Here the firing rate r, the mean input μ, the input power spectrum $S_{\eta\eta}$ and the spike-train power spectrum S are initially unknown. They are determined by the self-consistency conditions in Eq. (3.5) and, in turn, also define their solution. Even though the introduced network model is rather simple and many approximations have been used to derive the condition, the determination of the self-consistent solution remains a challenging problem.

White-noise approximation

Brunel (2000) approximates neural spike-trains by Poisson processes that are point processes without temporal correlations and possess a flat power spectrum. If the synaptic weights small, input as the sum of many presynaptic Poisson spike trains has the same effect on the membrane potential as a Gaussian white noise input $\eta(t) = \beta\xi(t)$ with constant power

spectrum proportional to the firing rate $S_{\eta\eta}(\omega) = \beta^2 = \phi r$. The model is thereby reduced to a one-dimensional LIF neuron driven by white noise for which the expression for the firing rate can be derived analytically by the stationary solution of the corresponding Fokker-Planck equation [see Ricciardi (1977) or Brunel (2000) for details]:

$$r = \left(\tau_{\mathrm{ref}} + \tau_m \int_{\sqrt{\tau_m}(v_{\mathrm{r}}-\mu)/\beta}^{\sqrt{\tau_m}(v_{\mathrm{th}}-\mu)/\beta} du \exp(u^2)(1+\mathrm{erf}(u)) \right)^{-1} . \tag{3.6}$$

Here the error function is denoted by $\mathrm{erf}(x)$ [see Abramowitz and Stegun (1970)]. In this approximation, both parameters of the neural input μ and β on the right hand side of Eq. (3.6) only depend on the firing rate r such that the problem is reduced to one unknown variable. The self-consistent firing rate can be determined either by approximations of Eq. (3.6) or numerically. For low synaptic weights, the result is a good approximation of the firing rate observed in the corresponding network simulation but differs from it if, synaptic weights are higher [see Ostojic (2014)]. Moreover, this analytical framework allows one to investigate in the stability of the self-consistent solution and is exploited by Brunel (2000) to associate parameter sets with dynamical regimes of the network.

However, neural spike trains exhibit non-trivial temporal correlations as shown by *in vivo* recordings (Ghose and Freeman, 1992; Edwards et al., 1993; Bair et al., 1994) and theoretical studies of single neurons [Lindner et al. (2002); Richardson (2008); Vellmer and Lindner (2019), see also chapter 2]. The approximation of spike trains by Poisson processes is only applicable in the limit of neurons in the excitable regime with very low firing rates. If spike trains with nontrivial temporal correlations are considered, neural input as the sum of many independent spike trains maintains the temporal correlations as shown in Eq. (3.4) [see also Lindner (2006)]. A more systematic but also more complicated approach to take into account the temporal correlations of spike trains can be made by the application of colored Gaussian noise as neural input.

Iterative scheme

To determine the self-consistent temporal correlations of spike trains, Lerchner et al. (2006) applied a numerical method developed for spin-glass systems by Eissfeller and Opper (1992) to a network of spiking neuron that is heterogeneous in the number of input connections per neuron. In this method, representative neurons are iteratively driven by surrogate input currents of which the means and fluctuations are determined by the firing rates and the averaged autocorrelation function of spike trains from the previous iteration, respectively. A simplified and more efficient method for homogeneous networks was proposed by Dummer et al. (2014) in which a single representative neuron is also iteratively driven by colored noise. In contrast to the above mentioned scheme, Gaussian input fluctuations are generated by the spike-train power spectrum of the previous iteration using an algorithm developed by Billah and Shinozuka (1990). The procedure is illustrated in Fig. 3.2. In the zeroth iteration, the representative neuron is driven by an arbitrary mean input μ_1 and Gaussian white noise with

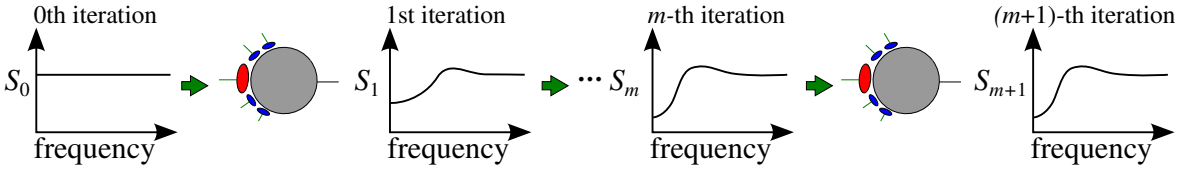

Figure 3.2.: Iterative scheme proposed by Dummer et al. (2014) to determine self-consistent spike-train power spectra in homogeneous networks. A single representative neuron is iteratively driven by Gaussian colored noise generated from the spike-train power spectrum of the previous iteration, until input and spike-train power spectra obey the condition of self-consistency in Eq. (3.4).

flat power spectrum $[S_{\eta\eta,1}(\omega) = \phi S_0(\omega)]$ and arbitrary strength. The resulting firing rate r_1 and spike-train power spectrum S_1 are calculated by direct simulations of the neuron and determine the mean input μ_2 and the input power spectrum $S_{\eta\eta,2}(\omega)$ for the next iteration by Eq. (3.5). For the m-th iteration, the mean input μ_m and the input power spectrum $S_{\eta\eta,m}(\omega)$ are given by the firing rate r_{m-1} and the spike-train power spectrum of the previous $(m-1)$-th iteration, respectively:

$$\mu_m = RI_{ext} + \tau_m J(C_E - gC_I) r_{m-1}, \qquad S_{\eta\eta,m}(\omega) = \phi S_{m-1}(\omega). \tag{3.7}$$

Gaussian input fluctuations $\eta_m(t)$ that exhibit the input spectrum $S_{\eta\eta,m}(\omega)$ are generated numerically by standard techniques developed by Billah and Shinozuka (1990). The frequency domain is discretized by bins of width $\Delta\omega$. For each of these bins, for instance at ω_k, two Gaussian distributed random numbers with unit variance and zero mean $\eta_{r,k,m}$ and $\eta_{i,k,m}$ are used to represent real and imaginary part of the Fourier-transformed fluctuations $\tilde{\eta}_m(\omega_k)$ by:

$$\tilde{\eta}_{k,m}(\omega) = \sqrt{\frac{S_{\eta\eta,m}(\omega)}{2\Delta\omega}}(\eta_{r,k,m} + i\eta_{i,k,m}), \tag{3.8}$$

[cf. Dummer et al. (2014)]. The fluctuations in time domain $\eta_m(t)$ are obtained by the inverse Fourier transformation. In this way, the representative neuron, driven by Gaussian fluctuations generated from the previous spike-train power spectrum, is iteratively simulated until input and spike-train power spectra are self-consistent and obey Eq. (3.5) and $S_m(\omega) \approx S_{m+1}(\omega)$. The numerical procedure is robust and converges after few iterations except in the case of an inhibition-dominated network with $gC_I > C_E$ in which the output firing rate is a monotonously decreasing function of the input firing rate. As shown by Pena et al. (2018), the method can be stabilized if not the firing rate of the previous iteration, but the average firing rate over all previous iterations is considered and the mean input is calculated by:

$$\mu_m = RI_{ext} + \tau_m J(C_E - gC_I) \frac{1}{m-1} \sum_{k=1}^{m-1} r_{m-1}. \tag{3.9}$$

In networks in which the Gaussian approximation is accurate, cross-correlations can be neglected and no significant global oscillations occur, the self-consistent power spectra deter-

mined by this iterative scheme coincide with the spike-train power spectra measured in network simulations.

To develop an analytical theory of the self-consistent temporal correlations of spike trains, an analytically tractable representation of general Gaussian colored noise is required to model neural input. In the following, I discuss how a multidimensional Ornstein-Uhlenbeck process may be used for this purpose [see also Schwalger et al. (2015)].

3.1.3 Multidimensional Ornstein-Uhlenbeck process as general source of colored Gaussian noise may model neural input

For the mean-field theory a general analytical representation of colored Gaussian noise $\eta(t)$ as an approximation of neural input is required that is capable to exhibit a power spectrum that resembles the self-consistent solution in Eq. (3.5). A proper candidate for this purpose is the sum of a multidimensional Ornstein-Uhlenbeck process plus white noise given by the Langevin equation:

$$\begin{aligned} \eta(t) &= \vec{\beta}^\intercal \vec{\xi}(t) + \vec{1}^\intercal \vec{a}(t), \\ \dot{\vec{a}}(t) &= -\mathbf{A}\vec{a} + \mathbf{B}\vec{\xi}(t). \end{aligned} \tag{3.10}$$

Here and in the following, the scalar product with the vector $\vec{1}$ denotes the sum of all components, put differently, all components of $\vec{1}$ are one. The matrix $\mathbf{A}$ has to have only positive eigenvalues in order to ensure that $\vec{a}$ stays finite in all its components such that a stationary distribution exists. The individual components of $\vec{a}$ do not have a physical meaning in themselves, they are only building blocks of the mathematical construction that generates the required temporal correlations. The reason for the choice of Eq. (3.10) as neural input lies in the structure of its power spectrum that can be calculated by the Fourier-transformed process:

$$\begin{aligned} -i\omega\tilde{\vec{a}} = -\mathbf{A}\tilde{\vec{a}} + \mathbf{B}\tilde{\vec{\xi}} \Leftrightarrow \tilde{\vec{a}} &= (\mathbf{A} - i\omega\mathbb{1})^{-1}\,\mathbf{B}\tilde{\vec{\xi}}, \\ \tilde{\eta} = \vec{\beta}^\intercal\tilde{\vec{\xi}} + \vec{1}^\intercal\tilde{\vec{a}} &= \vec{\beta}^\intercal\tilde{\vec{\xi}} + \vec{1}^\intercal\,(\mathbf{A} - i\omega\mathbb{1})^{-1}\,\mathbf{B}\tilde{\vec{\xi}} \end{aligned} \tag{3.11}$$

[cf. calculation in Eq. (1.7) for the Fourier transformation of the derivation with respect to the time]. By the Insertion of $\tilde{\eta}$ in the definition of the power spectrum (Eq. (2.7)), the formal expression can be obtained:

$$\begin{aligned} S_{\eta\eta}(\omega) &= \vec{\beta}^2 + 2\mathrm{Re}\left[\vec{1}^\intercal\,(\mathbf{A} - i\omega\mathbb{1})^{-1}\right]\mathbf{B}\vec{\beta} + \vec{1}^\intercal\,(\mathbf{A} - i\omega\mathbb{1})^{-1}\,\mathbf{B}\mathbf{B}^\intercal\,(\mathbf{A} + i\omega\mathbb{1})^{-1}\,\vec{1} \\ &= \vec{\beta}^2 + 2\mathrm{Re}[\vec{V}]\vec{\beta} + |\vec{V}|^2, \quad \vec{V} = \vec{1}^\intercal\,(\mathbf{A} - i\omega\mathbb{1})^{-1}\,\mathbf{B} \end{aligned} \tag{3.12}$$

[cf. Eq. 4.5.64 in Gardiner (1985) chapter 4.5]. However, this expression does not reveal the dependency of the power spectrum on ω. It is useful to consider that the inverse matrix can be expressed by the adjoint matrix and the determinant:

$$(\mathbf{A} - i\omega\mathbb{1})^{-1} = \frac{\mathrm{adj}(\mathbf{A} - i\omega\mathbb{1})}{\det(\mathbf{A} - i\omega\mathbb{1})} \tag{3.13}$$

[see for instance Cherney et al. (2016)]. Applying Eq. (3.13) for Eq. (3.12), the spectrum with a d-dimensional vector $\vec{a}$ can be presented by the fraction of two polynomials of even order plus a constant:

$$\boxed{S_{\eta\eta}(\omega) = \vec{\beta}^2 + \frac{\sum_{k=0}^{d-1} X_k(\mathbf{A}, \mathbf{B}, \vec{\beta})\omega^{2k}}{1 + \sum_{\ell=1}^{d} Y_\ell(\mathbf{A})\omega^{2\ell}},} \tag{3.14}$$

where relations between the coefficients X_k and Y_ℓ to $\mathbf{A}$, $\mathbf{B}$ and $\vec{\beta}$ are given by:

$$\begin{aligned}
\sum_{\ell=1}^{d} Y_\ell \det(\mathbf{A})^2\omega^{2\ell} =& |\det(\mathbf{A} + i\omega\mathbb{1})|^2 - \det(\mathbf{A})^2, \\
\sum_{k=0}^{d-1} X_k \det(\mathbf{A})^2\omega^{2k} =& \vec{1}^\intercal 2\mathrm{Re}\left[\mathrm{adj}(\mathbf{A} - i\omega\mathbb{1})\det(\mathbf{A} + i\omega\mathbb{1})\right]\mathbf{B}\vec{\beta} \\
&+ \vec{1}^\intercal \mathrm{adj}(\mathbf{A} - i\omega\mathbb{1})\mathbf{B}\mathbf{B}^\intercal \mathrm{adj}(\mathbf{A} + i\omega\mathbb{1})^\intercal \vec{1}.
\end{aligned} \tag{3.15}$$

At first glance, it still might be puzzling that the right hand sides of Eq. (3.15) can be written as the polynomials on the left hand sides. The structure may be revealed by taking into account that the determinant of the d-dimensional matrix $\det(\mathbf{A} + i\omega\mathbb{1})$ is in general a polynomial in $i\omega$ in which the highest order term is given by the product of its d diagonal elements. Thus, its squared absolute value is an even polynomial in ω of the order $2d$. In the second line I used that the components of the adjoint matrix $\mathrm{adj}(\mathbf{A} - i\omega)$ are given by the subdeterminants, i.e. polynomials of order $(d-1)$ in $i\omega$. In the first term, the adjoint matrix is multiplied with the determinant of the complex conjugated matrix which yields a matrix that has polynomials in $i\omega$ of order $2d-1$ as components from which only even terms up to the order $2d-2$ are real valued and contribute. The second term consists of the product of adjoint matrix and real valued matrix $\mathbf{B}$ and its complex conjugated from which only even polynomials of order $2d-2$ emerge. Thus the underlying structure of the right hand side of the second line is described by the even polynomial of order $2d-2$ on the left hand side. Remarkably, the coefficients Y_ℓ and X_k underlie restrictions that are implicitly included in Eq. (3.15) and ensure that the power spectrum cannot be negative or diverge. Further discussion of these restrictions for $d = 2$ is given in the Appendix Sec. B.1.

It was already shown in chapter 2 that the rational functions such as Eq. (3.14), resulting as the Padé approximations of the spike-train power spectra at $\omega = 0$ in Sec. (2.3), are well suited to approximate spike-train power spectra, and thereby also input power spectra, if the dimensionality d is sufficiently high. The high- and low-frequency limits of the input power spectrum can be identified easily. As spike-train power spectra saturate at the firing rate r for high frequencies, also the fraction term in Eq. (3.14) vanishes in the limit of high frequencies and the spectrum converges to the constant $\vec{\beta}^2$ due to the higher order of the denominator. In the limit of low frequencies, only X_0 remains in the fraction term such that both limits can be easily identified as:

$$\lim_{\omega\to\infty} S_{\eta\eta}(\omega) = \vec{\beta}^2, \qquad S_{\eta\eta}(0) \quad = \vec{\beta}^2 + X_0(\mathbf{A}, \mathbf{B}, \vec{\beta}). \tag{3.16}$$

For an input process with given power spectrum that should be represented by the multidimensional Ornstein-Uhlenbeck process, high and low-frequency limits can be matched exactly. The remaining coefficients X_k and Y_ℓ have to be chosen to obtain a good approximation for which some ideas are discussed later in Sec. (3.1.5). Without any mathematical proof, I assume that the higher degree of freedom in Eq. (3.14) by increased dimensionality d of the Ornstein-Uhlenbeck process can be exploited to improve the approximation such that the self-consistent power spectrum can be matched exactly in the theoretic limit of an infinite dimensional process.

Ambiguity and inverse problem for the three-dimensional Markovian embedding

For the practical application, also the inverse problem of determining the Ornstein-Uhlenbeck process with $\mathbf{A}$, $\mathbf{B}$ and $\vec{\beta}$ for given coefficients Y_ℓ and X_k is important. As already discussed in Sec. (2.1.3), even in the one dimensional case, the same noise with the same coefficients X_0 and Y_1 can be represented non-uniquely by two different Ornstein-Uhlenbeck processes. With increasing dimensionality also the representation as a Markovian embedding in Eq. (3.10) becomes more ambiguous. To avoid an unnecessarily complex representation, the ambiguity may be reduced in the case $d > 1$ by exploiting rotation symmetry in $\vec{\beta}$ and $\mathbf{B}$. For every rotation matrix $\mathbf{S}$, the power spectrum $S_{\eta\eta}(\omega)$ is invariant under the transformation:

$$\vec{\beta}' = \mathbf{S}\vec{\beta}, \quad \mathbf{B}' = \mathbf{B}\mathbf{S}^\intercal \quad \text{with } \mathbf{S}^\intercal = \mathbf{S}^{-\mathbf{1}}. \tag{3.17}$$

because the expressions in Eq. (3.12) and, hence, also in the second expression of Eq. (3.15) are invariant under this transformation:

$$\begin{aligned} \mathbf{B}'\vec{\beta}' &= \mathbf{B}\mathbf{S}^\intercal\mathbf{S}\vec{\beta} = \mathbf{B}\vec{\beta}, \\ \mathbf{B}'\mathbf{B}'^\intercal &= \mathbf{B}\mathbf{S}^\intercal\mathbf{S}\mathbf{B}^\intercal = \mathbf{B}\mathbf{B}^\intercal. \end{aligned} \tag{3.18}$$

A matrix $\mathbf{S}$ can always be found that rotates all components of $\vec{\beta}$ into the first component such that, without loss of generality of the power spectrum, the process η can be written with $\vec{\beta} = (\beta, 0, ..., 0)$ or by Eq. (3.10) simplified to

$$\eta(t) = \beta\xi_1(t) + \vec{1}^\intercal\vec{a}(t). \tag{3.19}$$

If we restrict β to positive values ($\beta > 0$), it is uniquely determined by the high frequency limit of the power spectrum (recalling Eq. (3.16)). Ambiguity remains in the choice of the matrices $\mathbf{A}$ and $\mathbf{B}$ in which $2d^2$ coefficients represent $2d$ degrees of freedom. For the special case $d = 2$ we may use:

$$\mathbf{A} = \begin{pmatrix} \mathrm{T}/2 & \frac{T^2/4-\mathcal{D}}{A_{21}} \\ A_{21} & T/2 \end{pmatrix}, \quad \mathbf{B} = \begin{pmatrix} B_{11} & 0 \\ 0 & 0 \end{pmatrix} \tag{3.20}$$

without loss of generality of the power spectrum (see details in the Appendix Sec. B.1). Here the trace and the determinant are denoted by $T = A_{11} + A_{22}$ and $\mathcal{D} = A_{11}A_{22} - A_{12}A_{21}$,

respectively. The solution of the inverse problem is given by:

$$\begin{aligned} \mathcal{D} &= 1/\sqrt{Y_2}, \qquad T = \pm\sqrt{\frac{Y_1}{Y_2} + \frac{2}{\sqrt{Y_2}}}, \qquad B_{11} = \mathcal{D}\frac{\sqrt{\beta^2 + X_0} - \beta}{T/2 - A_{21}}, \\ A_{21} &= \frac{TX_1/2 \pm (\sqrt{\beta^2 + X_0} - \beta)\sqrt{X_1 + \beta^2 Y_1 + 2\beta\sqrt{Y_2(X_0 + \beta^2)}}}{X_1 + 2\beta\sqrt{Y_2}(\sqrt{\beta^2 + X_0}) - \beta)} \end{aligned} \tag{3.21}$$

(see detailed derivation in the Appendix Sec. B.1).

However, for the use of the finite-difference method for the solution of the Fokker-Planck equation introduced in the Appendix Sec. A.4, second derivatives that arise from a noise term in the corresponding Langevin equation are beneficial since it stabilizes numerical solutions [see for instance Press et al. (2007) chapter 20]. Hence, for the sake of the stability of the numerical procedure, noise terms are applied in both dimensions of $\vec{a}(t)$ ($B_{22} > 0$, see Sec. B.1).

3.1.4 Mean-field theory

The application of the multidimensional Ornstein-Uhlenbeck process in Eq. (3.10) as neural input for an LIF neuron results in a multidimensional model described by Eq. (2.41) with $f(v, \vec{a}) = -v + \mu + \vec{1}^\intercal \vec{a}$, $\vec{g}(v, \vec{a}) = -\mathbf{A}\vec{a}$ and $\vec{\delta}_a = 0$. For given coefficients, the spike-train power spectrum can be calculated by the solution of the theory of the open-loop problem in Eq. (2.49). The extension of this theory by the conditions of self-consistent neural input and output in Eq. (3.5), yields the closed-loop problem which is the mean-field theory that reads in the short version:

$$\begin{aligned} S_{\eta\eta}(\mathbf{A}, \mathbf{B}, \vec{\beta}, \omega) &= \phi S(\tilde{Q}, r, \omega), \qquad \mu = RI_{ext} + \tau_m J(C_E - gC_I)r, \\ (i\omega + \hat{\mathcal{L}}(\mathbf{A}, \mathbf{B}, \vec{\beta}, \mu) + e_\tau \hat{\mathcal{R}}(\mathbf{A}, \mathbf{B}, \vec{\beta}))\tilde{Q} &= \left[1 + \left(\frac{e_\tau - 1}{i\omega} - \frac{e_\tau}{r}\right)\hat{\mathcal{R}}(\mathbf{A}, \mathbf{B}, \vec{\beta})\right] P_0, \\ (\hat{\mathcal{L}}(\mathbf{A}, \mathbf{B}, \vec{\beta}, \mu) + &\hat{\mathcal{R}}(\mathbf{A}, \mathbf{B}, \vec{\beta}))P_0 = 0. \end{aligned} \tag{3.22}$$

This short form only shows the most essential parts of the theory, the self-consistency conditions and the concise versions of the partial differential equations for the stationary density and $\tilde{Q}$ for $\omega \neq 0$. It has to be complemented by the definition of the stationary firing rate, the normalization of the stationary probability density, the partial differential equation for the special case $\omega = 0$ with normalization condition, the relation between the spike-train power spectrum $S(\omega)$ and the Fourier transformed probability density $\tilde{Q}$, the definition of the operators $\hat{\mathcal{L}}$ and $\hat{\mathcal{R}}$ and the boundary conditions for P_0 and $\tilde{Q}$. The full explicit theory is developed in Eq. (3.23) and reveals the whole mathematical complexity of the problem[1]:

[1] the only remaining non-explicit part is the probability transition during the refractory period that is incorporated by the function $\rho_{\text{ref}}(\vec{a}|\vec{a}')$ which can be calculated as shown in the Appendix Sec. B.2 or by Risken (1984) with the final result in Eq. 6.124

$$\vec{\beta}^2 + \vec{1}^\intercal \left[(\mathbf{A} + i\omega\mathbb{1})^{-1} + (\mathbf{A} - i\omega\mathbb{1})^{-1} \right] \mathbf{B}\vec{\beta} + \vec{1}^\intercal \left(\mathbf{A} + i\omega\mathbb{1} \right)^{-1} \mathbf{B}\mathbf{B}^\intercal \left((\mathbf{A} - i\omega\mathbb{1})^{-1} \right)^\intercal \vec{1}$$
$$= \tau_m^2 J^2 (C_E + C_I g^2)\, r \left(1 - 2\mathrm{Re} \int\limits_{M_{\vec{a}}} d\vec{a}\, \frac{\vec{\beta}^2}{2\tau_m^2} \partial_v \tilde{Q}(v, \vec{a}, \omega) \Big|_{v=v_{\mathrm{th}}} \right),$$
$$\mu = RI_{ext} + \tau_m J (C_E - g C_I) r,$$

$$-\partial_v \left(\tfrac{-v+\mu+\vec{1}^\intercal\vec{a}}{\tau_m} P_0(v, \vec{a}) \right) + \vec{\partial}_a^\intercal (\mathbf{A}\vec{a} P_0(v, \vec{a})) + \tfrac{1}{2} \vec{\partial}_a^\intercal \mathbf{B}\mathbf{B}^\intercal \vec{\partial}_a P_0(v, \vec{a}) + \tfrac{1}{\tau_m} \partial_v \vec{\beta}^\intercal \mathbf{B}^\intercal \vec{\partial}_a P_0(v, \vec{a})$$
$$- \delta(v - v_r) \int\limits_{M_{\vec{a}'}} d\vec{a}'\, \rho_{\mathrm{ref}}(\mathbf{A}, \mathbf{B}, \tau_{\mathrm{ref}}, \vec{a} | \vec{a}') \frac{\vec{\beta}^2}{2\tau_m^2} \partial_v P_0(v, \vec{a}') \Big|_{v=v_{\mathrm{th}}} = 0,$$
$$r = - \int\limits_{M_a} d\vec{a}\, \frac{\vec{\beta}^2}{2\tau_m^2} \partial_v P_0(v, \vec{a}') \Big|_{v=v_{\mathrm{th}}}, \qquad \int\limits_{-\infty}^{v_{\mathrm{th}}} dv \int\limits_{M_a} d\vec{a}\, P_0(v, \vec{a}) = 1 - \tau_{\mathrm{ref}} r,$$

$$i\omega \tilde{Q}(v, \vec{a}, \omega) - \partial_v \left(\frac{-v + \mu + \vec{1}^\intercal \vec{a}}{\tau_m} \tilde{Q}(v, \vec{a}, \omega) \right) + \vec{\partial}_a^\intercal (\mathbf{A}\vec{a}\tilde{Q}(v, \vec{a}, \omega)) + \frac{1}{2} \vec{\partial}_a^\intercal \mathbf{B}\mathbf{B}^\intercal \vec{\partial}_a \tilde{Q}(v, \vec{a}, \omega)$$
$$+ \frac{1}{\tau_m} \partial_v \vec{\beta}^\intercal \mathbf{B}^\intercal \vec{\partial}_a \tilde{Q}(v, \vec{a}, \omega) - e^{i\omega\tau_{\mathrm{ref}}} \delta(v - v_r) \int\limits_{M_{\vec{a}'}} d\vec{a}'\, \rho_{\mathrm{ref}}(\mathbf{A}, \mathbf{B}, \tau_{\mathrm{ref}}, \vec{a} | \vec{a}') \frac{\vec{\beta}^2}{2\tau_m^2} \partial_v \tilde{Q}(v, \vec{a}', \omega) \Big|_{v=v_{\mathrm{th}}}$$
$$= P_0(v, \vec{a}) - \left(\frac{e^{i\omega\tau_{\mathrm{ref}}} - 1}{i\omega} - \frac{e^{i\omega\tau_{\mathrm{ref}}}}{r} \right) \delta(v - v_r) \int\limits_{M_{\vec{a}'}} d\vec{a}'\, \rho_{\mathrm{ref}}(\mathbf{A}, \mathbf{B}, \tau_{\mathrm{ref}}, \vec{a} | \vec{a}') \frac{\vec{\beta}^2}{2\tau_m^2} \partial_v P_0(v, \vec{a}') \Big|_{v=v_{\mathrm{th}}}$$
(for $\omega \neq 0$),

$$-\partial_v \left(\tfrac{-v+\mu+\vec{1}^\intercal\vec{a}}{\tau_m} \tilde{Q} \right) + \vec{\partial}_a^\intercal (\mathbf{A}\vec{a}\tilde{Q}) + \tfrac{1}{2} \vec{\partial}_a^\intercal \mathbf{B}\mathbf{B}^\intercal \vec{\partial}_a \tilde{Q} + \tfrac{1}{\tau_m} \partial_v \vec{\beta}^\intercal \mathbf{B}^\intercal \vec{\partial}_a \tilde{Q} - \delta(v - v_r) \int\limits_{M_{\vec{a}'}} d\vec{a}' \rho_{\mathrm{ref}} \tfrac{\vec{\beta}^2}{2\tau_m^2} \partial_v \tilde{Q} \Big|_{v=v_{\mathrm{th}}}$$
$$= P_0(v, \vec{a}') + \left(\tau_{\mathrm{ref}} - \frac{1}{r} \right) \delta(v - v_r) \int\limits_{M_{\vec{a}'}} d\vec{a}'\, \rho_{\mathrm{ref}} \frac{\vec{\beta}^2}{2\tau_m^2} \partial_v P_0(v, \vec{a}') \Big|_{v=v_{\mathrm{th}}},$$
$$\int\limits_{M_{\vec{a}}} d\vec{a} \int\limits_{-\infty}^{v_{\mathrm{th}}} dv \left(\frac{\tilde{Q}}{\tau_{\mathrm{ref}}} - \frac{\vec{\beta}^2}{2\tau_m^2} \partial_v \tilde{Q} \Big|_{v=v_{\mathrm{th}}} \right) = \frac{\tau_{\mathrm{ref}} r}{2} - 1 \qquad \text{(for } \omega = 0\text{)},$$

$$F(v_{\mathrm{th}}, \vec{a}) = \lim_{v \to -\infty} F(v, \vec{a}) = \lim_{|\vec{a}| \to \pm\infty} F(v, \vec{a}) = 0, \text{ for } F(v, \vec{a}) = P_0(v, \vec{a}), \tilde{Q}(v, \vec{a}, \omega). \tag{3.23}$$

The coefficients of the Ornstein-Uhlenbeck process $\mathbf{A}$, $\mathbf{B}$, the vector $\vec{\beta}$ as well as the stationary probability density P_0, the firing rate r, the Fourier-transformed probability $\tilde{Q}$ and the spike-train power spectrum are initially unknown and determine the solution of the theory. The further investigation of the solution regarding its existence, uniqueness

and stability is a challenging theoretical problem that possibly requires novel mathematical techniques, however, it is worth to put effort in thinking about it because it may yield a better understanding and a more accurate classification of dynamical regimes. Also the discovery or exclusion of novel regimes such as the heterogeneous asynchronous state that was found and described by Ostojic (2014) could be possible by the detailed analysis of Eq. (3.23). Yet there are no analytical solutions known and further analysis is outside the scope of this thesis but, hopefully, the equations provide a starting point for future studies.

Until now, it was assumed that the process η is capable to exhibit the self-consistent power spectrum exactly. In general however, this assumption requires an infinite dimensional Ornstein-Uhlenbeck process that is not tractable in practice, but as already mentioned in Sec. (3.1.3), finite dimensional processes may serve as approximations. In the following, three approximations of the mean-field theory in Eq. (3.23) are introduced that deal with finite and rather low-dimensional Ornstein-Uhlenbeck processes up to $d = 2$. As a proof of principle numerical solutions of these approximations are presented for one example network in the asynchronous irregular state with dominating inhibition (see Tab. C.4 for used parameters).

3.1.5 Approximative solutions with finite-dimensional input processes

In the simplest case of a zero-dimensional Ornstein-Uhlenbeck process ($d = 0$), neural input fluctuations are approximated by white noise that directly enters the voltage dynamics. Assuming self-consistency for the first-order statistics (mean values, i.e. the firing rates) is equivalent to assuming self-consistency of the power spectrum's high-frequency limit, such that the condition $\beta^2 = \phi r$ is obtained and the theory developed by Brunel (2000) is recovered by:

$$\lim_{\omega\to\infty} S_{\eta\eta}(\omega) = \phi \lim_{\omega\to\infty} S(\omega) \Rightarrow \beta^2 = \phi r. \tag{3.24}$$

In that sense, the self-consistency condition with white-noise input is a zeroth-order approximation of the mean-field theory in Eq. (3.23) the solution of which is an estimate of the self-consistent firing rate, provided that the effect of colored noise on the first-order statistics is small. If finite-dimensional processes are applied, self-consistency may also be achieved at $\omega = 0$ yielding the condition:

$$S_{\eta\eta}(0) = \beta^2 + X_0 = \phi S(0) \Leftrightarrow X_0 = \phi[S(0) - r], \tag{3.25}$$

(see Eq. (3.15) for relation between $\mathbf{A}$, $\mathbf{B}$, $\vec{\beta}$ and X_0). While these two conditions are essential for every well suited approximation, in the following three different sets of conditions are presented that determine the remaining coefficients in order to approximate the self-consistent power spectrum with increasing accuracy for increasing dimensionality.

Self-consistency at predetermined frequencies

Additionally to the self-consistency at the high- and low-frequency limits, here the coefficients X_k and Y_ℓ are determined to obtain self-consistency also at further predetermined frequencies. In other words, the solution is given by the coefficients for which the input spectrum is larger by the factor of ϕ than the resulting spike-train spectrum at the certain frequencies:

$$S_{\eta\eta}(\mathbf{A}, \mathbf{B}, \vec{\beta}, \omega_m) = \phi S(\omega_m) \qquad \text{(for predetermined } \omega_m\text{)}. \tag{3.26}$$

The number frequencies ω_m that are required to uniquely determine the spectrum is given by the number of free coefficients X_k and Y_ℓ by $2d-1$, hence, $m \in [1, 2d-1]$. In the limit to an infinite-dimensional process ($d \to \infty$), self-consistency could theoretically be achieved at all points such that the approximation becomes exact. In the low-dimensional case, the choice of ω_m should represent relevant frequencies of the unknown power spectrum such as peaks or dips. However, the optimal choice of frequencies is a difficult problem, because in advance we do not know, where the peaks and dips are located. For the one-dimensional case ($d = 1$) with $\dot{a} = -Aa + B\xi(t)$ only one frequency ω_1 has to be set and the self-consistency conditions by the Eqs. (3.24), (3.25) and (3.26) read:

$$\begin{aligned} \beta^2 &= \phi r, \\ X_0 &= \left(\frac{B}{A}\right)^2 + 2\frac{B}{A}\beta = \phi[S(0) - r], \\ Y_1 &= \frac{1}{A^2} = \frac{S(0) - S(\omega_1)}{\omega_1^2[S(\omega_1) - r]} \qquad \text{(for } d = 1\text{)}. \end{aligned} \tag{3.27}$$

For the two-dimensional embedding, additionally to the high- and low-frequency limit, the coefficients are given by the solution of the linear system for three predetermined frequencies:

$$\phi[S(0) - r] + X_1\omega_m^2 = \phi[S(\omega_m) - r](1 + Y_1\omega_m^2 + Y_2\omega_m^4) \qquad \text{(for } d = 2,\ m = 1, 2, 3\text{)}. \tag{3.28}$$

Remarkably, different choices for the ω_m yield different approximations for the self-consistent spectrum and for some choices even no solutions exist, although both Eqs. (3.27) and (3.28) always have unique solutions for the coefficients Y_ℓ and X_k. It may happen that no coefficients of the Ornstein-Uhlenbeck process $\mathbf{A}$, $\mathbf{B}$ and β exist that obey Eq. (3.15) and, thus, no self-consistent input process can be found for the specific choice of the frequencies ω_m, for instance, if the approximation on the right hand side of Eq. (3.14) is negative or diverges at any ω. This can be further specified for $d = 1$. For an unfortunate choice of ω_1, the (initially unknown) self-consistent spike-train power spectrum $S(\omega)$ does not behave monotonously at the respective frequencies, i.e. $S(0) > S(\omega_1) < r$ or $S(0) < S(\omega_1) > r$ and the right hand side of the last line in Eq. (3.27) is negative such that no real-valued solution for A exists. Note that this is not a physical property of the system but just a shortcoming of the method that also occurs for higher-dimensional embeddings for which the conditions on $S(\omega_m)$ for an existing solution are much more difficult to describe.

As a proof of principle, solutions of the introduced approximation for $d = 0, 1, 2$ are deter-

mined and presented in Fig. 3.3 for one network with dominating inhibition (see Tab. C.4 for parameters and Tab. C.5 for coefficients of the approximations). The solutions are determined iteratively as follows:

- $\mathbf{d = 0}$: At first, the self-consistent firing rate is estimated by the theory of Brunel (2000) with $\eta = \beta\xi(t)$. Starting with an arbitrary input firing rate, the output firing rate is calculated by Eq. (3.6) and used as input firing rate to calculate the noise strength $\beta = \sqrt{\phi r}$ for the next iteration. To guarantee stability, the mean input is calculated by the average over all previous output firing rate as in Eq. (3.9). The iteration is repeated until input and output firing rate coincide with sufficient accuracy. As shown in Fig. 3.3, there is a discrepancy at low frequencies between the constant input spectrum divided by ϕ and the spike-train power spectrum presented as lighter dashed and solid green lines, respectively, that coincide at the high-frequency limit. The spike-train power spectrum is calculated by the analytical formula shown in Eq. (A.33) that was derived by Lindner et al. (2002). However, the resulting spike-train power spectrum is only a rough approximation on the spectrum from the network simulation presented as solid black line. Also the firing rate, i.e. the high frequency limit, is significantly lower in the network simulation than predicted by the approximation.

- $\mathbf{d = 1}$: Applying a one-dimensional input process, self-consistency may be additionally achieved at $\omega = 0$ and at one other frequency for which I chose the firing rate $\omega_1 = 2\pi r$. Note that this frequency slightly changes from iteration to iteration until the self-consistent solution is found. The firing rate r and the spike-train power spectrum $S(0)$ and $S(2\pi r)$ from the solution with $d = 0$ are used to determine the initial mean input and the initial input spectrum by determining A, B and β by Eq. (3.27). By the iterative numerical solution of Eq. (2.49), the firing rate r and the spike-train power spectrum at $\omega = 0$ and $\omega = 2\pi r$ are determined and used to calculate the input power spectrum for the next iteration by Eq. (3.27). Again, the mean input is determined by the average over all previous output firing rates by Eq. (3.9) and the iteration is repeated until A, B, β and r obey Eq. (3.27), here after 10 iterations. The resulting input (divided by ϕ) and spike-train spectra are presented by the lightblue dashed and the solid blue lines, respectively, and intersect at $\omega = 0$ and $\omega = 2\pi r$, indicated by the blue dotted vertical line. The lines also match at $\omega \to \infty$ and are characterized by a small difference at other ω. The resulting spike-train power spectrum is a significantly better approximation of the network spectrum, particularly at low frequencies.

- $\mathbf{d = 2}$: The use of a two-dimensional input process enables us to assume self-consistency at two more frequencies (three in total), for which I choose $\omega_1 = \pi r$, $\omega_2 = 2\pi r$ and $\omega_3 = 4\pi r$ in Eq. (3.28). Initially, the self-consistent firing rate r and the spike-train power spectrum $S(0)$, $S(\pi r)$, $S(2\pi r)$ and $S(4\pi r)$ from $d = 1$ are used to determine the mean input and the input power spectrum. The coefficients Y_ℓ and X_k are determined by the solution of Eq. (3.28) and the matrices $\mathbf{A}, \mathbf{B}$ could be calculated by Eq. (3.21). However, for the sake of stability of the following numerical calculation, a non-vanishing noise B_{22} is applied and $\mathbf{A}$ and $\mathbf{B}$ are determined numerically by Eq. (B.16) as described

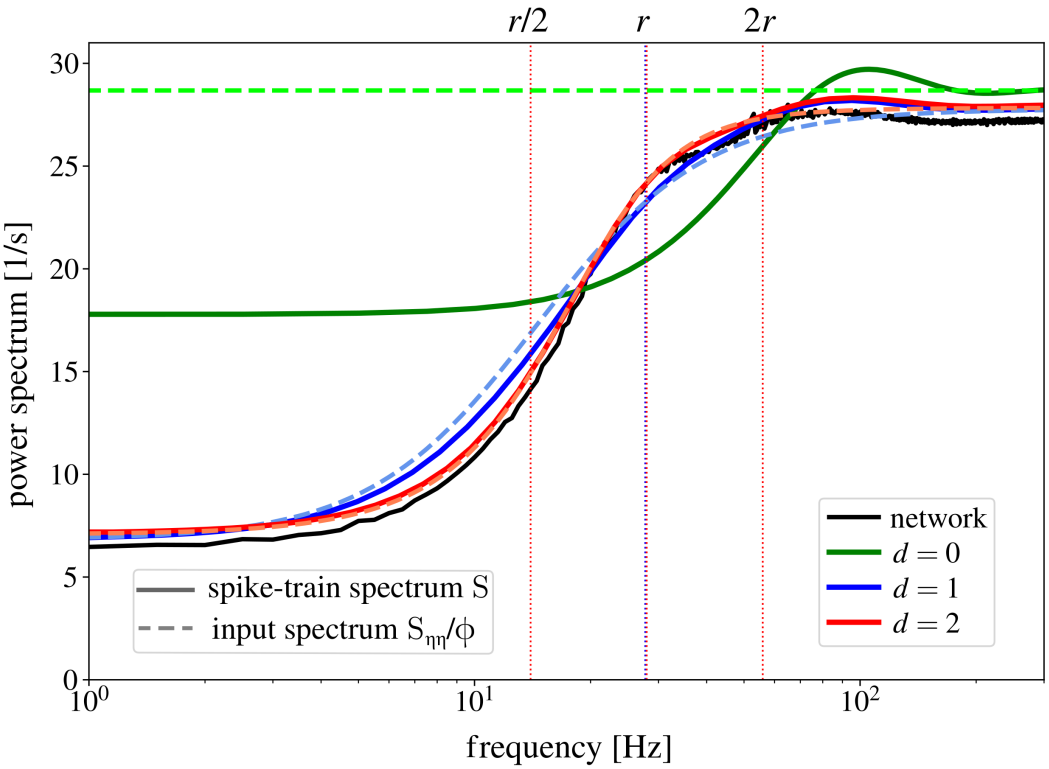

Figure 3.3.: Approximation of self-consistent power spectrum by self-consistency at predetermined frequencies. The spike-train power spectrum from the network simulation is presented as black line. Results of the approximation of neural input by a d-dimensional Markovian embedding are presented as dashed lines for the input divided by ϕ and corresponding spike-train spectra as solid lines. For $d = 0$ (green), the input is white noise and self-consistency is only achieved for the firing rates, that are represented by the high-frequency limit. For $d = 1$ (blue) and $d = 2$ (red), self-consistency is also achieved at zero frequency and at the $\omega_1 = 2\pi r$ and $\omega_m = \pi r$, $2\pi r$, $4\pi r$ as indicated by the blue vertical dotted line and the red dotted vertical lines, respectively. See Tabs. C.4, C.5, C.6 and C.7 for parameters.

in the Appendix Sec. B.1. By numerical solution of Eq. (2.49), the firing rate r and the spike-train power spectrum at ω_m $S(0), S(\pi r), S(2\pi r), S(4\pi r)$ are calculated and used to determine the input spectrum of the next iteration. Resulting spectra after seven iterations are presented in Fig. 3.3 as dashed light red and solid red lines that intersect at zero frequency, at ω_m indicated as red dotted vertical lines and at the high-frequency limit. Both lines are very close to each other at all ω and yield an improved approximation on the spike-train power spectrum observed in the network.

The remaining difference between the approximations on the self-consistent spectrum and the spectrum from the network is small and can be explained by the slight inaccuracy of the numerical solution of Eq. (2.49) for $d = 2$ due to the limited resolution, by the shot-noise character of neural input in the network and by the neglected contribution of small but

non-vanishing cross-correlations.

The shown spike-train power spectra are satisfactory approximations on the network spectrum. However, the choice of frequencies at which self-consistency has to be achieved is quite arbitrary, although it influences the result. Furthermore, although the increasing dimensionality improved the approximation in the presented example, the convergence behavior in general is unknown and there is no argument that input and spike-train power spectra may not strongly differ between the arbitrarily predetermined frequencies. By an unfortunate choice of frequencies, it might happen, that the increase of dimensionality is accompanied by a worsened approximation.

Self-consistent Padé approximation

Another approximation on the mean-field theory in Eq. (3.23) can be defined by the assumption that the input power spectrum is a Padé approximation of order $4d-2$ of the spike-train power spectrum times ϕ, yielding:

$$\begin{aligned} S_{\eta\eta}(\omega) &= \phi r + \frac{\phi[S(0)-r] + \sum_{k=1}^{d-1} X_k \omega^{2k}}{1 + \sum_{\ell=1}^{d} Y_\ell \omega^{2\ell}}, \\ \sum_{m=1}^{k} \frac{1}{(2m)!} \frac{\partial^{2m}}{\partial \omega^{2m}} S(\omega)\Big|_{\omega=0} Y_{k-m} &= \begin{cases} X_k/\phi & (\text{for } 1 \le k < d) \\ 0 & (\text{for } d \le k < 2d) \end{cases} \end{aligned} \tag{3.29}$$

[cf. Eq. (2.55)]. The derivatives of the spike-train power spectrum can be calculated by the solution of Eq. (2.53). In this approximation, the first $4d-2$ derivatives of the input power spectrum with respect to ω at $\omega = 0$ are ϕ times larger than the derivatives of the spike-train power spectrum. This local approximation is accurate at low frequencies and improves for an increasing dimensionality d at intermediate frequencies. However, as presented in Fig. 2.12, the Padé approximation of a spike-train power spectrum may diverge and/or be negative at some ω such that no corresponding input process as the solution of the inverse problem of Eq. (3.15) exists. If this is the case for the Padé approximation of order d for the self-consistent power spectrum, no solution of Eq. (3.29) exists and the approximation cannot be applied; however, a solution might be found for an approximation of higher order. Remarkably, it is not guaranteed that the increase of dimensionality yields a better approximation on the network power spectrum.

The solutions of Eq. (3.29) for the same network as in Fig. 3.3 for $d = 1$ and $d = 2$ are again determined iteratively and presented in Fig. 3.4. In each iteration, the input power spectrum is calculated by the Padé approximation of order $4d - 2$ of the previous spike-train power spectrum times ϕ. Self-consistency is approximately achieved after the tenth and after the fifth iterations for $d = 1$ and $d = 2$, respectively. For the considered network, also this procedure provides satisfactory approximations of the spike-train power spectrum of the network, although the scaled input spectra and spike-train power spectra differ at intermediate frequencies.

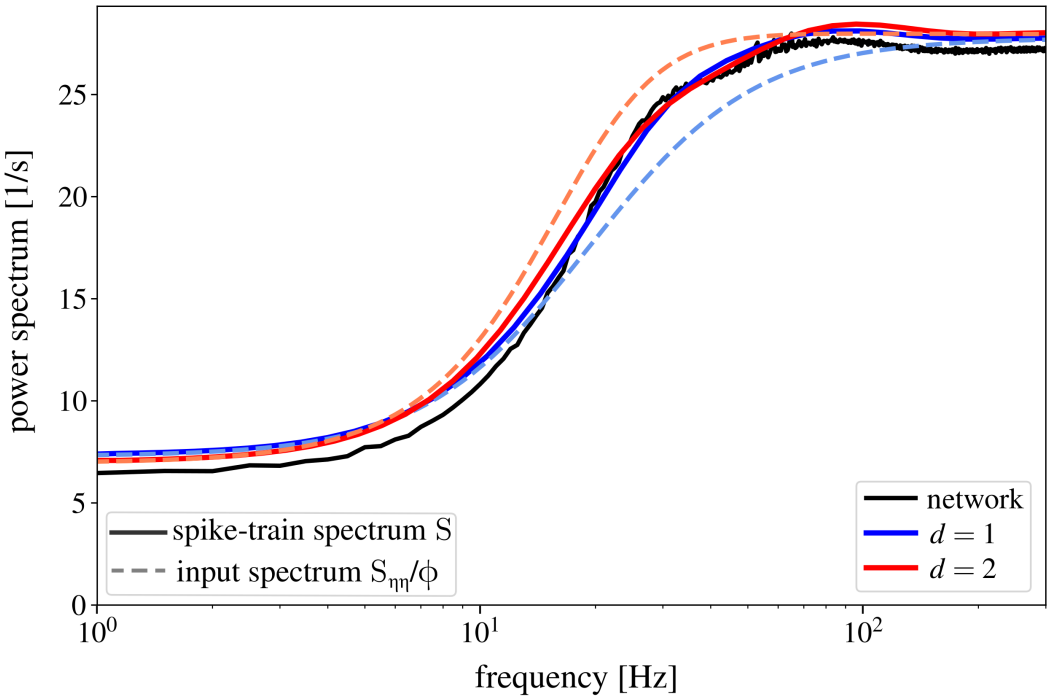

Figure 3.4.: Self-consistent Padé approximation. Input and spike-train power spectrum shown as light dashed and solid colored lines are determined such that the Padé approximation of order $4d - 2$ of the spike-train power spectrum at $\omega = 0$ times ϕ is equal to the input power spectrum. See Tabs. C.4, C.5, C.6 and C.7 for parameters.

Minimization of squared difference

Self-consistency can approximately be achieved if the input spectrum and the spike-train spectrum times ϕ are not equal, but sufficiently close to each other, in other words, if the difference between them is small at every frequency ω. Consequentially, approximate self-consistency can be defined as the solution of the minimization problem:

$$\arg\min_{\mathbf{A},\mathbf{B}} \int_0^\infty d\omega \left(r + \frac{S(0) - r + \sum_{k=1}^{d-1} X_k(\mathbf{A},\mathbf{B},\beta)\omega^{2k}/\phi}{1 + \sum_{\ell=1}^{d} Y_\ell(\mathbf{A},\mathbf{B},\beta)\omega^{2\ell}} - S(\omega) \right)^2 . \tag{3.30}$$

Note that Eq. (3.30) can be considered as a least squares fitting procedure if the integration is numerically treated as large sum up to a high but finite frequency at which the spectra are close to the high-frequency limit. If the analytical expression for the spike-train power spectrum would be known, the solution could also be determined analytically. In contrast to the previous methods, a solution always exists the approximation may not deteriorate with increasing dimensionality, except due to increasing numerical inaccuracies. However, the numerical determination of the solution requires the calculation of the spike-train power

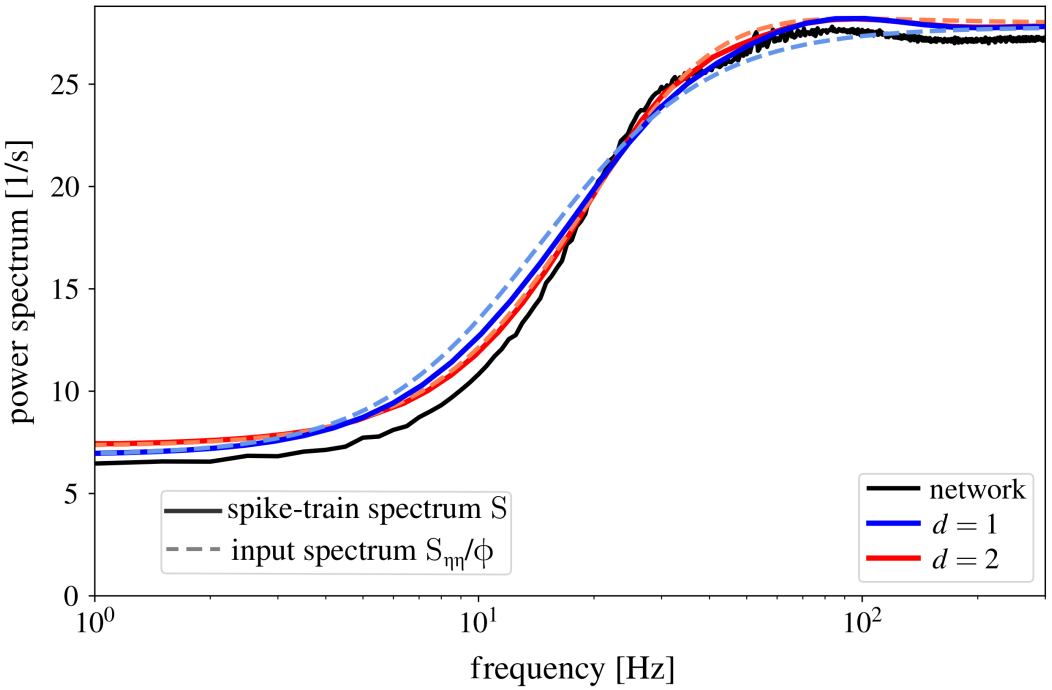

Figure 3.5.: Self-consistency approximated by minimization of the squared difference. Input and spike-train power spectra are defined by the minimization condition in Eq. (3.30) that is numerically solved by a least squares fitting procedure. See Tabs. C.4, C.5, C.6 and C.7 for parameters.

spectrum at many points in each iteration and, particularly in the higher dimensional case, the identification of the absolute minimum is a nontrivial problem. The iteratively determined numerical solutions for $d = 1$ and $d = 2$ are presented in Fig. 3.5. The coefficients X_k for $k > 1$ and Y_ℓ of the input power spectrum for one iteration are determined by least squares fitting of the spike-train power spectrum times ϕ of the previous iteration at 20 equidistant points between zero and $10\pi r$. Also this method yields a good approximation on the network spectrum.

3.2 Iterative scheme for heterogeneous networks

In biological networks, neuronal properties and firing rates are not homogeneous but distributed as it has been observed, for instance, by Griffith and G. Horn (1966); Koch and Fuster (1989); Shafi et al. (2007); Hromadka et al. (2008); O'Connor et al. (2010). Heterogeneities in networks with nearly balanced excitation and inhibition and approximately Gaussian distributed firing rates have already been taken into account in the original iterative scheme by Lerchner et al. (2006). Here the iterative scheme proposed by Dummer et al. (2014) is extended to determine the self-consistent temporal correlations of more general heterogeneous networks that may have any self-consistent distribution of firing rates

and unbalanced excitation and inhibition. Two different network topologies are considered. First, as in the study of Lerchner et al. (2006), binomially distributed numbers of presynaptic connections are applied that arise if synaptic connections are made by a fixed probability $p = C_E/N_E = C_I/N_I$. This network feature is also referred to as Erdős-Rényi topology after the mathematicians who studied it for the first time in the context of random graph theory (Erdős and Rényi, 1960). In a second example, the Erdős-Rényi topology is combined with exponentially distributed synaptic weights to incorporate experimental findings of long tailed distributions of synaptic weights, for instance by Song et al. (2005); Gilson and Fukai (2011).

In the iterative scheme, the self-consistent network dynamics are represented by M neurons, as illustrated in Fig. 3.6. In each iteration, the connection parameters for each neuron are randomly drawn from the respective distributions. One neuron α in the q-th iteration receives binomially distributed numbers $C^E_{k\alpha,q}$ and $C^I_{k\alpha,q}$ of excitatory and inhibitory spike trains from neurons that obey the statistics of neuron k from the previous iteration, given by the firing rate $r_{k,q-1}$ and the spike-train power spectrum $S_{k,q-1}$. Note that excitatory and inhibitory neurons are only distinguished by their effect on the postsynaptic neurons but exhibit the same spike-train statistics. For the Erdős-Rényi topology, the total mean input and the input power spectrum are given by:

$$\mu_{\alpha,q} = \tau_m J \sum_{k=1}^{M} (C^E_{k\alpha,q} - g C^I_{k\alpha,q}) r_{k,q-1}, \qquad S_{\eta\eta,\alpha,q}(\omega) = \tau_m^2 J^2 \sum_{k=1}^{M} \left(C^E_{k\alpha,q} + g^2 C^I_{k\alpha,q} \right) S_{k,q-1}(\omega). \tag{3.31}$$

The mean numbers of connections are given by $\langle C^E_{k\alpha,q} \rangle = \langle C_E \rangle / M$ and $\langle C^I_{k\alpha,q} \rangle = \langle C_I \rangle / M$. For the Erdős-Rényi topology and exponentially distributed synaptic weights $J^E_{k\alpha,l,q}$ and $J^I_{k\alpha,l',q}$, the mean input and the input power spectrum reads:

$$\begin{aligned} \mu_{\alpha,q} &= \tau_m \sum_{k=1}^{M} \left(\sum_{l=1}^{C^E_{k\alpha,q}} J^E_{k\alpha,l,q} - g \sum_{l'=1}^{C^I_{k\alpha,q}} J^I_{k\alpha,l',q} \right) r_{k,q-1}, \\ S_{\eta\eta,\alpha,q}(\omega) &= \tau_m^2 \sum_{k=1}^{M} \left(\sum_{l=1}^{C^E_{\alpha k,q}} (J^E_{k\alpha,l,q})^2 + g^2 \sum_{l'=1}^{C^I_{\alpha k,q}} (J^I_{k\alpha,l',q})^2 \right) S_{k,q-1}(\omega). \end{aligned} \tag{3.32}$$

Here inhibitory synapses are stronger by the factor g, but are drawn from the same distribution with $\langle J^I_{k\alpha,l'} \rangle = \langle J^E_{k\alpha,l} \rangle = J$. As it is the case in the homogeneous network, the iterative scheme is unstable for inhibition dominated networks ($g > C_E/C_I$). In this case, not the actual firing rates of the previous iteration $r_k, q-1$ are used in Eqs. (3.31) and (3.32), but shifted rates $\hat{r}_{k,q-1}$ of which the average over the firing rates within the respective iteration is equal to the average of all previous firing rates:

$$\hat{r}_{k,q-1} = r_{k,q-1} - \langle r_{k,q-1} \rangle_k + \frac{1}{q-1} \sum_{\ell=1}^{q-1} \langle r_{k,\ell} \rangle_k \tag{3.33}$$

[see also averaging procedure for homogeneous networks in Eq. (3.9)]. In the iterative scheme,

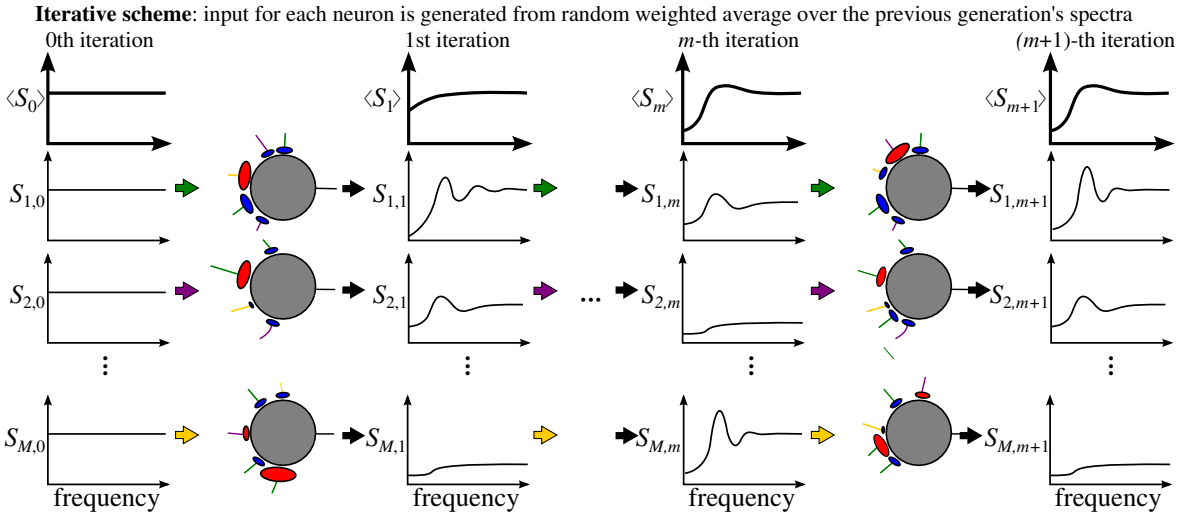

Figure 3.6.: Iterative scheme for heterogeneous networks with distributed number of presynaptic neurons and distributed synaptic strengths. The distribution of spike-train statistics is represented by the firing statistics of M neurons. Initially, white noise and random firing rates can be used (here $r_{k,0} = 70\,\mathrm{Hz}$). For each neuron in the scheme, the connection parameters to neurons from the previous iterations are randomly drawn. Mean input and input power spectrum are determined by Eqs. (3.31) and (3.32). The convergence of the scheme regarding to the distribution of spike-train power spectra can be indicated by the power spectrum averaged over the neurons within one iteration that does not significantly change due to the iterations after the scheme is converged.

Gaussian noise is generated for each neuron from the respective input spectrum using the method developed by Billah and Shinozuka (1990) in Eq. (3.8). The firing rates and the spike-train power spectrum are determined by simulations of 100 trials of the same duration and time step length as used in the corresponding network simulation (see Tab. C.8 for used parameters).

The Erdős-Rényi topology causes broad and skewed distributions of the firing rates in the network as shown by the histograms in Fig. 3.7a. Non-Gaussian features may arise due to the nonlinear dependency between input and firing rate of the neurons as discussed by Roxin et al. (2011). The additional distribution of synaptic weights in Fig. 3.7b yields only slightly broader distributions. The histograms can be well reproduced by the iterative scheme with a moderate number of $M = 50$ neurons per iteration. For the histograms, firing rates from ten iterations are used after the scheme converged in ten previous iterations. Initially, all firing rates were chosen to be the self-consistent firing rate in the balanced case estimated by the white-noise approximation that is $\approx 70\,\mathrm{Hz}$. All power spectra are initially flat.

More detailed results from the iterative scheme for distributed numbers of presynaptic connections are presented in Fig. 3.8. The mean values and the standard deviations of the firing rate histograms in the iterative scheme for each iteration are shown in Fig. 3.8a and b, respectively. The colored areas in Fig. 3.8a represent a standard error $\sigma_s = \sigma/\sqrt{M-1}$ that arises due to the finite number M of neurons per iteration as the number of samples,

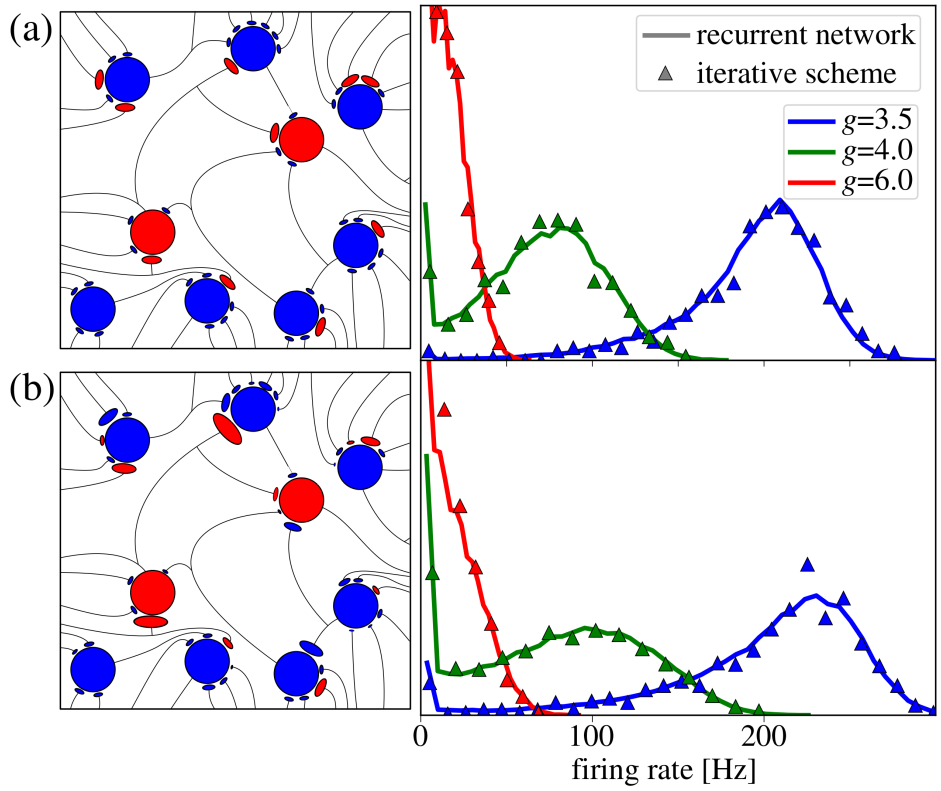

Figure 3.7.: Self-consistent distributions of firing rates. Networks of excitatory (blue) and inhibitory (red) neurons with binomially distributed numbers of presynaptic connections (panel a) and additionally distributed synaptic weights (panel b). Broad and skewed firing rate distributions caused by the Erdős-Rényi topology in panel a and even broader distributions due to additionally distributed synaptic weights in panel b can be reproduced by the iterative scheme for the inhibition dominated (red), balanced (green) and excitation dominated (blue) parameter sets with a moderate number of $M = 50$ neurons per iteration.

where σ is the standard deviation of the firing rates measured in the network. The iterative scheme rapidly converges after five iterations for g=3.5 and g=4 and after ten iterations for g=6. In the following iterations, the mean firing rates and the standard deviations are fluctuating around the values observed in the corresponding network simulation indicated as dashed black lines. The majority of the mean firing rates do not exceed the expected standard errors. Even for a low number of $M = 10$ neurons, results obtained with the iterative scheme are in accordance to network simulations.

Neurons in the network simulations exhibit different spike-train power spectra that are similar if neurons have a similar firing rate. To demonstrate that the iterative scheme with $M = 50$ may reproduce the spike-train power spectra of single neurons in the network, power spectra averaged over neurons with firing rates within 1 Hz intervals as noted in the legend are presented in Fig. 3.8c. Spectra from the iterative scheme agree with the spectra from the network simulation. Averaged power spectra over all neurons are presented in Fig. 3.8d.

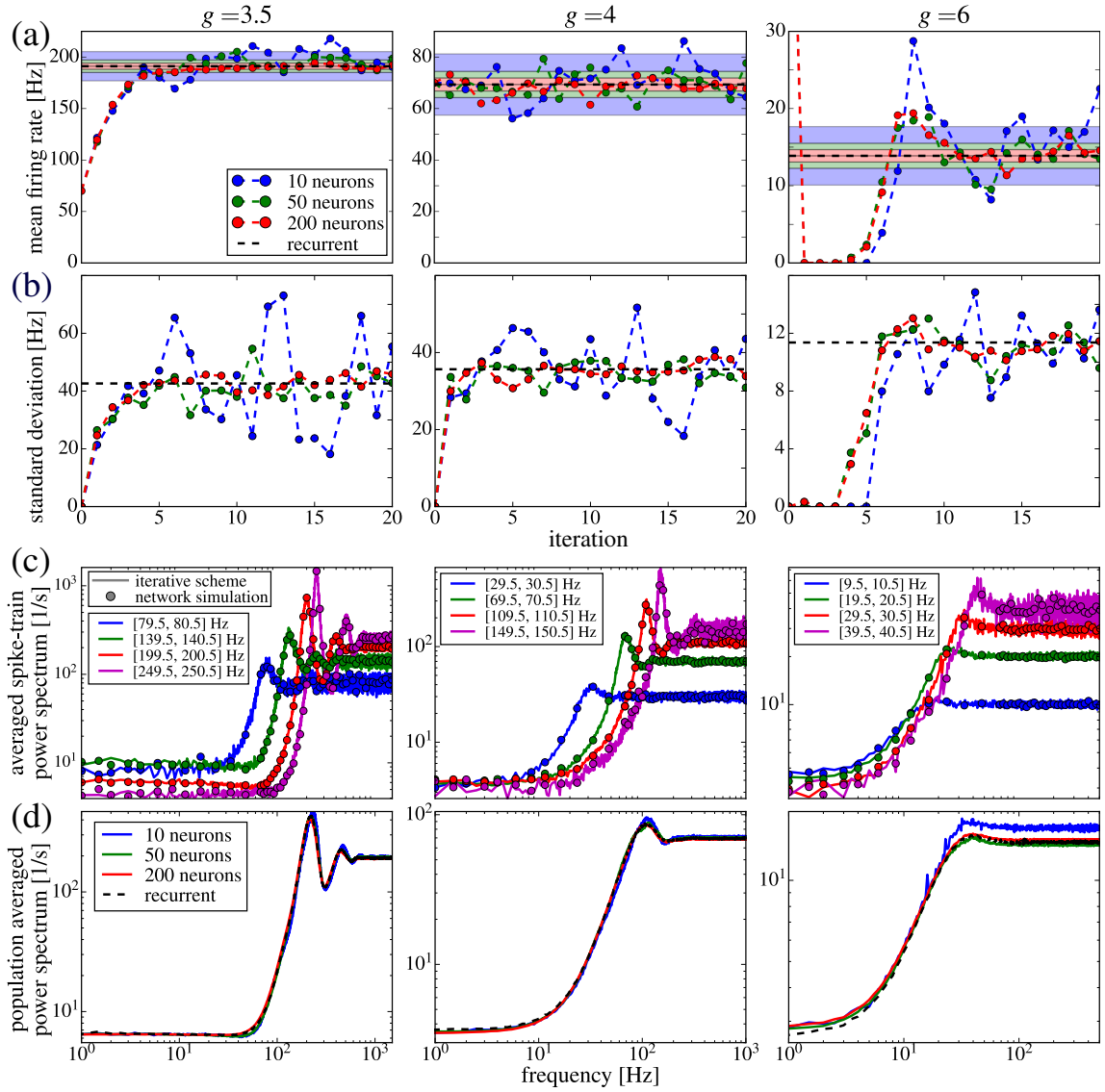

Figure 3.8.: Heterogeneous spike-train statistics from networks and iterative schemes with Erdős-Rényi topology. From top to bottom: mean firing rates (a) with standard error $\sigma_s = \sigma/\sqrt{M-1}$ (with σ being the standard deviation of the network firing rates) and standard deviations of firing rates (b) for each iteration as colored circles for different number of neurons per iteration M and as dashed black line from the network. (c) Power spectra averaged over spectra from single neurons with firing rates within the indicated intervals as lines from neurons in the iterative scheme (from iterations 6-20 for $g = 3.5$, 4 and 11–20 for $g = 6$) and as circles from neurons in the network. (d) Power spectra averaged over all neurons in the scheme as solid lines (all spectra from iterations 11 to 20) and dashed black line from the neurons in the network. Mean input for g=6 is calculated by the shifted firing rates in Eq. (3.33) to stabilize the scheme. See Tab. C.8 for used parameters.

Even for a small number of M=10 neurons, the iterative scheme may reproduce the averaged spectrum from the network simulation except for the case of dominating inhibition (g=6).

No qualitative changes are obtained if additionally distributed synaptic weights are considered as shown in Fig. 3.9. The mean firing rates in Fig. 3.9a are only slightly increased, whereas the standard deviations in Fig. 3.9b are increased by almost 50 percent compared to the case with equal weights. As presented in Fig. 3.9c and d, power spectra obtained from the iterative scheme and the network coincide except for the case of high inhibition. Due to the

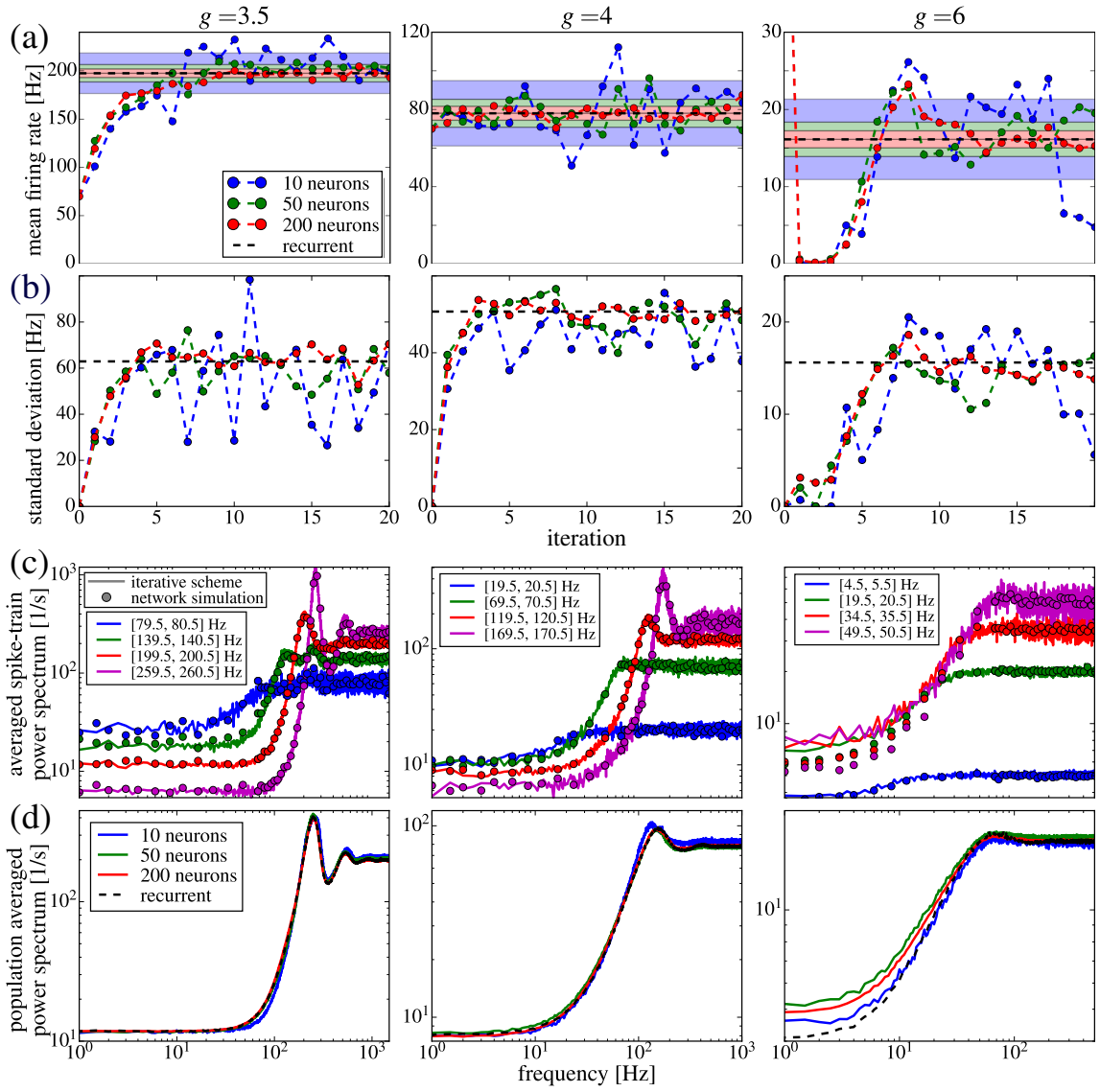

Figure 3.9.: Heterogeneous statistics caused by Erdős-Rényi topology and exponentially distributed synaptic weights. See Fig. 3.8 for detailed description and Tab. C.8 for used parameters.

low firing rate combined with strong synaptic weights, the distribution of the input noise is skewed and the Gaussian approximation of the input noise is inaccurate [see also Pena et al. (2018)]. A more accurate approximation of neural input might be given by approximating neural input by shot noise.

3.3 Summary and discussion

In this chapter, a mean-field theory for large and sparsely connected homogeneous networks of LIF neurons, first introduced by Brunel (2000), was developed that considers the self-consistent temporal correlations of spike trains represented by their power spectra. Neural input was approximated by colored Gaussian noise generated by a multidimensional Markovian embedding that yielded a multidimensional IF neuron model. The central result of this chapter was given by Eq. (3.23), in which the theory of spike-train power spectra for multidimensional IF neurons developed in the previous chapter was extended by the condition of self-consistent input and spike-train power spectra. The approach is complementary to the mean-field theory developed by van Meegen and Lindner (2018), in which the self-consistent temporal correlations are calculated in the limit of a strong mean input. The exploration of the existence, uniqueness and stability of its solution may reveal or exclude novel dynamical regimes and, thus, might improve our understanding of spiking neural network dynamics. However, the detailed analysis is a challenging objective for future investigations and might require the development of new mathematical techniques.

In the general theory, it is assumed that an infinite-dimensional Ornstein-Uhlenbeck process may generate noise that exactly obeys the self-consistency condition. However, since infinite-dimensional processes are difficult to treat, three different approximations were introduced that deal with finite-dimensional processes in Eqs. (3.26), (3.29) and (3.30) that contain the mean-field theory developed by Brunel (2000) as a zeroth-order approximation. As a proof of principle, numerical solutions of these approximations were determined iteratively for input processes with up to two dimensions for one large and sparsely connected network in the inhibition-dominated regime. This example network exhibited a power spectrum with reduced power at low frequencies as also observed in experiments with *in vivo* measurements, for instance by Bair et al. (1994). The power spectra that result as the solution of the theory, approximated the spike-train power spectrum in the network in all three cases and the increase of the dimensionality of the input process improved the approximation. However, two out of the three approximations may be unstable in the sense that no Ornstein-Uhlenbeck process exists that generates noise with a spectrum equal to the approximation of the self-consistent solution, for instance, if this approximation diverges or if it has negative values. Particularly for networks with more complicated spike-train power spectra, it would be important to study the convergence of the approximation for higher-dimensional Markovian embeddings. However, the numerical procedure used to solve the partial differential equations is very inefficient for higher-dimensional input processes and, thus, the method cannot be applied. As already mentioned in the discussion of the previous chapter, more efficient procedures might solve this issue.

In the second part of the chapter, the iterative scheme developed by Dummer et al. (2014) is

extended to heterogeneous networks with Erdős-Rényi topology and exponentially distributed synaptic weights. In contrast to the original iterative scheme by Lerchner et al. (2006) that has been proposed for Erdős-Rényi networks, not only individual mean input, but also individual input power spectra from a randomly weighted average over the spectra of the previous iteration's spectra were considered for each neuron in the iterative scheme. The firing rate distributions and spike-train power spectra resulting from the iterative scheme were compared in detail with the statistics of the corresponding networks. Even with a rather low number of neurons in the scheme, the self-consistent distributions of spike-train statistics in the corresponding network can be predicted accurately. The approach was also applicable in situations with very broad distributions of firing rates.

As already mentioned in the work of Brunel (2000), the synaptic dynamics considered in the network are oversimplified. A version of the iterative scheme has been developed that also takes into account the synaptic filtering of the input with equal time constants for excitatory and inhibitory synapses [see Pena et al. (2018)]. Such a synaptic filtering of neural input could also be considered in the mean-field theory by a further dimension of the input process or an adjusted self-consistency condition.

In the theory, correlations between spike trains are neglected. While this assumption is mostly valid in the asynchronous irregular state, many experiments discovered significant correlations of membrane potentials and spike trains across neurons [see for instance Lampl et al. (1999); Okun and Lampl (2008); Poulet and Petersen (2008)]. Cross-correlations might play an important role for the computation and signal transmission in neural networks and have been the subject of many studies, for instance by Ostojic et al. (2009); Helias et al. (2014); Doiron et al. (2016); Baker et al. (2019). Moreover, even small cross-correlations may have significant impact on the network dynamics as shown by Schneidman et al. (2006). However, due to complex network effects, the incorporation of such cross-correlations in a mean-field theory or in an iterative scheme is a challenging task but could be worth the effort.

In cases of low firing rates and high synaptic weights, the Gaussian approximation of neural input is inaccurate and, consequentially, the results of the iterative scheme disagree with the spectra from the network. Better results might be achieved if neural input is approximated by shot noise, however, the derivation and solution of a general framework that considers colored shot noise is difficult, although a framework has been developed for renewal processes by Ly and Tranchina (2009), for which also a version of the iterative scheme has been developed by Dummer et al. (2014) and, for Poissonian shot noise, even analytical formulas for the firing rates and the power spectrum have been derived by Richardson and Swarbrick (2010). In other cases with moderate synaptic weights and higher firing rates, the Gaussian approximation is more reasonable. The developed theory will hopefully be useful to gain further understanding of neural network dynamics and about information transmission therein.

4 Statistics of binary-decision sequences

How do we decide on which side to pass an oncoming pedestrian? Usually our brain perceives sensory impressions from the environment, interprets them as evidence for one or the other option and accumulates this evidence in order to decide which would be the better choice. In the optimal case, a rapid decision is intuitively made, possibly avoiding getting bitten by the threatening dog taken for a walk on the pedestrian's right hand side by passing on his left. Some decisions of humans are made on a high level of cognition. For instance, the decision to vote for a political representative requires that a lot of information is filtered, collected, analyzed and interpreted over months or even years. Understanding such complex decisions on a neural level is a huge challenge for scientists. However, in order to survive, higher animals also have the ability to make fast intuitive decisions on a low level of cognition and many studies in cognitive neuroscience are concerned with the identification and comprehension of the underlying mechanisms [see for instance Gold and Shadlen (2007); Heekeren et al. (2008); Chittka et al. (2009)].

There is a long history in which the problem has been addressed by analyzing the results from decision-making experiments by means of abstract phenomenological models that describe how noisy perceptual evidence is accumulated in order to make a decision. An important approach to model binary decision making is given by the diffusion-decision model (DDM) that dates back to the late seventies to Ratcliff (1978) and has become the standard model [see Ratcliff and Smith (2004) for a comparison with similar models and Ratcliff et al. (2016) for the latest review]. Many other models for binary decision making can be reduced to the DDM as shown by Bogacz et al. (2006). In its original version, evidence for a decision is modeled as Gaussian white noise with a finite mean value such that the accumulation of evidence is a one-dimensional diffusion process with constant drift. A decision is made when sufficient evidence is accumulated for one decision. Due to its simplicity, the model is analytically tractable as a first passage time problem which revealed theoretical insights in the optimal speed-accuracy trade off with respect to reward maximization (Bogacz et al., 2006; Bogacz, 2007). The following decades, the model with some modifications has been applied extensively for studies with different experiments with humans and monkeys [for instance in Ratcliff et al. (1999); Ratcliff (2002); Palmer et al. (2005); Ratcliff and McKoon (2008); Cisek et al. (2009); Johanson et al. (2018)]. To account for experimental findings, the model has been extended and adapted to many situations: trial-to-trial variability of the starting point (Ratcliff and Rouder, 1998) and of the drift, incorporation of a non-decision time (Ratcliff and Tuerlinckx, 2002), multi-alternative models (McMillen and Holmes, 2006; Krajbich and

Rangel, 2011) and urgency signals or collapsing boundaries (Cisek et al., 2009; Hawkins et al., 2015) are a few examples of such extensions.

The process of decision making was also studied from the perspective of neuroscientists. Electrophysiological recordings in alert monkeys during decisions-making tasks revealed that neural activity in certain brain areas correlates with the decisions [see review from Schall (2001); Romo and Salinas (2001)]. Decisions could even be manipulated by microstimulations in the study of Hanks et al. (2006). Wang (2002) introduced a model to explain how binary decision making may be implemented in a network of spiking neurons that replicates the psychophysical and physiological findings of Shadlen and Newsome (2001); Roitman and Shadlen (2002). In this model, evidence for one decision is encoded by a positive input to one population, evidence for the contradicting decision by a positive input to another population. Neurons within one population are predominantly excitatorily coupled yielding a positive feedback of the activity. Both populations are inhibitorily connected to each other via interneurons such that higher activity of one population reduces the activity in the other population. Decisions are made by the winner-take-all principle: sufficient evidence for one decision yields high activity in the corresponding population while the other population is silent due to the inhibition. By the application of mean-field techniques, assuming that the temporal correlations of spike trains can be neglected, the model has been reduced to a DDM by Wong and Wang (2006). As discussed by Roxin and Ledberg (2008), nonlinear dynamics of neural networks yield nonlinear DDMs for which the analytical solution is in general not known.

The statistics of binary decision making are experimentally measured by two-alternative forced-choice tasks of which the visual motion-discrimination task is a standard example used in many studies, for instance by Morgan and Ward (1980); Britten et al. (1992); Roitman and Shadlen (2002); Resulaj et al. (2009). The considered experimental paradigm for such an experiment is illustrated in Fig. 4.1. The subject is located in front of a screen on which randomly located dots appear at the beginning of an experimental trial. A subgroup of the dots moves coherently towards one of the two targets located on the left and right hand side of the screen while the other dots perform movements in randomly chosen directions. The difficulty of the experiment is adjusted by the fraction of coherently moving dots and their speed as the signal to noise ratio (Palmer et al., 2005). As soon as the subject perceives the direction of the coherent motion, it makes a decision by a saccade towards the respective target. The experiments are performed in consecutive trials and usually measure the reaction-time distributions and fractions of correct or incorrect decisions. At the beginning of each trial, the dots are randomly relocated and the direction of coherent motion is randomly chosen. It is also recommended by Green et al. (1983) to apply breaks of random duration in between the trials. In an experiment, slow transient dynamics may occur due to the loss of the subjects attention or improving of the performance due to learning. If only the reaction-time densities are considered, the transient dynamics and also correlations between decisions are neglected.

For a more comprehensive description of the experimental results, in this chapter the decision trains are considered in which sequences of decisions are represented as trains with positive and negative δ-pulses at the absolute decision times that encode correct and incorrect

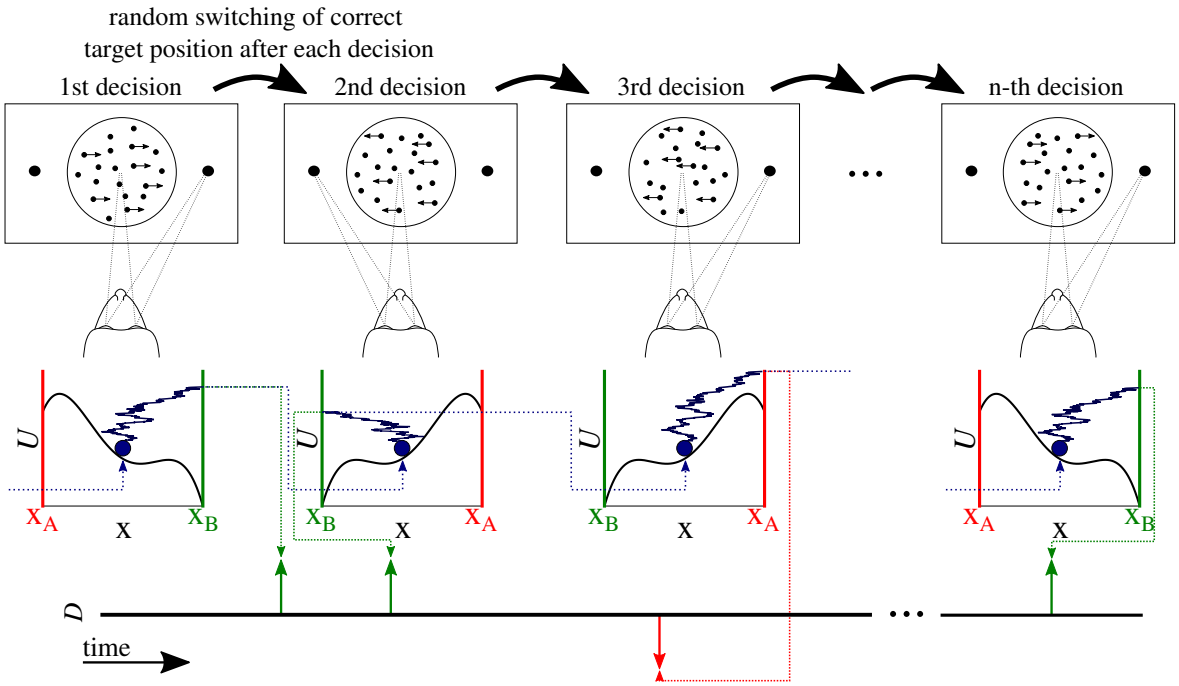

Figure 4.1.: Schematics of an experiment addressed by the theory in this chapter. This chapter is concerned with the statistics of sequences of binary decisions from a model for a two-alternative forced-choice task. As one example of a related experiment, a motion discrimination task used in e.g. Roitman and Shadlen (2002) is illustrated that may be performed as follows. At the beginning of a trial, the experimental subject, here a monkey, looks at a screen that displays a cloud of randomly located dots. Some dots perform motion in random directions, the other dots move coherently towards one of the targets placed on the left and right hand side of the screen. When the direction of coherent motion is perceived, a decision is made by a saccade to the respective target. The process of evidence accumulation is modeled as nonlinear DDM shown below in which incorrect A and correct B decisions are made when the overdamped Brownian particle (blue circle) in the potential U exceeds the threshold x_A and x_B indicated by vertical red and green lines, respectively. After the decision is made in one trial, the dots are randomly relocated an the experiment is repeated. The direction of the coherent motion may be changed randomly. In contrast to Roitman and Shadlen (2002) all other experimental parameters are fixed. The decision times are captured in the decision train as δ-spike in which the sign denotes correct or incorrect decisions as illustrated at the bottom.

decisions, respectively. In case of independent decisions, analytical formulas are derived that connect the decision-train statistics to each other, namely, the reaction-time densities, the interval distributions of consecutive decisions of the same kind and the decision-train power spectra. As the model for binary decision making the general one-dimensional DDM and the corresponding decision trains are introduced. For the simplest version of the DDM, a Wiener process within two absorbing boundaries, analytical formulas are derived by the solution of the first-passage time problem. To calculate the decision-train statistics of nonlinear DDMs, an efficient numerical method, the threshold-integration method, that was originally introduced

by Richardson (2007, 2008) to calculate the statistics of nonlinear IF neurons is extended. By means of this method, also the linear response for a weak temporal modulation of a parameter is calculated.

4.1 Decision-train statistics for renewal processes

The sequences of decisions are described by the decision trains d_A and d_B in which δ-functions are placed at the respective decision times. The decision trains for correct B decisions is defined positively, the one for incorrect A decisions negatively as shown in Fig. 4.1. The sum of both decision trains is the combined decision train D:

$$d_A(t) = -\sum_{i=0}^{N_A} \delta(t - t_{A,i}), \qquad d_B(t) = \sum_{j=0}^{N_B} \delta(t - t_{B,j}), \qquad D(t) \quad = d_A(t) + d_B(t). \quad (4.1)$$

The numbers of decisions A or B per time unit are given by the individual decision rates of r_A and r_B and their sum is the total rate R. If we consider an ensemble of DDMs, the rates are related to the decision trains by the averages:

$$r_A(t) = -\langle d_A(t)\rangle, \qquad r_B(t) = \langle d_B(t)\rangle, \qquad R(t) = r_A(t) + r_B(t). \quad (4.2)$$

Note that the rate of A-decisions is defined to be positive. For a stationary ensemble the averages do not depend on time. The stationary decision rates are denoted by $r_{A,0}$, $r_{B,0}$ and R_0.

In order to avoid repetitions, the statistics are introduced only for A decisions in the following. If not mentioned otherwise, the formulas for B-decisions can be found by swapping the indices A and B. One important measure in studies related to decision making are the probabilities to make a decision at the time T with reference to the start of the experiment at $T = 0$. Here these reaction-time densities, sometimes also referred to as response-time densities in literature, are denoted by ρ_A and ρ_B. The probability density to make either decision at time T regardless of which is chosen is given by:

$$\rho(T) = \rho_A(T) + \rho_B(T). \quad (4.3)$$

Only ρ is normalized to one while the integral over the densities ρ_A or ρ_B gives us the fraction of A or B decisions with respect to all decisions that are made. Since the accumulation of evidence in Eq. (4.13) and Eq. (4.14) is a Markov processes in our model, the resulting decision trains are renewal process with independent interdecision intervals. Consequentially, the decision trains are fully described by the densities ρ_A and ρ_B and all other statistics can be derived from them. The interval distribution between two A decisions is denoted by ϱ_A and can be calculated with given ρ_A and ρ_B as follows. For a reference decision A at time $T = 0$, the probability density that the next decision is also of kind A and at time T is given by $\rho_A(T)$. The density ϱ_A also considers all cases in which B decisions occur in between the two consecutive A decisions. The probability to have n B decisions between two A decisions occurring at time zero and time T is given by the n-th convolution of ρ_A with ρ_B. Thus, ϱ_A

can be written as the sum of all possible cases as:

$$\begin{aligned}\varrho_A(T) =& \overbrace{\rho_A(T)}^{AA} + \overbrace{\int_0^T dT' \rho_A(T-T')\rho_B(T')}^{ABA} + \overbrace{\int_0^T dT' \int_0^{T'} dT'' \rho_A(T-T')\rho_B(T'-T'')\rho_B(T'')}^{ABBA} + \overbrace{\quad ...}^{AB...BA} \\ =& \rho_A * \left(\delta(T) + \sum_{n=1}^{\infty} \underbrace{\rho_B * ... * \rho_B}_{n-\text{terms}} \right).\end{aligned} \tag{4.4}$$

Here the convolution is denoted by the asterisk. The density ϱ_A is normalized to one. Furthermore, the inverse of the stationary decision rate $r_{A,0}$ is the mean interdecision interval given by:

$$r_{A,0}^{-1} = \int_0^{\infty} dT \varrho_A(T) T. \tag{4.5}$$

By virtue of the convolution theorem, the Fourier transformation of ϱ_A is given by the simple expression:

$$\boxed{\tilde{\varrho}_A(\omega) = \tilde{\rho}_A(\omega) \left(\sum_{n=0}^{\infty} [\tilde{\rho}_B(\omega)]^n \right) = \frac{\tilde{\rho}_A(\omega)}{1 - \tilde{\rho}_B(\omega)},} \tag{4.6}$$

where I used the well-known sum formula for the geometric series in the last step.

The probability density that any, not necessarily consecutive, A decision is made at time τ with a reference A decision at zero is the conditional decision rate $m_A(\tau)$. Since the decision trains of the introduced model are renewal processes, $m_A(\tau)$ can be calculated from $\varrho_A(T)$ by including that an any number of A decisions can be made between reference decision and the considered decision. The probability density that the n-th A decision is made at T is given by the n-th convolution of $\varrho_A(T)$ such that $m_A(\tau)$ can be identified as:

$$m_A(\tau) = \begin{cases} \sum_{n=1}^{\infty} \overbrace{\varrho_A * ... * \varrho_A}^{n-\text{terms}}(\tau), & (\text{for } \tau \geq 0) \\ m_A(-\tau) & (\text{for } \tau < 0). \end{cases} \tag{4.7}$$

Decisions that have been made before the reference spike are included by the symmetry in τ in Eq. (4.7). A simple expression for the Fourier transformed conditional decision rate can be derived by applying the convolution theorem and, again, using the sum formula for the

geometric series as in Eq. (4.6). We obtain[1]:

$$\tilde{m}_A(\omega) = \int_0^\infty d\tau e^{i\omega\tau}[m_A(\tau) - r_{A,0}] = \begin{cases} \dfrac{\tilde{\varrho}_A(\omega)}{1-\tilde{\varrho}_A(\omega)} & (\text{for } \omega \neq 0), \\ \lim\limits_{\omega\to 0} \dfrac{\tilde{\varrho}_A(\omega)}{1-\tilde{\varrho}_A(\omega)} & (\text{for } \omega = 0). \end{cases} \tag{4.8}$$

In order to deal with well defined functions, I consider the Fourier transform of the difference between $m_A(\tau)$ and its high frequency limit, the stationary decision rate $r_{A,0}$. This is only important in the case $\omega = 0$. For the calculation of the temporal statistics of the decision train, the formulas for the spike-train statistics in Eq. (2.6) and Eq. (2.8) are used. The conditional decision rate is the essential part of the autocorrelation function of the decision train d_A:

$$c_A(\tau) = r_{A,0}(\delta(\tau) + m_A(\tau) - r_{A,0}) \tag{4.9}$$

[see Holden (1976) or Gabbiani and Koch (1998) Sec. 6]. The Wiener-Khinchin theorem can be applied to calculate the decision-train power spectrum $s_A(\omega)$ as introduced in Eq. (2.7) for neural spike trains by the Fourier transformation of the autocorrelation function over the full time range ($-\infty < \tau < \infty$):

$$\boxed{s_A(\omega) = \int_{-\infty}^\infty d\tau\, e^{i\omega\tau} c_A(\tau) = r_{A,0}(1 + 2\mathrm{Re}[\tilde{m}_A(\omega)]) = r_{A,0}\frac{1-|\tilde{\varrho}_A(\omega)|^2}{|1-\tilde{\varrho}_A(\omega)|^2} \qquad (\text{for } \omega \neq 0)} \tag{4.10}$$

[see Holden (1976)]. Note that the symmetry of the autocorrelation function [$c_A(\tau) = c_A(-\tau)$] was exploited such that the spectrum is given by two times the real part $\tilde{m}_A(\omega)$ for which the Fourier transform in is defined only over the positive half space in Eq. (4.8). The last step is only valid for $\omega \neq 0$ but the spectrum at zero frequency $s_A(0)$ can be calculated by the limes $\omega \to 0$.

The autocorrelation function of the combined decision train $C(\tau)$ can be calculated by the autocorrelation functions of the individual decision trains by inserting its definition in Eq. (4.1) into the definition of the autocorrelation function in Eq. (2.6) and using the autocorrelation functions of the individual decision trains in Eq. (4.9):

$$\begin{aligned} C(\tau) =& \langle D(t)D(t+\tau)\rangle - \langle D(t)\rangle^2 \\ =& c_A(\tau) + c_B(\tau) + 2r_{A,0}r_{B,0} + \langle d_A(t)d_B(t+\tau)\rangle + \langle d_B(t)d_A(t+\tau)\rangle \\ =& c_A(\tau) + c_B(\tau) + 2r_{A,0}r_{B,0} - r_{A,0}m_B(\tau) - r_{B,0}m_A(\tau) \\ =& c_A(\tau)\left(1 - \frac{r_{B,0}}{r_{A,0}}\right) + c_B(\tau)\left(1 - \frac{r_{A,0}}{r_{B,0}}\right) + R_0\delta(\tau). \end{aligned} \tag{4.11}$$

[1] The case distinction is necessary since the series $\sum_{n=0}^\infty \tilde{\varrho}_A(0)$ diverges because $\varrho_A(T)$ is normalized ($\tilde{\varrho}_A(0) = 1$).

The power spectrum of the combined decision train can be calculated by the application of the Wiener-Khinchin theorem as the Fourier-transformed autocorrelation function:

$$\boxed{S(\omega) = s_A(\omega)\left(1 - \frac{r_{B,0}}{r_{A,0}}\right) + s_B(\omega)\left(1 - \frac{r_{A,0}}{r_{B,0}}\right) + R_0.} \tag{4.12}$$

Remarkably, the power spectrum is constant if the stationary rates are equal for both decisions ($r_{A,0} = r_{B,0}$) regardless of the (possibly complicated) shape of the individual spectra. Note that also in this chapter, power spectra are plotted against the frequency $f = \omega/(2\pi)$ and *not* against the angular frequency ω, if not stated otherwise.

4.2 Diffusion-decision model and decision-train statistics

The general DDM is given by the accumulation of evidence x that evolves according to the Langevin equation:

$$\tau_x \dot{x} = f(x) + \sigma\sqrt{2\tau_x}\xi(t). \tag{4.13}$$

In the framework of Wang (2002) in which the decision making process is performed by two competing neural populations that are inhibiting each other, x is a dimensionless variable that quantifies the difference of activity of both populations [see also Wong and Wang (2006); Roxin and Ledberg (2008)]. The function $f(x)$ may contain a constant part μ that represents mean evidence towards one decision. Furthermore, the function incorporates the intrinsic dynamics of the system. The fluctuations in the model are captured by the second term on the right hand side as Gaussian white noise $\xi(t)$ that obeys $\langle \xi(t)\xi(t+\tau)\rangle = \delta(t-\tau)$ with strength $\sigma\sqrt{2\tau_x}$. This term includes both, intrinsic noise from stochastic neural network dynamics and fluctuations of the perceived evidence. A mechanical analogy to the dynamics of x is given by an overdamped Brownian particle in the potential $U(x)$ with $f(x) = -\partial_x U(x)$. The decisions are made when sufficient evidence, quantified by the thresholds x_A and x_B, for one of the contradicting decisions A or B is accumulated. Put differently, when x exceeds the threshold x_A or x_B, decision A or B is made, respectively. Here A and B denote incorrect and correct decisions, respectively, such that the mean evidence μ yields a drift towards x_B. After a decision was made, the variable x is reset to x_s:

$$\text{if } x(t) < x_A \text{ or } x(t) > x_B: \quad x(t+\Delta) \to x_\mathrm{s}, \quad x_A < x_\mathrm{s} < x_B. \tag{4.14}$$

A temporal gap between decision and reset is incorporated by the non-decision time Δ and accounts for any break, for instance, the time that is required for the physical reaction of the subject and for refocusing on the new task. For two-alternative forced choice tasks it is also useful to build in breaks with a random duration between trials as examined by Green et al. (1983). For simplicity, here only a constant Δ is considered. After the reset, x evolves according to Eq. (4.13) again until the next decision is made. Note that DDMs are basically white-noise driven IF neurons with an additional threshold. An example trajectory of x is shown in Fig. 4.2.

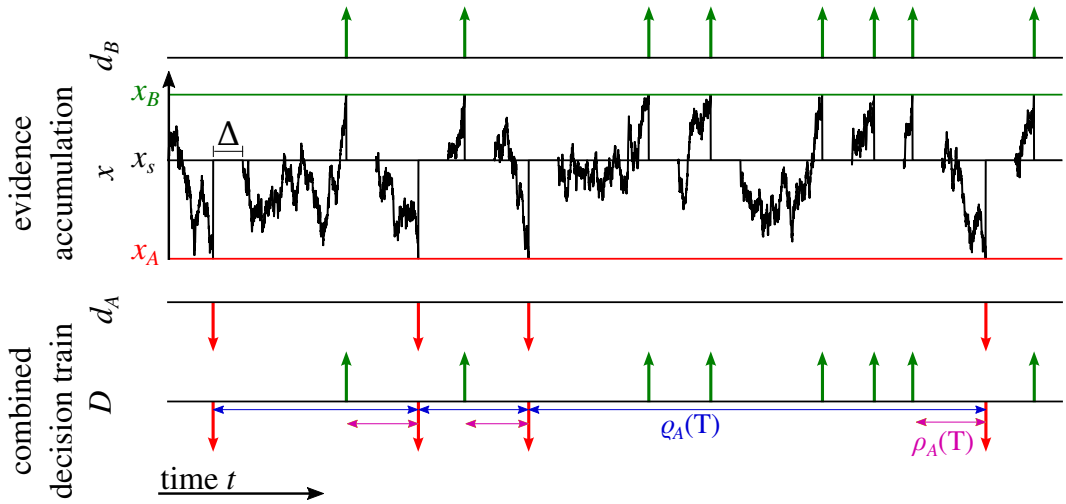

Figure 4.2.: Diffusion-decision model and decision trains. The noisy accumulation of evidence x obeys the dynamics in Eq. (4.13). When x exceeds the threshold x_A or x_B, a decision A or B is made and registered as a δ-function with positive or negative amplitude in the corresponding decision train, respectively. The A-decision train is defined negatively, the B-decision train positively. Their sum is the combined decision train D shown the bottom. The intervals of subsequent A decision that correspond to the density ϱ_A and intervals between A-decisions and the previous reset that correspond to ρ_A are indicated in blue and purple, respectively.

DDM as Wiener process

In its simplest version, the DDM is a Wiener process that arises from the general DDM in Eq. (4.13) by a constant deterministic part $f(x) = \mu$:

$$\tau_x \dot{x} = \mu + \sigma\sqrt{2\tau_x}\xi(t). \tag{4.15}$$

The expression is complemented by the decision-and-reset rule in Eq. (4.14). Without the non-decision time ($\Delta = 0$), this is the original DDM proposed by Ratcliff (1978). The statistics, namely the stationary decision rates and the probability densities of intervals between decisions ρ_A and ρ_B, can be derived analytically in the time domain as shown by Ratcliff (1978) [see also Gardiner (1985) section 5.5.1]. Here I derive explicit formulas for the interval densities in the Fourier domain from the solution of the Fokker-Planck equation. To simplify the calculation and the resulting formulas, I use $x_\mathrm{s} = 0$ without loss of generality since the model is invariant under translation in x if the translation is also applied to the thresholds. Only the distances between reset and thresholds are relevant.

The temporal evolution of an ensemble of DDMs in the subthreshold regime according to the Langevin equations in Eq. (4.15) is given by the Fokker-Planck equation that includes

drift and diffusion of probability (Risken, 1984):

$$\partial_t P(x,t) = \left[-\frac{\mu}{\tau_x}\partial_x + \frac{\sigma^2}{\tau_x}\partial_x^2 \right] P(x,t). \tag{4.16}$$

Due to the white noise term in Eq. (4.15) $P(x,t)$ is continuous in x and obeys absorbing boundary conditions at the thresholds $[P(x_A,t) = P(x_B,t) = 0]$ as described in Cox and Miller (1965) Sec. 5.7. The stationary solution $P_0(x)$ of the Fokker-Planck equation obeys the ordinary differential equation:

$$\begin{aligned} \partial_t P_0(x) = 0 &= \left[-\frac{\mu}{\tau_x}\partial_x + \frac{\sigma^2}{\tau_x}\partial_x^2 \right] P_0(x) + (r_{A,0} + r_{B,0})\delta(x), \\ r_{A,0} = \frac{\sigma^2}{\tau_x}\partial_x P_0(x)\Big|_{x=x_A}, &\quad r_{B,0} = -\frac{\sigma^2}{\tau_x}\partial_x P_0(x)\Big|_{x=x_B}. \end{aligned} \tag{4.17}$$

The efflux of probability at either threshold is given by the respective decision rate. To account for the reset after a decision is made, the total efflux that is quantified by the sum of the individual rates is reinserted at the reset position $x_\mathrm{s} = 0$ by the second term. The process either evolves according to Eq. (4.15) or does not evolve during the non-decision time Δ after a decision was made. The fraction of DDMs that are in the non-decision time is given by $(r_{A,0} + r_{B_0})\Delta$, thus, $P_0(x)$ obeys the normalization condition:

$$\int_{x_A}^{x_B} dx\, P_0(x) = 1 - (r_{A,0} + r_{B_0})\Delta. \tag{4.18}$$

For $\mu \neq 0$ the solution of the ordinary differential equation is given by $c_1 + c_2 \exp(\mu x \sigma^{-2})$ between $x_A \leq x \leq x_\mathrm{s}$ and $c_3 + c_4 \exp(\mu x \sigma^{-2})$ between $x_\mathrm{s} < x \leq x_B$. The coefficients c_1, c_2, c_3 and c_4 are chosen such that the conditions of the absorbing boundaries, continuity of P_0 at x_s and the normalization in Eq. (4.17) are fulfilled. Then the stationary probability density for the decision process reads:

$$\begin{aligned} P_0(x) &= [x_A e_B - x_B e_A - \frac{\mu}{\tau_x}\Delta(e_A - e_B)]^{-1} \begin{cases} e_B \left[\exp\left(\frac{\mu}{\sigma^2}[x - x_A] \right) - 1 \right] & (\text{for } x \leq 0) \\ e_A \left[\exp\left(\frac{\mu}{\sigma^2}[x - x_B] \right) - 1 \right] & (\text{for } x > 0), \end{cases} \\ e_A &= 1 - \exp\left(-\frac{\mu}{\sigma^2} x_A \right), \qquad e_B = 1 - \exp\left(-\frac{\mu}{\sigma^2} x_B \right). \end{aligned} \tag{4.19}$$

The analytical result for the stationary decision rates $r_{A,0}$ is given by the efflux at x_A in Eq. (4.19) and reads in our notation:

$$r_{A,0} = \frac{\mu e_B}{\tau_x [x_A e_B - x_B e_A] + \mu\Delta(e_B - e_A)}. \tag{4.20}$$

To calculate the reaction-time densities, an ensemble of DDMs is considered that made a

decision at $T = 0$. The evolution of such ensemble is described by the Fokker-Planck equation in which all probability is reinserted after the non-decision time has elapsed ($T = \Delta$):

$$\partial_T P(x,T) = \left[-\frac{\mu}{\tau_x}\partial_x + \frac{\sigma^2}{\tau_x}\partial_x^2 \right] P(x,T) + \delta(x)\delta(T-\Delta). \tag{4.21}$$

Here the interval distribution to the next decision is calculated such that no reset is taken into account. The probability density that the next A or B decision is made at T is equivalent to the interval distribution $\rho_A(T)$ and $\rho_B(t)$, respectively, and given by the efflux at the respective threshold:

$$\rho_A(T) = \frac{\sigma^2}{\tau_x}\partial_x P(x,T)\Big|_{x=x_A}, \qquad \rho_B(T) = -\frac{\sigma^2}{\tau_x}\partial_x P_0(x,T)\Big|_{x=x_B}. \tag{4.22}$$

To determine the analytical solution of the partial differential equation, a method described and used for IF neuron models in Lindner (2002) Sec. (2.4) is applied in which the equation is transformed to an ordinary differential equation. The Fourier-transformed version of Eq. (4.21) reads:

$$-i\omega\tilde{P}(\omega) = \left[-\frac{\mu}{\tau_x}\partial_x + \frac{\sigma^2}{\tau_x}\partial_x^2 \right] \tilde{P}(x,\omega) + e^{i\omega\Delta}\delta(x) \tag{4.23}$$

(see also Eq. (1.7) for the Fourier transformation of the derivative of $P(x,T)$ with respect to the time) and the Fourier-transformed interval distributions:

$$\tilde{\rho}_A(\omega) = \frac{\sigma^2}{\tau_x}\partial_x \tilde{P}(x,\omega)\Big|_{x=x_A}, \qquad \tilde{\rho}_B(\omega) = -\frac{\sigma^2}{\tau_x}\partial_x \tilde{P}(x,\omega)\Big|_{x=x_B}. \tag{4.24}$$

In order to further simplify the differential equation, the first order derivative can be removed by the transformation:

$$\tilde{P}(x,\omega) = \exp\left(\frac{\mu x}{2\sigma^2}\right) q(x,\omega). \tag{4.25}$$

The resulting differential equation for $q(x,\omega)$ is given by:

$$\frac{\sigma^2}{\tau_x}\frac{d^2}{dx^2}q(x,\omega) + \left(\frac{\mu^2}{4\sigma^2\tau_x} + i\omega\right) q(x,\omega) = -e^{i\omega\Delta}\delta(x) \tag{4.26}$$

in which $q(x,\omega)$ is also continuous and obeys absorbing boundary conditions at the thresholds. For this differential equation, the homogeneous solutions are given by:

$$q_1(x,\omega) = \exp[\kappa(\omega)x], \quad q_2(x,\omega) = \exp[-\kappa(\omega)x], \qquad \kappa(\omega) = \sqrt{\frac{\mu^2}{4\sigma^4} - \frac{i\omega\tau_x}{\sigma^2}} \tag{4.27}$$

The inhomogeneous solution $q(x,\omega)$ can be constructed by the linear combination of the

homogeneous solutions yielding the Ansatz:

$$q(x,\omega) = \begin{cases} c_1 q_1 + c_2 q_2 & (\text{for } x_A \le x \le x_\mathrm{s}) \\ c_3 q_1 + c_4 q_2 & (\text{for } x_\mathrm{s} \le x \le x_B). \end{cases} \tag{4.28}$$

The coefficients c_1, c_2, c_3 and c_4 are determined by the continuity of $q(x,\omega)$ at the reset $x_\mathrm{s} = 0$, the absorbing boundary conditions at the thresholds and the jump of the second derivative at $x = 0$ due to the inhomogeneity on the right hand side of Eq. (4.26):

$$\begin{aligned} &q(x_A,\omega) = q(x_B,\omega) = 0, \qquad \lim_{\varepsilon\to 0} q(x_\mathrm{s}+\varepsilon,\omega) - q(x_\mathrm{s}-\varepsilon,\omega) = 0 \\ &\lim_{\varepsilon\to 0} \frac{d}{dx}\, q(x,\omega)|_{x_\mathrm{s}-\varepsilon} - \frac{d}{dx}\, q(x,\omega)|_{x_\mathrm{s}+\varepsilon} = \frac{\exp(i\omega\Delta)\tau_x}{\sigma^2}. \end{aligned} \tag{4.29}$$

The solution of the resulting linear system yields us:

$$q(x,\omega) = \frac{\tau_x \exp(i\omega\Delta)}{\kappa(\omega)\sigma^2 \sinh[(x_B - x_A)\kappa(\omega)]} \begin{cases} \sinh[x_B\kappa(\omega)]\sinh[(x-x_A)\kappa(\omega)] & (\text{for } x_A \le x \le x_\mathrm{s}) \\ \sinh[x_A\kappa(\omega)]\sinh[(x-x_B)\kappa(\omega)] & (\text{for } x_\mathrm{s} < x \le x_B). \end{cases} \tag{4.30}$$

The Fourier-transformed reaction-time densities ρ_A and ρ_B can be calculated by Eqs. (4.24) and (4.26) as:

$$\tilde\rho_A(\omega) = \frac{\sigma^2}{\tau_x} \exp\left(\frac{\mu x_A}{2\sigma^2}\right) \frac{d}{dx} q(x,\omega)\Big|_{x=x_A}, \qquad \tilde\rho_B(\omega) = -\frac{\sigma^2}{\tau_x} \exp\left(\frac{\mu x_B}{2\sigma^2}\right) \frac{d}{dx} q(x,\omega)\Big|_{x=x_B} \tag{4.31}$$

which yields the analytical expression for $\tilde\rho_A$:

$$\boxed{\tilde\rho_A(\omega) = \frac{\exp\left(\frac{\mu x_A}{2\sigma^2} + i\omega\Delta\right)\sinh\left(x_B\kappa(\omega)\right)}{\sinh\left([x_B - x_A]\kappa(\omega)\right)}, \qquad \kappa(\omega) = \sqrt{\frac{\mu^2}{4\sigma^4} - \frac{i\omega\tau_x}{\sigma^2}}.} \tag{4.32}$$

The interval density of subsequent A decisions can be derived by inserting the results into Eq. (4.6):

$$\boxed{\tilde\varrho_A(\omega) = \frac{\exp\left(i\omega\Delta + \frac{\mu x_A}{2\sigma^2}\right)\sinh[x_B\kappa(\omega)]}{\sinh[(x_B - x_A)\kappa(\omega)] + \exp\left(i\omega\Delta + \frac{\mu x_B}{2\sigma^2}\right)\sinh[x_A\kappa(\omega)]}.} \tag{4.33}$$

It is also possible to write down analytical formula for the power spectra of the decision trains using Eq. (4.10) and Eq. (4.12) but the lengthy and complicated expression is not very insightful and thus not shown here.

In Fig. 4.3 theoretical results are tested by a comparison to direct numerical simulations of the Langevin equation. The results agree excellently (see Fig. 4.3c-d). For the chosen parameters (see Tab. C.9) correct B decisions are more likely than incorrect A decisions as can be seen by the number of spikes in the combined decision train shown in Fig. 4.3a. The

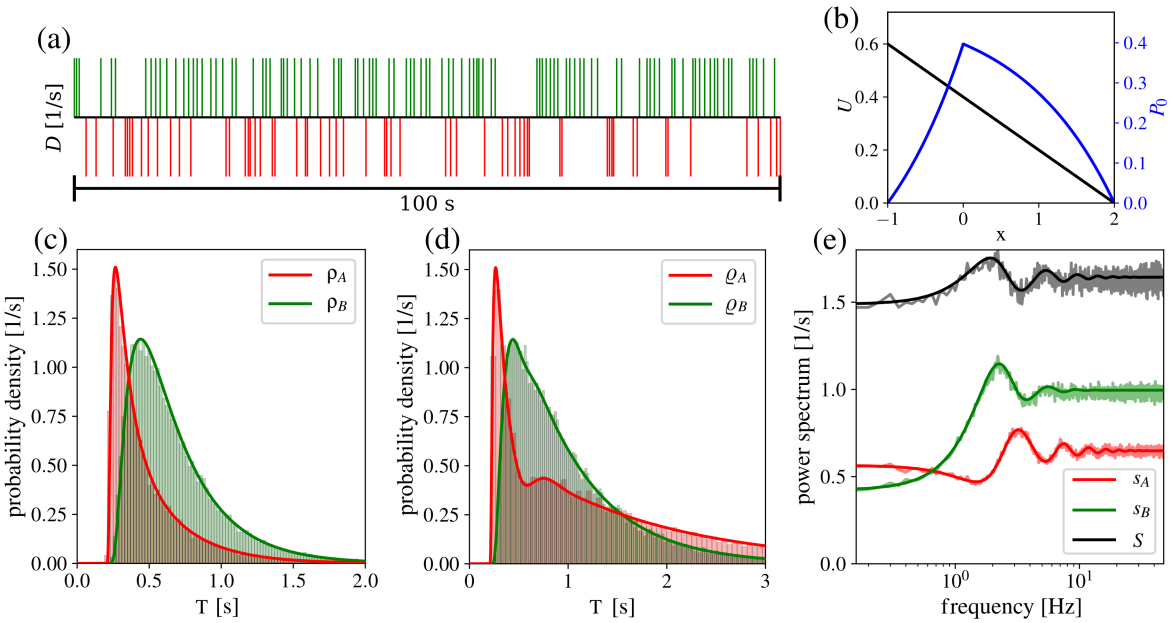

Figure 4.3.: Decision train statistics of linear DDM. Combined decision train with red A and green B decisions (panel a); linear potential $U(x)$ (black) and stationary solution $P_0(x)$ (blue) (b); reaction-time densities from latest reset (c), interdecision densities of individual decision trains from direct simulations (histograms) and theory (straight lines) (d); spectra of individual (colored) and combined (black) decision trains (e).

stationary probability density in Eq. (4.19) and the linear potential $U(x) = -\mu(x-2)$ are displayed in Fig. 4.3b. Due to the reset, P_0 is characterized by the kink at the start point $x_s = 0$. In Fig. 4.3c the interval probability densities $\rho_A(T)$ and $\rho_B(T)$ calculated by inverse Fourier transformation of Eq. (4.32) and from direct simulations are presented as lines and histograms, respectively. In this example the boundaries are located asymmetrically from the reset, thus, intervals between reset and A decisions are shorter on average than between reset and B decisions. The area under $\rho_A(T)$ is smaller than under $\rho_B(T)$ because B decisions are more likely to occur. The interval density for consecutive decisions of the same kind can be unimodal or multimodal as shown in Fig. 4.3d. Here the bimodality of $\varrho_A(T)$ arises due to the likely case that between two consecutive A decision is one B decision. In contrast, the sequence of BAB decisions is less likely due to the lower probability of A decisions, thus, it only yields a small shoulder of $\varrho_B(T)$. The power spectra in Fig. 4.3e are characterized by peaks that reflect typical time scales of the interdecision intervals; for the individual spectra, they are located at frequencies that correspond to the maxima of $\varrho_A(T)$ and $\varrho_B(T)$. The low frequency limit of the power spectrum s_B is significantly lower than the high-frequency limit indicating that the coefficient of variation is lower than one, and thus, the decision train d_B is more regular than a Poisson process.

In the general case with a nonlinear function $f(x)$ in Eq. (4.13), the used techniques to analytically calculate ρ_A and ρ_B cannot be applied. Instead, in the following an efficient

numerical procedure that was introduced to calculate the statistics of nonlinear integrate-and-fire neurons by Richardson (2007, 2008), the threshold-integration method, is extended to one-dimensional nonlinear models with two thresholds, the general DDM.

4.3 Threshold-integration method

To calculate the statistics of the general DDM given by Eqs. (4.13) and (4.14), I consider a large ensemble that is described by the probability density denoted by $P(x,t)$ and the corresponding flux $J(x,t)$. The evidence accumulation x is restricted between the thresholds due to the decision rule in Eq. (4.14). Consequentially, probability density $P(x,t)$ and flux $J(x,t)$ are only nonzero in between the thresholds $x_A < x < x_B$. The white noise term in the dynamics of x causes absorbing boundaries at the thresholds [see e.g. Cox and Miller (1965)]:

$$P(x_A,t) = P(x_B,t) = 0. \tag{4.34}$$

The probability $P(x,t)$ is continuous while the absorption and injection of probability at the thresholds and at the reset due to the decision rule in Eq. (4.14) yield discontinuities of the current $J(x,t)$ at these locations. The initial injection, the reinjection and the absorption of probability are incorporated by the source-and-sink function $\nu(x,t)$. Note that the absorption terms are also incorporated by the absorbing boundaries in Eq. (4.34) and do not need to be mentioned explicitly. As in the procedure of Richardson (2008), the continuity equation can be formulated with the help of this function by:

$$\partial_t P(x,t) + \partial_x J(x,t) = \nu(x,t). \tag{4.35}$$

The probability flux $J(x,t)$ that results from the dynamics in Eq. (4.13) can be written as:

$$\tau_x J(x,t) = f(x)P(x,t) - \sigma^2 \partial_x P(x,t) \tag{4.36}$$

[see Risken (1984) Eq. (4.47)]. Combining Eq. (4.36) into Eq. (4.35) leads to the Fokker-Planck equation that contains a second derivative with respect to x. However, here it is beneficial to write the problem as the two differential equations of first order.

Using different reset or initial conditions all of which are represented by the function $\nu(x,t)$, all the statistics introduced in the previous section, namely the rates, reaction-time densities, interdecision intervals and decision-train spectra can be derived from the corresponding solutions $P(x,t)$ and $J(x,t)$. To obtain these solution, the threshold integration method is applied as shown in the following.

4.3.1 Stationary solution

If the DDM is running for a long period of time, the ensemble becomes independent of the initial condition and ensemble averages are independent from the time. In this stationary case, the corresponding sink-and-source function $\nu_0(x)$ only incorporates the absorption at the thresholds and reinsertion of probability due to the reset and not the initial condition.

The efflux of probability at each threshold is given by the decision rate such that $\nu_0(x)$ reads:

$$\nu_0(x) = (r_{A,0} + r_{B,0})\delta(x - x_\mathrm{s}) - r_{A,0}\delta(x - x_A) - r_{B,0}\delta(x - x_B). \tag{4.37}$$

The corresponding stationary probability density $P_0(x)$ does not depend on time ($\partial_t P_0(x) = 0$) and the stationary current $J_0(x)$ is piecewise constant with jumps at the threshold and the reset as can be seen by inserting $P_0(x)$ into Eq. (4.35). With Eq. (4.36) the stationary solution obeys the two ordinary differential equations of first order:

$$\begin{aligned} \partial_x J_0 &= -\, r_{A,0}\delta(x - x_A) - r_{B,0}\delta(x - x_B) + (r_{A,0} + r_{B,0})\delta(x - x_\mathrm{s}) \\ \partial_x P_0 &= -\,\frac{1}{\sigma^2}(\tau_x J_0 - f(x)P_0). \end{aligned} \tag{4.38}$$

The solution can be found by the introduction of the two unnormalized densities $p_A(x) = P_0(x)/r_{A,0}$ and $p_B(x) = P_0(x)/r_{B,0}$ and the corresponding currents $j_{A,0}(x) = J_0(x)/r_{A,0}$ and $j_{B,0}(x) = J_0(x)/r_{B,0}$. For these functions, the values at the thresholds are known as

$$p_{A,0}(x_A) = p_{B,0}(x_B) = 0 \qquad \text{and} \qquad -\, j_{A,0}(x_A) = j_{B,0}(x_B) = 1. \tag{4.39}$$

Moreover, they obey the ordinary differential equations derived from Eq. (4.38):

$$\begin{aligned} \partial_x j_{A,0} &= -\delta(x - x_A), & \partial_x p_{A,0} &= -\frac{1}{\sigma^2}(\tau_x j_{A,0} - f(x)p_{A,0}), \\ \partial_x j_{B,0} &= -\delta(x - x_B), & \partial_x p_{B,0} &= -\frac{1}{\sigma^2}(\tau_x j_{B,0} - f(x)p_{B,0}). \end{aligned} \tag{4.40}$$

The solutions and particularly the densities at the reset $p_{A,0}(x_\mathrm{s})$ and $p_{B,0}(x_\mathrm{s})$ can be determined by numerical integration from the respective threshold to reset using e.g. a simple Euler procedure [see Press et al. (2007)]. Resulting functions of the procedure are presented in Fig. 4.4a,b for one example.

With these functions, the decision rates can be calculated by exploiting continuity and normalization of $P_0(x)$:

$$\begin{aligned} &r_{A,0}p_{A,0}(x_\mathrm{s}) = r_{B,0}p_{B,0}(x_\mathrm{s}), \\ &\int_{x_A}^{x_B} P_0(x)\,dx = r_{A,0}\int_{x_A}^{x_\mathrm{s}} p_{A,0}(x)\,dx + r_{B,0}\int_{x_\mathrm{s}}^{x_B} p_{B,0}(x)\,dx = 1 - (r_{A,0} + r_{B,0})\Delta. \end{aligned} \tag{4.41}$$

The fraction of probability that does not evolve due to the non-decision time is captured in the term $(r_{A,0} + r_{B,0})\Delta$ since it is not included in the probability density $P_0(x)$. Both rates are uniquely determined by:

$$r_{A,0}^{-1} = \int_{x_\mathrm{s}}^{x_A} p_{A,0}\,dx + \frac{p_{A,0}(x_s)}{p_{B,0}(x_\mathrm{s})}\left(\Delta + \int_{x_B}^{x_\mathrm{s}} p_{B,0}\,dx\right) + \Delta, \qquad r_{B,0} = \frac{r_{A,0}p_{A,0}(x_\mathrm{s})}{p_{B,0}(x_\mathrm{s})}. \tag{4.42}$$

The stationary density and current is related to the rates as:

$$P_0(x) = \begin{cases} r_{A,0}p_{A,0}(x) & (\text{for } x_A \le x \le x_\mathrm{s}) \\ r_{B,0}p_{B,0}(x) & (\text{for } x_\mathrm{s} < x \le x_B) \end{cases}, \qquad J_0(x) = \begin{cases} -r_{A,0} & (\text{for } x_A \le x \le x_\mathrm{s}) \\ r_{B,0} & (\text{for } x_\mathrm{s} < x \le x_B). \end{cases} \tag{4.43}$$

Two examples for $P_0(x)$ with the corresponding nonlinear potentials $U(x)$ are shown in Fig. 4.5b and g.

4.3.2 Time-dependent solutions: reaction-time densities, interdecision- interval distributions and decision-train power spectra

The time-dependent problem is given by the partial differential Eqs. 4.35 and 4.36 for which a direct numerical treatment is difficult. It is useful to consider the Fourier-transformed equations instead that are two ordinary differential equations of first order [cf. Fourier transform of the time derivative in Eq. (1.7)]:

$$\begin{aligned} \partial_x \tilde{J}(x,\omega) =& i\omega\tilde{P}(x,\omega) + \tilde{\nu}(x,\omega), \\ \partial_x \tilde{P}(x,\omega) =& -\frac{1}{\sigma^2}(\tau_x\tilde{J} - f(x)\tilde{P}(x,\omega)). \end{aligned} \tag{4.44}$$

Similarly to the stationary case, the key to determine the solution is the introduction of probability densities and currents scaled by the efflux of probability at the respective threshold for which the values at the thresholds are known:

$$\tilde{p}_A(x,\omega) = \frac{\tilde{P}(x,\omega)}{-\tilde{J}(x_A,\omega)}, \quad \tilde{p}_B(x,\omega) = \frac{\tilde{P}(x,\omega)}{\tilde{J}(x_B,\omega)}, \quad \tilde{\jmath}_A(x,\omega) = \frac{\tilde{J}(x,\omega)}{-\tilde{J}(x_A,\omega)}, \quad \tilde{\jmath}_B(x,\omega) = \frac{\tilde{J}(x,\omega)}{\tilde{J}(x_B,\omega)},$$
$$\text{with } \tilde{p}_A(x_A) = \tilde{p}_B(x_B) = 0 \text{ and } -\tilde{\jmath}_A(x_A) = \tilde{\jmath}_B(x_B) = 1. \tag{4.45}$$

With the negative sign for functions related to threshold x_A, it is taken into account that probability crosses this threshold from right to left yielding a negative current $J(x_A,T)$ in time domain. From Eq. (4.44) the partial differential equations of the scaled functions are given by:

$$\begin{aligned} \partial_x\tilde{\jmath}_A &= i\omega\tilde{p}_A - \delta(x-x_A), \quad \partial_x\tilde{p}_A = -\frac{1}{\sigma^2}(\tau_x\tilde{\jmath}_A - f\tilde{p}_A), \\ \partial_x\tilde{\jmath}_B &= i\omega\tilde{p}_B - \delta(x-x_B), \quad \partial_x\tilde{p}_B = -\frac{1}{\sigma^2}(\tau_x\tilde{\jmath}_B - f\tilde{p}_B) \end{aligned} \tag{4.46}$$

and can be solved by numerical integration from each threshold to the reset. One example of the result from the numerical integration is presented in Fig. 4.4c. By exploiting continuity of $\tilde{P}(x,\omega)$ and by a proper choice of the reset condition in $\tilde{\nu}(x,\omega)$ that determines the current jump at x_s, the resulting values at the reset $\tilde{p}_{A,s} = \tilde{p}_A(x_\mathrm{s},\omega)$, $\tilde{p}_{B,s} = \tilde{p}_B(x_\mathrm{s},\omega)$, $\tilde{\jmath}_{A,s} = \tilde{\jmath}_A(x_\mathrm{s},\omega)$ and $\tilde{\jmath}_{B,s} = \tilde{\jmath}_B(x_\mathrm{s},\omega)$ can be related to the temporal statistics of the decision trains. The results of the numerical integration are shown in Fig. 4.4c for one example.

Reaction-time densities

The reaction-time densities $\rho_A(T)$ and $\rho_B(T)$ are the probabilities that, under the condition that a previous decision was made at time zero, the consecutive decision is A or B at T, respectively. Their determination corresponds to a classical first-passage-time problem with two absorbing boundaries. Since only the next made decision is relevant, the reset of probability must not be considered. The reference decision at zero time is equivalent to an injection of all probability after the non-decision time has elapsed yielding the sink-and-source function in time domain:

$$\nu_{\mathrm{FPT}}(x,T) = \delta(T-\Delta)\delta(x-x_{\mathrm{s}}) - \rho_A(T)\delta(x-x_A) - \rho_B(T)\delta(x-x_B). \tag{4.47}$$

The first-passage-time densities $\rho_A(T) = -J(x_A,T)$ and $\rho_B(T) = J(x_B,T)$ measure the efflux of probability at the corresponding threshold. The Fourier transformed function is given by:

$$\tilde{\nu}_{\mathrm{FPT}}(x,\omega) = e^{i\omega\Delta}\delta(x-x_{\mathrm{s}}) - \tilde{\rho}_A(\omega)\delta(x-x_A) - \tilde{\rho}_B(\omega)\delta(x-x_B). \tag{4.48}$$

With help of the continuity of $\tilde{P}(x,\omega)$ and the jump of $\tilde{J}(x,\omega)$ at x_{s} the densities can be related to the scaled probabilities and currents:

$$\begin{aligned} \tilde{\rho}_A(\omega)\tilde{p}_{A,s} &= \tilde{\rho}_B(\omega)\tilde{p}_{B,s}, \\ \tilde{\rho}_A(\omega)\tilde{\jmath}_{A,s} + e^{i\omega\Delta} &= \tilde{\rho}_B(\omega)\tilde{\jmath}_{B,s} \end{aligned} \tag{4.49}$$

from which the Fourier transformed first-passage-time densities are give by:

$$\boxed{\tilde{\rho}_A(\omega) = \frac{\tilde{p}_{B,s}e^{i\omega\Delta}}{\tilde{p}_{A,s}\tilde{\jmath}_{B,s} - \tilde{p}_{B,s}\tilde{\jmath}_{A,s}}, \quad \tilde{\rho}_B(\omega) = \frac{\tilde{\rho_A}\tilde{p}_{A,\mathrm{s}}}{\tilde{p}_{B,\mathrm{s}}}.} \tag{4.50}$$

Interdecision-interval distributions of individual decision trains

Regarding the intervals of the individual decision trains, it is important to consider that within one interval an arbitrary number of the contradicting decision can be made. Thus, to calculate the interval distributions for consecutive decisions of the same type given by $\varrho_A(T)$ and $\varrho_B(T)$, probability that crosses the threshold A or B, respectively is not reset, while the efflux at the opposing threshold has to be reset. The resulting the sink-and-source functions for intervals between A and B decisions read:

$$\begin{aligned} \tilde{\nu}_A(\omega) &= (1+\tilde{\beta}_B(\omega))\delta(x-x_{\mathrm{s}})e^{i\omega\Delta} - \tilde{\varrho}_A(\omega)\delta(x-x_A) - \tilde{\beta}_B(\omega)\delta(x-x_B), \\ \text{and } \tilde{\nu}_B(\omega) &= (1+\tilde{\beta}_A(\omega))\delta(x-x_{\mathrm{s}})e^{i\omega\Delta} - \tilde{\beta}_A(\omega)\delta(x-x_A) - \tilde{\varrho}_B(\omega)\delta(x-x_B). \end{aligned} \tag{4.51}$$

The functions $\tilde{\beta}_A = -\tilde{J}(x_A,\omega)$ and $\tilde{\beta}_B(\omega) = \tilde{J}(x_B,\omega)$ are the Fourier transformed efflux at the corresponding threshold x_A and x_B, respectively. For the two cases, the modified reset conditions yield other jump conditions. Combined with the continuity in $\tilde{P}(x,\omega)$ the

conditions are:

$$\begin{aligned} \tilde{\varrho}_A(\omega)\tilde{p}_{A,s} = \tilde{\beta}_B(\omega)\tilde{p}_{B,s}, \quad \tilde{\varrho}_A(\omega)\tilde{\jmath}_{A,s} + (1+\tilde{\beta}_B(\omega))e^{i\omega\Delta} = \tilde{\beta}_B(\omega)\tilde{\jmath}_{B,s}, \\ \text{and } \tilde{\beta}_A(\omega)\tilde{p}_{A,\mathrm{s}} = \tilde{\varrho}_B(\omega)\tilde{p}_{B,\mathrm{s}}, \quad \tilde{\beta}_A(\omega)\tilde{\jmath}_{A,s} + (1+\tilde{\beta}_A(\omega))e^{i\omega\Delta} = \tilde{\varrho}_B(\omega)\tilde{\jmath}_{B,s}, \end{aligned} \tag{4.52}$$

that determine the densities $\tilde{\varrho}_A(\omega)$ and $\tilde{\varrho}_B(\omega)$ by:

$$\boxed{\tilde{\varrho}_A(\omega) = \frac{\tilde{p}_{B,s}e^{i\omega\Delta}}{\tilde{p}_{A,s}(\tilde{\jmath}_{B,s} - e^{i\omega\Delta}) - \tilde{p}_{B,s}\tilde{\jmath}_{A,s}} \text{ and } \tilde{\varrho}_B(\omega) = \frac{\tilde{p}_{A,s}e^{i\omega\Delta}}{\tilde{p}_{A,s}\tilde{\jmath}_{B,s} - \tilde{p}_{B,s}(\tilde{\jmath}_{A,s} + e^{i\omega\Delta})}.} \tag{4.53}$$

Note that the same expression can also be derived by the insertion of Eq. (4.50) into Eq. (4.6).

Decision-train power spectra

The essential parts of the decision-train power spectra are the conditional decision rates $\tilde{m}_A(\omega)$ and $\tilde{m}_B(\omega)$ (cf. Eq. (4.10)) that represent the probability to obtain an A or B decision that does not necessarily be the consecutive one under the condition of a reference decision at time zero of type A or B, respectively. Thus, the densities are given by the efflux of probability at the corresponding threshold under the condition that the total efflux is reinjected yielding the Fourier-transformed sink-and-source function:

$$\tilde{\nu}_S(\omega) = (1 + \tilde{m}_A(\omega) + \tilde{m}_B(\omega))\delta(x - x_{\mathrm{s}})e^{i\omega\Delta} - \tilde{m}_A(\omega)\delta(x - x_A) - \tilde{m}_B(\omega)\delta(x - x_B). \tag{4.54}$$

The continuity and jump conditions read:

$$\begin{aligned} \tilde{m}_A(\omega)\tilde{p}_{A,s} = \tilde{m}_B(\omega)\tilde{p}_{B,s}, \\ \tilde{m}_A(\omega)\tilde{\jmath}_{A,s} + (1 + \tilde{m}_A(\omega) + \tilde{m}_B(\omega))e^{i\omega\Delta} = \tilde{m}_B(\omega)\tilde{\jmath}_{B,s}, \end{aligned} \tag{4.55}$$

with which we obtain:

$$\begin{aligned} \tilde{m}_A(\omega) = \tilde{p}_{A,s}e^{i\omega\Delta}\theta(\omega), \qquad \tilde{m}_B(\omega) = \tilde{p}_{B,s}e^{i\omega\Delta}\theta(\omega), \\ \theta(\omega) = \left[\tilde{p}_{A,s}(\tilde{\jmath}_{B,s} - e^{i\omega\Delta}) - \tilde{p}_{B,s}(\tilde{\jmath}_{A,s} + e^{i\omega\Delta})\right]^{-1}. \end{aligned} \tag{4.56}$$

The individual decision-train power spectra result from the insertion into Eq. (4.10) from which the combined spectrum can be calculated by Eq. (4.12):

$$\boxed{\begin{aligned} &s_A(\omega) = r_{A,0}\left(1 + 2\mathrm{Re}\left[\tilde{p}_{A,s}e^{i\omega\Delta}\theta(\omega)\right]\right), \;\; s_B(\omega) = r_{B,0}\left(1 + 2\mathrm{Re}\left[\tilde{p}_{B,s}e^{i\omega\Delta}\theta(\omega)\right]\right), \\ &S(\omega) = (r_{A,0} - r_{B,0})2\mathrm{Re}\left[e^{i\omega\Delta}\theta(\omega)(\tilde{p}_{A,s} - \tilde{p}_{B,s})\right] + R_0. \end{aligned}} \tag{4.57}$$

These expressions may also be derived from Eqs. (4.10), (4.12) and (4.53).

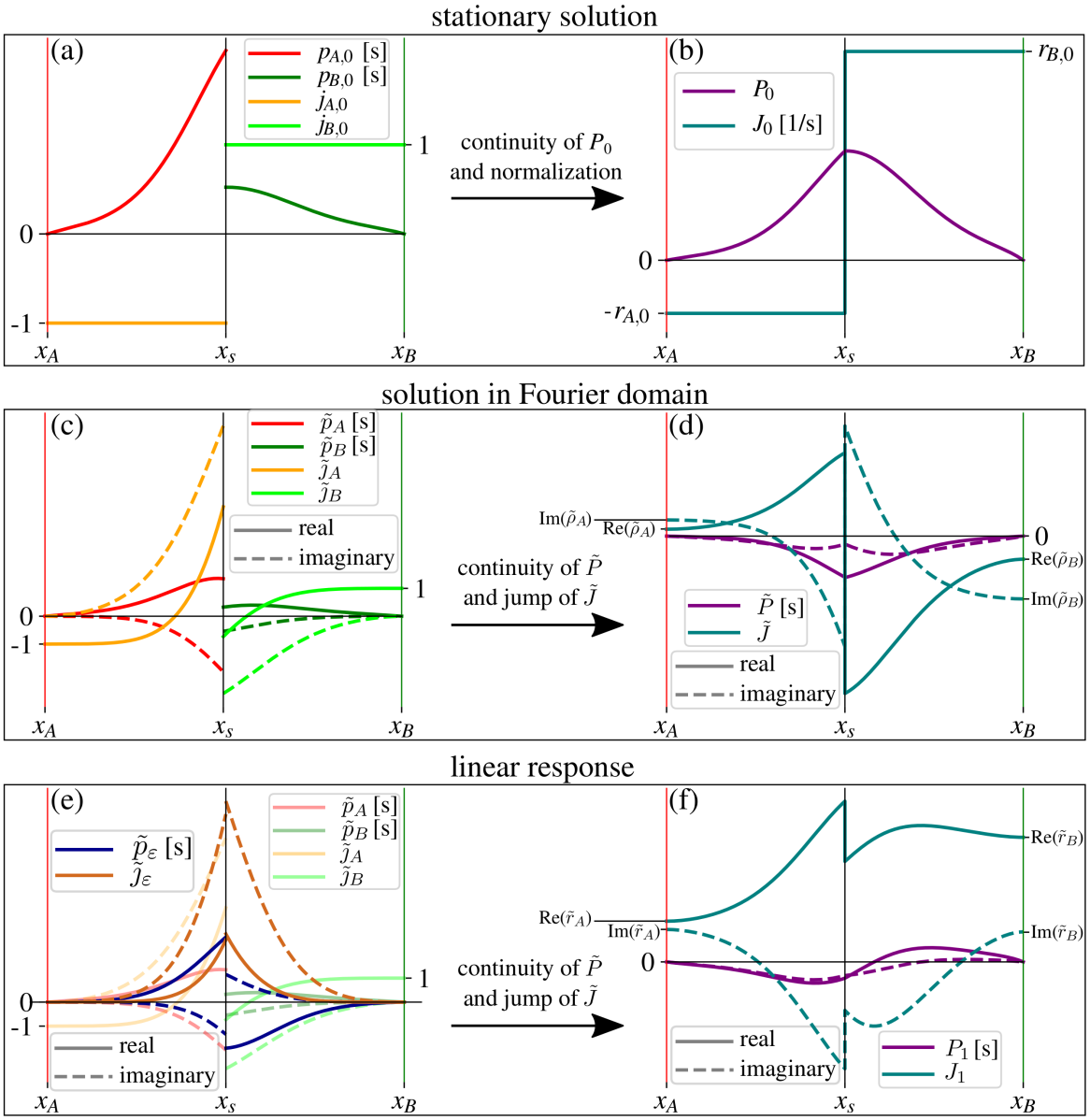

Figure 4.4.: Threshold-integration method for nonlinear DDM. From top to bottom: **stationary solution** (a,b): stationary probability density and current scaled to effluxes at thresholds, i.e. decision rates, with $p_{A,0}(x_s) = p_{B,0}(x_s) = 0$ and $-j_{A,0}(x_s) = j_{B,0}(x_s) = 1$ are obtained by numerical integration of Eq. (4.40) from thresholds to reset (a) and yield decision rates by assuming normalization and continuity of P_0 in Eq. (4.42). Decision rates yield P_0 and J_0 (b); **solution in Fourier domain** (c,d): Fourier-transformed probability densities and currents scaled to the effluxes at thresholds with $\tilde{p}_A(x_s,\omega) = \tilde{p}_B(x_s,\omega) = 0$ and $-\tilde{j}_A(x_s,\omega) = \tilde{j}_B(x_s,\omega) = 1$ determined by integration of Eq. (4.46) from thresholds to reset (c) are used to calculate the effluxes by exploiting continuity of $\tilde{P}$ and jump at x_s of $\tilde{J}$ here shown for $\tilde{\rho}_A$ and $\tilde{\rho}_B$ by (Eq. (4.50)) (d). Jump conditions incorporate initial insertion and reinsertion of probability and can be modified for other statistics for Eq. (4.53) and Eq. (4.56); **linear response** (e,f): $\tilde{j}_\varepsilon$ and $\tilde{p}_\varepsilon$, both 0 at thresholds, from integration of Eq. (4.66) from thresholds to reset (opaque lines left) yield, together with $\tilde{p}_A(x_s,\omega)$,$\tilde{p}_B(x_s,\omega)$, $j_A(x_s,\omega)$ and $j_B(x_s,\omega)$ (same lines as above but drawn pale), decision rate modulations by Eq. (4.70) via continuity of P_1 and jump of J_1 (shown in f). DDM is example one in Fig. 4.5 and $\omega = 12\,\mathrm{Hz}$.

Examples

The method is applied to two different nonlinear DDMs. The numerical integrations of Eqs. (4.40) and (4.46) are performed by the explicit Euler method [see Press et al. (2007)] with a step size $\Delta x = (x_B - x_A)/n$ and $n = 10^4$ steps. If x_s is not hit exactly due to the finite step size, integration is performed to the nearest discretization point instead. Due to the high resolution, the resulting numerical error can be neglected. In the first example shown in Fig. 4.5(a-e), the thresholds are located symmetrically around $x_\mathrm{s} = 0$ and $f(x)$ is an odd polynomial with constant drift towards B decisions (see Tab. C.9 for all parameters). The corresponding tilted potential[2] shown in Fig. 4.5b has been proposed by Roxin and Ledberg (2008) as the reduced dynamics of two competing neural populations. The constant drift breaks the symmetry of the model regarding A and B decisions and yields a higher probability of B decisions as can be seen in the combined decision train in Fig. 4.5a. The temporal statistics of the decision trains determined by the threshold-integration method via Eqs. (4.50), (4.53) and (4.57) are confirmed by the results of direct simulations as shown in Fig. 4.5(c-e). The shape of the resulting densities ρ_A and ρ_B resembles a γ-distribution in Fig. 4.5c. The lower probability of A decisions yields a long tailed interval distribution $\varrho_A(T)$ in Fig. 4.5d since it is likely that in between two consecutive A decisions many B decisions are made. The sequence of ABA decisions yields the second peak of $\varrho_A(T)$. In contrast, $\varrho_B(T)$ is similar to $\rho_B(T)$ with a short tail and only one sharp peak. The features of the decision trains are also reflected by the power spectra in Fig. 4.5e: the long tailed distribution ϱ_A yields a flat power spectrum s_A close to the one of a Poisson process. The low power at the low-frequency limit and the peaks at the decision rate and its higher harmonics of s_B indicate a regular decision train. The combined power spectra, predominantly reflects the properties of both spectra.

Another example is presented in Fig. 4.5(f-j) in which an asymmetric nonlinear potential[3] with several maxima and minima is chosen and the threshold x_A is placed three times as far from the reset as x_B (see panel g). The constant drift towards B decisions is tuned in order to compensate the asymmetry such that the decision rates are equal for both decisions. Thus, a similar amount of A and B decisions is obtained in the combined decision train in Fig. 4.5f. Again, all statistics calculated by the threshold-integration method are confirmed by the direct simulations in Fig. 4.5(h-j). Due to the longer distance from reset to x_A compared to x_B, A decisions are made slower than B decisions. Hence, the reaction-time density ρ_A is broader and its maximum is located at a higher time compared to ρ_B. The interval distributions of the individual decision trains d_A is monomodal but differs significantly from ρ_A while ϱ_B is bimodal (cf. panel i). The absolute maxima of the individual power spectra in Fig. 4.5j are located at the inverse times at which the maximum of ϱ_A and ϱ_B are located. Since the decision rates are equal, both spectra saturate at the same high-frequency limit. Although the individual spectra exhibit several peaks at different locations, the combined spectra is perfectly flat as predicted by Eq. (4.12) due to the tuning to equal decision rates.

[2] $U_I(x) = -0.5x^4 + 0.5x^2 - 0.2x + 0.2$

[3] $U_{II}(x) = \frac{2}{3}x^3 + \frac{1}{2}x^2 + \frac{1}{2}\exp(x) - 4\pi^{-1}\cos(2\pi x) - 1.085x$

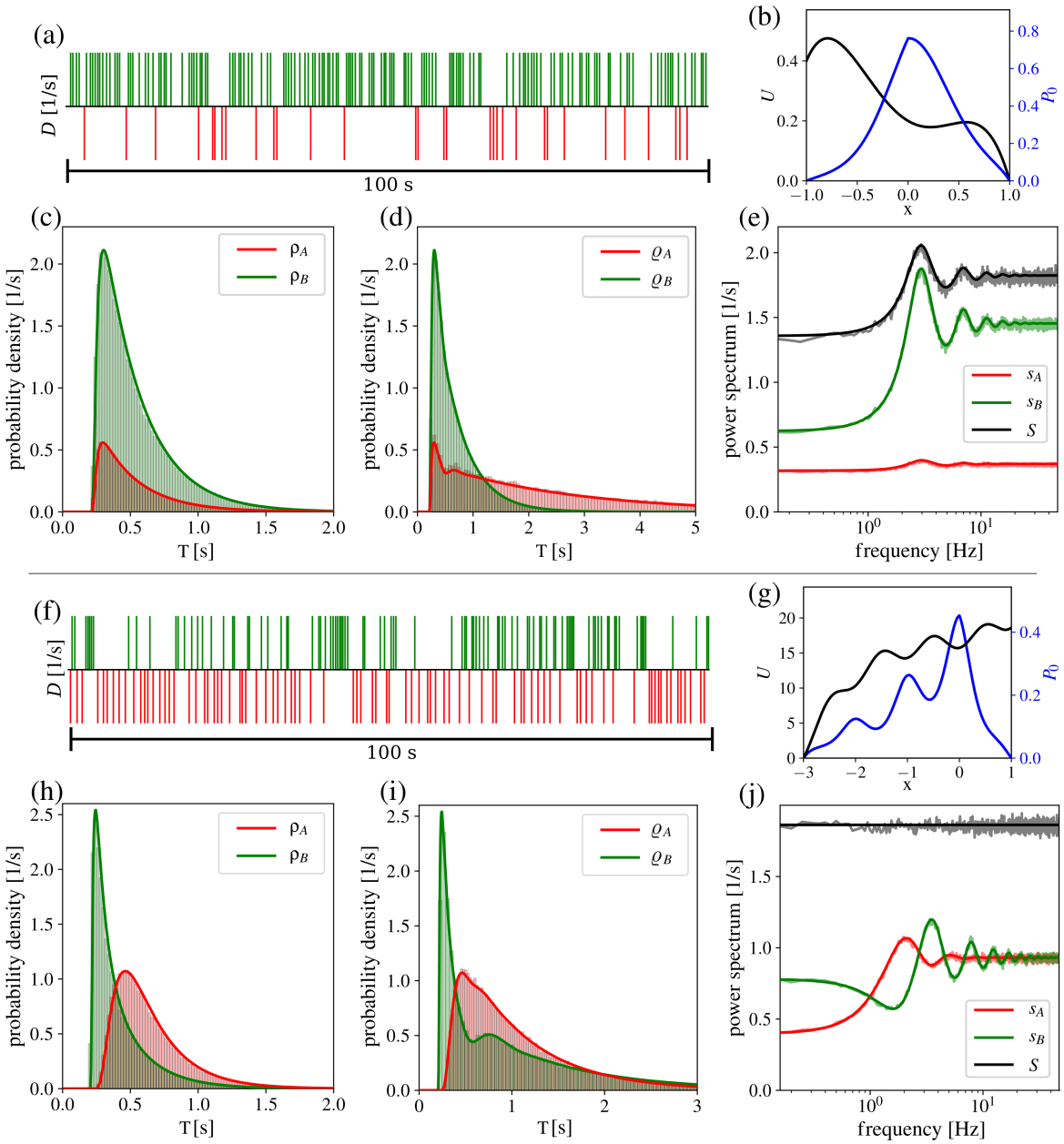

Figure 4.5.: Statistics of nonlinear DDMs. Example one with symmetric thresholds and a polynomial as potential (a-j) and example two with asymmetric potential and boundaries but equal decision rates (f-j). Combined decision trains with red A and green B decisions (panel a,f); potential $U(x)$ (black) and stationary solution $P_0(x)$ (blue) (b,g); reaction-time densities from latest reset (c,h) and interdecision interval distributions of individual decision trains (d,i) from direct simulations (histograms) and threshold-integration method (straight lines); spectra of individual (colored) and combined (black) decision trains (e,j) from simulation (jagged bright lines) and threshold-integration method (solid lines). See Tab. C.9 for parameters.

4.3.3 Linear response to modulation of input

Decision-making experiments can also be performed with a time-dependent signal. For instance, the direction or the ratio of coherently moving dots may be modulated in time in a visual motion-discrimination task. For such a situation, the threshold-integration method can be used to calculate the linear response to a temporal modulation of a parameter as presented by Richardson (2007). Here I assume a weak modulation of a parameter α of the DDM that is either part of the function $f(x)$ or σ with a small amplitude ε:

$$\alpha(t) = \alpha_0 + \varepsilon \cos(\omega t). \tag{4.58}$$

The Ansatz of the linear expansion of probability density and current reads:

$$P(x,t) \approx P_0(x) + \varepsilon P_1(x,\omega) e^{i\omega t}, \qquad J(x,t) \approx J_0(x) + \varepsilon J_1(x,\omega) e^{i\omega t}, \tag{4.59}$$

in which $P_1(x,\omega)$ and $J_1(x,\omega)$ denote the Fourier-transformed linear response functions, the susceptibilities, of the probability density and current, respectively. As the probability density $P(x,t)$ and current $J(x,t)$, also the susceptibilities are only nonzero in between the thresholds and $P_1(x,\omega)$ obeys absorbing boundary conditions at the thresholds ($P_1(x_A,\omega) = P_1(x_B,\omega) = 0$). Also the modulations of the decision rates are described in linear order by the complex susceptibilities $\tilde{r}_A(\omega)$ and $\tilde{r}_B(\omega)$:

$$r_A(t) = -J(x_A,t) = r_{A,0} + \varepsilon \tilde{r}_A(\omega) e^{i\omega t}, \qquad r_B(t) = J(x_B,t) = r_{B,0} + \varepsilon \tilde{r}_B(\omega) e^{i\omega t}. \tag{4.60}$$

The amplitudes of the rate modulations are given by the absolute value of the susceptibilities $|\tilde{r}_A(\omega)|$ and $|\tilde{r}_B(\omega)|$ and the phases by $\Phi(\tilde{r}_A) = \arctan[\mathrm{Im}(\tilde{r}_A)/\mathrm{Re}(\tilde{r}_A)]$ and $\Phi(\tilde{r}_B) = \arctan[\mathrm{Im}(\tilde{r}_B)/\mathrm{Re}(\tilde{r}_B)]$. If the modulated parameter is either part of the function $f(x)$ or σ, the linear response terms for probability density and current are given by [see (Richardson, 2008)]:

$$\begin{aligned} \partial_x J_1 =& i\omega P_1 + (\tilde{r}_A + \tilde{r}_B) e^{i\omega\Delta} \delta(x - x_\mathrm{s}) - \tilde{r}_A \delta(x - x_A) - \tilde{r}_B \delta(x - x_B), \\ \partial_x P_1 =& -\frac{1}{\sigma^2} \left(\tau_x J_1 - f P_1 - \partial_\alpha (f - \sigma^2 \partial_x) \Big|_{\alpha=\alpha_0} P_0 \right). \end{aligned} \tag{4.61}$$

In order to determine the solution, probability density and current are split into three terms:

$$J_1 = \tilde{r}_A \tilde{\jmath}_A + \tilde{r}_B \tilde{\jmath}_B + \tilde{\jmath}_\varepsilon, \quad P_1 = \tilde{r}_A \tilde{p}_A + \tilde{r}_B \tilde{p}_B + \tilde{p}_\varepsilon, \tag{4.62}$$

in which the densities and currents $\tilde{p}_A, \tilde{\jmath}_A$ and $\tilde{p}_B, \tilde{\jmath}_B$ are nonzero only in the intervals $[x_A, x_\mathrm{s}]$ and $(x_\mathrm{s}, x_B]$, respectively. Each of these two parts considers the absorption of probability at the corresponding threshold such that they obey the two ordinary differential in Eq. (4.46) here repeated for the convenience of the reader:

$$\begin{aligned} \partial_x \tilde{\jmath}_A &= i\omega \tilde{p}_A - \delta(x - x_A), \quad \partial_x \tilde{p}_A = -\frac{1}{\sigma^2} (\tau_x \tilde{\jmath}_A - f(x) \tilde{p}_A), \\ \partial_x \tilde{\jmath}_B &= i\omega \tilde{p}_B - \delta(x - x_B), \quad \partial_x \tilde{p}_B = -\frac{1}{\sigma^2} (\tau_x \tilde{\jmath}_B - f(x) \tilde{p}_B). \end{aligned} \tag{4.63}$$

Due to the absorbing boundary conditions of P_1 and the choice in Eq. (4.62) the values at each threshold are known as:

$$-\tilde{\jmath}_A(x_A,\omega)=\tilde{\jmath}_B(x_B,\omega)=1 \qquad \text{and} \qquad \tilde{p}_A(x_A,\omega)=\tilde{p}_B(x_B,\omega)=0. \tag{4.64}$$

By numerical integration from the respective thresholds to the reset we obtain the values:

$$\tilde{p}_{A,s}=\tilde{p}_A(x_\mathrm{s},\omega),\quad \tilde{\jmath}_{A,s}=\tilde{\jmath}_A(x_\mathrm{s},\omega) \text{ and } \tilde{p}_{B,s}=\lim_{x\to x_\mathrm{s}}\tilde{p}_B(x,\omega),\quad \tilde{\jmath}_{B,s}=\lim_{x\to x_\mathrm{s}}\tilde{\jmath}_B(x,\omega). \tag{4.65}$$

Here I use the limes because exactly at the reset $\tilde{p}_B(x_\mathrm{s},\omega)=\tilde{\jmath}_B(x_\mathrm{s},\omega)$ has to be zero, otherwise Eq. (4.62) is not valid at the reset. In the numerical practice, however, the values can be determined from integration until the exact reset. The remaining functions in Eq. (4.62) $\tilde{\jmath}_\varepsilon(x,\omega)$ and $\tilde{p}_\varepsilon(x,\omega)$ incorporate the linear response term with the derivative in α and the stationary density $P_0(x)$ by the ordinary differential equations:

$$\begin{aligned}\partial_x\tilde{\jmath}_\varepsilon =& i\omega\tilde{p}_\varepsilon+\lambda_{\jmath,\varepsilon}\delta(x-x_\mathrm{s}),\\ \partial_x\tilde{p}_\varepsilon =& -\frac{1}{\sigma^2}\left(\tau_x\tilde{\jmath}_\varepsilon-f\tilde{p}_\varepsilon-\partial_\alpha(f-\sigma^2\partial_x)\Big|_{\alpha=\alpha_0}P_0\right)+\lambda_{p,\varepsilon}\delta(x-x_\mathrm{s}).\end{aligned} \tag{4.66}$$

Note that the probability density $\tilde{p}_\varepsilon$ is not continuous but is characterized by a jump at the reset as indicated by the δ-function. Only the sum of the three parts of the probability density in Eq. (4.62) is continuous. The jump heights $\lambda_{\jmath,\varepsilon}$ and $\lambda_{p,\varepsilon}$ are important values since they have to be compensated in order to fulfill continuity and jump condition of P_1 and J_1 at the reset. For their determination, we remind ourselves that the efflux of the probability P_1 is already considered in the other two parts in Eq. (4.62) such not only the probability density $\tilde{p}_\varepsilon$ but also the current $\tilde{\jmath}_\varepsilon$ vanishes at the thresholds:

$$\tilde{\jmath}_\varepsilon(x_A,\omega)=\tilde{\jmath}_\varepsilon(x_B,\omega)=\tilde{p}_\varepsilon(x_A,\omega)=\tilde{p}_\varepsilon(x_A,\omega)=0. \tag{4.67}$$

With these values, Eq. (4.66) can be integrated numerically from both thresholds to the reset. The results yield us the jump heights as:

$$\lambda_{p,\varepsilon}=\lim_{\substack{x\to x_\mathrm{s}\\ x>x_\mathrm{s}}}\tilde{p}_\varepsilon(x,\omega)-\lim_{\substack{x\to x_\mathrm{s}\\ x<x_\mathrm{s}}}\tilde{p}_\varepsilon(x,\omega) \quad \text{and} \quad \lambda_{\jmath,\varepsilon}=\lim_{\substack{x\to x_\mathrm{s}\\ x>x_\mathrm{s}}}\tilde{\jmath}_\varepsilon(x,\omega)-\lim_{\substack{x\to x_\mathrm{s}\\ x<x_\mathrm{s}}}\tilde{\jmath}_\varepsilon(x,\omega). \tag{4.68}$$

Going back to Eq. (4.62), the determined values determine the susceptibilities of the decision rates by the continuity of P_1 and jump of J_1 at the threshold as:

$$\tilde{r}_B\tilde{p}_{B,s}-\tilde{r}_A\tilde{p}_{A,s}+\lambda_{p,\varepsilon}=0,\quad \tilde{r}_B\tilde{\jmath}_{B,s}-\tilde{r}_A\tilde{\jmath}_{A,s}+\lambda_{\jmath,\varepsilon}+(\tilde{r}_A=\tilde{r}_B)e^{i\omega\Delta}, \tag{4.69}$$

that can be reformulated to the final result:

$$\boxed{\tilde{r}_A=\frac{\lambda_{p,\varepsilon}(\tilde{\jmath}_{B,s}-e^{i\omega\Delta})-\lambda_{\jmath,\varepsilon}\tilde{p}_{B,s}}{\tilde{p}_{A,s}(\tilde{\jmath}_{B,s}-e^{i\omega\Delta})-\tilde{p}_{B,s}(\tilde{\jmath}_{A,s}+e^{i\omega\Delta})},\quad \tilde{r}_B=\frac{\tilde{r}_A\tilde{p}_{A,s}-\lambda_{p,\varepsilon}}{\tilde{p}_B(x_\mathrm{s})}.} \tag{4.70}$$

As one example, the susceptibilities of the decision rates are calculated for a weak sinusoidal

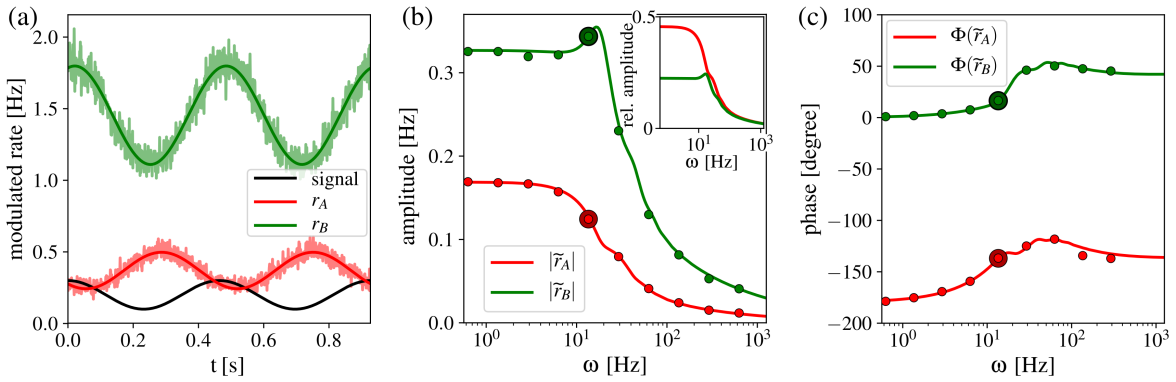

Figure 4.6.: Linear response of symmetric nonlinear DDM with polynomial potential to a weak cosinusoidal modulation of drift. Two periods of the modulated drift (black line without unit) from Eq. (4.71) with $\varepsilon = 0.1$ and $\omega = 13.54\,\mathrm{Hz}$, corresponding modulated decision rates (jagged lines in red for A and B decisions in red and green, respectively) and results from the linear response calculation (smooth solid lines) are shown in (a). Amplitude (in inset relative to stationary rates) (b) and phase (c) of the decision rate responses in dependence on the frequency of the drift modulation. Dots are determined by numerical simulations and lines by the threshold-integration method. Marked points belong to the frequency in panel (a).

modulation of the drift for the DDM used in example one of Fig. 4.5(a-e) [see Tab. C.2 for parameters]. The corresponding Langevin equation is given by:

$$\tau_x \dot{x} = f(x) + \varepsilon\cos(\omega t) + \sigma\sqrt{2\tau_x}\xi(t) \qquad (\text{here } f(x) = 2x^3 - x + 0.2). \tag{4.71}$$

The modulation amplitude is $\varepsilon = 0.1$. In this example, the second equation in Eq. (4.61) reads:

$$\partial_x P_1 = -\frac{1}{\sigma^2}(\tau_x J_1 - f(x)P_1 - P_0). \tag{4.72}$$

The results of the linear response calculation are presented and compared to results of direct simulations of Eq. (4.71) in Fig. 4.6. Here the modulated drift term and the resulting modulations of incorrect and correct decision rates are shown Fig. 4.6 in black, red and green, respectively. Here the angular frequency of the modulation is $\omega = 13.54\,\mathrm{Hz}$. For the calculation of the smooth lines, the susceptibilities resulting from Eq. (4.70) are used. The pale jagged lines are determined by averages over a finite ensemble of decision trains that result from simulations of Eq. (4.71) in which δ-spikes are approximated as rectangular pulses with small but finite size. In this example the linear response theory provides an adequate prediction of the decision-rate responses.

The amplitude and phase of the rate modulations as a function of ω are presented in Fig. 4.6b and c, respectively. The solid lines represent the results from the threshold-integration method, again in red for A and green for B decisions. The dots are calculated from numerical simulations as follows: firstly, the modulated rates are estimated by an ensemble average for two periods of the modulation as shown in (a), secondly, the amplitude and phase of the response are determined as the absolute value and the argument of the Fourier-

transformed noisy rate modulations at the frequency of the input modulations. For all considered frequencies, the theory is capable to adequately predict amplitudes and phases of the rate responses. The amplitude of the rate modulation for A decisions decreases monotonously. For B decisions, the modulation amplitude reaches its maximum at $\omega = 16\,\mathrm{Hz} \approx 2\pi r_{A,0}$ and decreases afterwards. The absolute modulation for B decisions, that are also preferred in the unperturbed case, is higher than for A decisions for the entire frequency range. In contrast, the modulation relative to the stationary decision rate is higher for A decisions as shown in the inset of Fig. 4.6b. The positive half cycle of the drift increases the evidence towards B decisions whereas the negative half cycle pushes towards A decisions. Consequentially, for slow modulations with a small ω, the phase for B decisions is only slightly higher than $0°$ while the response of A decisions is shifted by -180°. For a faster modulation, both phases increase.

4.4 Summary and discussion

Inspired by the insightful modeling of neural spike trains, the decision trains have been introduced that describe sequences of binary decisions by trains of positive and negative pulses at the absolute decision times that encode correct and incorrect decisions, respectively. For the simplest case of a renewal process characterized by uncorrelated decisions and no transient dynamics, the statistics of the stationary decision trains are fully described by the reaction-time densities. The stationary decision rates, the interdecision-interval distributions of the individual decision trains and the power spectra of individual and combined decision trains are determined by the analytical formulas in Eqs. (4.5; 4.6; 4.10). The derived relations in Eqs. (4.6) and (4.10) might be applied to prove the renewal character of a given decision train. Surprisingly, the spectrum of the combined train in Eq. (4.12) is flat if both decisions occur equally likely, independent of the shape of the individual power spectra. One may argue that decision trains are not an appropriate description if decisions are made as a renewal process since all information is already presented in the reaction-time densities. However, decision trains capture possible correlations between decisions and transient dynamics that are neglected in the usual approach which only focuses on single reaction times. Thus, the approach becomes much more relevant for experimental data or models in which the renewal approach is not valid, since the decision-train power spectra may reveal hidden features of the underlying dynamics in this case. The determination and explanation of deviations from the derived equations for decision trains from more complex decision models and, particularly, from experiments are worthwhile tasks for future studies.

The decision-train statistics have been calculated for a general DDM with constant non-decision time. Decision trains generated by this model class are by definition renewal processes. Explicit formulas for the decision-train statistics in the Fourier domain have been derived in Eqs. (4.32) and (4.33) for the simplest version of DDMs that is analytically tractable, the original model introduced by Ratcliff (1978) with a constant non-decision time. Note that the stationary decision rates and the reaction-time densities in the time domain have already been calculated in the paper of Ratcliff (1978). For DDMs with nonlinear subthreshold dynamics that arise for instance by a reduction of biophysical decision models [see Wang (2002);

Wong and Wang (2006); Roxin and Ledberg (2008)] or the incorporation of changing environments in Veliz-Cuba et al. (2016), no analytical solution is known. In order to compute their statistics, Richardson's threshold-integration method has been extended. The numerical procedure can easily be applied and it provides the calculation of the above mentioned statistics within a few seconds if implemented on a standard personal computer. Due to the efficiency of the procedure, it might be used to fit nonlinear models to experimental data and possibly verify or falsify theoretical predictions. Most revealing would be a procedure that determines the subthreshold dynamics for given decision trains. This inverse problem is challenging to solve, but the threshold-integration method might be a first step in an approach.

The model considered in this chapter was kept simple. Neither the recommendation of Green et al. (1983) to apply breaks with random duration between experimental trials nor other trial-to-trial variability of experimental parameters were incorporated. One possibility to apply the theory to experiments with distributed breaks would be to simply subtract the duration from each reaction time such that the decision train does not reflect the physical time anymore. However, due to such cutouts, correlations of the reaction times are distorted. The preferable way would be to extend the theory to models with trial-to-trial variability.

The last part of the chapter presented how the linear response of a DDM with a time-dependent input can be calculated by the threshold-integration method. It was shown by Vilela and Lindner (2009) that IF neurons with different subthreshold nonlinearities may have very similar stationary statistics but are clearly distinguished by their response properties. This observation might be applicable to nonlinearities in DDMs as could be shown by the threshold-integration method. If this is the case, the comparison of theoretically predicted susceptibilities with measurements might be a better way to verify or falsify models than the comparison of the stationary statistics. A corresponding experiment for binary decision making might be realized by a visual motion-discrimination task in which either the ratio of the dots with coherent motion or the coherent motion direction is modulated.

One of the underlying assumptions of the introduced DDM is that fluctuations of perceived evidence can be represented as temporally uncorrelated Gaussian noise. However, the distraction noise, i.e. perceived evidence that does not belong to the signal, may be temporally correlated. Furthermore, the intrinsic noise involved in spiking neural networks that perform the decision-making process is always characterized by temporal correlations (Bair et al., 1994; Brunel, 2000; Dummer et al., 2014; Pena et al., 2018). Temporally correlated fluctuations, also called colored noise, can be incorporated into models by a Markovian embedding that yields a multidimensional model as discussed in chapters two and three for IF neurons. Furthermore, additional dimensions can provide the model with other properties that yield qualitatively different decision-train statistics. The generalization of the method presented in chapter two might be feasible for the calculation of temporal statistics of the resulting decision trains from multidimensional DDMs.

5 Summary and conclusion

In this thesis, methods have been developed to determine the temporal correlations of point processes generated by different stochastic systems, namely, stochastic multidimensional integrate-and-fire neurons, networks of leaky integrate-and-fire neurons and linear and non-linear diffusion-decision models by means of the corresponding Fokker-Planck equation. The derived equations might serve as the basis of analytical investigations and/or be applicable to study neural behavior.

The main result of the second chapter was given by the set of equations (2.49) the solution of which determines firing rate, probability density and the spike-train power spectrum of a general, stochastic, multidimensional integrate-and-fire neuron. The presented approach is the generalization of the work of Schwalger et al. (2015) in which the spike-train statistics and also the power spectrum are calculated for a perfect integrate-and-fire neuron with strong mean input and weak colored noise generated by a multidimensional Ornstein-Uhlenbeck process. By approximations, the derived equations might become the basis of analytical studies for other special cases of IF neurons. As illustrated by the many examples in this chapter resulting from the numerical solution of the theory, the spike-train power spectra may indicate underlying neural dynamics. However, the interpretation of experimentally observed power spectra remains a challenging task and conclusions on them can only be made with some caution. A surprising finding was that new maxima and minima may emerge in the spike-train power spectra due to colored input noise with monotonously increasing and decreasing spectra, respectively, without any obvious oscillatory mechanism, but only due to the lack and the excess of input power at low frequencies. The numerical techniques that have been used to determine the equations' solutions are quite inefficient for models with a higher dimensionality than two. For higher-dimensional models, other methods might be better suited and applicable to gain insights in their spiking behavior. This would allow one to study also the influence of the combination of different features on the spike-train power spectra.

Highlight of this work was the mean-field theory for large and sparsely connected networks of spiking neurons that considers the temporal correlations of spike trains by approximating neural input by Gaussian colored noise and assuming self-consistency of input and power spectrum presented in Eq. (3.23). The approach was an extension of the theory from Brunel (2000) that approximated neural input as white noise and assumed self-consistency only for the firing rates. Furthermore, it was complementary to the theory developed by van Meegen and Lindner (2018) in which the self-consistent temporal correlations are calculated in the

limit of a strong mean input. As demonstrated for one example, approximate solutions of the theory are capable to describe the self-consistent spike-train power spectra observed in network simulations. The development of the theory was merely one small step towards a full understanding of the temporal correlations in the complex dynamics of neural networks by means of analytical insights. Further analysis of the theory's solution regarding its existence, stability and uniqueness could reveal or exclude novel dynamical regimes. However, the detailed analysis is a challenging objective for future investigations and might require the development of new mathematical techniques. The theory was only developed for homogeneous networks in which all neurons obey equal dynamics and connection properties. Furthermore, only simplified synaptic dynamics were considered in the network model. Apparently, this network model could only represent a rough approximation of biological networks that serve a purpose in the brain. The self-consistency of the temporal correlations of spike trains of slightly more realistic heterogeneous networks has been studied in the second part of the third chapter by means of the extension of the iterative scheme developed by Dummer et al. (2014). The heterogeneity of neural properties, namely binomially distributed numbers of presynaptic connections and, additionally, exponentially distributed synaptic weights yielded broad distributions of firing rates and a variety of spike-train power spectra in the networks. It was possible to capture the distributions of spike-train power spectra by a relatively small number of neurons in the developed iterative scheme.

In the fourth chapter, the decision trains were introduced that could describe experimentally measured sequences of binary decisions, for instance, the results of an experiment similar to the one performed by Roitman and Shadlen (2002). This approach would take into account possible correlations of decision times and transient dynamics that are neglected if only single decision times are considered. The statistics of measured decision trains could reveal underlying dynamics of the decision making process's implementation in neural networks. Analytical formulas have been derived that connect the statistics of the decision train for independent decision times and stationary decision trains. Unexpectedly, the decision-train power spectrum for correct and incorrect decisions is always flat if the decision rates are equal, independent on the shape of the individual spectra. However, in this case the decision trains do not contain more information and are not beneficial to the single decision times. Moreover, methods based on the Fokker-Planck equation have been developed to calculate the statistics of the decision trains generated by diffusion-decision models. For one version, a Wiener process within two boundaries, analytical formulas for the decision train statistics have been derived. To efficiently determine the decision-train statistics and the susceptibility of the decision rates of nonlinear diffusion-decision models that have been proposed by Roxin and Ledberg (2008), the threshold-integration method was generalized that has been developed by Richardson (2007, 2008) for nonlinear integrate-and-fire neurons. The method could be used to study the influence of nonlinear dynamics on the decision-train statistics by a comparison to the analytical results. It might also be applicable to fit experimental data in order to falsify or verify theoretical predictions on the underlying non-linearities that arise due to the implementation of the decision making process in neural networks with nonlinear dynamics.

A | Spike-train power spectra of multidimensional integrate-and-fire neurons

A.1 Additional condition for Fourier transformed probability density $\tilde{Q}$ for $\omega \to 0$ and $\omega = 0$

Since the left hand side in the first equation Eq. (2.31) is invariant under the transformation $\tilde{Q}'(v,a,0) = \tilde{Q}(v,a,0) + \alpha P_0(v,a)$ $[(\hat{\mathcal{L}}+\hat{\mathcal{R}})\tilde{Q}(v,a,0) = (\hat{\mathcal{L}}+\hat{\mathcal{R}})(\tilde{Q}(v,a,0)+\alpha P_0)]$, an additional condition is required to uniquely determine the Fourier transformed probability density $\tilde{Q}$ at $\omega = 0$ for the calculation of the power spectra in Eq. (2.32). For its derivation, we consider the normalization of the probability densities in time domain in Eq. (2.21):

$$\int_{-\infty}^{v_{\mathrm{th}}} dv \int_{-\infty}^{\infty} da\, P(v,a,t) = 1 - \int_{t-\tau_{\mathrm{ref}}}^{t} d\tau\, r(\tau). \tag{A.1}$$

For the Fourier transformed probability density $\tilde{Q}(v,a,\omega)$ this condition yields:

$$\begin{aligned}
\int_{-\infty}^{v_{\mathrm{th}}} dv \int_{-\infty}^{\infty} da\, \tilde{Q}(v,a,\omega) &= \int_{0}^{\infty} dt\, e^{i\omega t} \int_{-\infty}^{v_{\mathrm{th}}} dv \int_{-\infty}^{\infty} da\, (P(v,a,t) - P_0) \\
&= \int_{0}^{\infty} dt\, e^{i\omega t} \left[\Theta(t-\tau_{\mathrm{ref}}) \left(1 - \int_{t-\tau_{\mathrm{ref}}}^{t} dt'\, m(t') \right) - \left(1 - \int_{t-\tau_{\mathrm{ref}}}^{t} dt'\, r_0 \right) \right] \\
&= -\int_{\tau_{\mathrm{ref}}}^{\infty} dt\, e^{i\omega t} \int_{t-\tau_{\mathrm{ref}}}^{t} dt'\, [m(t') - r_0] + \int_{0}^{\tau_{\mathrm{ref}}} dt\, e^{i\omega t} (r_0 \tau_{\mathrm{ref}} - 1) \\
&= \frac{(r_0\tau_{\mathrm{ref}} - 1)(e^{i\omega\tau_{\mathrm{ref}}} - 1)}{i\omega} \\
&\quad \underbrace{-\int_{\tau_{\mathrm{ref}}}^{\infty} \partial_t \left(\frac{e^{i\omega t}}{i\omega} \int_{t-\tau_{\mathrm{ref}}}^{t} (m(t') - r_0)\, dt' \right) dt}_{\mathrm{I}} + \underbrace{\int_{\tau_{\mathrm{ref}}}^{\infty} \frac{e^{i\omega t}}{i\omega} [(m(t) - r_0) - (m(t-\tau_{\mathrm{ref}}) - r_0)]\, dt}_{\mathrm{II}}.
\end{aligned} \tag{A.2}$$

Here the two terms (I) and (II) arise due to integration by parts in the last step. The Heaviside function $\Theta(t-\tau_{\mathrm{ref}})$ in the second line reflects the insertion of all probability at $t=\tau_{\mathrm{ref}}$. For term (I) we obtain:

$$\mathrm{I} = -\lim_{t\to\infty}\frac{e^{i\omega t}}{i\omega}\int_{t-\tau_{\mathrm{ref}}}^{t}\underbrace{(m(t')-r_0)}_{=0 \text{ for } t'\to\infty}dt' + \frac{e^{i\omega\tau_{\mathrm{ref}}}}{i\omega}\int_{0}^{\tau_{\mathrm{ref}}}\underbrace{(m(t')-r_0)}_{=-r_0 \text{ for } t'\leq\tau_{\mathrm{ref}}}dt' = -\frac{e^{i\omega\tau_{\mathrm{ref}}}}{i\omega}r_0\tau_{\mathrm{ref}} \tag{A.3}$$

by the insertion of the integration limits ∞ and τ_{ref}. For term (II) we obtain:

$$\begin{aligned}\mathrm{II} &= \frac{1}{i\omega}\left(\int_0^\infty e^{i\omega t}(m(t)-r_0)\,dt + \int_0^{\tau_{\mathrm{ref}}} e^{i\omega t}r_0\,dt - e^{i\omega\tau_{\mathrm{ref}}}\int_0^\infty e^{i\omega t}(m(t)-r_0)\,dt)\right)\\ &= \frac{1}{i\omega}\left((1-e^{i\omega\tau_{\mathrm{ref}}})\tilde{m}(\omega) + \int_0^{\tau_{\mathrm{ref}}} e^{i\omega t}r_0\,dt\right) = \frac{\left(\tilde{m}(\omega)-\frac{r_0}{i\omega}\right)\left(1-e^{i\omega\tau_{\mathrm{ref}}}\right)}{i\omega}.\end{aligned} \tag{A.4}$$

In the first term it is exploited that $m(t)=0$ for $0<t<\tau_{\mathrm{ref}}$ and in the second term the time variable is shifted by τ_{ref}. The whole normalization term is given by:

$$\frac{1}{i\omega}\left[\left(1-e^{i\omega\tau_{\mathrm{ref}}}\right)\left(\tilde{m}(\omega)-\frac{r_0}{i\omega}+1\right)-r_0\tau_{\mathrm{ref}}\right] \xrightarrow{\omega\to 0} \tau_{\mathrm{ref}}\left(\frac{\tau_{\mathrm{ref}}r_0}{2}-1-\tilde{m}(0)\right). \tag{A.5}$$

The limes can be identified by the Taylor expansion to second order at $\omega=0$:

$$1-e^{i\omega\tau_{\mathrm{ref}}} \approx -i\omega\tau_{\mathrm{ref}} + \frac{\omega^2\tau_{\mathrm{ref}}^2}{2} + \mathcal{O}(\omega^3). \tag{A.6}$$

The normalization can written be as:

$$\lim_{\omega\to 0}\int_{-\infty}^{v_{th}}dv\int_{-\infty}^{\infty}da\left(\frac{1}{\tau_{\mathrm{ref}}}+\hat{\mathcal{R}}\right)\tilde{Q}(v,a,\omega) = \frac{\tau_{\mathrm{ref}}r_0}{2}-1. \tag{A.7}$$

If any solution $\tilde{Q}'$ is known for the partial differential equation in Eq. (2.31), we may find the one that fulfills the normalization by inserting $\tilde{Q}=\tilde{Q}'+\alpha P_0$:

$$\begin{aligned}\lim_{\omega\to 0}\int_{-\infty}^{v_{th}}dv\int_{-\infty}^{\infty}da\left(\frac{1}{\tau_{\mathrm{ref}}}+\hat{\mathcal{R}}\right)(\tilde{Q}'+\alpha P_0) &= \lim_{\omega\to 0}\int_{-\infty}^{v_{th}}dv\int_{-\infty}^{\infty}da\left(\frac{1}{\tau_{\mathrm{ref}}}+\hat{\mathcal{R}}\right)\tilde{Q}' + \frac{\alpha}{\tau_{\mathrm{ref}}} = \frac{\tau_{\mathrm{ref}}r_0}{2}-1\\ &\Leftrightarrow \alpha = \tau_{\mathrm{ref}}\left(\frac{\tau_{\mathrm{ref}}r_0}{2}-1\right) - \int_{-\infty}^{v_{th}}dv\int_{-\infty}^{\infty}da\left(1+\tau_{\mathrm{ref}}\hat{\mathcal{R}}\right)\tilde{Q}'.\end{aligned} \tag{A.8}$$

The analogous calculation for the multidimensional neuron models in Eq. (2.49) only yields an exchange of the argument $a\to\vec{a}$, moreover, the integration has to be performed over the entire manifold $M_{\vec{a}}$ instead only over a.

It turns out that the numerical solutions of Eq. (2.32) and Eq. (2.49) are influenced by the ambiguity of $\tilde{Q}'$ already at small but finite frequencies. As presented by the circles in Fig. A.1, this artifact yields a steep rise of the naively calculated power spectra at low frequencies because the calculated probability densities do not fulfill the normalization in Eq. (A.5) at low frequencies. The increase of the resolution by a higher N (see Sec. (A.2)) and the related improvement of the numerical approximation reduces the error at finite frequencies but also increases its amplitude at $\omega = 0$. In order to reduce the error also at low frequencies, the normalization condition is already used at finite frequencies up to $\omega/(2/\pi) > 1\,\mathrm{Hz}$. We proceed as follows: a solution $\tilde{Q}'$ is determined as the solution of the partial differential for finite $\omega \neq 0$, then we assume that the normalization for $\omega = 0$ holds approximately true and calculate $\tilde{Q} = \tilde{Q}' + \alpha P_0$ with α in Eq. (A.8). As shown by the crosses in Fig. A.1, this application strongly reduces the error even if a small N is used.

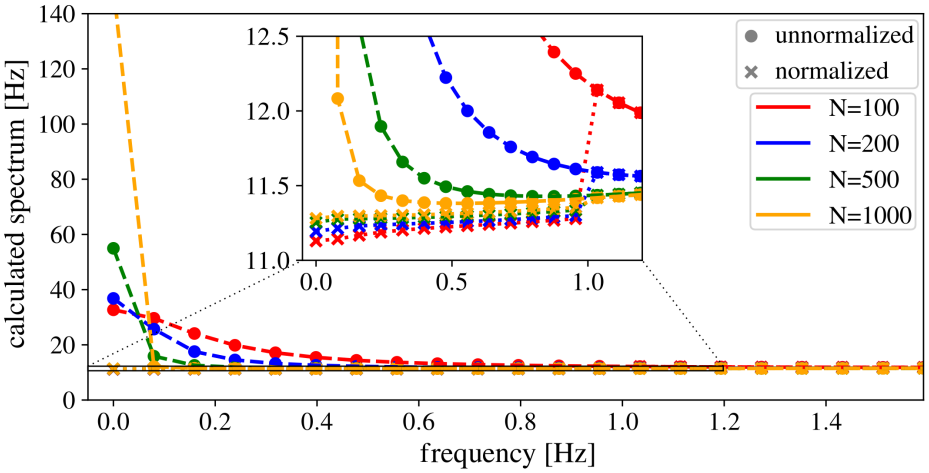

Figure A.1.: Numerical artifact at low frequencies and effect of normalization. Naive solutions of Eqs. (A.28) and (A.31) (circles) and solutions with applied normalization condition (crosses) for an increasing number of discretization points N. The used model is introduced in Sec. (2.1.3). Parameters are presented in Sec. (C.1).

A.2 Numerical solution of the theory of spike-train power spectra for two-dimensional integrate-and-fire neurons

The general analytical solution for the partial differential equation that determines the spike-train power spectrum in Eq. (2.32) is not known and has to be determined numerically in this work. Here the numerical standard procedure *finite differences* is applied (see Press et al. (2007) for general description of the method). In the following, the application of the method is explained in detail.

A.2.1 Discretization and boundary conditions

The phase space v, a is discretized by N steps:

$$\begin{aligned} v &\to v_i = v_0 + i\Delta v \\ a &\to a_j = a_0 + j\Delta a \end{aligned} \tag{A.9}$$

with $i, j \in [0, 1, \ldots, N-1]$. The last considered element of the v-space is arranged right in front of the threshold $v_{N-1} = v_0 + (N-1)\Delta v = v_{\mathrm{th}} - \Delta v$. The values of $P_0(v_i, a_j)$ and $\tilde{Q}(v_i, a_j, \omega)$ at the discretized points are regarded as vectors $\vec{P}_0$, $\vec{\tilde{Q}}(\omega)$:

$$P_{0\ i+jN} = P_0(v_i, a_j), \qquad \tilde{Q}_{i+jN}(\omega) = \tilde{Q}(v_i, a_j, \omega) \tag{A.10}$$

(see Fig. A.2a for the transformation into a vector). The probability density at the threshold is always zero such that $v_N = v_{\mathrm{th}}$ does not need to be considered explicitly. The range of the phase space is defined by the numerical values of v_0, a_0 and a_{N-1} (see all used values in Tab. C.1 for $d = 1$ and in Tab. C.3 for $d = 2$). It is chosen to contain almost all probability such that the increase of the range with equal bin size Δv and Δv only has a negligible effect on the results. The proper choice can be estimated in some cases, here it is also ensured by visual inspection of the resulting stationary density.

The number of discretization steps N has to be sufficiently large to obtain an adequate resolution, for which the effect of the further increase of N for a fixed phase space is negligibly small. One example of the influence of the resolution on the resulting power spectra is shown in Fig. A.3. In this example we see that a low number of discretization steps N yields an overestimation of the power spectrum at high frequencies. As a standard value $N = 1000$ steps are used (see Tab. C.1). However, the calculation of probability densities with a high curvature that may occur in the case of a strong mean input in combination with low noise or due to nonlinearities in the dynamics requires a higher resolution.

The discretized phase space is restricted and does not incorporate the natural boundary conditions for the auxiliary process and the negative membrane voltage. Instead, the boundary conditions are approximated by absorbing boundaries with sufficient distance to the main location of probability, that is ensured by the proper choice of v_0, a_0 and a_{N-1}.

With the help of the introduced discretization, the differential operators $\hat{\mathcal{L}}$ and $\hat{\mathcal{R}}$ in Eq. (2.32) are approximated by large and sparse matrices of dimension $N^2 \times N^2$ that act on the vectors $\vec{P}_0$ and $\vec{\tilde{Q}}(\omega)$.

A.2.2 Subthreshold dynamics

For a discretized variable $x_i = x_0 + i\Delta x$, the first and second derivatives of an arbitrary function $\theta(x_i)$ can be approximated by the symmetric *finite differences* (see Press et al. (2007)):

$$\partial_x \theta(x)|_{x=x_i} \approx \frac{\theta(x_{i+1}) - \theta(x_{i-1})}{2\Delta x}, \ \partial_x^2 \theta(x)|_{x=x_i} \approx \frac{\theta(x_{i+1}) - 2\theta(x_i) + \theta(x_{i-1})}{\Delta x^2}. \tag{A.11}$$

The operator that incorporates the subthreshold dynamics $\hat{\mathcal{L}}$ introduced in Eq. (2.13) is given by:

$$\hat{\mathcal{L}} = -\partial_v \frac{f(v,a)}{\tau_m} + \frac{\beta^2}{2\tau_m^2}\partial_v^2 - \partial_a \frac{g(v,a)}{\tau_a} + \frac{b_1^2+b_2^2}{2\tau_a^2}\partial_a^2 + \frac{\beta b_1}{\tau_m \tau_a}\partial_v \partial_a. \tag{A.12}$$

By the approximation of the first and second order derivatives by finite differences, a tridiagonal matrix given by the first and second derivatives in v with two additional secondary tridiagonals that arise from the derivatives in a and the mixed derivative in v and a is obtained for $\hat{\mathcal{L}}$ (cf. Fig. A.2b). The components of the matrix can be written as:

$$\begin{aligned}
\hat{\mathcal{L}}_{i+jN,m} = &-\left(\frac{\beta^2}{\tau_m^2\Delta v^2} + \frac{b_1^2+b_2^2}{\tau_a^2\Delta a^2}\right)\delta_{i+jN,m} \\
&+\left(\frac{\beta^2}{2\tau_m^2\Delta v^2} - \frac{f(v_{i+1},a_j)}{2\tau_m\Delta v}\right)\bar{\delta}_{i,N-1}\delta_{i+1+jN,m} + \left(\frac{\beta^2}{2\tau_m^2\Delta v^2} + \frac{f(v_{i-1},a_j)}{2\tau_m\Delta v}\right)\bar{\delta}_{i,0}\delta_{i-1+jN,m} \\
&+\left(\frac{b_1^2+b_2^2}{2\tau_a^2\Delta a^2} - \frac{g(v_i,a_{j+1})}{2\tau_a\Delta a}\right)\bar{\delta}_{j,N-1}\delta_{i+(j+1)N,m} + \left(\frac{b_1^2+b_2^2}{2\tau_a^2\Delta a^2} + \frac{g(v_i,a_{j-1})}{2\tau_a\Delta a}\right)\bar{\delta}_{j,0}\delta_{i+(j-1)N,m} \\
&+\frac{\beta b_1}{4\tau_m\tau_a\Delta v\Delta a}\times\Big[\bar{\delta}_{i,0}\left(\bar{\delta}_{j,0}\delta_{i-1+(j-1)N,m} - \bar{\delta}_{j,N-1}\delta_{i-1+(j+1)N,m}\right) \\
&\qquad + \bar{\delta}_{i,N-1}\left(\bar{\delta}_{j,N-1}\delta_{i+1+(j+1)N,m} - \bar{\delta}_{j,0}\delta_{i+1+(j-1)N,m}\right)\Big].
\end{aligned} \tag{A.13}$$

The '*anti*'-Kronecker symbols $\bar{\delta}_{k,m} = 1-\delta_{k,m}$ ensure that sequential components of the vector that do *not* represent neighboring elements of $P_0(v_i,a_j)$ or $\tilde{Q}(v_i,a_j)$ do not contribute to the derivatives in $\hat{\mathcal{L}}$ and cause the regularly missing components in the off-diagonal structures of $\hat{\mathcal{L}}$ in Fig. A.2b. In this notation, the operator incorporates the absorbing boundaries at a_{-1}, a_N, v_{-1} and v_N. The sparse matrix has only nine nonzero components in each row and even less if the corresponding element is located next to a boundary. In the special case of only independent Gaussian noise entering both equations ($b_1 = 0$), the last term vanishes and the numerical problem is easier to solve since the matrix has only five non-vanishing components per line.

A.2.3 Fire-and-reset operation

As introduced in Eq. (2.19), the fire-and-reset operator $\hat{\mathcal{R}}$ performs four different steps:

$$\hat{\mathcal{R}}\,\tilde{Q}(v,a,\omega) = -\delta(v-v_\mathrm{r})\int_{-\infty}^{\infty} da'\,\rho_\mathrm{ref}(a|a')\frac{\beta^2}{2\tau_m^2}\partial_v\tilde{Q}(v,a'-\delta_a,\omega)\Big|_{v=v_\mathrm{th}} \tag{A.14}$$

1. The operator measures the absorbed probability at the voltage threshold v_th.
2. If spike-triggered adaptation is applied ($\delta_a > 0$), the operator instantaneously shifts the probability along the a-axis.
3. The operator performs the evolution of the probability in the auxiliary variable during

the refractory period .

4. Finally, it reinserts the evolved probability at the reset voltage v_r.

Each of these steps is approximated by the multiplication with a matrix and the whole operator $\hat{\mathcal{R}}$ reads:

$$\hat{\mathcal{R}} = \hat{R}\hat{E}\hat{S}\hat{F}. \tag{A.15}$$

The probability current that crosses the threshold is given by the negative derivative in v at the threshold [J_v in Eq. (2.12)]. Due to the absorbing boundary at the threshold, the left-hand derivative is used that reads:

$$\partial_x \theta(x)|_{x=x_i} \approx \frac{\theta(x_i) - \theta(x_{i-1})}{\Delta x}. \tag{A.16}$$

Consequentially, the derivative of the probability density with respect to v at the threshold is given by its value at v_{N-1} divided by Δv since it is zero at the threshold. The non-vanishing components of the $N \times N^2$ dimensional matrix $\hat{F}$ that measures the efflux of probability are given by:

$$\hat{F}_{m,i+jN} = \frac{\beta^2}{2\tau_m^2 \Delta v}\delta_{m,j}\delta_{i,N-1} \tag{A.17}$$

The spike-triggered adaptation causes a shift of the probability along the a-axis by the constant amount δ_a. The numerical implementation considers that δ_a does not necessarily be the multiple of the bin size Δa by transferring the probability from one into two neighboring bins with distance $n_a = \delta_a/\Delta a - (\delta_a \bmod \Delta a)$ and $n_a + 1$, respectively. The probability from the m-th bin is transferred into the $(m + n_a)$-th and the $(m + n_a + 1)$-th bin with the fractions $1 - \kappa_a = 1 - (\delta_a \bmod \Delta a)$ and κ_a, respectively. The shift operator $\hat{S}_{m',m}$ is given by the $N \times N$ matrix:

$$\hat{S}_{m',m} = (1 - \kappa_a)\delta_{m'-n_a,m} + \kappa_a \delta_{m'-1-n_a,m}, \tag{A.18}$$

The probability that is shifted from outside ($-n_a < m < 0$) or out of the range of a ($m+n_a > N$) is not considered. By the proper choice of a_0 and a_{N-1}, the probability that is neglected in this manner is sufficiently small. A problem arises with the spike-triggered adaptation regarding the choice of a_0 and a_{N-1}. The maximum value of a depends on the time constant τ_a and the firing rate that is not known in the beginning. Hence, visual inspection of the solution is necessary to ensure that the error due to the choice of boundaries is low.

The numerical treatment of the evolution of the probability during the refractory period is different for qualitatively different dynamics of a. In the case of an Ornstein-Uhlenbeck process the propagation function $\rho_\mathrm{ref}(a|a')$ is known as shown in Eq. (2.18) and the operator is given by the $N \times N$ matrix:

$$\hat{E}_{m'',m'} = \rho_\mathrm{ref}(a_{m''}|a_{m'}) \qquad \text{(for } b_1 \neq 0 \text{ or } b_2 \neq 0\text{)}. \tag{A.19}$$

For nonlinear dynamics, the propagator function can be determined numerically by the solution of the reduced Fokker-Planck equation $\partial_t p(a,t) = \hat{\mathcal{L}}_\mathrm{ref}\, p(a,t)$ in which the differential operator only contains the drift and diffusion terms in a (cf. Eq. (2.13)).

A deterministic auxiliary process ($b_1 = b_2 = 0$) requires a different treatment. The probability that is located $a_{m'}$ at the beginning of the refractory period is relocated to $a_{\mathrm{det}}(\tau_{\mathrm{ref}}; a_{m'})$ at end of the refractory period. Here, $a_{\mathrm{det}}(\tau_{\mathrm{ref}}; a_{m'})$ denotes the solution of the ordinary differential equation $\tau_a \dot{a} = g(v_{\mathrm{ref}}, a)$ at time τ_{ref} with the initial condition $a(0) = a_{m'}$. For linear dynamics $g(v_{\mathrm{ref}}, a) = -a + G(v_{\mathrm{ref}})$, the solution is given by $a_{\mathrm{det}}(\tau_{\mathrm{ref}}; a_{m'}) = G(v_{\mathrm{ref}}) + (a_{m'} - G(v_{\mathrm{ref}}))e^{-\tau_{\mathrm{ref}}/\tau_a}$.

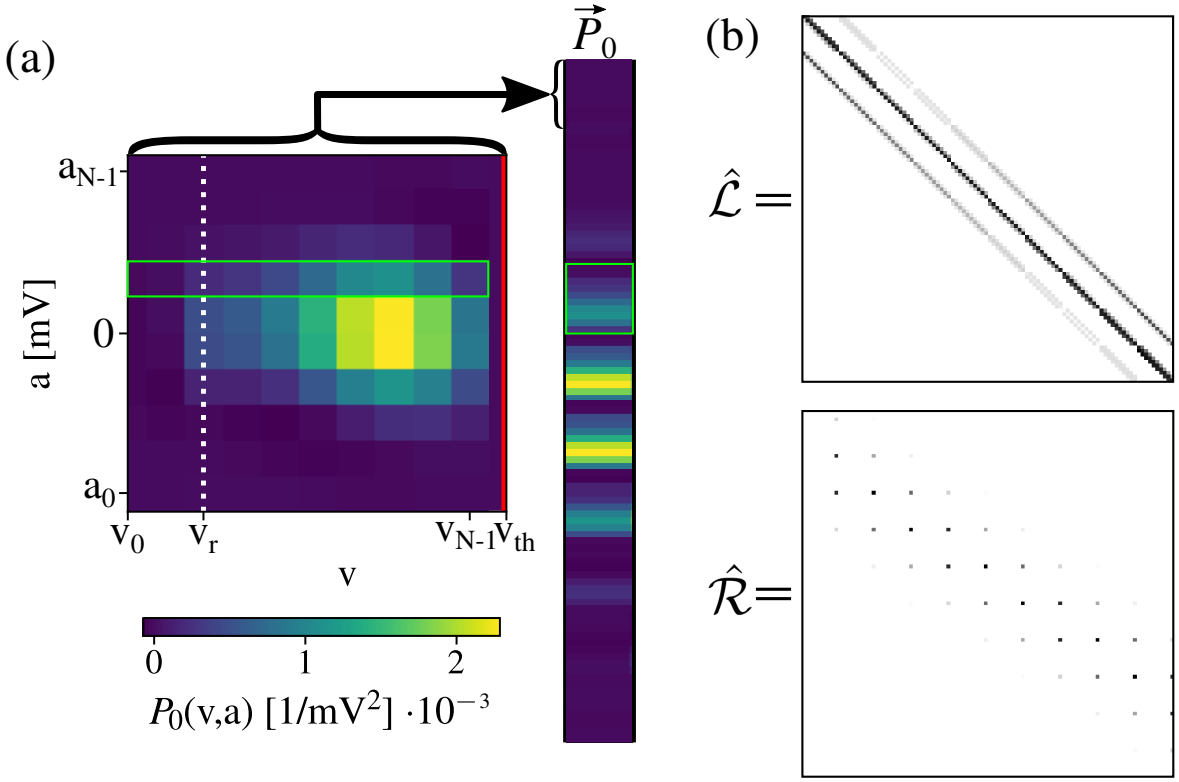

Figure A.2.: Discretization and finite-difference approximation of the operators. Panel a: approximation on the stationary density P_0 with very rough resolution ($N = 10$). Voltage threshold and reset are presented as solid red and dashed white lines, respectively. The components in the green window in $P_0(v, a)$ correspond to the components in the green window drawn in the vector $\vec{P}_0$. Through the low resolution the resulting vector $\vec{P}_0$ as the solution of Eq. (A.22) has negative values that turn positive by increasing N. Panel b: approximation of the linear operators $\hat{\mathcal{L}}$ and $\hat{\mathcal{R}}$ as large and sparse matrices. The greyscale encodes the absolute value of the components, where zero is white and black is the maximum. The nonzero elements of $\hat{\mathcal{L}}$ are located at the main tridiagonal and at two secondary tridiagonals. The structure of $\hat{\mathcal{R}}$ results from a finite refractory period.

Similar to the incorporation of the spike-triggered adaptation, it is important to take into account that $a_{\mathrm{det}}(\tau_{\mathrm{ref}}; a_{m'})$ may be located between two neighboring bins:

$$\begin{aligned} \hat{E}_{m'',m'} &= (1-\kappa^E_{m'})\delta_{m'',n^E_{m'}} + \kappa^E_{m'}\delta_{m'',n^E_{m'}+1} \quad (\text{for } b_1 = b_2 = 0), \\ \kappa^E_{m'} &= a_{\mathrm{det}}(\tau_{\mathrm{ref}}; a_{m'}) - (a_0 \bmod \Delta a), \\ n^E_{m'} &= \frac{a_{\mathrm{det}}(\tau_{\mathrm{ref}}; a_{m'}) - a_0}{\Delta a} - [a_{\mathrm{det}}(\tau_{\mathrm{ref}}; a_{m'}) - a_0 \bmod \Delta_a]. \end{aligned} \tag{A.20}$$

The last operator incorporates the reinsertion of probability by the approximation of the δ-function at the reset v_{r} that might be located between two neighboring bins as well. The transfer of probability is incorporated by the $N^2 \times N$ matrix with the components:

$$\begin{aligned} \hat{R}_{i'+j'N,m''} &= \frac{(1-\kappa_v)\delta_{i',n_{\mathrm{r}}} + \kappa_v \delta_{i',n_{\mathrm{r}}+1}}{\Delta v}\delta_{j',m''} \\ \kappa_v &= ((v_{\mathrm{r}} - v_0) \bmod \Delta v) \\ n_{\mathrm{r}} &= \frac{v_{\mathrm{r}} - v_0}{\Delta_v} - (v_{\mathrm{r}} - v_0 \bmod \Delta v). \end{aligned} \tag{A.21}$$

An example of the sparse structure of the resulting operator $\hat{\mathcal{R}}$ is shown in Fig. A.2b.

A.2.4 Stationary density and firing rate

The introduced approximations for the operators yield a large and sparse linear system for the stationary solution in Eq. (2.22):

$$\left((\hat{\mathcal{L}} + \hat{\mathcal{R}})\vec{P}_0\right)_{i+jN} = 0. \tag{A.22}$$

To exclude the trivial solution $\vec{P}_0 = 0$, I set an arbitrary element, here located at the $n_{\mathrm{r}} + N^2/2$-th bin, in each equation to one and solve the uniquely determined inhomogeneous system:

$$((\hat{\mathcal{L}} + \hat{\mathcal{R}} + \delta_{m,n_{\mathrm{r}}+N^2/2})\vec{P}'_0)_m = 1. \tag{A.23}$$

The linear system in Eq. (A.23) is solved by the direct LU-decomposition algorithm implemented in the SUPERLU package in Python by Li (2005).

The physically relevant solution also fulfills the normalization condition in Eq. (2.22) that depends on the stationary firing rate r_0 and reads in the discretized form:

$$\sum_{i,j=0}^{N-1} \Delta a \Delta v \, \vec{P}_{0\; i+jN} = 1 - \tau_{\mathrm{ref}} r_0. \tag{A.24}$$

In turn, the stationary firing rate is given by the discritization of Eq. (2.23) in which the

derivative in v is approximated as left-hand derivative:

$$r_0 = \frac{\beta^2}{2\tau_m^2 \Delta v} \sum_{j=0}^{N-1} \Delta a \, \vec{P}_{0\ N-1+jN}. \tag{A.25}$$

Put together, Eqs. (A.24) and (A.25) determine the factor for the normalization $\gamma_{\text{norm}} \vec{P}_0' = \vec{P}_0$:

$$\begin{aligned} \gamma_{\text{norm}} \sum_{i,j=0}^{N-1} \Delta a \Delta v \, P'_{0\ i+jN} &= 1 - \gamma_{\text{norm}} \tau_{\text{ref}} \frac{\beta^2}{2\tau_m^2 \Delta v} \sum_{j=0}^{N-1} \Delta a \, P'_{0\ N-1+jN} \\ \Leftrightarrow \gamma_{\text{norm}} &= \left(\sum_{i,j=0}^{N-1} \Delta a \Delta v \, P'_{0\ i+jN} + \tau_{\text{ref}} \frac{\beta^2}{2\tau_m^2 \Delta v} \sum_{j=0}^{N-1} \Delta a \, P'_{0\ N-1+jN} \right)^{-1}. \end{aligned} \tag{A.26}$$

Inserting the expression for the normalized denstiy $\vec{P}_0 = \gamma_{\text{norm}} \vec{P}_0'$ into Eq. (A.25) yields the firing rate:

$$r_0 = \left(\tau_{\text{ref}} + \frac{2\tau_m^2 \Delta v^2}{\beta^2} \frac{\sum_{i,j=0}^{N-1} P'_{0\ i+jN}}{\sum_{j=0}^{N-1} P'_{0\ N-1+jN}} \right)^{-1}. \tag{A.27}$$

A.2.5 Solution in Fourier domain and spike-train power spectrum

With the stationary probability density $\vec{P}_0$ we also know the inhomogeneity in Eq. (2.32). With help of the introduced discretization, the Fourier transformed density $\vec{\tilde{Q}}(\omega)$ is approximated by the solution of the complex sparse linear system of equations:

$$(i\omega + \hat{\mathcal{L}} + e_\tau \hat{\mathcal{R}}) \vec{\tilde{Q}}'(\omega) = \left[1 + \left(\frac{e_\tau - 1}{i\omega} - \frac{e_\tau}{r_0} \right) \hat{\mathcal{R}} \right] \vec{P}_0, \tag{A.28}$$

for $\omega \neq 0$ or for $\omega = 0$:

$$(\hat{\mathcal{L}} + \hat{\mathcal{R}}) \vec{\tilde{Q}}'(\omega) = [1 + (\tau_{\text{ref}} - r_0^{-1}) \, \hat{\mathcal{R}}] \vec{P}_0. \tag{A.29}$$

To find its solution we apply the same methods as for Eq. (A.23). Subsequentially, the normalization condition from Sec. (A.1) is applied if $\omega/(2\pi) < 1\,\text{Hz}$:

$$\vec{\tilde{Q}}(\omega) = \begin{cases} \vec{\tilde{Q}}'(\omega) + \left[\tau_{\text{ref}}(0.5\tau_{\text{ref}} r_0 - 1) - \Delta v \Delta a \sum_{i,j=0}^{N-1} \left(\left[1 + \tau_{\text{ref}} \hat{\mathcal{R}} \right] \vec{\tilde{Q}}'(\omega) \right)_{i+jN} \right] \vec{P}_0 & (\omega < 2\pi\,\text{Hz}), \\ \vec{\tilde{Q}}'(\omega) & (\text{else}). \end{cases} \tag{A.30}$$

Using the left-hand derivative, the spike-train power spectrum is according to Eq. (2.7) given by:

$$S(\omega) = r_0 \left(1 + 2 \frac{\beta^2 \Delta a}{2\tau_m^2 \Delta v} \sum_{j=0}^{N-1} \mathrm{Re}[\tilde{Q}_{N-1+jN}(\omega)] \right) . \tag{A.31}$$

A.2.6 Convergence and accuracy of the numerical solution

For a large number of points N, the numerical approximation converges to the exact solution and matches with the direct simulation of the Langevin equations. In Fig. A.3 numerical solutions of Eq. (2.32) for the LIF neuron driven by cyan noise from Fig. 2.5 are shown for increasing number of discretization steps N and for both representations of the same colored noise with the two values of $b = (\pm\sqrt{0.1} - 1)\beta$ as solid for strong and brighter dashed lines for weak noise, respectively. For the sake of comparability, absorbing boundaries are placed at $a_0 = -3\sqrt{b^2/\tau_a}$ and $a_{N-1} = -a_0$ such that the probability neglected due to the absorbing boundary conditions is the same in both cases. Only for a low resolution $N = 50$ shown as blue lines, the two solutions significantly differ from each other. In this case, we may also see the effect of the normalization condition used for frequencies smaller than 1 Hz. The difference between the spectra determined with $N = 800$ and $N = 1200$ is negligibly small. Both solutions match the results of direct simulations shown as gray line.

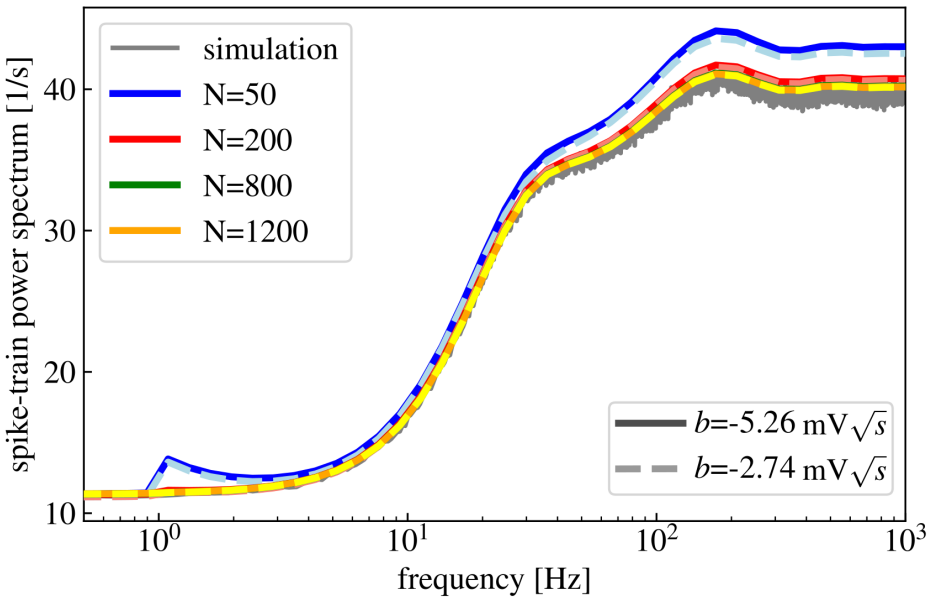

Figure A.3.: Accuracy and convergence of numerical solution. Numerically determined spike-train power spectra of of LIF neuron driven by cyan noise for increasing discretization number N and the two representations of the colored noise shown as solid and brighter dashed lines for strong [$b = (-\sqrt{0.1}-1)\beta$] and weak [$b = (\sqrt{0.1}-1)\beta$] noise, respectively. For sufficiently high N, the spectra converge to the power spectrum obtained by direct simulation as shown in gray.

A.3 Power spectrum of white-noise-driven LIF neuron

The one-dimensional LIF neuron driven by white noise is given by:

$$\tau_m \dot{v} = -v + \mu + \beta\xi(t), \qquad \text{if } v(t_k) > v_{\text{th}} : v(t_k + \tau_{\text{ref}}) \to v_{\text{r}} \tag{A.32}$$

The solution of the corresponding Fokker-Planck equation and, thus, the solution of the first passage time problem is known (Darling and Siegert, 1953). Since the model generates spike trains with independent inter-spike intervals, the spike-train power spectrum can be calculated by the first-passage-time density. The resulting analytical formula was found by Lindner et al. (2002) and reads in my notation:

$$S(\omega) = r_0 \frac{\left|\mathcal{D}_{i\omega\tau_m}\left(\frac{\sqrt{2}\tau_m(\mu-v_{\text{th}})}{\beta}\right)\right|^2 - e^{2\delta}\left|\mathcal{D}_{i\omega\tau_m}\left(\frac{\sqrt{2}\tau_m(\mu-v_{\text{r}})}{\beta}\right)\right|^2}{\left|\mathcal{D}_{i\omega\tau_m}\left(\frac{\sqrt{2}\tau_m(\mu-v_{\text{th}})}{\beta}\right) - e^{\delta}e^{i\omega\tau_{\text{ref}}}\mathcal{D}_{i\omega\tau_m}\left(\frac{\sqrt{2}\tau_m(\mu-v_{\text{r}})}{\beta}\right)\right|^2}, \quad \delta = \frac{v_{\text{r}}^2 - v_{\text{th}}^2 + 2\mu(v_{\text{th}} - v\text{r})}{2\beta^2}. \tag{A.33}$$

The parabolic cylinder functions are here denoted by $\mathcal{D}_a(z)$ [see Abramowitz and Stegun (1970)]. The stationary firing rate r_0 is given by the mean first passage time calculated by Ricciardi (1977) or also in Brunel (2000) and reads:

$$r_0 = \left(\tau_{\text{ref}} + \tau_m \int_{\sqrt{\tau_m}(v_{\text{r}}-\mu)/\beta}^{\sqrt{\tau_m}(v_{\text{th}}-\mu)/\beta} du \exp(u^2)(1+\text{erf}(u))\right)^{-1}. \tag{A.34}$$

Here the error function is denoted by $\text{erf}(x)$.

A.4 Numerical solution for three-dimensional IF neurons

The finite-difference method introduced in Sec. A.2 can be extended to calculate the spike-train power spectrum of a three-dimensional IF neuron as the solution of Eq. (2.49) for $d = 2$. The phase space v, a_1 and a_2 is discretized in a similar manner as in the two-dimensional case:

$$\begin{aligned} v &\to v_i = v_0 + i\Delta v \\ a_1 &\to a_{1\,j} = a_{1\,0} + j\Delta a_1 \\ a_2 &\to a_{2\,k} = a_{2\,0} + k\Delta a_2 \end{aligned} \tag{A.35}$$

with $i \in [0, 1, \ldots, N_v - 1]$, $j \in [0, 1, \ldots, N_{a1} - 1]$ and $k \in [0, 1, \ldots, N_{a2} - 1]$. Since the procedure is computationally very demanding, the resolution can be adjusted for each dimension by an individual number of discretization steps N_v, N_{a1} and N_{a2}. The probability densities are regarded as $(N_v N_{a1} N_{a2})$-dimensional vectors $\vec{P}_0$ and $\vec{\tilde{Q}}(\omega)$ with the components:

$$P_{0\;i+jN_v+kN_vN_{a1}} = P_0(v_i, a_{1\,j}, a_{2\,k}), \qquad \tilde{Q}_{i+jN_v+kN_vN_{a1}}(\omega) = \tilde{Q}(v_i, a_{1\,j}, a_{2\,k}, \omega). \tag{A.36}$$

The operator that incorporates the subthreshold dynamics $\hat{\mathcal{L}}$ in Eq. (2.43) for $d = 2$ is given by:

$$\hat{\mathcal{L}} = -\partial_v \frac{f(v,a_1,a_2)}{\tau_m} + \frac{\beta_1^2+\beta_2^2}{2\tau_m^2}\partial_v^2 - \partial_{a1} g_1(v,a_1,a_2) + \frac{B_{11}^2+B_{12}^2}{2}\partial_{a1}^2 - \partial_{a2} g_2(v,a_1,a_2) + \frac{B_{21}^2+B_{22}^2}{2}\partial_{a2}^2 + \frac{\beta_1 B_{11}+\beta_2 B_{12}}{\tau_m}\partial_v\partial_{a1} + \frac{\beta_1 B_{21}+\beta_2 B_{22}}{\tau_m}\partial_v\partial_{a2} + (B_{11}B_{21}+B_{12}B_{22})\partial_{a1}\partial_{a2}. \tag{A.37}$$

Due to the approximation of the first and second derivatives in $\hat{\mathcal{L}}$ by *finite differences* in Eq. (A.11) I obtain the $(N_v N_{a1} N_{a2}) \times (N_v N_{a1} N_{a2})$ tridiagonal matrix with four secondary tridiagonals:

$$\begin{aligned}
\hat{\mathcal{L}}_{i+jN_v+kN_vN_{a1},m} &= -\left(\frac{\beta_1^2+\beta_2^2}{\tau_m^2\Delta v^2} + \frac{B_{11}^2+B_{12}^2}{(\Delta a_1)^2} + \frac{B_{21}^2+B_{22}^2}{(\Delta a_2)^2}\right)\delta_{i+jN_v+kN_vN_{a1},m} \\
&+ \left(\frac{\beta_1^2+\beta_2^2}{2\tau_m^2\Delta v^2} - \frac{f(v_{i+1},a_{1\,j},a_{2\,k})}{2\tau_m\Delta v}\right)\bar{\delta}_{i,N-1}\delta_{i+1+jN_v+kN_vN_{a1},m} \\
&+ \left(\frac{\beta_1^2+\beta_2^2}{2\tau_m^2\Delta v^2} + \frac{f(v_{i-1},a_{1\,j},a_{2\,k})}{2\tau_m\Delta v}\right)\bar{\delta}_{i,0}\delta_{i-1+jN_v+kN_vN_{a1},m} \\
&+ \left(\frac{B_{11}^2+B_{12}^2}{2(\Delta a_1)^2} - \frac{g(v_i,a_{j+1},a_k)}{2\Delta a_1}\right)\bar{\delta}_{j,N-1}\delta_{i+(j+1)N_v+kN_vN_{a1},m} \\
&+ \left(\frac{B_{11}^2+B_{12}^2}{2(\Delta a_1)^2} + \frac{g(v_i,a_{j-1},a_k)}{2\Delta a_1}\right)\bar{\delta}_{j,0}\delta_{i+(j-1)N_v+kN_vN_{a1},m} \\
&+ \left(\frac{B_{21}^2+B_{22}^2}{2(\Delta a_2)^2} - \frac{g(v_i,a_j,a_{k+1})}{2\Delta a_2}\right)\bar{\delta}_{k,N-1}\delta_{i+jN_v+(k+1)N_vN_{a1},m} \\
&+ \left(\frac{B_{21}^2+B_{22}^2}{2(\Delta a_2)^2} + \frac{g(v_i,a_j,a_{k-1})}{2\Delta a_2}\right)\bar{\delta}_{k,0}\delta_{i+jN_v+(k-1)N_vN_{a1},m} \\
&+ \frac{\beta_1 B_{11}+\beta_2 B_{12}}{4\tau_m\Delta v\Delta a_1} \times \Big[\bar{\delta}_{i,0}\left(\bar{\delta}_{j,0}\delta_{i-1+(j-1)N_v+kN_vN_{a1},m} - \bar{\delta}_{j,N-1}\delta_{i-1+(j+1)N_v+kN_vN_{a1},m}\right) \\
&\qquad + \bar{\delta}_{i,N-1}\left(\bar{\delta}_{j,N-1}\delta_{i+1+(j+1)N_v+kN_vN_{a1},m} - \bar{\delta}_{j,0}\delta_{i+1+(j-1)N_v+kN_vN_{a1},m}\right)\Big] \\
&+ \frac{\beta_1 B_{21}+\beta_2 B_{22}}{4\tau_m\Delta v\Delta a_2} \times \Big[\bar{\delta}_{i,0}\left(\bar{\delta}_{k,0}\delta_{i-1+jN_v+(k-1)N_vN_{a1},m} - \bar{\delta}_{k,N-1}\delta_{i-1+jN_v+(k+1)N_vN_{a1},m}\right) \\
&\qquad + \bar{\delta}_{i,N-1}\left(\bar{\delta}_{k,N-1}\delta_{i+1+jN_v+(k+1)N_vN_{a1},m} - \bar{\delta}_{k,0}\delta_{i+1+jN_v+(k-1)N_vN_{a1},m}\right)\Big] \\
&+ \frac{B_{11}B_{21}+B_{12}B_{22}}{4\Delta a_1\Delta a_2} \times \Big[\bar{\delta}_{j,0}\left(\bar{\delta}_{k,0}\delta_{i+(j-1)N_v+(k-1)N_vN_{a1},m} - \bar{\delta}_{k,N-1}\delta_{i+(j-1)N_v+(k+1)N_vN_{a1},m}\right) \\
&\qquad + \bar{\delta}_{j,N-1}\left(\bar{\delta}_{k,N-1}\delta_{i+(j+1)N_v+(k+1)N_vN_{a1},m} - \bar{\delta}_{k,0}\delta_{i+(j+1)N_v+(k-1)N_vN_{a1},m}\right)\Big].
\end{aligned} \tag{A.38}$$

The general fire-and-reset operator in Eq. (2.46) for $d = 2$ is given by:

$$\hat{\mathcal{R}}\,\tilde{Q}(v, a_1, a_2, \omega) = \\ -\delta(v - v_\mathrm{r}) \int_{-\infty}^{\infty} da_1' \int_{-\infty}^{\infty} da_2'\, \rho_\mathrm{ref}(a_1, a_2 | a_1', a_2') \frac{\beta_1^2 + \beta_2^2}{2\tau_m^2} \partial_v \tilde{Q}(v, a_1' - \delta_{a1}, a_2' - \delta_{a2}, \omega)\Big|_{v=v_\mathrm{th}} . \tag{A.39}$$

As described in Sec. A.2.3, the operator incorporates four steps that can be regarded as matrix multiplications $\hat{\mathcal{R}} = \hat{R}\hat{E}\hat{S}\hat{F}$. In the case $d = 2$ the, $(N_{a1}N_{a2}) \times (N_v N_{a1} N_{a2})$ matrix $\hat{F}$ that measures the efflux of probability at v_th reads:

$$\hat{F}_{m,i+jN_v+kN_vN_{a1}} = \frac{\beta_1^2 + \beta_2^2}{2\tau_m^2 \Delta v} \delta_{m,j+kN_{a1}} \delta_{i,N-1}. \tag{A.40}$$

The shift of probability due to spike-triggered adaptation along the vector $\vec{\delta}_a = (\delta_{a1}, \delta_{a2})^\intercal$ is incorporated by the operator $\hat{S}$ given by the $(N_{a1}N_{a2}) \times (N_{a1}N_{a2})$ matrix:

$$\begin{aligned} \hat{S}_{m',m} &= (1-\kappa_{a1})(1-\kappa_{a2})\delta_{m'-n_{a1}-N_{a1}n_{a2},m} + \kappa_{a1}(1-\kappa_{a2})\delta_{m'-1-n_{a1}-N_{a1}n_{a2},m} \\ &\quad + (1-\kappa_{a1})\kappa_{a2}\delta_{m'-n_{a1}-N_{a1}(n_{a2}+1),m} + \kappa_{a1}\kappa_{a2}\delta_{m'-1-n_{a1}-N_{a1}(n_{a2}+1),m}, \\ n_{a1} &= \delta_{a1}/\Delta a_1 - (\delta_{a1} \bmod \Delta a_1), \qquad \kappa_{a1} = \delta_{a1} \bmod \Delta a_1, \\ n_{a2} &= \delta_{a2}/\Delta a_2 - (\delta_{a2} \bmod \Delta a_2), \qquad \kappa_{a2} = \delta_{a2} \bmod \Delta a_2. \end{aligned} \tag{A.41}$$

The matrix $\hat{E}$ describes the evolution of the probability density in the refractory state and is given by:

$$\hat{E}_{j'+k'N_{a1},j+kN_{a1}} = \rho_\mathrm{ref}(a_{1\,j'}, a_{2\,k'} | a_{1\,j}, a_{2\,k}) \qquad (\text{for } (B_{11}^2 + B_{12}^2 \neq 0 \text{ or } B_{21}^2 + B_{22}^2 \neq 0). \tag{A.42}$$

In the case that $\vec{a}$ is a two-dimensional Ornstein Uhlenbeck process, the transition probability $\rho_\mathrm{ref}(a_1, a_2 | a_1', a_2')$ can be calculated as described in Sec. B.2. As the last step, the operator $\hat{R}$ performs the reset of probability at v_th given by:

$$\begin{aligned} \hat{R}_{i''+j''N_v+k''N_vN_{a1},m'} &= \frac{(1-\kappa_v)\delta_{i'',n_\mathrm{r}} + \kappa_v \delta_{i'',n_\mathrm{r}+1}}{\Delta v} \delta_{j''+k''N_{a1},m'} \\ \kappa_v &= (v_\mathrm{r} - v_0) \bmod \Delta v \\ n_\mathrm{r} &= \frac{v_\mathrm{r} - v_0}{\Delta v} - [(v_\mathrm{r} - v_0) \bmod \Delta v]. \end{aligned} \tag{A.43}$$

To calculate the stationary density, the trivial solution $\vec{P}_0 = 0$ is excluded by setting an arbitrary element, here located at $n_\mathrm{r} + N_v N_{a1}/2 + N_v N_{a1} Na2/2$ in each equation to one yielding the uniquely determined system of equations:

$$((\hat{\mathcal{L}} + \hat{\mathcal{R}} + \delta_{m,n_\mathrm{r}+N_vN_{a1}/2+N_vN_{a1}N_{a2}/2})\vec{P}_0')_m = 1. \tag{A.44}$$

To find the solution, I use the stabilized biconjugated gradient method with an incomplete LU decomposition as preconditioner (see Press et al. (2007) chapter 2.7.6) provided in the Eigen library (Guennebaud et al., 2010). By applying the normalization of $\vec{P}_0$, the stationary firing rate r_0 can be calculated from the unnormalized density $\vec{P}_0'$ as in Eq. (A.27) by:

$$r_0 = \left(\tau_{\mathrm{ref}} + \frac{2\tau_m^2 \Delta v^2}{\beta_1^2 + \beta_2^2} \frac{\sum_{i=0}^{N_v-1} \sum_{j=0}^{N_{a1}-1} \sum_{k=0}^{N_{a2}-1} P_{0\,i+jN_v+kN_vN_{a1}}'}{\sum_{j=0}^{N_{a1}-1} \sum_{k=0}^{N_{a2}-1} P_{0\,N-1+jN_v+kN_vN_{a1}}'} \right)^{-1}. \tag{A.45}$$

The normalized probability density is given by $\vec{P}_0 = \gamma_{\mathrm{norm}} \vec{P}_0'$ with the factor:

$$\begin{aligned} \gamma_{\mathrm{norm}} = \Bigg(& \Delta v \Delta a_1 \Delta a_2 \sum_{i=0}^{N_v-1} \sum_{j=0}^{N_{a1}-1} \sum_{k=0}^{N_{a2}-1} P_{0\,i+jN_v+kN_vN_{a1}}' \\ & + \tau_{\mathrm{ref}} \frac{\beta_1^2 + \beta_2^2}{2\tau_m^2 \Delta v} \sum_{j=0}^{N_{a1}-1} \sum_{k=0}^{N_{a2}-1} \Delta a_1 \Delta a_2 \, P_{0\,N-1+jN_v+kN_vN_{a1}}' \Bigg)^{-1}. \end{aligned} \tag{A.46}$$

The Fourier transformed probability density is given by the solution of the linear system:

$$(i\omega + \hat{\mathcal{L}} + e_\tau \hat{\mathcal{R}}) \vec{\tilde{Q}}'(\omega) = \left[1 + \left(\frac{e_\tau - 1}{i\omega} - \frac{e_\tau}{r_0} \right) \hat{\mathcal{R}} \right] \vec{P}_0, \tag{A.47}$$

for $\omega \neq 0$ or for $\omega = 0$:

$$(\hat{\mathcal{L}} + \hat{\mathcal{R}}) \vec{\tilde{Q}}'(\omega) = [1 + (\tau_{\mathrm{ref}} - r_0^{-1}) \, \hat{\mathcal{R}}] \vec{P}_0. \tag{A.48}$$

To avoid the numerical artifact discussed in Sec. A.1, I apply the normalization condition given in Eq. (2.49) for $\omega < 2\pi\,\mathrm{Hz}$:

$$\vec{\tilde{Q}}(\omega) = \begin{cases} \vec{\tilde{Q}}'(\omega) + \left[\tau_{\mathrm{ref}}(0.5\tau_{\mathrm{ref}} r_0 - 1) - \Delta v \Delta a_1 \Delta a_2 \sum_{i,j,k} \left(\left[1 + \tau_{\mathrm{ref}} \hat{\mathcal{R}} \right] \vec{\tilde{Q}}'(\omega) \right)_{i+jN_v+kN_vN_{a1}} \right] \vec{P}_0 & (\omega < 2\pi\,\mathrm{Hz}), \\ \vec{\tilde{Q}}'(\omega) & (\text{else}). \end{cases} \tag{A.49}$$

The spike-train power spectrum is calculated by Eq. (2.49) using the left-hand derivative with respect to v:

$$S(\omega) = r_0 \left(1 + 2 \frac{(\beta_1^2 + \beta_2^2) \Delta a_1 \Delta a_2}{2\tau_m^2 \Delta v} \sum_{j=0}^{N_{a1}-1} \sum_{k=0}^{N_{a2}-1} \mathrm{Re}[\tilde{Q}_{N-1+jN_v+kN_vN_{a1}}(\omega)] \right). \tag{A.50}$$

A.5 Derivatives of the spike-train power spectrum at $\omega = 0$

Here I derive the set of partial differential equations that determines the n-th derivative of the spike-train power spectrum with respect to ω at $\omega = 0$. The spike-train power spectrum is given in Eq. (2.49) by:

$$S(\omega) = r_0 - 2r_0 \mathrm{Re}\left(\int\limits_{M_{\vec{a}}} d\vec{a}\, \frac{\vec{\beta}^2}{2\tau_m^2} \partial_v \tilde{Q}(v, \vec{a}, \omega)\Big|_{v=v_{\mathrm{th}}} \right). \tag{A.51}$$

Its n-th derivative with respect to ω at $\omega = 0$ is simply given by:

$$S_0^{(n)} = \frac{d^n}{d\omega^n} S(\omega)\Big|_{\omega=0} = \delta_{n,0} r_0 - 2r_0 \mathrm{Re}\left(\int\limits_{M_{\vec{a}}} d\vec{a} \frac{\vec{\beta}^2}{2\tau_m^2} \partial_v \tilde{Q}_0^{(n)}\Big|_{v=v_{\mathrm{th}}} \right), \quad \tilde{Q}_0^{(n)} = \frac{d^n}{d\omega^n} \tilde{Q}(v, \vec{a}, \omega)\Big|_{\omega=0} \tag{A.52}$$

[see Eq. (2.53)]. The partial differential equation that determines the function $\tilde{Q}_0^{(n)}$ arises by the derivative of the equation for $\tilde{Q}(v, a, \omega)$ given in Eq. (2.49):

$$(i\omega + \hat{\mathcal{L}} + e_\tau \hat{\mathcal{R}}) \tilde{Q}(v, \vec{a}, \omega) = \left[1 + \left(\frac{e_\tau - 1}{i\omega} - \frac{e_\tau}{r_0} \right) \hat{\mathcal{R}} \right] P_0(v, \vec{a}) \tag{A.53}$$

with $e_\tau = \exp(i\omega\tau_{\mathrm{ref}})$. The n-th derivative of the left hand side reads:

$$\frac{d^n}{d\omega^n}[(i\omega + \hat{\mathcal{L}} + e_\tau \hat{\mathcal{R}})\tilde{Q}] = (i\omega + \hat{\mathcal{L}} + e_\tau \hat{\mathcal{R}}) \frac{d^n}{d\omega^n} \tilde{Q} + ni \frac{d^{n-1}}{d\omega^{n-1}} \tilde{Q} + \sum_{k=0}^{n-1} \binom{n}{k} (i\tau_{\mathrm{ref}})^{n-k} e_\tau \hat{\mathcal{R}} \frac{d^k}{d\omega^k} \tilde{Q}, \tag{A.54}$$

here the second and third term arise by the n-th application of the product rule. For the third term I used that the n-th derivative of the product of an exponential function with an arbitrary function reads:

$$\frac{d^n}{dx^n}[\exp(\alpha x) f(x)] = \sum_{k=0}^{n} \binom{n}{k} \alpha^{n-k} \exp(\alpha x) \frac{d^k}{dx^k} f(x). \tag{A.55}$$

Here the brackets with the stacked integer numbers n and k denote the binomial coefficient n over k. Note that any derivative of $\tilde{Q}$ with respect to ω obeys the same boundary conditions. The limes for $\omega \to 0$ of the n-th derivative of the right hand side of Eq. (A.53) is given by:

$$\lim_{\omega \to 0} \frac{d^n}{d\omega^n} \left[1 + \left(\frac{e_\tau - 1}{i\omega} - \frac{e_\tau}{r_0} \right) \hat{\mathcal{R}} \right] P_0 = \delta_{n,0} P_0 + (i\tau_{\mathrm{ref}})^n \left(\frac{\tau_{\mathrm{ref}}}{n+1} - \frac{1}{r_0} \right) \hat{\mathcal{R}}\, P_0 \tag{A.56}$$

[determined with *Mathematica* (Wolfram Research Inc., 2019)[1]]. The combination of the limes $\omega \to 0$ in Eq. (A.54) and Eq. (A.56) yields the partial differential equation for $\tilde{Q}_0^{\prime(n)}$:

$$(\hat{\mathcal{L}} + \hat{\mathcal{R}})\tilde{Q}_0^{\prime(n)} = \delta_{n,0} P_0 + (i\tau_{\mathrm{ref}})^n \left(\frac{\tau_{\mathrm{ref}}}{n+1} - \frac{1}{r_0} \right) \hat{\mathcal{R}}\, P_0 - ni\tilde{Q}_0^{(n-1)} - \sum_{k=0}^{n-1} \binom{n}{k} (i\tau_{\mathrm{ref}})^{n-k}\, \hat{\mathcal{R}}\, \tilde{Q}_0^{(k)} \tag{A.57}$$

[see Eq. (2.53)]. As explained in Sec. A.1 for $\tilde{Q}$, also in this case an additional condition is required to uniquely determine $\tilde{Q}_0^{(n)}$. This condition can be derived by the normalization condition of $\tilde{Q}$ in Eq. (A.2) that reads:

$$\int_{-\infty}^{v_{\mathrm{th}}} dv \int_{M_{\vec{a}}} d\vec{a}\, \tilde{Q}(v,a,\omega) = \frac{1}{i\omega} \left[(1 - e^{i\omega\tau_{\mathrm{ref}}}) \left(\int_{-\infty}^{v_{\mathrm{th}}} dv \int_{M_{\vec{a}}} d\vec{a}\, \hat{\mathcal{R}}\, \tilde{Q}(v,a,\omega) - \frac{r_0}{i\omega} + 1 \right) - r_0 \tau_{\mathrm{ref}} \right]. \tag{A.58}$$

The n-th derivative of this equation at $\omega \to 0$ is given by:

$$\int_{-\infty}^{v_{\mathrm{th}}} dv \int_{M_{\vec{a}}} d\vec{a}\, \tilde{Q}_0^{(n)} = -\frac{i^n \tau_{\mathrm{ref}}^{n+1}}{n+1} + \frac{i^n r_0 \tau_{\mathrm{ref}}^{n+2}}{\sum_{k=1}^{n+1} 2k} - \int_{-\infty}^{v_{\mathrm{th}}} dv \int_{M_{\vec{a}}} d\vec{a} \left(\sum_{k=0}^{n} \binom{n}{k} \frac{i^{n-k} \tau_{\mathrm{ref}}^{n-k+1}}{n-k+1}\, \hat{\mathcal{R}}\, \tilde{Q}_0^{(k)} \right) \tag{A.59}$$

[determined with *Mathematica* (Wolfram Research Inc., 2019)[1]]. Applying this normalization condition, the derivative $\tilde{Q}_0^{(n)}$ can be calculated from any solution $\tilde{Q}_0^{\prime(n)}$ by:

$$\tilde{Q}_0^{(n)} = \tilde{Q}_0^{\prime(n)} - P_0 \left[\frac{i^n \tau_{\mathrm{ref}}^{n+1}}{n+1} - \frac{i^n r_0 \tau_{\mathrm{ref}}^{n+2}}{\sum_{k=1}^{n+1} 2k} + \int_{-\infty}^{v_{\mathrm{th}}} dv \int_{M_{\vec{a}}} d\vec{a} \left(\tilde{Q}_0^{\prime(n)} + \sum_{k=0}^{n} \binom{n}{k} \frac{i^{n-k} \tau_{\mathrm{ref}}^{n-k+1}}{n-k+1}\, \hat{\mathcal{R}}\, \tilde{Q}_0^{\prime(k)} \right) \right] \tag{A.60}$$

which is the additional condition in Eq. (2.53).

[1] Wolfram Research, Inc. Mathematica Ver. 12 (2019) `https://www.wolfram.com/mathematica`

B Mean-field theory that considers temporal correlations of spike trains

B.1 Two-dimensional Ornstein-Uhlenbeck process

Here I show that the coefficients in $\mathbf{A}$, $\mathbf{B}$, β of the input process $\eta(t)$ in Eq. (3.10) with a two-dimensional Ornstein-Uhlenbeck process can be reduced to:

$$\mathbf{A} = \begin{pmatrix} T/2 & \frac{T^2/4-\mathcal{D}}{A_{21}} \\ A_{21} & T/2 \end{pmatrix}, \quad \mathbf{B} = \begin{pmatrix} B_{11} & 0 \\ 0 & 0 \end{pmatrix}, \quad \vec{\beta} = \begin{pmatrix} \beta \\ 0 \end{pmatrix} \tag{B.1}$$

without loss of the spectrum's generality. As discussed in Sec. (3.1.3), the power spectrum corresponding to η can be written as:

$$S_{\eta\eta}(\omega) = \beta^2 + \frac{X_0 + X_1\omega^2}{1 + Y_1\omega^2 + Y_2\omega^4}. \tag{B.2}$$

Furthermore, I derive the solution of the inverse problem of determining the Ornstein-Uhlenbeck process with given coefficients β, X_0, X_1, Y_1 and Y_2 in Eq. (3.21).

Admissible ranges of X_0, X_1, Y_1 and X_2

As the first step, I show the maximum range of the coefficients β, X_k and Y_ℓ that are restricted since the power spectrum is positive and finite. In the second step I show that this range is fully covered by the choice of coefficients in Eq. (B.1).

In the general case, the power spectrum may have every positive high-frequency limit given by β^2, thus, the range of β are the real numbers. For simplicity and to avoid unnecessary ambiguity, we restrict β to positive values ($0 \leq \beta < \infty$). The low-frequency limit given by $S_{\eta\eta}(0) = X_0 + \beta^2$ is only restricted to be non-negative and finite, consequentially, $-\beta^2 \leq X_0 < \infty$. To ensure that the spectrum is finite, the denominator of the fraction term must not have zero crossings and has to be positive for all ω. Thus, its highest order term has to be positive ($0 < Y_2 < \infty$). Also Y_1 has to be chosen such that no zero crossing occurs. Hence, the maximum range of Y_1 can be determined by the calculation of the zero crossings:

$$1 + Y_1\omega^2 + Y_2\omega^4 = 0 \Leftrightarrow \omega^2 = \frac{-Y_1 \pm \sqrt{Y_1^2 - 4Y_2}}{2Y_2}. \tag{B.3}$$

For all positive values of Y_1, the right hand side is negative or complex valued and no real-valued solution for ω exists. The minimum value can be identified by the square root term in the numerator that is imaginary if $Y_1^2 - 4Y_2 < 0$. The whole range can be identified by $-2\sqrt{Y_2} < Y_1 < \infty$. The remaining coefficient X_1 has to ensure that the spectrum is larger or equal to zero at its absolute minimum at $\omega_{\min}$. For the minimum admissible value of X_1, the frequency axes is the tangent to the spectrum at ω_{min} and the spectrum is only zero at $\pm\omega_{min}$:

$$\begin{aligned} S_{\eta\eta}(\omega_{\min}) &= \beta^2 + \frac{X_0 + X_1\omega_{\min}^2}{1 + Y_1\omega_{\min}^2 + Y_2\omega_{\min}^4} \stackrel{!}{=} 0 \\ \Leftrightarrow \omega_{\min}^2 &= -\frac{X_1 + Y_1\beta^2}{2\beta^2 Y_2} \pm \sqrt{\frac{(X_1 + Y_1\beta^2)^2 - 4\beta^2 Y_2(X_0 + \beta^2)}{4Y_2^2\beta^4}}. \end{aligned} \tag{B.4}$$

This is the case, if the square-root term vanishes, such that the minimal value of X_1 is identified as:

$$\begin{aligned} &(X_1 + Y_1\beta^2)^2 - 4\beta^2 Y_2(X_0 + \beta^2) = 0 \\ \Leftrightarrow\ &X_1 = -Y_1\beta^2 \pm 2\beta\sqrt{Y_2(X_0 + \beta^2)}. \end{aligned} \tag{B.5}$$

For the positive sign, the right handside in Eq. (B.4) is negative such that no zero crossing is found. We identify the range as $-Y_1\beta^2 - 2\beta\sqrt{Y_2(x_0 + \beta^2)} \le X_1 < \infty$. In summary, the ranges of the coefficients are:

$$\begin{aligned} 0 \le \beta &< \infty, \\ -\beta^2 \le X_0 &< \infty, \\ -Y_1\beta^2 - 2\beta\sqrt{Y_2(X_0 + \beta^2)} \le X_1 &< \infty, \\ -2\sqrt{Y_2} < Y_1 &< \infty, \\ 0 < Y_2 &< \infty. \end{aligned} \tag{B.6}$$

As the next step, I show that all values within these limits can be reached if we insert the relations between X_k and Y_ℓ and the coefficients in Eq. (B.1) and derive the solution of the inverse problem. Following Eq. (3.15) these relations for the Y_ℓ are given by:

$$\begin{aligned} \mathcal{D}^2 Y_1\omega^2 + \mathcal{D}^2 Y_2\omega^4 &= (T^2 - 2\mathcal{D})\omega^2 + \omega^4, \\ \Rightarrow Y_1 = (T^2 - 2\mathcal{D})\mathcal{D}^{-2}, &\quad Y_2 = \mathcal{D}^{-2}. \end{aligned} \tag{B.7}$$

To ensure stability of the Ornstein-Uhlenbeck process, the determinant $\mathcal{D}$ is restricted to positive values. Note that all values between the limits in Eq. (B.6) for Y_1 and Y_2 can be reached:

$$\lim_{\mathcal{D}\to\infty} \frac{T^2 - 2\mathcal{D}}{\mathcal{D}^2} = -2\mathcal{D}^{-1} = -2\sqrt{Y_2},\ \lim_{T\to\infty} \frac{T^2 - 2\mathcal{D}}{\mathcal{D}^2} = \infty,\ \lim_{\mathcal{D}\to\infty} \mathcal{D}^{-2} = 0,\ \lim_{\mathcal{D}\to 0} \mathcal{D}^{-2} = \infty. \tag{B.8}$$

I show that the full range of X_0 and X_1 can be reached by the choice of Eq. (B.1) by the following solution of the inverse problem.

Solution of the inverse problem and ambiguity

For the inverse problem of determining the matrices $\mathbf{A}$ and $\mathbf{B}$ for given X_k and X_ℓ I find:

$$\mathcal{D} = 1/\sqrt{Y_2}, \qquad T = \pm\sqrt{\frac{Y_1}{Y_2} + \frac{2}{\sqrt{Y_2}}} \tag{B.9}$$

[cf. Eq. (3.21)] For the coefficients X_k, the relations are given by Eq. (3.15) as:

$$\mathcal{D}^2 X_0 + \mathcal{D}^2 X_1 \omega^2 = 2\beta\mathcal{D}B_{11}(T/2 - A_{21}) + B_{11}^2(T/2 - A_{21})^2 + [2B\beta(T_2 + A_{21}) + B_{11}^2]\omega^2. \tag{B.10}$$

The comparison of the coefficients on the left and right hand sides yields:

$$\mathcal{D}^2 X_0 = 2\beta\mathcal{D}B_{11}(T/2 - A_{21}) + B_{11}^2(T/2 - A_{21})^2 \Leftrightarrow B_{11} = \mathcal{D}\frac{\pm\sqrt{\beta^2 + X_0} - \beta}{T/2 - A_{21}}. \tag{B.11}$$

As we can see, for all X_0 with $-\beta^2 \leq X_0 < \infty$ two solutions for B_{11} can be determined such that the full range of X_0 can be reached. Inserting B_{11} into the relation for X_1 that arises from the comparison of the coefficients of ω^2 terms in Eq. (B.10), the remaining coefficient of the inverse problem A_{21} can be identified as:

$$\begin{aligned} X_1 &= \frac{2\sqrt{Y_2}\beta\kappa(T/2 + A_{21})}{T/2 - A_{21}} + \frac{\kappa^2}{(T/2 - A_{21})^2} \\ \Leftrightarrow A_{21} &= \frac{TX_1/2 \pm \kappa\sqrt{X_1 + T^2\beta^2 Y_2 + 2\beta\sqrt{Y_2}\kappa}}{X_1 + 2\beta\sqrt{Y_2}\kappa}, \qquad \kappa = \pm\sqrt{\beta^2 + X_0} - \beta. \end{aligned} \tag{B.12}$$

The lower limit of X_1 for which a coefficient A_{21} can be found is given by the value at which the square root vanishes:

$$X_1 + \beta^2 Y_1 \pm 2\beta\sqrt{Y_2(X_0 + \beta^2)} = 0 \Leftrightarrow X_1 = -Y_1\beta^2 \mp 2\beta\sqrt{Y_2(X_0 + \beta^2)}, \tag{B.13}$$

where I used the expression for T in Eq. (B.9). This lower limit is in accordance to the lower limit of X_1 that ensures that the power spectrum is not negative in Eq. (B.6) if we consider the positive sign for κ and thereby also only the positive sign for B_{11}. Consequentially, the choice of $\mathbf{A}$, $\mathbf{B}$ and $\vec{\beta}$ in Eq. (B.1) reduces ambiguity but does not restrict the generality of the power spectrum. Still there is ambiguity and four combinations of parameters of the Ornstein-Uhlenbeck process yield the same power spectrum.

However, noise stabilizes the numerical solution of Eq. (2.49) such that a non-vanishing B_{22} is applied and $\mathbf{B}$ reads:

$$\mathbf{B} = \begin{pmatrix} B_{11} & 0 \\ 0 & B_{22} \end{pmatrix}. \tag{B.14}$$

From Eq. (3.15) it can be obtained:

$$
\begin{aligned}
&X_0(T,\mathcal{D},A_{21},B_{11},B_{22}) = \frac{\left(\frac{T}{2}-A_{21}\right)\beta B_{11}}{\mathcal{D}} + \mathcal{D}^{-2}\left[B_{11}^2(\frac{T}{2}-A_{21})^2 + B_{22}^2\left(\frac{T}{2}-\frac{\frac{T}{4}-\mathcal{D}}{A_{21}}\right)^2\right],\\
&X_1(T,\mathcal{D},A_{21},B_{11},B_{22}) = \mathcal{D}^{-2}[2\beta B_{11}(T/2+A_{21}) + B_{11}^2 + B_{22}^2],\\
&Y_1(T,\mathcal{D}) = (T^2-2\mathcal{D})\mathcal{D}^{-2}, \qquad Y_2(\mathcal{D}) = \mathcal{D}^{-2}.
\end{aligned}
\tag{B.15}
$$

For given coefficients β, X_0', X_1', Y_1' and Y_2', the inverse problem is solved as follows. $\mathcal{D}$ and T are directly determined by inserting $Y_1 = Y_1'$ and $Y_2 = Y_2'$ in Eq. (B.15). The other coefficients are determined by numerical minimization of a cost function:

$$
\underset{A_{21},B_{11},B_{22}}{\arg\min}\; Z = \left[[X_0(T,\mathcal{D},A_{21},B_{11},B_{22}) - X_0']^2 + [X_1(T,\mathcal{D},A_{21},B_{11},B_{22}) - X_1']^2\right]. \tag{B.16}
$$

The solution has to fulfill $Z(A_{21},B_{11},B_{22}) \approx 0$.

B.2 Probability transition due to refractory period for $d > 1$

To apply the theory of spike-train power spectra for multidimensional integrate-and-fire neurons with refractory period $\tau_{\mathrm{ref}} > 0$, the probability transition during the refractory period is required. For the case of a multidimensional Ornstein-Uhlenbeck process with dimensionality $d \geq 1$, the probability can be calculated analytically. The detailed derivation can be found in the book by Risken (1984) [see chapter 6.5 with the final result in Eq. (6.124)]. Here I only present the resulting equations in my notation in which the Langevin equation for the multidimensional Ornstein-Uhlenbeck process reads:

$$
\dot{\vec{a}} = -\mathbf{A}\vec{a} + \mathbf{B}\vec{\xi}(t). \tag{B.17}
$$

The components of the vector $\vec{\xi}(t)$ are independent Gaussian white noise sources that obey $\langle \xi_i(t)\xi_j(t+\tau)\rangle = \delta_{ij}\delta(t-\tau)$. The temporal evolution for of a probability density is given by the Fokker-Planck equation:

$$
\partial_t p(\vec{a},t) = \sum_{k=1}^{d} \partial_{a_k} \mathbf{A}\vec{a}\, p(\vec{a},t) + \sum_{k,l,m=1}^{d} \frac{B_{kl}Bml}{2} \partial_{a_k}\partial_{a_m} p(\vec{a},t). \tag{B.18}
$$

The evolution during the refractory period can be represented by the transition probability $\rho_{\mathrm{ref}}(\vec{a}|\vec{a}')$:

$$
p(\vec{a}, t+\tau_{\mathrm{ref}}) = \int\limits_{M_{\vec{a}}} d\vec{a}'\, \rho_{\mathrm{ref}}(\vec{a}|\vec{a}')p(\vec{a}',t). \tag{B.19}
$$

For the Ornstein-Uhlenbeck process, the transition probability can be calculated as follows [cf. (Risken, 1984) chapter 6.5 Eq. 6.124]:

$$\rho_{\mathrm{ref}}(\vec{a}|\vec{a}') = (2\pi)^{-d/2}\sqrt{\det(\mathbf{H})}\exp\left(-\frac{1}{2}(\vec{a}-\mathbf{G}\vec{a}')^{\intercal}\mathbf{H}^{-1}(\vec{a}-\mathbf{G}\vec{a}')\right). \tag{B.20}$$

Here the matrix $\mathbf{G}$ is determined by the matrix exponential function of $\mathbf{A}\tau_{\mathrm{ref}}$:

$$\mathbf{G} = \exp(-\mathbf{A}\tau_{\mathrm{ref}}) = \sum_{k=0}^{\infty}\frac{1}{k!}(-\mathbf{A}\tau_{\mathrm{ref}})^k. \tag{B.21}$$

The matrix $\mathbf{H}$ is given by the solution of the linear system:

$$\sum_{l=1}^{d}(A_{il}H_{\infty,lj} + A_{jl}H_{\infty,li}) = \sum_{l=1}^{d}\frac{B_{il}B_{jl}}{2}, \qquad H_{ij} = \sum_{s,r=1}^{d}[\delta_{j,s}\delta_{j,r} - G_{is}G_{jr}]H_{\infty,sr}. \tag{B.22}$$

In the case $d = 2$ considered in this thesis, the result of Eq. (B.22) is given by:

$$\begin{aligned}
H_{\infty,11} &= \frac{B_{11}^2 + B_{12}^2}{2A_{11}} - \frac{2A_{12}B_{12}B_{21}A_{11}A_{22} - A_{12}A_{21}A_{22}(B_{11}^2 + B_{12}^2) - A_{11}A_{12}^2(B_{21}^2 + B_{22}^2)}{2A_{11}(A_{11} + A_{22})(A_{11}A_{22} - A_{12}A_{21})},\\
H_{\infty,12} &= \frac{2B_{12}B_{21}A_{11}A_{22} - (B_{11}^2 + B_{12}^2)A_{22}A_{21} - A_{11}A_{12}(B_{21}^2 + B_{22}^2)}{2(A_{11} + A_{22})(A_{11}A_{22} - A_{12}A_{21})},\\
H_{\infty,21} &= H_{12},\\
H_{\infty,22} &= \frac{B_{21}^2 + B_{22}^2}{2A_{22}} - \frac{2A_{21}B_{12}B_{21}A_{11}A_{22} - A_{11}A_{12}A_{21}(B_{21}^2 + B_{22}^2) - A_{22}A_{21}^2(B_{11}^2 + B_{12}^2)}{2A_{22}(A_{11} + A_{22})(A_{11}A_{22} - A_{12}A_{21})},\\
\mathbf{H} &= \mathbf{H}_{\infty} - \mathbf{G}\mathbf{H}_{\infty}.
\end{aligned} \tag{B.23}$$

By the naive use of $\rho_{\mathrm{ref}}(\vec{a}|\vec{a}')$ in $\hat{\mathcal{R}}$, a huge number of terms with vanishing contribution will emerge and hence the procedure cannot be applied. For the sake of efficiency, the function ρ_{ref} is set to zero if the exponential factor in Eq. (B.20) is smaller than $\exp(-7)$. To take into account the neglected probability, the function $\rho_{\mathrm{ref}}(\vec{a}|\vec{a}')$ is renormalized numerically. The approximation was tested for a rough resolution and did not significantly changed the results.

C Parameters

C.1 Theory of spike-train power spectra

Table C.1.: Parameters of the numerical solution and simulation for the two-dimensional Fokker-Planck equation.

Fig.	v_0 [mV]	a_0 [mV]	a_{N-1} [mV]	N	method	T [s]	Δt [μs]	# Trials
2.5a	-40	-223.37	223.37	1200	direct	4	1	16000
2.5b	-40	-116.04	116.04	1200	direct	4	1	16000
2.6a	-8	-7	-7	1000	direct	4	10	10000
2.6b	-10	-15	15	1000	direct	4	10	10000
2.6c,m	-7	-27	30	1000	direct	4	10	10000
2.6d	-60	-18	18	1000	direct	4	10	10000
2.6e	-60	-40	40	1000	direct	4	10	10000
2.6f	-40	-100	120	1000	direct	4	10	10000
2.6h	-5	-8	8	1000	direct	4	10	10000
2.6i,n	-7	-20	20	1000	direct	4	10	10000
2.6j	-8	-35	35	1000	direct	4	10	10000
2.6k	-50	-30	30	1000	direct	4	10	10000
2.6l	-50	-40	40	1000	direct	4	10	10000
2.7a	-7	-4	4	1000	direct	4	10	10000
2.7b	-10	-6	6	1000	direct	4	10	10000
2.7c ,m	-15	-20	20	1000	direct	4	10	10000
2.7d	-60	-10	10	1000	direct	4	10	10000
2.7e	-70	-25	25	1000	direct	4	10	10000
2.7f	-75	-65	65	1000	direct	4	10	10000
2.7h	-5	-4	4	1000	direct	4	10	10000
2.7i,n	-8	-8	8	1000	direct	4	10	10000
2.7j	-8	-20	20	1000	direct	4	10	10000
2.8a	-60	-20	20	1000	direct	20	10	20000
2.8b	-60	-20	20	1000	direct	20	10	20000
2.9a	-50	0	15	1000	direct	4	10	10000
	-50	0	15	1000	direct	4	10	10000
	-50	0	30	1000	direct	4	10	10000

	-60	0	40	1000	direct	4	10	10000
2.9b	-50	0	0.1	1000	direct	4	10	10000
	-50	0	10	1000	direct	4	10	10000
	-60	0	30	1000	direct	4	10	10000
	-60	0	50	1000	direct	4	10	10000
2.9c	-12	-40	50	2000	direct	4	10	10000
	-12	-20	40	2000	direct	4	10	10000
	-12	-10	30	2000	direct	4	10	10000
	-12	5	25	2000	direct	4	10	10000
2.9d	-10	0	15	2000	direct	4	10	10000
	-8	-5	20	2000	direct	4	10	10000
	-8	-10	25	2000	direct	4	10	10000
	-10	-20	40	2000	direct	4	10	10000
2.9e	-40	-5	20	2000	direct	4	10	10000
	-40	-20	40	2000	direct	4	10	10000
	-45	-60	80	2000	direct	4	10	10000
2.9f	-50	-20	40	2000	direct	4	10	10000
	-60	-200	220	2000	direct	4	10	10000
2.10	-20	-1	15	2500	direct	20	1	40000
A.1,A.3	-40	-223.37	223.37	100–1200	direct	-	-	-
A.3	-40	-116.04	116.04	100–1200	direct	-	-	-

Table C.2.: Parameters used in chapter 2. Fig. 3-8 and 13,14 correspond to the LIF neuron driven by colored noise and Fig 9-12 to the EIF neuron with spike frequency adaptation.

Fig.	v_{th} [mV]	v_{r} [mV]	τ_{ref} [ms]	τ_m [ms]	μ [mV]	β [mV$\sqrt{\text{s}}$]	τ_a [ms]	δ_a [mV]	A	b_1 [mV$\sqrt{\text{s}}$]	b_2 [mV$\sqrt{\text{s}}$]	v_{ref} [mV]	
2.2	20	0	10	20	15	1	100	5	0.1	0	0.5	50	
	v_{th} [mV]	v_{r} [mV]	τ_{ref} [ms]	τ_m [ms]	μ [mV]	β [mV$\sqrt{\text{s}}$]	τ_a [ms]	b [mV$\sqrt{\text{s}}$]					
2.5,A.3	20	0	2	20	15	4	5	-5.26, -2.74					
2.6	20	0	2	20	15,30	1,4	5,40,200	-0.68,-2.74					
2.7	20	0	2	20	15,30	1,4	5,40,200	0.41,1.66					
2.8	20	0	0,10,100	20	15	3	40	-2.05, 1.24					
A.1	20	0	2	20	15	4	5	-5.26					
	v_{th} [mV]	v_r [mV]	τ_{ref} [ms]	τ_m [ms]	μ [mV]	v_T [mV]	Δ_T [mV]	β_1 [mV$\sqrt{\text{s}}$]	τ_a [ms]	δ_a [mV]	A	b [mV$\sqrt{\text{s}}$]	v_{ref} [mV]
2.9a	28	0	0	20	15	20	2	3	40–500	3	0	0	–
2.9b	28	0	0	20	15	20	2	3	100	0.01–15	0	0	–
2.9c	28	0	0	20	30	20	2	$\sqrt{2}$	40–500	3	0	3	–
2.9d	28	0	0	20	30	20	2	$\sqrt{2}$	100	3	0	0.01–4	–
2.9e,f	28	0	0	20	15	20	2	3	100	3	0–100	0	–
2.10	3	0	2	20	-3	-3	2	0.5	200	3	0.2	0	50
	v_{th} [mV]	v_r [mV]	τ_{ref} [ms]	τ_m [ms]	μ [mV]	β_1 [mV$\sqrt{\text{s}}$]	Γ [1/s]	Ω_0 [1/s]	β_2 [mV/$\sqrt{s^3}$]				
2.11	20	0	0	20	35	0.5	5	$2\pi \cdot 23$	2500				

Table C.3.: Parameters of the numerical solution and simulation for three-dimensional Fokker-Planck equation.

Fig.	v_0 [mV]	y_0 [mV]	y_{Ny} [mV]	s_0 [mV/s]	s_{Ns} [mV/s]	N_v	N_y	N_s	method	T [s]	Δt [μs]	# Trials
2.11 ($\omega \neq \omega_0$)	-1	-22	22	-3300	3300	1000	100	100	iterative	25	2	4000
2.11 ($\omega = \omega_p$)	"	"	"	"	"	1000	150	150	"	"	"	"

C.2 Mean-field theory

Table C.4.: Parameters of the network simulation (shown in Fig. 3.3, 3.4 and 3.5).

Fig	N_E	N_I	C_E	C_I	J [mV]	g	D [ms]	τ_m [ms]	RI_{ext} [mV]	v_{th} [mV]	τ_{ref} [ms]	T [s]	Δt [μs]
3.2	200000	50000	500	125	0.4	4.5	2	20	30	20	2	2	10

Table C.5.: Parameters of the self-consistent solutions (Figs. 3.3, 3.4 and 3.5).

Figure	d	**A**	**B** [mV/$\sqrt{\text{s}}$]	$\vec{\beta}$ [mV/$\sqrt{\text{s}}$]
3.3	0			2.360
	1	91.43	-107.0	2.321
	2	$\begin{pmatrix} 103.5 & 202.8 \\ -21.56 & 103.5 \end{pmatrix}$	$\begin{pmatrix} -233.3 & 0 \\ 0 & 167.7 \end{pmatrix}$	$\begin{pmatrix} 2.324 \\ 0 \end{pmatrix}$
3.4	1	120.9	-136.8	2.321
	2	$\begin{pmatrix} 105.2 & 169.1 \\ -19.01 & 105.2 \end{pmatrix}$	$\begin{pmatrix} -394.1 & 0 \\ 0 & 85.00 \end{pmatrix}$	$\begin{pmatrix} 2.329 \\ 0 \end{pmatrix}$
3.5	1	92.05	-107.5	2.322
	2	$\begin{pmatrix} 201.7 & -14.89 \\ -263.0 & 201.7 \end{pmatrix}$	$\begin{pmatrix} -90.57 & 0 \\ 0 & 19.22 \end{pmatrix}$	$\begin{pmatrix} 2.330 \\ 0 \end{pmatrix}$

Table C.6.: Parameters of the numerical solution for two-dimensional Fokker-Planck equation.

Fig.	v_0 [mV]	a_0 [mV]	a_N [mV]	N	method
3.3	-30	-40	40	1000	direct
3.4	-30	-40	40	1000	direct
3.5	-30	-40	40	1000	direct

Table C.7.: Parameters of the numerical solution for three-dimensional Fokker-Planck equation.

Fig.	v_0 [mV]	$a_{1\,0}$ [mV]	$a_{1\,N_{a1}}$ [mV]	$a_{2\,0}$ [mV]	$a_{2\,N_{a2}}$ [mV]	N_v	N_{a1}	N_{a2}	method
3.3	-25	-32.22	32.22	-29.14	29.14	500	100	100	iterative
3.4	-25	-108.3	108.3	-26.03	26.03	500	100	100	iterative
3.5	-25	-17.20	17.20	-16.66	16.66	500	100	100	iterative

Table C.8.: Parameters of the heterogeneous network simulation with Erdös-Renyi topology. Other network in Figs. 3.7b and 3.9 with same parameters and exponentially distributed synaptic weights with $\langle J \rangle = 0.1\,\mathrm{mV}$.

Fig	N_E	N_I	$\langle C_E \rangle$	$\langle C_I \rangle$	J [mV]	g	D [ms]	τ_m [ms]	RI_{ext} [mV]	v_{th} [mV]	τ_{ref} [ms]	T [s]	Δt [μs]
3.7a,3.8	100000	25000	1000	250	0.1	3.5,4,6	2	20	30	20	2	10	10

C.3 Diffusion-decision model

Table C.9.: Parameters of the Drift Diffusion models and simulation parameters in chapter 4. In all cases, $x_s = 0$ and $\Delta = 0.2$.

Fig.	τ_x [s]	σ	x_A	x_B	$f(x)$	T [s]	Δt [ms]	# Trials
5.2	0.1	0.5	-1	2	0.2	20	0.1	10000
5.3 (a-e), 5.4, 5.5	0.1	0.4	-1	1	$2x^3$-x+0.2	20	0.1	10000
5.3 (f-h)	1.0	2	-3	1	1.085-$2x^2$-x-0.5e^x-8sin($2\pi x$)	20	0.1	

Bibliography

Abbott, L. and van Vreeswijk, C. Asynchronous states in networks of pulse-coupled oscillators. *Phys. Rev. E.*, 48:1483, 1993.

Abramowitz, M. and Stegun, I. A. *Handbook of Mathematical Functions*. Dover, New York, 1970.

Alijani, A. and Richardson, M. J. E. Rate response of neurons subject to fast or frozen noise: From stochastic and homogeneous to deterministic and heterogeneous populations. *Phys. Rev. E*, 84:011919–1, 2011.

Aljadeff, J., Stern, M., and Sharpee, T. Transition to chaos in random networks with cell-type-specific connectivity. *Phys. Rev. Lett.*, 114(8):088101, 2015.

Almog, M. and Korngreen, A. Is realistic neuronal modeling realistic? *J. Neurophys.*, 116: 2180, 2016.

Amit, D. J. and Brunel, N. Model of global spontaneous activity and local structured delay activity during delay periods in the cerebral cortex. *Cereb. Cortex*, 7:237, 1997.

Apfaltrer, F., Ly, C., and Tranchina, D. Population density methods for stochastic neurons with realistic synaptic kinetics: Firing rate dynamics and fast computational methods. *Network*, 17:373, 2006.

Augustin, M., Ladenbauer, J., Baumann, F., and Obermayer, K. Low-dimensional spike rate models derived from networks of adaptive integrate-and-fire neurons: comparison and implementation. *PLoS Comput. Biol.*, 13:e1005545, 2017.

Avila-Akerberg, O. and Chacron, M. J. Nonrenewal spike train statistics: causes and consequences on neural coding. *Exp. Brain Res.*, 210:353, 2011.

Badel, L., Lefort, S., Brette, R., Petersen, C. C. H., Gerstner, W., and Richardson, M. J. E. Dynamic I-V curves are reliable predictors of naturalistic pyramidal-neuron voltage traces. *J. Neurophysiol.*, 99:656, 2008.

Bair, W., Koch, C., Newsome, W., and Britten, K. Power spectrum analysis of bursting cells in area MT in the behaving monkey. *J. Neurosci.*, 14:2870, 1994.

Baker, C., Ebsc, C., Lampl, I., and Rosenbaum, R. Correlated states in balanced neuronal networks. *Phys. Rev. E*, 99(5):052414, 2019.

Bauermann, J. and Lindner, B. Multiplicative noise is beneficial for the transmission of sensory signals in simple neuron models. *Biosystems*, 178:25–31, 2019.

Bauermeister, C., Schwalger, T., Russell, D., Neiman, A. B., and Lindner, B. Characteristic effects of stochastic oscillatory forcing on neural firing: Analytical theory and comparison to paddlefish electroreceptor data. *PLoS Comput. Biol.*, 9:e1003170, 2013.

Benda, J. and Herz, A. V. M. A universal model for spike-frequency adaptation. *Neural Comput.*, 15:2523, 2003.

Billah, K. and Shinozuka, M. Numerical method for colored-noise generation and its application to a bistable system. *Phys. Rev. A.*, 42:7492, 1990.

Blankenburg, S., Wu, W., Lindner, B., and Schreiber, S. Information filtering in resonant neurons. *J. Comput. Neurosci.*, 39:349, 2015.

Bogacz, R. Optimal decision-making theories: linking neurobiology with behaviour. *Trends Cogn. Sci.*, 11(3):118–125, 2007.

Bogacz, R., Brown, E., Moehlis, J., Holmes, P., and Cohen, J. D. The physics of optimal decision making: a formal analysis of models of performance in two-alternative forced-choice tasks. *Psychol. Rev.*, 113(4):700, 2006.

Brette, R. and Gerstner, W. Adaptive exponential integrate-and-fire model as an effective description of neuronal activity. *J. Neurophysiol.*, 94:3637, 2005.

Britten, K., Shadlen, M., Newsome, W., and Movshon, A. The analysis of visual motion: a comparison of neuronal and psychophysical performance. *J. Neurosci.*, 12(12):4745–4765, 1992.

Brunel, N. Dynamics of sparsely connected networks of excitatory and inhibitory spiking neurons. *J. Comput. Neurosci.*, 8:183, 2000.

Brunel, N. and Hakim, V. Fast global oscillations in networks of integrate-and-fire neurons with low firing rates. *Neural Comput.*, 11:1621, 1999.

Brunel, N. and Sergi, S. Firing frequency of leaky integrate-and-fire neurons with synaptic current dynamics. *J. Theor. Biol.*, 195:87, 1998.

Brunel, N., Chance, F. S., Fourcaud, N., and Abbott, L. F. Effects of synaptic noise and filtering on the frequency response of spiking neurons. *Phys. Rev. Lett.*, 86:2186, 2001.

Brunel, N., Hakim, V., and Richardson, M. J. E. Firing-rate resonance in a generalized integrate-and-fire neuron with subthreshold resonance. *Phys. Rev. E.*, 67:051916, 2003.

Buice, M. A., Cowan, J. D., and Chow, C. C. Systematic fluctuation expansion for neural network activity equations. *Neural Comput.*, 22(2):377–426, 2010.

Burkitt, A. N. A review of the integrate-and-fire neuron model: I. homogeneous synaptic input. *Biol. Cyber.*, 95:1, 2006a.

Burkitt, A. N. A review of the integrate-and-fire neuron model: II. inhomogeneous synaptic input and network properties. *Biol. Cyber.*, 95:97, 2006b.

Casti, A., Omurtag, A., Sornborger, A., Kaplan, E., Knight, B., Victor, J., and Sirovich, L. A population study of integrate-and-fire-or-burst neurons. *Neural Comput.*, 14:957, 2002.

Câteau, H. and Reyes, A. D. Relation between single neuron and population spiking statistics and effects on network activity. *Phys. Rev. Lett.*, 96:058101, 2006.

Chacron, M. J., Longtin, A., St-Hilaire, M., and Maler, L. Suprathreshold stochastic firing dynamics with memory in P-type electroreceptors. *Phys. Rev. Lett*, 85:1576, 2000.

Chacron, M. J., Longtin, A., and Maler, L. Negative interspike interval correlations increase the neuronal capacity for encoding time-dependent stimuli. *J. Neurosci.*, 21:5328, 2001.

Chen, N. and Maida, A. Efficient statistically accurate algorithms for the fokker-planck equation in large dimensions. *J. Comput. Phys.*, 354:242–268, 2018.

Cherney, D., Denton, T., and Waldron, A. *Linear Algebra*. CreateSpace Independent Publishing Platform, 2016.

Chittka, L., Skorupski, P., and Raine, N. Speed–accuracy tradeoffs in animal decision making. *Trends Ecol. Evol.*, 24(7):400–407, 2009.

Cisek, P., Puskas, G. A., and El-Murr, S. Decisions in changing conditions: the urgency-gating model. *J. Neurosci.*, 29(37):11560–11571, 2009.

Clopath, C., Jolivet, R., Rauch, A., Luescher, H.-R., and Gerstner, W. Predicting neuronal activity with simple models of the threshold type: Adaptive Exponential Integrate-and-Fire model with two compartments. *Neurocomputing*, 70:1668, 2007.

Cox, D. R. and Miller, H. D. *The Theory of Stochastic Processes*. Methuen & Co, London, 1965.

Crisanti, A. and H. Sompolinsky, H. Path integral approach to random neural networks. *Phys. Rev. E*, 98(6):062120, 2018.

Darling, D. A. and Siegert, A. J. F. The 1st passage problem for a continuous markov process. *Ann. Math. Stat.*, 24:624, 1953.

Dayan, P. and Abbott, L. F. *Theoretical Neuroscience*. MIT Press, Cambridge MA, 2001.

De Mayo, B. *The Everyday Physics of Hearing and Vision.* Morgan & Claypool Publishers, 2014.

Deger, M., Schwalger, T., Naud, R., and Gerstner, W. Fluctuations and information filtering in coupled populations of spiking neurons with adaptation. *Phys. Rev. E*, 90:062704, 2014.

Deniz, T. and Rotter, S. Solving the two-dimensional Fokker-Planck equation for strongly correlated neurons. *Phys. Rev. E*, 95:012412, 2017.

Destexhe, A. and Rudolph-Lilith, M. *Neuronal noise*, volume 8. Springer Science & Business Media, 2012.

Destexhe, A., Rudolph, M., and Paré, D. The high-conductance state of neocortical neurons in vivo. *Nat. Rev. Neurosci.*, 4:739, 2003.

Di Volo, M., Romagnoni, A., Capone, C., and Destexhe, A. Biologically realistic mean-field models of conductance-based networks of spiking neurons with adaptation. *Neural Comput.*, 31(4):653–680, 2019.

Doiron, B., Litwin-Kumar, A., Rosenbaum, R., Ocker, G. K., and Josić, K. The mechanics of state-dependent neural correlations. *Nat. Neurosci.*, 19:383, 2016.

Doose, J., Doron, G., Brecht, M., and Lindner, B. Noisy juxtacellular stimulation in vivo leads to reliable spiking and reveals high-frequency coding in single neurons. *J. Neurosci.*, 36:11120, 2016.

Dummer, B., Wieland, S., and Lindner, B. Self-consistent determination of the spike-train power spectrum in a neural network with sparse connectivity. *Front. Comput. Neurosc.*, 8: 104, 2014.

Dygas, M., Matkowsky, B., and Schuss, Z. A singular perturbation approach to non-markovian escape rate problems. *SIAM J. Appl. Math.*, 46:265, 1986.

Edwards, B. W., Wakefield, G. H., and Powers, N. L. The spectral shaping of neural discharges by refractory effects. *J. Acoust. Soc. Am.*, 93:3353, 1993.

Eissfeller, H. and Opper, M. New Method for Studying the Dynamics of Disordered Spin Systems Without Finite-Size Effects. *Phys. Rev. Lett.*, 68:2094, 1992.

Engel, T. A., Schimansky-Geier, L., Herz, A. V. M., Schreiber, S., and Erchova, I. Subthreshold membrane-potential resonances shape spike-train patterns in the entorhinal cortex. *J. Neurophysiol.*, 100:1576, 2008.

Engel, T. A., Helbig, B., Russell, D. F., Schimansky-Geier, L., and Neiman, A. B. Coherent stochastic oscillations enhance signal detection in spiking neurons. *Phys. Rev. E.*, 80: 021919, 2009.

Erdős, P. and Rényi, A. On the evolution of random graphs. *Publ. Math. Inst. Hung. Acad. Sci*, 5(1):17–60, 1960.

Farkhooi, F., Strube-Bloss, M. F., and Nawrot, M. P. Serial correlation in neural spike trains: Experimental evidence, stochastic modeling, and single neuron variability. *Phys. Rev. E.*, 79:021905, 2009.

Fisch, K., Schwalger, T., Lindner, B., Herz, A., and Benda, J. Channel noise from both slow adaptation currents and fast currents is required to explain spike-response variability in a sensory neuron. *J. Neurosci.*, 32:17332, 2012.

Fourcaud, N. and Brunel, N. Dynamics of the firing probability of noisy integrate-and-fire neurons. *Neural Comput.*, 14:2057, 2002.

Fourcaud-Trocmé, N., Hansel, D., van Vreeswijk, C., and Brunel, N. How spike generation mechanisms determine the neuronal response to fluctuating inputs. *J. Neurosci.*, 23:11628, 2003.

Frobenius, G. Ueber relationen zwischen den näherungsbrüchen von potenzreihen. *J. Reine Angew. Math.*, 90:1–17, 1881.

Fusi, S. and Mattia, M. Collective behavior of networks with linear (vlsi) integrate-and-fire neurons. *Neural Comput.*, 11:633, 1999.

Gabbiani, F. and Koch, C. Principles of spike train analysis. In *Methods in Neuronal Modeling: From Synapses to Networks*, page 313. Cambridge, MA: MIT Press, 1998.

Gammaitoni, L., Hänggi, P., Jung, P., and Marchesoni, F. Stochastic resonance. *Rev. Mod. Phys.*, 70:223, 1998.

Gardiner, C. W. *Handbook of Stochastic Methods*. Springer-Verlag, Berlin, 1985.

Gerstein, G. L. and Mandelbrot, B. Random walk models for the spike activity of a single neuron. *Biophys. J.*, 4:41, 1964.

Gerstner, W., Kistler, W. M., Naud, R., and Paninski, L. *Neuronal Dynamics From single neurons to networks and models of cognition*. Cambridge University Press, Cambridge, 2014.

Ghose, G. and Freeman, R. Oscillatory discharge in the visual system: does it have a functional role? *J. Neurophysiol.*, 68(5):1558–1574, 1992.

Gilson, M. and Fukai, T. Stability versus neuronal specialization for stdp: long-tail weight distributions solve the dilemma. *PloS one*, 6(10), 2011.

Ginzburg, I. and Sompolinsky, H. Correlation functions in a large stochastic network. In Cowan, J., Tesauro, G., and Alspector, J., editors, *Advances in Neural Information Processing Systems*, volume 6, page 471, 1994.

Gold, J. and Shadlen, M. The neural basis of decision making. *Annu. Rev. Neurosci.*, 30, 2007.

Green, D. M., Smith, A. F., and Gierke, S. M. Choice reaction time with a random foreperiod. *Percept. Psychophys.*, 34(3):195–208, 1983.

Griffith, J. and G. Horn, G. An analysis of spontaneous impulse activity of units in the striate cortex of unrestrained cats. *J. Physiol.*, 186(3):516, 1966.

Guardia, E., Marchesoni, F., and Miguel, M. S. Escape times in systems with memory effects. *Phys. Lett. A*, 100:15, 1984.

Guennebaud, G., Jacob, B., et al. Eigen v3. http://eigen.tuxfamily.org, 2010.

Gutfreund, Y., Yarom, Y., and Segev, I. Subthreshold oscillations and resonant frequency in guinea-pig cortical neurons: physiology and modelling. *J. Physiol.*, 483(3):621–640, 1995.

Guz, S. and Sviridov, M. Brownian motion with "green" noise in a periodic potential. *Phys. Lett. A*, 240:43, 1998.

Guz, S. and Sviridov, M. "green" noise in quasistationary stochastic systems. *Chaos: An Interdisciplinary Journal of Nonlinear Science*, 11(3):605–610, 2001.

Hänggi, P. and Jung, P. Colored noise in dynamical-systems. *Adv. Chem. Phys.*, 89:239, 1995.

Hänggi, P., Jung, P., Zerbe, C., and Moss, F. Can colored noise improve stochastic resonance. *J. Stat. Phys.*, 70:25, 1993.

Hanks, T., Ditterich, G., and Shadlen, M. Microstimulation of macaque area lip affects decision-making in a motion discrimination task. *Nat. Neurosci.*, 9(5):682–689, 2006.

Hansel, D. and Sompolinsky, H. Synchronization and computation in a chaotic neural network. *Phys. Rev. Lett.*, 68(5):718, 1992.

Harrison, P. M., Badel, L., Wall, M. J., and Richardson, M. J. E. Experimentally Verified Parameter Sets for Modelling Heterogeneous Neocortical Pyramidal-Cell Populations. *PLoS Comput. Biol.*, 11:8, 2015.

Hawkins, G. E., Forstmann, B. U., Wagenmakers, E. J., Ratcliff, R., and Brown, S. D. Revisiting the evidence for collapsing boundaries and urgency signals in perceptual decision-making. *J. Neurosci.*, 35(6):2476–2484, 2015.

Heekeren, H., Marrett, S., and Ungerleider, L. The neural systems that mediate human perceptual decision making. *Nat. Rev. Neurosci.*, 9(6):467, 2008.

Helias, M., Deger, M., Diesmann, M., and Rotter, S. Equilibrium and response properties of the integrate-and-fire neuron in discrete time. *Front. Comput. Neurosc.*, 3:29, 2010.

Helias, M., Tetzlaff, T., and Diesmann, M. The correlation structure of local neuronal networks intrinsically results from recurrent dynamics. *PLoS Comput. Biol.*, 10(1), 2014.

Hessler, N., Shirke, A., and Malinow, R. The probability of transmitter release at a mammalian central synapse. *Nature*, 366(6455):569–572, 1993.

Hodgkin, A. L. and Huxley, A. F. A quantitative description of membrane current and its application to conduction and excitation in nerve. *J. Physiol. (Lond.)*, 10:500, 1952.

Holden, A. V. *Models of the Stochastic Activity of Neurones*. Springer-Verlag, Berlin, 1976.

Hromadka, T., DeWeese, M. R., and Zador, A. M. Sparse representation of sounds in the unanesthetized auditory cortex. *Plos Biol.*, 6:124, 2008.

Izhikevich, E. M. Simple model of spiking neurons. *IEEE T. Neural Networks*, 14:1569, 2003.

Izhikevich, E. M. *Dynamical Systems in Neuroscience: The Geometry of Excitability and Bursting*. The MIT Press, Cambridge, London, 2007.

Johanson, D., Cesario, J., and Pleskac, T. How prior information and police experience impact decisions to shoot. *J. Pers. Soc. Psychol.*, 115(4):601, 2018.

Johnson, J. B. Thermal agitation of electricity in conductors. *Phys. Rev.*, 32:97, 1928.

Jolivet, R., Kobayashi, R., Rauch, A., Naud, R., Shinomoto, S., and Gerstner, W. A benchmark test for a quantitative assessment of simple neuron models. *J. Neurosci. Meth.*, 169: 417, 2008.

Kadmon, J. and Sompolinsky, H. Transition to chaos in random neuronal networks. *Phys. Rev. X*, 5:041030, 2015.

Kandel, E. R., Schwartz, J. H., and Jessel, T. M. *Principles of Neural Science*. McGraw-Hill Companies, U. S., 2000.

Kawaguchi, Y. Groupings of nonpyramidal and pyramidal cells with specific physiological and morphological characteristics in rat frontal cortex. *J. Neurophysiol.*, 69(2):416–431, 1993.

Kistler, W. M., Gerstner, W., and van Hemmen, J. L. Reduction of the hodgkin-huxley equations to a single-variable threshold model. *Neural Comput.*, 9:1015, 1997.

Knight, B. W., Omurtag, A., and Sirovich, L. The approach of a neuron population firing rate to a new equilibrium: an exact theoretical result. *Neural Comput.*, 12:1045, 2000.

Koch, C. *Biophysics of Computation - Information Processing in Single Neurons*. Oxford University Press, New York, Oxford, 1999.

Koch, K. and Fuster, J. Unit activity in monkey parietal cortex related to haptic perception and temporary memory. *Exp. Brain Res.*, 76(2):292–306, 1989.

Krajbich, I. and Rangel, A. Multialternative drift-diffusion model predicts the relationship between visual fixations and choice in value-based decisions. *PNAS*, 108(33):13852–13857, 2011.

Kuhn, A., Aertsen, A., and Rotter, S. Higher-order statistics of input ensembles and the response of simple model neurons. *Neural Comput.*, 15(1):67–101, 2003.

Kupferman, R. Fractional kinetics in kac–zwanzig heat bath models. *J. stat. phys.*, 114:291, 2004.

Lampl, I., Reichova, I., and Ferster, D. Synchronous membrane potential fluctuations in neurons of the cat visual cortex. *Neuron*, 22:361, 1999.

Langer, J. Statistical theory of the decay of metastable states. *Ann. Phys.*, 54:258, 1969.

Lapicque, L. Recherches quantitatives sur l'excitation électrique des nerfs traitéecomme une polarization. *J. Physiol. Pathol. Gen.*, 9:620, 1907.

Lerchner, A., Ursta, C., Hertz, J., Ahmadi, M., Ruffiot, P., and Enemark, S. Response variability in balanced cortical networks. *Neural Comput.*, 18:634, 2006.

Li, X. An overview of SuperLU: Algorithms, implementation, and user interface. *ACM Transactions on Mathematical Software*, 31(3):302–325, 2005.

Lindner, B. *Coherence and Stochastic Resonance in Nonlinear Dynamical Systems.* Logos-Verlag, Berlin, 2002.

Lindner, B. Interspike interval statistics of neurons driven by colored noise. *Phys. Rev. E.*, 69:022901, 2004.

Lindner, B. Superposition of many independent spike trains is generally not a Poisson process. *Phys. Rev. E.*, 73:022901, 2006.

Lindner, B., Schimansky-Geier, L., and Longtin, A. Maximizing spike train coherence or incoherence in the leaky integrate-and-fire model. *Phys. Rev. E.*, 66:031916, 2002.

Lindner, B., García-Ojalvo, J., Neiman, A., and Schimansky-Geier, L. Effects of noise in excitable systems. *Phys. Rep.*, 392:321, 2004.

Liu, Y. H. and Wang, X. J. Spike-frequency adaptation of a generalized leaky integrate-and-fire model neuron. *J. Comput. Neurosci.*, 10:25, 2001.

London, M. and Häusser, M. Dendritic computation. *Annu. Rev. Neurosci.*, 28:503–532, 2005.

Longtin, A. Stochastic resonance in neuron models. *J. Stat. Phys.*, 70:309, 1993.

Ly, C. and Tranchina, D. Spike train statistics and dynamics with synaptic input from any renewal process: A population density approach. *Neural Comp.*, 21:360, 2009.

Manwani, A. and Koch, C. Detecting and estimating signals in noisy cable structures, i: Neuronal noise sources. *Neural Comput.*, 11(8):1797–1829, 1999.

Mari, C. Random networks of spiking neurons: instability in the xenopus tadpole moto-neural pattern. *Phys. Rev. Lett.*, 85(1):210, 2000.

Markram, H. and Tsodyks, M. Redistribution of synaptic efficacy between neocortical pyramidal neurons. *Nature*, 382:807, 1996.

Markram, H., Toledo-Rodriguez, M., Wang, Y., Gupta, A., Silberberg, G., and Wu, C. Z. Interneurons of the neocortical inhibitory system. *Nat. Rev. Neurosci.*, 5:793, 2004.

Markram, H., Muller, R., Ramaswamy, S., Reimann, M., Abdellahn, M., Sanchez, C., Ailamaki, A., Alonso-Nanclares, L., Antille, N., Arsever, S., et al. Reconstruction and simulation of neocortical microcircuitry. *Cell*, 163(2):456–492, 2015.

McCormick, D., Connors, B., Lighthall, J., and Prince, D. Comparative electrophysiology of pyramidal and sparsely spiny stellate neurons of the neocortex. *J. Neurophysiol.*, 54(4): 782–806, 1985.

McMillen, T. and Holmes, P. The dynamics of choice among multiple alternatives. *J. Math. Psychol.*, 50(1):30–57, 2006.

Middleton, J. W., Chacron, M. J., Lindner, B., and Longtin, A. Firing statistics of a neuron model driven by long-range correlated noise. *Phys. Rev. E.*, 68:021920, 2003.

Mirollo, R. and Strogatz, S. Synchronization of pulse-coupled biological oscillators. *Siam J. Appl. Math.*, 50:1645, 1990.

Moreno-Bote, R. and Parga, N. Role of synaptic filtering on the firing response of simple model neurons. *Phys. Rev. Lett.*, 92:028102, 2004.

Moreno-Bote, R. and Parga, N. Auto- and crosscorrelograms for the spike response of leaky integrate-and-fire neurons with slow synapses. *Phys. Rev. Lett.*, 96:028101, 2006.

Moreno-Bote, R. and Parga, N. Response of integrate-and-fire neurons to noisy inputs filtered by synapses with arbitrary timescales: Firing rate and correlations. *Neural Comput.*, 22: 1528, 2010.

Morgan, M. J. and Ward, R. Conditions for motion flow in dynamic visual noise. *Vision Res.*, 20(5):431–435, 1980.

Mori, H. A continued-fraction representation of the time-correlation functions. *Prog. Theor. Phys.*, 34:399, 1965.

Naud, R., Marcille, N., Clopath, C., and Gerstner, W. Firing patterns in the adaptive exponential integrate-and-fire model. *Biol. Cybern.*, 99:335, 2008.

Naundorf, B., Geisel, T., and Wolf, F. Action potential onset dynamics and the response speed of neuronal populations. *J. Comput. Neurosci.*, 18:297, 2005.

Neiman, A. B. and Russell, D. F. Two distinct types of noisy oscillators in electroreceptors of paddlefish. *J. Neurophysiol.*, 92:492, 2004.

Nykamp, D. Q. and Tranchina, D. A population density approach that facilitates large-scale modeling of neural networks: Analysis and an application to orientation tuning. *J. Comput. Neurosci.*, 8:19, 2000.

Nyquist, H. Thermal agitation of electric charge in conductors. *Phys. Rev.*, 32:110, 1928.

O'Connor, D., Peron, S., Huber, D., and Svoboda, K. Neural activity in barrel cortex underlying vibrissa-based object localization in mice. *Neuron*, 67(6):1048–1061, 2010.

Okun, M. and Lampl, I. Instantaneous correlation of excitation and inhibition during ongoing and sensory-evoked activities. *Nat. Neurosci.*, 11(5):535, 2008.

Ostojic, S. Two types of asynchronous activity in networks of excitatory and inhibitory spiking neurons. *Nat. Neurosci.*, 17:594, 2014.

Ostojic, S., Brunel, N., and Hakim, V. How connectivity, background activity, and synaptic properties shape the cross-correlation between spike trains. *J. Neurosci.*, 29:10234, 2009.

Ostojic, S., Szapiro, G., Schwartz, E., Barbour, B., Brunel, N., and Hakim, V. Neuronal Morphology Generates High-Frequency Firing Resonance. *J. Neurosci.*, 35:7056, 2015.

Palmer, J., Huk, A. C., and Shadlen, M. N. The effect of stimulus strength on the speed and accuracy of a perceptual decision. *J. Vision*, 5(5):1–1, 2005.

Pena, R., Vellmer, S., Bernardi, D., Roque, A., and Lindner, B. Self-consistent scheme for spike-train power spectra in heterogeneous sparse networks. *Front. Comput. Neurosc.*, 12 (9), 2018.

Pichler, L., Masud, A., and Bergman, L. A. Numerical solution of the fokker–planck equation by finite difference and finite element methods—a comparative study. In *Computational Methods in Stochastic Dynamics*, pages 69–85. Springer, 2013.

Poulet, J. F. A. and Petersen, C. C. H. Internal brain state regulates membrane potential synchrony in barrel cortex of behaving mice. *Nature*, 454:881, 2008.

Press, W. H., Teukolsky, S. A., Vetterling, W. T., and Flannery, B. P. *Numerical Recipes 3rd Edition: The Art of Scientific Computing.* Cambridge University Press, Cambridge, 2007.

Puil, E., Gimbarzevsky, B., and R.M. Miura, R. Quantification of membrane properties of trigeminal root ganglion neurons in guinea pigs. *J. Neurophysiol.*, 55(5):995–1016, 1986.

Ratcliff, R. A theory of memory retrieval. *Psychol. Rev.*, 85(2):59, 1978.

Ratcliff, R. A diffusion model account of response time and accuracy in a brightness discrimination task: Fitting real data and failing to fit fake but plausible data. *Psychon. B. Rev.*, 9(2):278, 2002.

Ratcliff, R. and McKoon, G. The diffusion decision model: theory and data for two-choice decision tasks. *Neural Comput.*, 20(4):873–922, 2008.

Ratcliff, R. and Rouder, J. N. Modeling response times for two-choice decisions. *Psychol. Sci.*, 9(5):347–356, 1998.

Ratcliff, R. and Smith, P. L. A comparison of sequential sampling models for two-choice reaction time. *Psychol. Rev.*, 111(2):333, 2004.

Ratcliff, R. and Tuerlinckx, F. Estimating parameters of the diffusion model: Approaches to dealing with contaminant reaction times and parameter variability. *Psychon. B. Rev.*, 9 (3):438–481, 2002.

Ratcliff, R., Zandt, T. V., and McKoon, G. Connectionist and diffusion models of reaction time. *Psychol. Rev.*, 106(2):261, 1999.

Ratcliff, R., Smith, P. L., Brown, S. D., and McKoon, G. Diffusion decision model: current issues and history. *Trends Cogn. Sci.*, 20(4):260–281, 2016.

Ratnam, R. and Nelson, M. E. Nonrenewal statistics of electrosensory afferent spike trains: Implications for the detection of weak sensory signals. *J. Neurosci.*, 20:6672, 2000.

Renart, A., Rocha, J. D. L., Bartho, P., Hollender, L., Parga, N., Reyes, A., and Harris, K. D. The Asynchronous State in Cortical Circuits. *Science*, 327:587, 2010.

Resulaj, A.-K., Kiani, R., Wolpert, D., and Shadlen, M. Changes of mind in decision-making. *Nature*, 461(7261):263–266, 2009.

Ricciardi, L. M. *Diffusion Processes and Related Topics on Biology.* Springer-Verlag, Berlin, 1977.

Richardson, M. J. E. Effects of synaptic conductance on the voltage distribution and firing rate of spiking neurons. *Phys. Rev. E.*, 69:051918, 2004.

Richardson, M. J. E. Firing-rate response of linear and nonlinear integrate-and-fire neurons to modulated current-based and conductance-based synaptic drive. *Phys. Rev. E.*, 76:021919, 2007.

Richardson, M. J. E. Spike-train spectra and network response functions for non-linear integrate-and-fire neurons. *Biol. Cybern.*, 99:381, 2008.

Richardson, M. J. E. and Gerstner, W. Synaptic shot noise and conductance fluctuations affect the membrane voltage with equal significance. *Neural Comput.*, 17:923, 2005.

Richardson, M. J. E. and Gerstner, W. Statistics of subthreshold neuronal voltage fluctuations due to conductance-based synaptic shot noise. *Chaos*, 16:026106, 2006.

Richardson, M. J. E. and Swarbrick, R. Firing-rate response of a neuron receiving excitatory and inhibitory synaptic shot noise. *Phys. Rev. Lett.*, 105:178102, 2010.

Richardson, M. J. E., Brunel, N., and Hakim, V. From subthreshold to firing-rate resonance. *J. Neurophysiol.*, 89:2538, 2003.

Risken, H. *The Fokker-Planck Equation*. Springer, Berlin, 1984.

Roitman, J. D. and Shadlen, M. N. Response of neurons in the lateral intraparietal area during a combined visual discrimination reaction time task. *J. Neurosci.*, 22(21):9475–9489, 2002.

Romo, R. and Salinas, E. Touch and go: decision-making mechanisms in somatosensation. *Annu. Rev. Neurosci*, 24(1):107–137, 2001.

Roxin, A. and Ledberg, A. Neurobiological models of two-choice decision making can be reduced to a one-dimensional nonlinear diffusion equation. *PLoS Computational Biology*, 4(3):e1000046, 2008.

Roxin, A., Brunel, N., Hansel, D., Mongillo, G., and van Vreeswijk, C. On the distribution of firing rates in networks of cortical neurons. *J. Neurosci.*, 31:16217, 2011.

Schall, J. Neural basis of deciding, choosing and acting. *Nat. Rev. Neurosci.*, 2(1):33–42, 2001.

Schimansky-Geier, L. and Zülicke, C. Harmonic noise: Effect on bistable systems. *Z. Phys. B*, 79:451, 1990.

Schmidt-Hieber, C., Toleikyte, G., Aitchison, L., Roth, A., Clark, B., Branco, T., and Häusser, M. Active dendritic integration as a mechanism for robust and precise grid cell firing. *Nat. Neurosci.*, 20(8):1114, 2017.

Schneidman, E., Berry, M. J., Segev, R., and Bialek, W. Weak pairwise correlations imply strongly correlated network states in a neural population. *Nature*, 440:1007, 2006.

Schwalger, T. and Lindner, B. Analytical approach to an integrate-and-fire model with spike-triggered adaptation. *Phys. Rev. E Stat. Nonlin. Soft Matter Phys.*, 92:062703, 2015.

Schwalger, T. and Schimansky-Geier, L. Interspike interval statistics of a leaky integrate-and-fire neuron driven by gaussian noise with large correlation times. *Phys. Rev. E.*, 77: 031914, 2008.

Schwalger, T., Fisch, K., Benda, J., and Lindner, B. How noisy adaptation of neurons shapes interspike interval histograms and correlations. *PLoS Comp. Biol.*, 6:e1001026, 2010.

Schwalger, T., Droste, F., and Lindner, B. Statistical structure of neural spiking under non-poissonian or other non-white stimulation. *J. Comput. Neurosci.*, 39:29, 2015.

Schwalger, T., Deger, M., and Gerstner, W. Towards a theory of cortical columns: From spiking neurons to interacting neural populations of finite size. *PLoS Comput. Biol.*, 13: e1005507, 2017.

Shadlen, M. and Newsome, W. Neural basis of a perceptual decision in the parietal cortex (area lip) of the rhesus monkey. *J. Neurophysiol.*, 86(4):1916–1936, 2001.

Shafi, M., Zhou, Y., Quintana, J., Chow, C., Fuster, J., and Bodner, M. Variability in neuronal activity in primate cortex during working memory tasks. *Neuroscience*, 146(3): 1082–1108, 2007.

Siegle, P., Goychuk, I., Talkner, P., and Hänggi, P. Markovian embedding of non-markovian superdiffusion. *Phys. Rev. E*, 81:011136, 2010.

Sjöström, P., Rancz, E., Roth, A., and Häusser, M. Dendritic excitability and synaptic plasticity. *Physiol. Rev.*, 88(2):769–840, 2008.

Sompolinsky, H., Crisanti, A., and Sommers, H. J. Chaos in Random Neural Networks. *Phys. Rev. Lett.*, 61:259, 1988.

Song, S., Sjöström, P., Reigl, M., Nelson, S., and Chklovskii, D. Highly nonrandom features of synaptic connectivity in local cortical circuits. *Plos Biol.*, 3:0507, 2005.

Sun, Y. and Kumar, M. Numerical solution of high dimensional stationary fokker–planck equations via tensor decomposition and chebyshev spectral differentiation. *Comput.Math.Appl.*, 67:1960, 2014.

Teeter, C., Iyern, R., Menon, V., Gouwens, N., Feng, D., Berg, J., Szafer, A., Cain, N., Zeng, H., and Hawrylycz, M. Generalized leaky integrate-and-fire models classify multiple neuron types. *Nat. Commun.*, 9:709, 2018.

Touboul, J. and Brette, R. Dynamics and bifurcations of the adaptive exponential integrate-and-fire model. *Biol.cybern.*, 99:319, 2008.

Treves, A. Mean-field analysis of neuronal spike dynamics. *Network: Comput. Neural Syst.*, 4:259, 1993.

Tuckwell, H. C. *Stochastic Processes in the Neuroscience*. SIAM, Philadelphia, Pennsylvania, 1989.

Uhlenbeck, G. E. and Ornstein, L. S. On the theory of the Brownian motion. *Phys. Rev.*, 36:823, 1930.

van Meegen, A. and Lindner, B. Self-consistent correlations of randomly coupled rotators in the asynchronous state. *Phys. Rev. Lett.*, 121(25):258302, 2018.

van Vreeswijk, C. and Sompolinsky, H. Chaos in neuronal networks with balanced excitatory and inhibitory activity. *Science*, 274:1724, 1996.

van Vreeswijk, C. and Sompolinsky, H. Chaotic balanced state in a model of cortical circuits. *Neural Comput.*, 10:1321, 1998.

Veliz-Cuba, A., Kilpatrick, Z. P., and Josic, K. Stochastic models of evidence accumulation in changing environments. *SIAM Review*, 58(2):264–289, 2016.

Vellmer, S. and Lindner, B. Theory of spike-train power spectra for multidimensional integrate-and-fire neurons. *Phys. Rev. Res.*, 1(2):023024, 2019.

Vilela, R. D. and Lindner, B. A comparative study of three different integrate-and-fire neurons: spontaneous activity, dynamical response, and stimulus-induced correlation. *Phys. Rev. E.*, 80:031909, 2009.

Wang, X. J. Probabilistic decision making by slow reverberation in cortical circuits. *Neuron*, 36(5):955–968, 2002.

White, J. A., Rubinstein, J. T., and Kay, A. R. Channel noise in neurons. *Trends Neurosci.*, page 131, 2000.

Wieland, S., Bernardi, D., Schwalger, T., and Lindner, B. Slow fluctuations in recurrent networks of spiking neurons. *Phys. Rev. E*, 92:040901(R), 2015.

Wolfram Research Inc. Mathematica, Version 12.0, 2019. Champaign, IL, https://www.wolfram.com/mathematica.

Wong, K. F. and Wang, X. J. A recurrent network mechanism of time integration in perceptual decisions. *J. Neurosci.*, 26(4):1314–1328, 2006.

Danksagung/Acknowledgments

Ich möchte mich für die engagierte Betreuung durch meinen wissenschaftlichen Lehrer Prof. Dr. Benjamin Lindner herzlich bedanken, der stets ein offenes Ohr für mich hatte und sehr an dem Fortschritt meiner Arbeit interessiert war. In vielen Diskussionen nahm sich Prof. Lindner Zeit meine Fragen umfassend zu beantworten. Er versorgte mich stets mit guten Ideen, Lösungsansätzen und detaillierten Erklärungen und hat damit wesentlich zu der Entstehung dieser Arbeit beigetragen.

Ich möchte mich auch bei meinen Kollegen und Freunden in der Arbeitsgruppe für komplexe Systeme und Neurophysik der Humboldt Universität zu Berlin bedanken. Neben vielen fachlichen Diskussionen, die mir sehr geholfen haben Sachverhalte besser zu verstehen, weiß ich auch den angenehmen Arbeitsalltag und die hilfsbereite und freundliche Atmosphäre sehr zu schätzen und möchte mich für eine gute Zeit bedanken.

I would also like to thank the members of the Laboratório de Sistemas Neurais at the USP in Ribeirão Preto for the warm welcome and for helping me to manage the many difficulties arising due to the different language and culture making my stay in Brazil educational, interesting and exciting.

Ich möchte mich auch bei den Mitgliedern des IRTG 1740 bedanken, durch das ich nicht nur finanzielle Unterstützung, sondern auch viele interessante Einblicke in andere Forschungsdisziplinen rund um komplexe Netzwerke erhalten habe.

Zuletzt möchte ich mich bei meinen Eltern bedanken, deren Unterstützung mir das Studium der Physik überhaupt erst ermöglichte.

List of scientific publications

- **Vellmer S.** and Lindner B. Decision-time statistics of nonlinear diffusion models: Characterizing long sequences of subsequent trials. Submitted to *J. Math. Psychol.*, 2020.
- **Vellmer S.** and Lindner B. Theory of spike-train power spectra for multidimensional integrate-and-fire neurons. *Phys. Rev. Res.*, 1(2):023024, 2019.
- Maximov I.I. and **Vellmer S.** Isotropically weighted intravoxel incoherent motion brain imaging at 7T. *Magn. Reson. Imaging*, 57:124-132, 2019.
- Pena R.F.O.[1], **Vellmer S.**[1], Bernardi D., Roque A.C. and Lindner B. Self-consistent scheme for spike-train power spectra in heterogeneous sparse networks. *Front. Comput. Neurosc.*, 12(9), 2018.
- **Vellmer S.**, Tonoyan A.S., Suter D., Pronin I.N. and Maximov I.I. Validation of DWI pre-processing procedures for reliable differentiation between human brain gliomas. *Z. Med. Phys.*, 28:14-24, 2018.
- **Vellmer S.**, Edelhoff D., Suter D. and Maximov I.I. Anisotropic diffusion phantoms based on microcapillaries. *J. Magn. Reson.*, 279:1-10, 2017.
- **Vellmer S.**, Stirnberg R., Edelhoff D., Suter D., Stöcker T. and Maximov I.I. Comparative analysis of isotropic diffusion weighted imaging sequences. *J. Magn. Reson.*, 275:137-147, 2017.
- Vinding M.S., Brenner, D., Desmond H.Y., **Vellmer S.**, Vosegaard T., Suter D. Stöcker T. and Maximov I.I. Application of the limited-memory quasi-Newton algorithm for multi-dimensional, large flip-angle RF pulses at 7T. *Magn. Reson. Mater. Phy.*, 30(1):29-39, 2017.

[1]These authors have contributed equally to this work.